Development of Lab, Field, and In-Situ Image Collection Systems and Analysis Methods for Soil Characterization

by

Andrea Ventola

A dissertation submitted in partial fulfillment
of the requirements for the degree of
Doctor of Philosophy
(Civil Engineering)
in the University of Michigan
2022

Doctoral Committee:

Professor Roman D. Hryciw, Chair
Associate Professor Adda Athanasopoulos-Zekkos, University of California Berkeley
Assistant Professor F. Estéfan T. Garcia
Professor Radoslaw Michalowski
Professor Clayton Scott

Andrea Ventola

acvent@umich.edu

ORCID iD: 0000-0001-6603-9707

Dedication

This dissertation is dedicated to my family (both my family of orientation and my found families) for caring for and caring about me. I would not be able to write this dissertation if not for their unwavering support and love. This is also dedicated to those who came before me who have sacrificed their time, resources, and own education to make mine possible. My privilege in writing this dissertation is wholly because of their sacrifices. This dissertation is not only my own, but also that of Wilma Ventola, Dominic Ventola, Emily Ventola, Evelyn Ventola, Annigje Verwey, Willem Verwey, Vincenza Ventola, Nick Ventola, Dr. Elizabeth Kupser, and all those who I hold dear in my heart. You have made me into the person I am today. Lastly, this dissertation is dedicated to those who have achieved in the face of adversity. Your success makes our world kinder, more empathetic, and hopeful.

Acknowledgements

There are many people to thank in both my professional and personal lives who have made this dissertation possible. I would first like to thank my advisor, Dr. Roman Hryciw for providing me the opportunity to work with him throughout my graduate studies. Through his guidance, I have had the opportunity to teach, consult, and participate in unique field testing projects during my doctoral studies. I will be forever grateful for these experiences, and for the skills and lessons I have learned from them. I also want to thank Dr. Hryciw for his continual support, transparency, advice, and honesty throughout our time working together. I will strive to emulate Dr. Hryciw's thoroughness and intellectual merit in my future professional endeavors.

I would next like to thank the other members of my committee: Dr. Radoslaw Michalowski, Dr. Adda Athanasopoulos-Zekkos, Dr. Clayton Scott, and Dr. F. Estéfan T. Garcia and for their time, suggestions, insights, and overall guidance for my dissertation. I value each of their involvement in my committee and am honored to present my work to them. To Dr. Michalowski, I want to thank you for being the primary instructor for my first GSI position and for nominating me for the Rackham 2021 Outstanding Graduate Student Instructor Award. Thank you to Dr. Scott for being my cognate committee member and providing fruitful research suggestions throughout my program. I want to thank Dr. Garcia for his flexibility and willingness to join my committee in the summer of 2021. Lastly, I want to extend a warm thank you to Dr. Athanasopoulos-Zekkos. She was my instructor for my first introduction to geotechnical engineering. Through that course, I discovered my deep passion for a field of study of which I previously had no knowledge. She also once gave me a pin that says, "Women also know geotech: you should ask them about it."

Several years later, I still have this pin. Visibility of all genders, races, ethnicities, disabilities, sexual identities, and socioeconomic levels in engineering, including geotechnical engineering, is paramount. Dr. Athanasopoulos-Zekkos is part of this important work.

I would like to thank ConeTec, and more specifically Ron Dolling for his work to fabricate the VisCPT. His diligence and expertise were always, and will always be appreciated for this project. Thank you to the Rackham Graduate School at the University of Michigan for awarding me the 2021 Outstanding Graduate Student Instructor Award and for providing financial support throughout my doctoral education. Also thank you to the staff and faculty of the Civil and Environmental Engineering (CEE) Department for their support, financial and otherwise. They have been my educational home since my undergraduate education and I have always felt valued and supported by them. A special thank you is for Anne Speigle for continually having my best interest in mind. I would next like to extend a deep thank you to Steve Donajkowski. I could not have asked for a kinder, more helpful, and more dedicated teammate and friend than I found in Steve. My research with the FieldSed and Sed360 systems would not have been possible without his expert design suggestions and fabrication skills. I would also like to thank the team at the Center for Research on Learning and Teaching in Engineering (CRLT-Engin) for providing me the unique opportunity to share my passion for teaching by supporting other student instructors throughout the College of Engineering. To my CRLT-Engin boss Audra Baleisis, thank you for showing me that vulnerability and goodwill are immeasurable strengths in a team leader.

My final set of thanks and praise is for my family and friends. Thank you to my mother and father, Wilma and Dominic for your unwavering love, emotional and financial support, unflinching reliability, and generosity. I love you eternally. To my older sisters Emily and Evelyn, thank you for your love, fierce loyalty, and for always making sure no one forgets my embarrassing

and awkward moments. I look forward to more of those moments as I walk through life with both of you always right by my side. Thank you to my grandparents Annigje, Willem, Vincenza, and Nick; my success is from your sacrifices and I hope I have made you proud. Thank you to Izzie Ventola for the always-entertaining conversations. Deep love and appreciation is also extended to the rest of my family including Len Verwey and Heather Johnson.

To my dear friends, thank you. You are my family and I love you: Dr. Elizabeth Kupser, a doyenne of her own right and my life-long friend; Goldie Gunawan, a trailblazer in our industry who always gracefully loses at air hockey; Tova S. Lentz, an inspiring educator and climbing partner; Gabe Draughon and Anna Stuhlmacher, two delightful campaign companions and proud parents of my godchild; Athina Grizi, Sampurna Datta Bhattacharya, Nina Zabihi, Saloni Dagli, Christian Flores Carreras, Cassandra Champagne, Shuvajit Das, Emily Sheetz, and all of my other friends who have helped me see the beauty and power of unconditional, timeless friendship.

Table of Contents

Dedication ii

Acknowledgements iii

List of Tables ix

List of Figures x

List of Appendices xvi

Abstract xvii

Chapter 1 Introduction 1

1.1 Motivation 7

1.2 Objectives 11

1.3 Tasks and organization 15

Chapter 2 Literature Review 17

2.1 Soil assembly image-based characterization: deterministic methods 21

2.2 Soil assembly image-based characterization: pixel intensity spatial methods 28

Chapter 3 SedImaging Systems 32

3.1 Original Hardware: LabSed 32

3.2 FieldSed 36

3.2.1 The FieldSed System 36

3.2.2 Specimen Prewashing 40

3.2.3 Example FieldSed Results 44

3.2.4 Particle size distribution of Kalamazoo River sediments by FieldSed 46

3.3 Sed360 62
3.3.1 The Sed360 system 63
3.3.2 Performing a Sed360 test 68
3.3.3 Sed360 specimen utilization in the image analysis 73
3.3.4 Summary of Sed360 improvements over previous SedImaging systems 73
3.4 Chapter Summary 74
Chapter 4 Haar Wavelet Transform (HWT)-Based Image Analysis 76
4.1 Original HWT-based image analysis for SedImaging 76
4.2 Advancements to SedImaging's HWT-based image analysis method 84
4.2.1 The New PPD-CA calibration 84
4.2.2 Autoadaptive HWT-based image analysis for SedImaging 87
4.2.3 Sed360 PSD results using the autoadaptive HWT-based analysis method 97
4.3 Chapter Summary 110
Chapter 5 Vision Cone Penetrometer (VisCPT) 112
5.1 First and Second Generation VisCPT Hardware Systems 112
5.2 Third Generation VisCPT Hardware System 114
5.2.1 3D-Printed Prototype for Benchtop Calibration Testing 114
5.2.2 Third Generation VisCPT for Calibration Chamber Testing 118
5.3 Haralick Spatial Gray Level Dependence Method (SGLDM) Image Analysis 122
5.4 Benchtop calibration testing with the third generation VisCPT prototype 125
5.4.1 Haralick SGLDM analysis of VisCPT images 125
5.4.2 HWT-based image analysis of VisCPT images 130
5.4.3 Soil differentiation by the SGLDM and HWT-based method 133
5.5 Chapter Summary 144
Chapter 6 Summary and Future Recommendations 146

6.1 Summary 148

6.1.1 Summarizing SedImaging research 148

6.1.2 Summarizing VisCPT research 151

6.1.3 Research Significance and Broader Impacts 153

6.2 Future Recommendations 156

Appendix A: Investigating the effect of uneven particle illumination on HWT-based PSDs 165

Appendix B: Overview of Haralick et al. (1973)'s Spatial Gray Level Dependence Method (SGLDM) textural indices 181

Appendix C: CPT vs. VisCPT data for a Treasure Island soil profile 183

Appendix D: Section 5.4.3 separated *CA-PPD* data and corresponding trend lines for the eight soils tested with the VisCPT 186

Appendix E: Comparing *CA-PPD* results for different 2NS data sets gathered with the VisCPT 191

Bibliography 192

List of Tables

Table 1-1. Selection of standard sieves and their mesh openings..... 2

Table 1-2. Comparing SedImaging systems and sieving..... 13

Table 2-1. Types of image-based soil characterization methods with selected examples..... 19

Table 3-1. Comparing LabSed and FieldSed systems. 40

Table 3-2. Verification testing of select Kalamazoo River specimens..... 57

Table 4-1. 2NS sand ranges for Sed360 calibration testing..... 85

Table 4-2. Details and results of the five sands tested in the Sed360..... 101

Table 5-1. 2NS sand particle size ranges used in VisCPT benchtop calibrations testing..... 126

Table A-1 Comparing PSD Data for Images 1 and 2. 171

List of Figures

Figure 1-1. Sieve stack. 2

Figure 1-2. Sieve stack loaded into sieve shaker. 3

Figure 1-3. Example Particle Size Distribution (PSD) for a medium sand (according to the USCS). 4

Figure 1-4. Cone penetration test (CPT) (americangeoservices.org) 7

Figure 2-1. Illustrations of soil particle at the time of image capture for image-based soil characterization methods. (a) Line, dispersed, dynamic, non-sorted, (b) Plane, dispersed, dynamic, non-sorted, (c) Plane, dispersed, static, non-sorted, (d) Plane, dispersed, static, sorted, (e) Plane, contacting, static, non-sorted, (f) Plane, contacting, static, sorted, (g) Assembly, contacting, static, non-sorted, (h) Assembly, contacting, static, sorted. 18

Figure 2-2. Set up used for the Automated Grain Sizing (AGS) Method. (Graham et al. 2005b) 23

Figure 2-3. Screenshot of BASEGRAIN where a known scale (white and red pole located at the top of the image) is used to establish the image magnification. (BASEGRAIN 2013)..... 25

Figure 2-4. Example of necessary manual correction during the OPTGRAN-CS method. (a) Original soil image, (b) Automatically-generated soil segmentation, (c) Manually-corrected soil segmentation (Adapted from Chávez et al. 2015). 28

Figure 3-1. The LabSed. 34

Figure 3-2. The LabSed presorter tube. 34

Figure 3-3. LabSed presorter tube's vacuum-release system. (a) Vacuum-sealed rubber membrane, (b) Soil specimen remains in the presorter after the membrane is removed, (c) Presorter is moved to the top of the sedimentation column and the rubber stopper is removed. . 35

Figure 3-4. The FieldSed. 37

Figure 3-5. FieldSed positioning bracket. (a) Unlocked, (b) Locked. 37

Figure 3-6. FieldSed rubber stopper, base, and positioning dowels. 38

Figure 3-7. Soil specimen release from the FieldSed presorter. (a) Prior to release, (b) Several seconds after release. 39

Figure 3-8. FieldSed parallel testing hardware. (a) Sedimentation columns in a testing rack, (b) A technician preparing many sedimentation columns. 40

Figure 3-9. Prewashing and SedImaging by FieldSed summary design. 43

Figure 3-10. SedImaging results using the FieldSed. (a) Sand A, (b) Sand B. 45

Figure 3-11. Kalamazoo River and this project's testing locations. 47

Figure 3-12. Field laboratory for testing the Kalamazoo River sediments. 48

Figure 3-13. Specimen A. (Top) verification PSDs, (Bottom) Field [left], Field-Repeat [center], and Lab [right] photographed FieldSed sides. 50

Figure 3-14. Specimen B. (Top) verification PSDs, (Bottom) Field [left], Field-Repeat [center], and Lab [right] photographed FieldSed sides. 51

Figure 3-15. Specimen C. (Top) verification PSDs, (Bottom) Field [left], Field-Repeat [center], and Lab [right] photographed FieldSed sides. 52

Figure 3-16. Specimen D. (Top) verification PSDs, (Bottom) Field [left], Field-Repeat [center], and Lab [right] photographed FieldSed sides. 53

Figure 3-17. Specimen E. (Top) verification PSDs, (Bottom) Field [left], Field-Repeat [center], and Lab [right] photographed FieldSed sides. 54

Figure 3-18. Specimen F. (Top) verification PSDs, (Bottom) Field [left], Field-Repeat [center], and Lab [right] photographed FieldSed sides. 55

Figure 3-19. Specimen G. (Top) verification PSDs, (Bottom) Field [left], Field-Repeat [center], and Lab [right] photographed FieldSed sides. 56

Figure 3-20. Particle size distributions by size ranges for quality control Specimens A through G. 60

Figure 3-21. The Sed360. (a) Full view, (b) Detailed view of bottom. 64

Figure 3-22. Sed360 positioning bracket. (a) Closed, (b) Opened, (c) Sedimentation column inserted. 65

Figure 3-23. Sed360 pedestal, load transfer system, and rotation stage. 65

Figure 3-24. Sed360 load transfer system. (a) Drive block, (b) Flexible shaft coupling, (c) Bearing block, (d) Rotation platform. 67

Figure 3-25. Image stitching of the Sed360 system. 71

Figure 3-26. Unwrapped cylinder image of example sand tested with the Sed360 system. 72

Figure 4-1. HWT analysis squares for a Sed360 soil specimen. 77

Figure 4-2. Energy curves of three example HWT analysis squares from Fig. 4.1. 79

Figure 4-3. Example of the HWT method used with SedImaging. (a)Analysis area and corresponding Energy versus decomposition level plot, (b) grayscale averaging areas for the 5^{th}, (c) 6^{th}, and (d) 7^{th} decomposition levels. 81

Figure 4-4. HWT calibration results for three example HWT analysis squares from Fig. 4.1. 82

Figure 4-5. Sed360 PSD results from Fig. 4.1 highlighting three example HWT analysis squares 83

Figure 4-6. *PPD-CA* calibration using the Sed360 data from Table 4.1. 85

Figure 4-7. Analyzing the same sand specimen image using different sizes of HWT analysis squares. (A) Sand in Sed360, (b) PSD results. 87

Figure 4-8. Examples of analysis squares with "acceptable" E-distributions. (a) Analysis square containing smaller particles, and (b) Square containing larger particles. 89

Figure 4-9. Examples of analysis squares with “unacceptable” E-distributions. (a) HWT analysis square is too small relative to the soil particles, (b) Range of particle sizes is too large and (c) Energy curve impacted by particle coloring. 90

Figure 4-10. Example illustrating guiding principle (d) of the autoadaptive sizing method of HTW analysis squares. 94

Figure 4-11. Flow chart followed in Step 3 of the autoadaptive HWT analysis square sizing method. 96

Figure 4-12. Sed360 sand specimens containing various size percentages per sieve analysis (coarse/medium/fine sands): (a) 67/23/10, (b) 50/0/50, (c) 37/51/12, (d) 31/46/23, and (e) 10/40/50. 98

Figure 4-13. Sed360 Results for Specimen A. (a) Autoadaptively determined analysis squares used to generate the HWT-based PSD, (b) PSD results. 99

Figure 4-14. Sed360 Results for Specimen B. (a) Autoadaptively determined analysis squares used to generate the HWT-based PSD, (b) PSD results. 99

Figure 4-15. Sed360 Results for Specimen C. (a) Autoadaptively determined analysis squares used to generate the HWT-based PSD, (b) PSD results. 100

Figure 4-16. Sed360 Results for Specimen D. (a) Autoadaptively determined analysis squares used to generate the HWT-based PSD, (b) PSD results. 100

Figure 4-17. Sed360 Results for Specimen E. (a) Autoadaptively determined analysis squares used to generate the HWT-based PSD, (b) PSD results. 101

Figure 4-18. Composition breakdown of the five specimens by percent. (a) Sand type percentages within each specimen according to sieve results, and (b) percentage of the specimen images analyzed using each of the autoadaptively-selected HWT square sizes. 102

Figure 4-19. A Specimen B 256 x 256 pix^2 analysis square and its corresponding 128 x 128 pix^2 quadrants. 104

Figure 4-20. Investigating the HWT analysis squares at the coarse and fine sand interface in Specimen B. 107

Figure 4-21. Invalid 512 x 512 pix^2 energy curves leads to an undersizing of the Specimen E's coarse sand. 109

Figure 5-1. Earlier Vision Cone Penetrometers (VisCPTs). Top: First generation VisCPT (1997), Bottom: Second generation VisCPT (2005). 113

Figure 5-2. 3D-printed prototype of the third generation VisCPT vision module. (a) Vision module, (b) Schematic of the module's cross-section. 116

Figure 5-3. Images of 2NS sand captured with the VisCPT prototype. Midpoint particle sizes of (a) medium sand, 1.85mm, (b) medium sand, 0.86mm, (c) fine sand, 0.256mm, (d) silt, 0.046mm. 117

Figure 5-4. Benchtop calibration testing setup using the VisCPT prototype. 117

Figure 5-5. Third generation VisCPT. 118

Figure 5-6. Smoothed transition areas in the VisCPT's vision module. 120

Figure 5-7. Images of soils captured with the third generation VisCPT. Midpoint particle sizes of the sands (a) 2NS medium sand, 1.85mm, (b) 2NS medium sand, 0.86mm, (c) 2NS fine sand, 0.256mm, (d) 2NS silt, 0.046mm, (e) Red clay, (f) Sand used in upcoming calibration chamber testing. 121

Figure 5-8. Profile logs for Energy, Contrast, and Local Homogeneity Haralick texture indices of a known soil profile (Ghalib et al. 2000). 124

Figure 5-9. Photos of each 2NS sieve size range from Table 5.1. 127

Figure 5-10. Haralick textural indices versus Pixels per Particle Diameter (PPD) as part of the VisCPT benchtop calibration testing for 2NS sand. (a) Contrast, (b) Correlation, (c) Homogeneity, (d) Variance, (e) Energy. 129

Figure 5-11. *CA* versus *PPD* for 2NS particles photographed with the VisCPT prototype. 131

Figure 5-12. Adjusted VisCPT 2NS *CA-PPD* data compared to the Sed360's Eq. 4.5. 133

Figure 5-13. Testing different soils with the VisCPT prototype. 136

Figure 5-14. *CA* versus *PPD* results for different soils tested with the VisCPT. 137

Figure 5-15. Empirical *CA-PPD* trend lines of the soils from Figs. 5.13 and 5.14. 139

Figure 5-16. Contrast vs. *PPD* for various soils. 141

Figure 5-17. Correlation vs. *PPD* for various soils. 141

Figure 5-18. Homogeneity vs. *PPD* for various soils. 142

Figure 5-19. Variance vs. *PPD* for various soils. 142

Figure 5-20. Energy vs. *PPD* for various soils. 143

Figure 6-1. Different sands tested in the Sed360. (a) Brady, Texas, (b) Ottawa, and (c) Nesika Beach..... 159

Figure 6-2. Example SedImaging PSD results for the Brady, Texas, sand in Fig. 6.1. 161

Figure 6-3. Example SedImaging PSD results for the Ottawa sand in Fig. 6.1..... 162

Figure 6-4. Example SedImaging PSD results for the Nesika Beach sand in Fig. 6.1. 163

Figure A-1. Two soil images with known with a particle size range between 0.3mm and 0.212mm (material retained between the US Standard No. 50 and No. 70 sieves). (a) Image 1, (b) Image 2..... 166

Figure A-2. Average grayscale pixel intensity values for Image 1 in Fig. A.1(a). (a) Row values, (b) Column values. 167

Figure A-3. Average grayscale pixel intensity values for Image 2 in Fig. A.1(b). (a) Row values, (b) Column values. 168

Figure A-4. PSD data using two different analysis area sizes in the original HWT-based method. (a) Image 1, (b) Image 2. 170

Figure A-5. Image 1 analyzed using two different analysis areas in the original HWT-based method. (a) 1024 x 1024 pix^2 and 512 x 512 pix^2 analysis areas and their PSD data points, (b) 512 x 512 pix^2 energy using Eq. 4.1's energy definition, (c) 1024 x 1024 pix^2 energy distributions using Eq. 4.1's energy definition. 173

Figure A-6. Average grayscale pixel intensity values for each of Image 1's 1024 x 1024 pix^2 analysis areas. (a) Row values, (b) Column values. 175

Figure A-7. Image 1 analyzed using two different analysis areas in the original HWT-based method. (a) 1024 x 1024 pix^2 and 512 x 512 pix^2 analysis areas and their PSD data points, (b) 512 x 512 pix^2 energy using Eq. A.1's energy definition, (c) 1024 x 1024 pix^2 energy distribution using Eq. A.1's energy definition. 178

Figure A-8. Image 1 analyzed using two different analysis areas in the original HWT-based method. (a) 1024 x 1024 pix^2 and 512 x 512 pix^2 analysis areas and their PSD data points, (b) 512 x 512 pix^2 energy using Eq. A.2's energy definition, (c) 1024 x 1024 pix^2 energy distributions using Eq. A.2's energy definition. 179

Figure C-1. Soil profile logs for a Treasure Island case study. (a) CPT data, (b) VisCPT data. (Ghalib et al. 2000). 184

Figure D-1. 2NS *CA-PPD* data in Section 5.4.3 VisCPT testing. 187

Figure D-2. Costa Rica *CA-PPD* data in Section 5.4.3 VisCPT testing. 187

Figure D-3. Nesika Beach *CA-PPD* data in Section 5.4.3 VisCPT testing. 188

Figure D-4. Upper Peninsula *CA-PPD* data in Section 5.4.3 VisCPT testing. 188

Figure D-5. Treasure Island *CA-PPD* data in Section 5.4.3 VisCPT testing. 189

Figure D-6. Scotts Valley *CA-PPD* data in Section 5.4.3 VisCPT testing. 189

Figure D-7. Ottawa *CA-PPD* data in Section 5.4.3 VisCPT testing. 190

Figure D-8. Nevada *CA-PPD* data in Section 5.4.3 VisCPT testing. 190

Figure E-1. *CA-PPD* data for 2NS data photographed by the VisCPT at different illumination voltages. 191

List of Appendices

Appendix A: Investigating the effect of uneven particle illumination on HWT-based PSDs 165

Appendix B: Overview of Haralick et al. (1973)'s Spatial Gray Level Dependence Method (SGLDM) textural indices 181

Appendix C: CPT vs. VisCPT data from a Treasure Island soil profile 183

Appendix D: Section 5.4.3 separated *CA-PPD* data and corresponding tend lines for the eight soils tested with the VisCPT 186

Appendix E: Comparing *CA-PPD* for different 2NS data sets gathered with the VisCPT 191

Abstract

Image-based soil characterization methods are proven to be rapid, accurate, clean, lower-cost, and (semi-)automated procedures for determining the particle size distribution (PSD) of coarse-grained materials. A PSD is used to classify a soil as well as provide an initial estimate for various properties including its compressibility, permeability, and unit weight. Soil PSDs are utilized extensively throughout geotechnical, environmental, and construction engineering; earth sciences; and related industries. The traditional method for determining a soil's PSD is by sieving, a time-, resource-, and energy-intensive procedure. Therefore, there has been an increased demand for determining soil PSDs using image-based methods as an alternative to sieving.

One such image-based method was developed in 2014 and is called "SedImaging." Short for "sediment imaging," SedImaging captures an image of a soil specimen that has sedimented through a water column. The photographed soil assembly is analyzed by a sieve-calibrated mathematical wavelet method. The results are a PSD with excellent agreement to sieving without any of the procedural disadvantages of sieving. This dissertation details two SedImaging hardware systems, "FieldSed" (2017) and "Sed360" (2020) which were developed by the author to expand upon the advantages of the original 2014 SedImaging method. These newer systems have different applications; the FieldSed is a field-portable device that was used in a large-scale soil characterization project for the Kalamazoo River, and the Sed360 is a largely automated test that has expanded the range of testable soils by SedImaging by over a factor of 2.5. The image analysis method used with the original SedImaging system has also undergone a major transformation that is described within this dissertation. When used with the Sed360, this new autoadaptive image

analysis method can correctly size soil particles across the entire sand size range (as defined by the Unified Soil Classification System), as well as accurately generate soil PSDs for a range of gradations, including gap-graded specimens. The SedImaging hardware and image analysis advancements detailed in this dissertation transform this sieving alternative into a nearly fully automated, low cost, rapid, and robust soil characterization technique.

Image-based soil characterization methods can also be combined with existing geotechnical testing systems to enhance the original system's capabilities. An example of this is with the popular cone penetrometer (CPT). A CPT was fitted with cameras that were used to photograph passing soil layers during CPT advance. Known as the "VisCPT" (short for the "vision cone penetrometer"), this newer system refines CPT soil layer delineation and is capable of even detecting thin (several centimeter thick) soil layers that are missed by CPT results. To do so, textural indices are determined for VisCPT soil images. These textural indices have been correlated to soil particle size. The latest research involving the VisCPT is presented in this dissertation. This includes replacing the multiple cameras required in the earlier VisCPT generations with a single high-resolution camera and recalibrating the textural indices analysis method. This dissertation also details exploratory research on combining the textural indices and the mathematical wavelet method (previously used mainly with SedImaging) to expand the application of both the VisCPT and SedImaging. The results of this research will be used with the latest VisCPT system to detect thin soil layers in scheduled calibration chamber testing and in earthquake prone regions of the world.

Chapter 1 Introduction

A soil's particle size distribution (PSD) is an essential index property in geomechanics, geotechnical engineering, and related fields for classifying coarse-grained soils. The PSD, along with particle shape and relative density, also provide an initial estimate of soil properties such as compressibility, the angle of internal friction, and soil unit weight. There is also a continual need for determining numerous, repetitive, rapid, low energy, and low cost PSDs. The applications of these PSDs for sands include filtration, beach nourishment, roadwork, hydro-fracking, foundry casting, concrete making, sandblasting, manufacturing of abrasives, glass-making, quarrying operations, and others.

The traditional method for determining a soil's PSD is through sieving. Sieving is a standardized (ASTM C136/C136M-19) laboratory procedure that uses a stack of wire meshes with various-sized openings. The sieves are stacked with the largest opening mesh on the top of the stack, with progressively smaller opening meshes farther down. Six sieves with different mesh sizes typically form a sieve stack. At the base of the stack is a pan. Figure 1.1 shows a sieve stack ready for testing. Sieves can have a variety of dimensions, but the ones shown in Fig. 1.1 have a diameter of 20.3cm (8in). Table 1.1 lists a selection of standard sieves and their mesh opening sizes. The table also includes soil particle types defined by the sieve openings (e.g. gravel, sand, silt etc.) according to the Unified Soil Classification System (USCS) (ASTM D2487-17ε1).

Figure 1-1. Sieve stack.

Table 1-1. Selection of standard sieves and their mesh openings.

Standard Sieve Number	Mesh Opening [mm]	Mesh Opening [in]	Soil Particle Type Retained on Sieves [a]
3”	75	3	*Cobbles and boulders are coarser than 3” sieve*
2 ½”	63	2.5	Coarse Gravel
1”	25	1	
¾”	19	0.75	
¼”	6.3	0.25	Fine Gravel
No. 4	4.75	0.19	
No. 8	2.36	0.09	Coarse Sand
No. 10	2.0	0.08	
No. 20	0.85	0.03	Medium Sand
No. 30	0.6	0.024	
No. 40	0.425	0.017	
No. 50	0.3	0.012	Fine Sand
No. 100	0.15	5.9×10^{-3}	
No. 200	0.075	2.95×10^{-3}	
			Silts and clays are finer than No. 200 sieve

[a] According to the Unified Soil Classification System (USCS)

To determine a coarse-grained soil's PSD by sieving, the soil is first oven-dried. It is then poured into the top of the sieve stack and the whole system (sieves, soil, and pan) are covered and placed into a device that mechanically shakes the systems for a fixed amount of time. A sieve stack in a sieve shaker is pictured in Fig. 1.2.

The shaking causes the soil particles to fall through the various mesh openings. A soil particle naturally rests on top of the sieve that has a mesh opening smaller than an intermediate dimension across a diagonal of the soil particle. Through this process, the soil specimen will sort by particle size; larger soil particles will be retained on the sieves located at the top of the sieve stack (which have larger mesh size openings), and smaller particles will eventually rest on lower sieves (with smaller mesh openings). Any soil particles that are finer than all of the mesh sizes in the sieve stack are retained in the pan at the bottom of the stack.

Figure 1-2. Sieve stack loaded into sieve shaker.

After the shaking is complete, the sieve stack is removed, and the portion (by weight) of the soil specimen that is retained on each of the sieves is recorded. From there, the soil's weight-based PSD is calculated. With this PSD, the soil can be classified using a number of standardized classification systems, the USCS (ASTM D2487-17ε1) being common in the field of civil engineering. A soil's classification provides an initial estimate of soil behavior for infrastructure design decisions, such as building foundation design, roadway construction, slope stability, and tunnel engineering. An example PSD of a sand is plotted in Fig. 1.3. Based on USCS soil particle size classifications, over 50% of the soil particles in this example specimen fall within the medium sand range, therefore classifying this specimen as a medium sand.

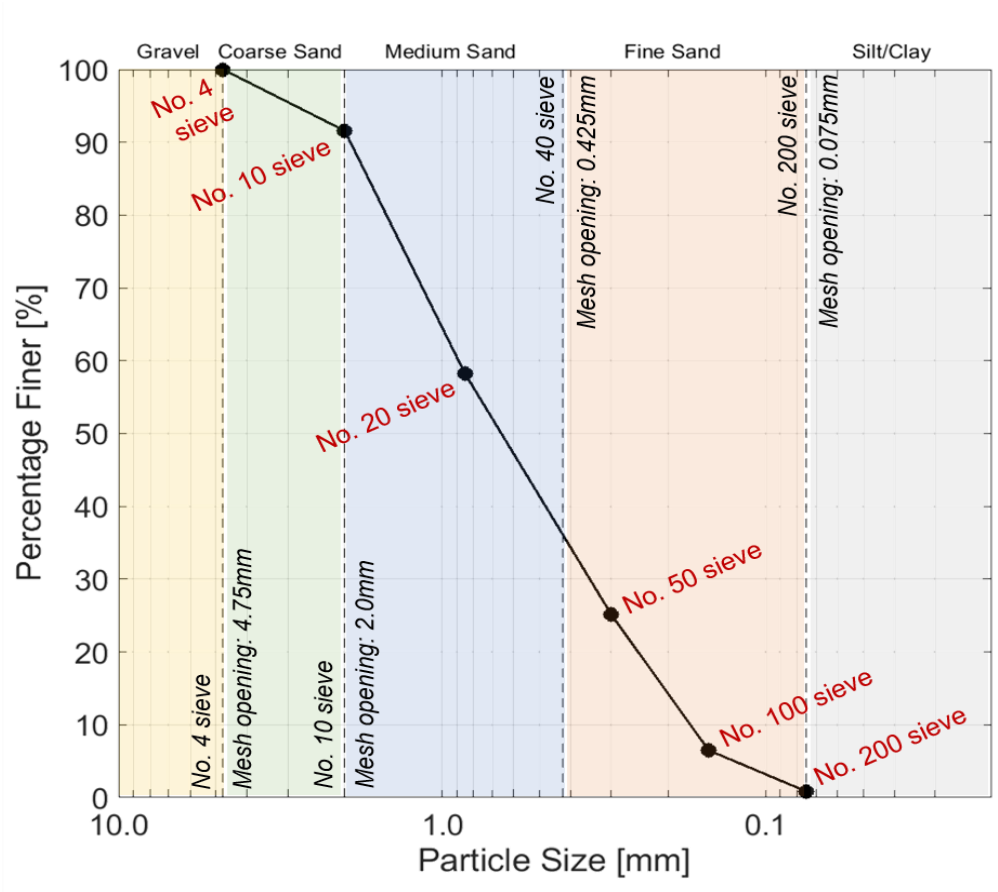

Figure 1-3. Example Particle Size Distribution (PSD) for a medium sand (according to the USCS).

Despite its simplicity, sieving is costly and time-consuming, as will be discussed in Section 1.1 (and later in Chapter 3). The many shortcomings of sieving are tipping the scales toward more advanced and less expensive methods for PSD determination. Because of rapid advances in camera technology and analysis methods, image-based methods are leading the way among alternatives to sieving. While there is still no single test that can size particles spanning the many orders of magnitude of particle sizes in soils (cobbles, gravels, sands, etc.), image based methods (Chapter 2) hold the promise of doing so. One such method was developed by Ohm and Hryciw (2014) and is called SedImaging. **SedImaging and its evolution is one of the two main areas of focus for this dissertation.**

***

Though most image-based soil characterizations are typically performed ex-situ in a laboratory setting (including SedImaging, as will be discussed in Section 1.1), in-situ methods are also available. In-situ image-based characterization methods often provide less detailed, though still useful, results than those performed ex-situ. For instance, a medium sand's complete PSD cannot be determined by an in-situ method, but the in-situ method *can* differentiate this sand from the other soil layers in the strata, such as finer sands or clays. This type of soil profile delineation was previously possible with traditional (non image-based) in-situ methods, but is now enhanced by introducing image-based methods into the existing testing procedures.

An example of this involves the cone penetration test (CPT). Developed in the early to mid-20th century, the CPT is an accurate (though not image-based) in-situ soil test that generates nearly continuous soil profiles through correlations between the device's tip resistance, side friction, and pore pressure with soil types (Robertson et al. 1986, Kulhawy and Mayne 1990, Schneider et al. 2008, Abbaszadeh Shahri et al. 2015). The CPT test pushes a slender circular rod

with a circular cone tip at a fixed rate (typically 2cm/s, 0.79in/s) vertically through a soil profile while recording the aforementioned data (tip resistance, side friction, and pore pressure). The CPT cone tip can come in a variety of dimensions, but $10cm^2$ ($1.55in^2$) and $15cm^2$ ($2.33in^2$) are the most common cone cross sections. A schematic of a CPT is shown in Fig. 1.4.

The CPT holds many advantages (Shin 2005) over another common in-situ (non image-based) testing method known as the Standard Penetration Test (SPT), which correlates the mechanical properties of a soil to the number of hammer blows required to incrementally advance a cylindrical sampler through it. However, the SPT does afford the ability to gather soil samples for laboratory testing, something that is not possible with the CPT. In response to this, the Vision CPT (known as the "VisCPT") was created. The VisCPT equips a traditional CPT with camera(s) to obtain video and images of in-situ soil during CPT advance. Image analysis is performed on the continuous stream of images. This analysis is able to detect thin soil strata not revealed in traditional CPT logs (Ghalib et al. 2000, Hryciw et al. 2009). **The VisCPT and its evolution is the second of the two main areas of focus for this dissertation.**

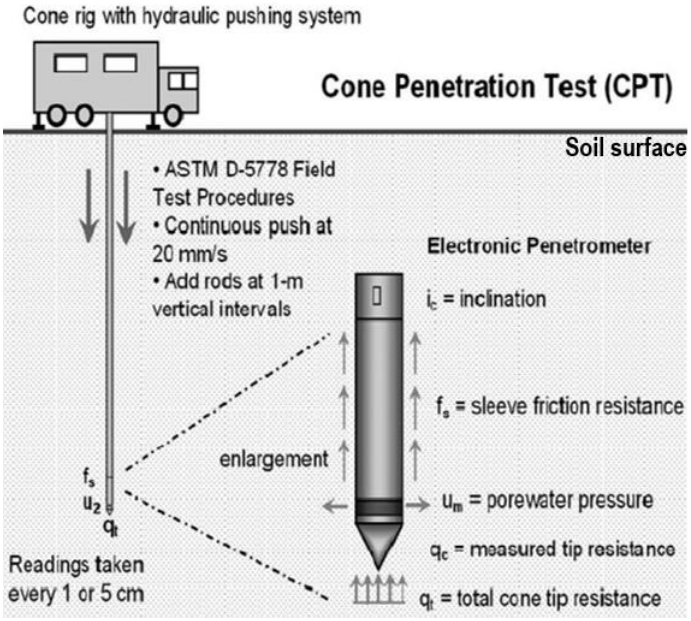

Figure 1-4. Cone penetration test (CPT) (americangeoservices.org)

1.1 Motivation

Although sieving is the industry standard for determining PSDs of coarse-grained materials, the test is time- and energy-intensive. Soils need to be fully oven-dried before being sieved, adding to the testing time of this procedure. Sieves require constant cleaning between tests, and even with regular maintenance, the wire meshes can easily become clogged and torn. Replacing a sieve costs $70 to over $250 per sieve, depending on the sieve diameter and mesh opening. The sieve shaker is loud and can cause fine soil particles to become airborne, leading to an unhealthy testing environment. The sieve test also requires electricity for both oven drying and running the sieve shaker. This limits the sieve test to a laboratory environment. Sieving also requires user intervention throughout the testing procedure, from loading a soil specimen into the sieve stack, to weighing each sieve after testing, to cleaning the individual sieves. Ohm et al. (2013) details these and other disadvantages of sieving.

Ohm and Hryciw (2014) developed "SedImaging" (short for sediment imaging) in response to the disadvantages of sieving. The original SedImaging system (referred to throughout this

dissertation as “LabSed” to differentiate it from its successor systems) is a laboratory device used to determine PSDs of coarse-grained soils. The LabSed was developed as a clean and rapid alternative to sieving. The test involves releasing a soil specimen into a tall column of water. When soil particles settle through water, they naturally sort by size. The particles deposit in an assembly with the coarsest grains at the bottom and progressively finer particles grading to the top. The settled soil assembly is photographed through a glass viewing window. Ohm and Hryciw (2014) showed that image analysis of such a sorted soil can produce the soil’s PSD. To do so, a SedImaging soil assembly image is incrementally analyzed using a mathematical analysis called the Haar (1910) Wavelet Transform (HWT).

Wavelet analysis has become a powerful tool in various civil engineering disciplines and related fields including tunneling (Ding et al. 2011), constitutive modeling of soils (Ohkami et al. 2006), structural dynamics (Chatterjee 2015), geophysics (Pang et al. 2020), seismology (Vassiliou and Makris 2011, Mollaioli and Bosi 2011), seismic exploration (Cabrera-Navarrete et al. 2019), site characterization (Ching et al. 2015), sedimentary geology (Prokoph and Patterson 2004), and soil particle characterization (Sudarsan et al. 2018, and Shin and Hryciw 2004).

Chapter 4 discusses the HWT-based image analysis method used with SedImaging, but an overview of the method is introduced here. The analysis method developed by Ohm and Hryciw (2014) utilizes the HWT to produce hundreds of data points for a SedImaging PSD. Each data point comes from a small (originally 128 pixel by 128 pixel) “analysis square” section of the captured image. There are hundreds of such squares in a grid pattern covering the entire captured image. Since porosities in the sedimented soil column have been shown to be relatively uniform (Hryciw and Jung 2008), each analysis square represents the same volume percentage of the specimen’s soil solids.

The HWT-based method does not determine the actual size of individual particles. Instead, it utilizes the image's grayscale distribution to yield one data point representing the size of the particles within each analysis area. For each analysis square, an HWT index calibrated to a sieve-defined particle size is calculated. Because of this calibration, there is overall excellent agreement between sieve and SedImaging PSDs. Previous publications have documented this success (Hryciw et al. 2015, Ohm and Hryciw 2014, Ventola and Hryciw 2019, Ventola et al. 2020b), including a detailed report published by the Michigan Department of Transportation (MDOT) that compares SedImaging to sieving results on a rigorous statistical basis (Hryciw and Ohm 2012).

The HWT method requires that an analysis square be *small enough* that the particles contained within it are approximately the same size. (This is why soil specimens are sedimented through a tall water column as part of SedImaging testing.) At the same time, the analysis square must be *large enough* so that it contains a statistically significant number of particles for the grayscale analysis. Because of this, the range of testable soils for the original LabSed was limited to medium and fine sands (2.0mm to 0.075mm or between the US standard No. 10 and No. 200 sieves).

Unlike sieving, SedImaging does not require soil specimens to be oven dried prior to testing. As such, SedImaging can be performed in a fraction of the time to run a sieve test. SedImaging is low noise, cleaner, and requires less maintenance than sieves. SedImaging PSDs are formed from hundreds of data points, while those from sieving are often formed from only six to 10 data points. Therefore, SedImaging PSDs are able to capture more detail in a soil's gradation than is realistically possible with sieving PSDs.

However, SedImaging via LabSed is not without its own set of limitations, as will be outlined in Chapters 3 and 4. In addition to the aforementioned limited size range of testable soils

for LabSed, the system consists of large, heavy hardware, which restricts the system to a laboratory environment. Also, similar to sieving, analyzing a soil via the LabSed requires user intervention throughout the testing procedure. These three LabSed limitations (limited range of testable soils, cumbersome hardware, and non-automated testing) form the crux of the SedImaging research motivations presented within this dissertation. The outcome is two new SedImaging systems, the FieldSed and the Sed360, as well as a reformulated HWT-based image analysis method to use with SedImaging. Section 1.2 introduces these research areas.

***

This dissertation's research motivations for SedImaging, its evolution, and its HWT-based image analysis method are evident when discussing the pitfalls of sieving and the limitations of LabSed. However, the motivations involving the VisCPT have to be discussed with less specificity because of this system's originality. The VisCPT takes an existing system, the CPT, and transforms it into a device with a new set of applications. By equipping a CPT with camera(s), the system can now be used to detect thin (several centimeters thick) soil layers that go unnoticed by SPT and CPT methods. This is particularly useful when these thin layers are liquefiable and in earthquake-prone regions (see future work in Section 6.2). The VisCPT can also be used to observe in-situ soil migration and soil piping susceptibility (Hryciw and Ohm 2013, Zheng and Hryciw 2014), as well as characterizing the effects an advancing probe has on soil layer interfaces (Shin 2005, Hryciw et al. 2005).

The first generation of the VisCPT was developed in 1997 and the second generation in 2005. Both VisCPT generations were the centerpiece of numerous successful laboratory and in-situ testing programs (Hryciw et al. 1998, Ghalib et al. 2000, Hryciw et al. 2005). Physically smaller and higher resolution camera technology drove the development of the third generation

VisCPT. The geotechnical engineering firm ConeTec Investigations Ltd. fabricated a prototype of the third generation VisCPT in 2019, and the final system in 2022. Research involving both the prototype and the final third generation VisCPT device is presented within this dissertation and is foundational for propelling this powerful in-situ geotechnical tool into full-scale use in the future. The research presented within this dissertation involving the third generation VisCPT is introduced in Section 1.2.

1.2 Objectives

In response to the limitations of LabSed, two additional SedImaging systems have been developed by the author. The first is a field-portable system known as "FieldSed" (Section 3.2). Created in 2017, the FieldSed is similar in operation as the LabSed. However several of the main hardware components have been redesigned using smaller and lightweight materials. As a result, the FieldSed holds several powerful advantages over LabSed. The newer system is portable and can be cleaned easily and quickly. SedImaging via FieldSed can be performed for a smaller soil specimen (85 $\pm$ 15g) than is required for both LabSed and sieving (250 to 500g for fine and medium sands), all while still providing a statistically-valid PSD. Table 1.2 summarizes some of the key advantages of FieldSed over LabSed and sieving; Chapter 3 discusses these advantages in depth.

While developing the FieldSed, the author also created a prewashing procedure used before testing a soil in the FieldSed. Using this procedure, the percentage of fines (and of material coarser than the soil particle testing range of FieldSed) of a sand specimen is determined. The prewashing procedure is adaptable for use with any SedImaging system. The procedure expands the range of application for soil characterization using SedImaging. The FieldSed and the prewashing procedure were the cornerstones of a 2017 large-scale characterization program of river sediments.

Section 3.2.2 details the prewashing testing procedure. The riverbed characterization project is documented in Section 3.2.4.

The second SedImaging system developed by the author is the Sed360. Created in 2020, the Sed360 is a nearly fully-automated SedImaging test. The Sed360 uses low cost, lightweight hardware like the FieldSed. Additionally, Sed360 hardware and procedural changes (discussed in Section 3.3) have reduced the amount of user-intervention during Sed360 testing, nearly fully automating SedImaging testing by this newest system. Table 1.2 includes key advantages of Sed360 over sieving while also comparing Sed60 to the other SedImaging systems. The equipment, testing, and analysis details of the SedImaging items in Table 1.2 will be discussed in Chapters 3 and 4.

Table 1-2. Comparing SedImaging systems and sieving.

Item	Sieving	SedImaging Systems		
		LabSed (2014)	FieldSed (2017)	Sed360 (2020)
Required oven-dried soil prior to testing [Y/N]	Y	N	N	N
Testable particle size range (per USCS)	Gravels and entire sand range	Medium and fine sand and gravel/coarse sand & fines percentages [a]	Medium and fine sand and gravel/coarse sand & fines percentages [a]	Entire sand range and gravel & fines percentages [a]
Required soil specimen size	250 to 500 g [b]	250 to 500 g	85 g ± 15 g	85 g ± 15 g
Testing time [min]	10 [b], plus time for oven-drying and sieve cleaning	< 10 minutes (well-graded sands), and < 5 (clean, poorly-graded medium sands)	< 10 minutes (well-graded sands), and < 5 (clean, poorly-graded medium sands)	< 10 minutes (well-graded sands), and < 5 (clean, poorly-graded medium sands)
Automated testing [Y/N]	N	N	N	Y
Number of data points for PSD	Approximately 5 to 15 (typ. 6)	Hundreds	Hundreds	Hundreds
Field portable [Y/N]	N	N	Y	Y
Parallel testing multiple specimens using one testing system [Y/N]	N	N	Y	Y
Noise pollution [Y/N]	Y	N	N	N
Estimated equipment costs (as of 2022)	$800 (six sieves lid, and pan) $1500 (sieve shaker) $750 (laboratory oven)	$30 (aluminum tubing for water column) $700 (Nikon camera and lens)	$10 (acrylic tubing for water column) $700 (Nikon camera and lens)	$10 (acrylic tubing for water column) $700 (Nikon camera and lens) $1400 (rotation stage)
	TOTAL: $3,050	**TOTAL: $730**	**TOTAL: $710**	**TOTAL: $2,110**

[a] Via prewashing procedure (Section 3.2.2)

[b] For fine and medium sands per ASTM C136/C136M-19

In addition to testing automation, the Sed360 expands the range of testable soil particle sizes by SedImaging (Table 1.2). For the first time with any SedImaging system, soil particles across the entire sand range, as defined by the Unified Soil Classification System (4.75mm to 0.075mm or between the US standard No. 4 and No. 200 sieves), can be accurately tested with the Sed360. When combined with the prewashing procedure, the Sed360 can classify any sand, as well as its percentage of gravel and fines. This particle size expansion widens the applications of using SedImaging as a rapid, accurate, and low cost alternative to sieving.

The particle size expansion made possible by the Sed360 necessitated a reexamination of the existing HWT-based image analysis method used with SedImaging. In order to accurately size the entire sand particle size range, a major redesign of the existing HWT-based image analysis method was completed. Chapter 4 documents the existing and the redesigned HWT-based image analysis methods used with SedImaging. The chapter also presents PSD results of a variety of sand gradations tested in the Sed360 and analyzed with the new HWT-based method. This method is not only successful in accurately sizing the entire range of sand particles, but it can also be used to characterize unique soil gradations, such as gap-graded sands. The PSD results of an engineered gap-graded sand are also included in Chapter 4.

***

Detailed in Chapter 5, extensive benchtop calibration research with both the prototype and the final version of the third generation Vision Cone Penetrometer (VisCPT) has been conducted. As part of this work, a wide range of soil particles of various sizes, colors, transparency, and shapes were photographed by the VisCPT (see Fig. 5.13). These soils were first analyzed using the original image analysis method of the two previous VisCPT generations. This method is based upon the Spatial Gray Level Dependence Method (SGLDM) proposed by Haralick et al. (1973).

The SGLDM and its application with the VisCPT are presented in Section 5.3. These VisCPT images were also analyzed using the HWT-based analysis method that is mainly used with SedImaging. In doing so, this preliminary research will be used to expand the application of both the VisCPT and SedImaging systems to more accurately characterize a wide variety of soil particle types. This research is also part of the foundational work for future calibration chamber and in-situ thin soil layer detection using the third generation VisCPT (Section 6.2).

1.3 Tasks and organization

This dissertation is organized into six chapters:

Chapter 1 introduces the motivation and objectives for the research that forms this dissertation. Embedded in this discussion is a broad overview of the two main systems of this dissertation: SedImaging and the Vision Cone Penetrometer (VisCPT).

Chapter 2 is a literature review of existing image-based grain sizing methods, and how SedImaging and the VisCPT fall within this broader area of research.

Chapter 3 details the evolution of SedImaging and its three hardware systems: the LabSed, and the two newer systems developed by the author, the FieldSed and the Sed360. This chapter also details an extensive 2017 characterization program of riverbed sediments that utilized the FieldSed.

Chapter 4 is dedicated to a comprehensive discussion of the image analysis method used (mainly) with the SedImaging system. Referred throughout this dissertation as the “Haar Wavelet

Transform (HWT)-based analysis method", this approach has undergone a foundational redesign since the method's first application with the LabSed. The necessity for this redesign, its details, as well as its research impact is discussed within this chapter.

Chapter 5 presents the evolution of the VisCPT through its three generations of hardware systems. The chapter also details the image analysis method that has been used with the VisCPT since its inception. The method uses several image textural indices from Haralick et al. (1973)'s Spatial Gray Level Dependence Method (SGLDM). The research with the third generation VisCPT and a variety of soil types is presented. Concluding this chapter is a discussion of the burgeoning ongoing work of using both the Haralick textural indices from the SGLDM and SedImaging's HWT-based analysis method to expand the application and accuracy of both the VisCPT and SedImaging.

Chapter 6 summarizes the research presented in this dissertation, and outlines future research avenues for the VisCPT and SedImaging.

Chapter 2 Literature Review

Image-based soil characterization methods can be grouped into three categories: (1) those that analyze images of individual particles placed along a one-dimensional line (Pan and Tutumluer 2005, White 2003), (2) methods that analyze images of particles on a two-dimensional plane (Altuhafi et al. 2013, Zhang et al. 2012, Abhik et al. 2016, Ohm and Hryciw 2013, Zheng and Hryciw 2016, Koh et al. 2009, Coban et al. 2020), and (3) methods that analyze images of three-dimensional particle assemblies (Ventola et al. 2020a, Chávez et al. 2015, Kozakiewicz 2018, Graham et al. 2005a, Graham et al. 2005b, Black et al. 2014, Buscombe et al. 2010, Detert and Weitbrecht 2012, Detert and Weitbrecht 2013, Nie et al. 2015, Ohm and Hryciw 2014, Ventola and Hryciw 2019, Ventola et al. 2022a). The one-dimensional line methods will be referred to as "line", the two-dimensional methods as "plane", and the three-dimensional as "assembly".

Within these three categories, the image analysis methods are further categorized. The soil particles can either be stationary ("static") or moving ("dynamic") at the time of image capture. Particles can be in contact ("contacting") with other particles or physically separated ("dispersed"). Additionally, the particles can be sorted or non-sorted by size upon image capture. Figure 2.1 illustrates the different types of image-based soil characterization methods. The figure includes eight schematics showing the (non-)movement, (non-)sorting, and (non-)contact of the soil particles (represented as brown circles in Fig. 2.1) relative to one another at the time of image capture. Table 2.1 lists the different types of image-based soil characterization methods as well as select examples of each method. These examples were chosen to illustrate the wide range of

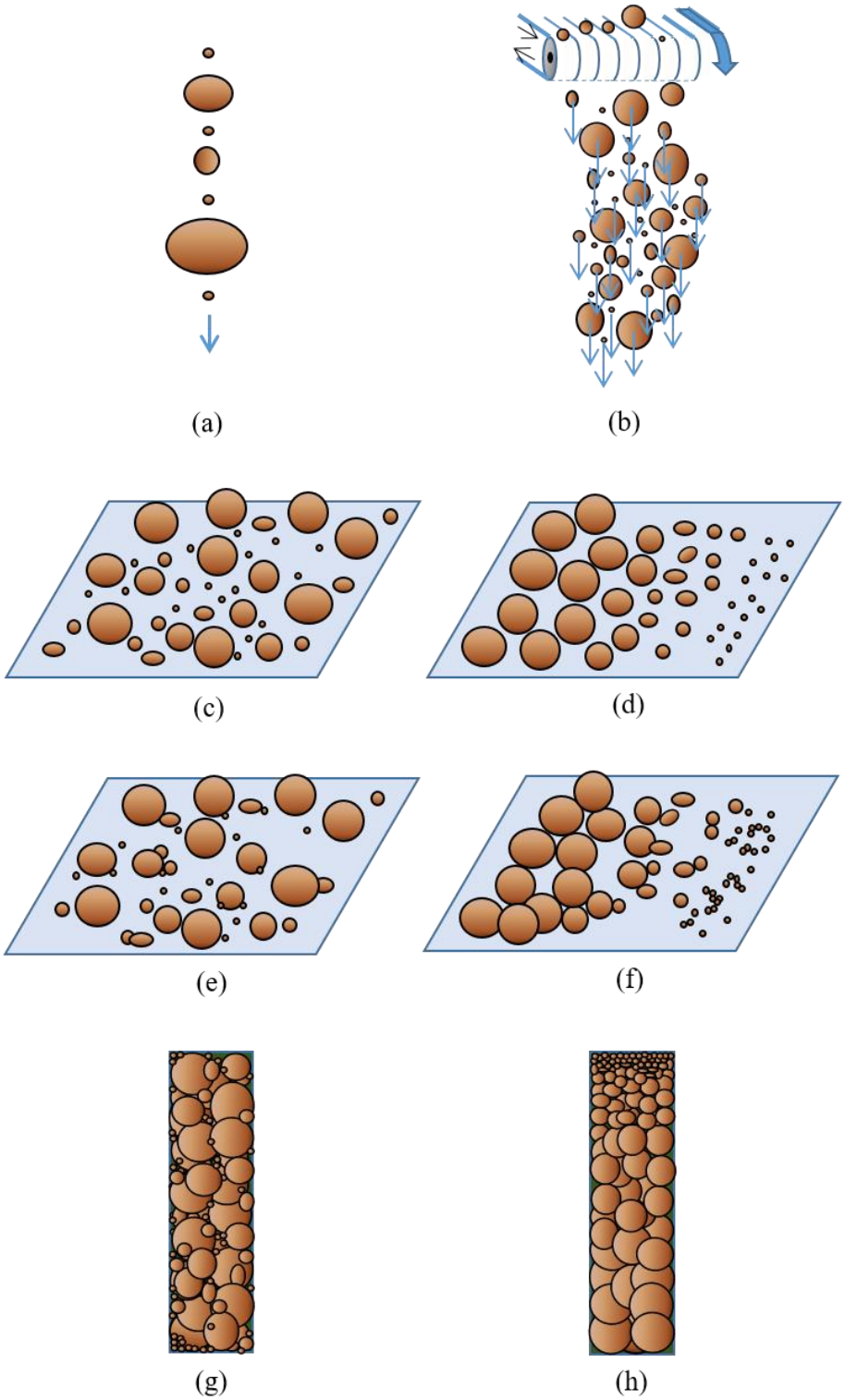

Figure 2-1. Illustrations of soil particle at the time of image capture for image-based soil characterization methods. (a) Line, dispersed, dynamic, non-sorted, (b) Plane, dispersed, dynamic, non-sorted, (c) Plane, dispersed, static, non-sorted, (d) Plane, dispersed, static, sorted, (e) Plane, contacting, static, non-sorted, (f) Plane, contacting, static, sorted, (g) Assembly, contacting, static, non-sorted, (h) Assembly, contacting, static, sorted.

Table 2-1. Types of image-based soil characterization methods with selected examples.

Approach	Particle Contact	Particle Motion	Particle Size Sorting	Visualization of Soil Particles (from Fig. 2.1)	Examples
Line	Dispersed	Dynamic	Non-sorted	a	Single Particle Optical Sizer (SPOS) (White 2003) Univ. of Illinois Aggregate Image Analyzer (UIAIA) (Pan and Tutumluer 2005)
Plane	Dispersed	Dynamic	Non-sorted	b	CAMSIZER® QICPIC Imaging System by Sympatec (Altuhafi et al. 2013)
	Dispersed	Static	Non-sorted	c	Improved Mass Model (Zhang et al. 2012) Mass Model (Abhik et al. 2016)
	Dispersed	Static	Sorted	d	Translucent Segregation Table (TST) (Ohm and Hryciw 2013)
	Contacting	Static	Non-sorted	e	Modified Watershed Analysis (Zheng and Hryciw 2015) Shanthi et al. (2014) Multi-Flash Imaging (MFI) (Koh et al. 2009)
	Contacting	Static	Sorted	f	Translucent Segregation Table (TST) (Ohm and Hryciw 2013)
Assembly	Contacting	Static	Non-sorted	g	**Vision Cone Penetrometer (VisCPT)** Particle Detection and Measurement (PADM) (Kozakiewicz 2018)[a] Automated Grain Sizing (AGS) method (Graham et al. 2005a 2005b)[a] BASEGRAIN (Detert and Weitbrecht 2012, 2013)[a] Semisupervised Affinity Propagation Model (SAPM) (Nie et al. 2015)[a] OPTGRAN-CS (Chávez et al. 2015)[a] Buscombe et al. (2010)[b] Black et al. (2014)[b] Buscombe and Masselink (2009) (discusses several statistical spatial methods, not included in Section 2.2)
	Contacting	Static	Sorted	h	**SedImaging**

[a] Discussed in Section 2.1

[b] Discussed in Section 2.2

applications, limitations, required user knowledge, automation, and ease of use of these methods.

The one- and two-dimensional image-based soil sizing methods are time-, cost-, and labor-intensive. They either require costly equipment, such as the QICPIC imaging system (Altuhafi et al. 2013), or require users to manually separate soil particles before photographing (Abhik et al. 2016). By contrast, the methods that analyze images of three-dimensional soil assemblies require less user-interaction prior to photographing and less specialized equipment. The two systems that are the focus of this dissertation, SedImaging and VisCPT, fall within this final category.

Some image-based, three-dimensional particle assembly analysis methods deterministically characterize a soil (namely its PSD) by segmenting and sizing individual particles in an image (Chávez et al. 2015, Kozakiewicz 2018, Graham et al. 2005a, Graham et al. 2005b, Detert and Weitbrecht 2012, Detert and Weitbrecht 2013, Nie et al. 2015). Others, including the methods used with SedImaging and the VisCPT, as well those by Buscombe et al. (2010) and Black et al. (2014), do not size soil particles individually. Instead, they characterize a soil by analyzing the spatial distribution of pixel color or grayscale intensities of the photographed soil assembly. Individual soil particles are not counted or analyzed using these spatial methods. These pixel intensity spatial methods eliminate the need for user-defined thresholds for deterministic segmentation analysis, and are less computationally-intensive than deterministic approaches.

The three-dimensional assembly examples (deterministic and spatial) in Table 2.1 are worth deeper descriptions. Section 2.1 includes examples of the deterministic method, and Section 2.2 describes the pixel intensity spatial methods. The methods are compared to one another, as well as to the methods used with SedImaging and VisCPT. Each example has its own set of limitations, some of which are discussed in this Chapter. The SedImaging and VisCPT methods also have their own limitations. However these are not discussed as part of this Chapter; instead,

they are included within Chapters 3, 4, and 5 alongside the deeper discussions of these two systems. The one- and two-dimensional image-based soil sizing methods in Table 2.1 are not discussed further.

2.1 Soil assembly image-based characterization: deterministic methods

The **Particle Detection and Measurement (PADM) method** was introduced by Kozakiewicz (2018). The PADM can determine particle size distributions using photographs of soil samples with non-uniform, inconsistent lighting. This ability is not possible among all assembly grain size characterization methods. The PADM method determines grain size distributions of soil images taken on the ground surface. The method first passes a computing filter over a soil image to remove noise and background information. The filter is either a common top-hat transform (in cases when soil samples are brighter than the background) or a bottom-hat transform (when the soil is darker than the surroundings) using a disk-shaped structuring element. Once the filtering is complete, grain detection and sizing can begin. The PADM method considers several image analysis segmentation techniques for contacting soil particles: binarization, edge detection, and the watershed method. Kozakiewicz (2018) notes that the type of technique selected for use with an image depends on the specific lighting and sizing conditions of the soil particles. After the image is segmented, the PADM method estimates the size of each particle as the diameter of a disk that has the same equivalent area.

The largest limitation of the PADM method is its required user-defined thresholds. The filtering procedure of the PADM requires a user to set a grayscale threshold value separating the soil particles from the background; this value changes depending on the image content (i.e. darker soil particles with a lighter background, larger soil particles with a multi-colored, textured background etc.). There are several other thresholds throughout the PADM method that need to be

set by users, such as selecting the threshold between which pixels become a 0 or a 1 in the binarization process, and determining the size of the kernel used in the Gaussian filtering during the watershed procedure. These thresholds influence the final grain sizing in the PADM method. Kozakiewicz (2018) also does not specify what type of soil images work best for the various segmentation methods; instead, all of the methods are utilized on soil assemblies, and no conclusion is made as to which method should be used for a given soil. This leaves the selection to users. Thus, the PADM method requires users to have a strong knowledge of image analysis techniques. Additionally, Kozakiewicz (2018) notes that the number of detected soil particles varies between each of the segmentation methods, and manual corrections for this particle count discrepancy are recommended. By comparison, the SedImaging and VisCPT image-based analysis methods are automated and do not require users to select threshold values in order to perform tests.

The **Automated Grain Sizing (AGS) method** was originally proposed by Graham et al. (2005a) and is widely referenced by other researchers, including Strom et al. (2010). Similar to the PADM method, AGS can be used to analyze ground surface soil assemblies. The AGS method is an automated procedure, like those used with SedImaging and the VisCPT. The method requires that an approximately 1m by 0.75m (3.3ft by 2.5ft) oversized frame be placed around a soil assembly in order to outline the testing area. Figure 2.2 shows an illustration of the required set up for the AGS method. An overhead photograph is taken of the area. Graham et al. (2005a, 2005b) uses the AGS method to test riverbed gravels, but the image analysis techniques can be applied at a reduced scale for smaller soil particles.

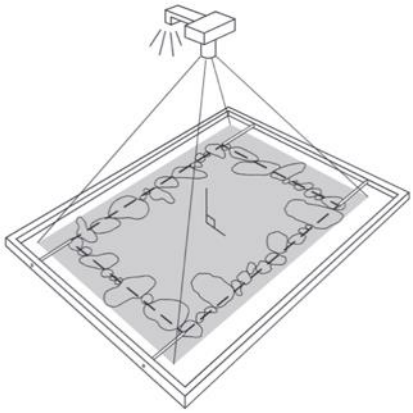

Figure 2-2. Set up used for the Automated Grain Sizing (AGS) Method. (Graham et al. 2005b)

After the photo is captured, a smoothing computing filter is passed over the image to remove noise and preserve particle edges. Similar to the PADM method, a bottom-hat transform is later applied. Next, particle edges are defined using a watershed segmentation algorithm. The AGS method does not require user-specified threshold values, and instead defines the values for its watershed method in terms of "percentiles in the image-intensity frequency distribution," thus reducing threshold-induced errors acknowledged by Kozakiewicz (2018) in the PADM method. After segmenting the particles, the AGS method fits each particle with an ellipse. The minor axes of the ellipses are recorded as the estimated particle sizes, and a grain size distribution for the image is generated. Similar to the calibration equation used in the HWT-based analysis for SedImaging (Chapter 4), the AGS method has a sieve-correction factor that is used to correlate the method's estimated PSD to sieve-derived data.

As with the PADM method, the AGS method is susceptible to errors due to the watershed procedure. The procedure can either over- or under-count the number of particles in an image. However, the more significant concern of the AGS method involves the size of the oversized frame (Fig. 2.2) relative to that of the photographed particles. As the size of the soil particles increases,

the number of particles fully inside the framed area decreases, and the accuracy of the grain size distribution decreases; more particles that lie partially within the framed photographed area are miscounted as smaller particles. Another source of error with the AGS method involves non-uniform lighting. Graham et al. (2005b) notes that the AGS method is sensitive to "irreducible random errors" when non-uniform lighting is present during image capture.

BASEGRAIN was first introduced by Detert and Weibrecht (2012, 2013) and later analyzed by Stahly et al. (2017), among others. Like the PADM and AGS methods, BASEGRAIN is an image-based analysis method used for ground surface soil assemblies. This approach follows a similar algorithm as AGS: a bottom-hat transform is applied to a soil image, followed by the watershed segmentation process. Eventually, equivalent particle sizes are determined by fitting identified particles with ellipses. However, BASEGRAIN has two key features that distinguish it from AGS. Unlike AGS, BASEGRAIN does not require an oversized frame to take a photo of a sample. Instead, BASEGRAIN users simply need to include a scale of known length within the photo, as seen in the BASEGRAIN screenshot in Fig. 2.3. This is a powerful improvement from the AGS method. In the AGS method, the particle size range of testable soils was limited by the edge effects of the system's oversized frame; this is not a limitation of BASEGRAIN. Like SedImaging's image analysis and PADM (and unlike AGS), BASEGRAIN can be utilized with a range of camera magnifications.

The second useful feature of BASEGRAIN that neither the PADM nor the AGS methods possess is its accessibility and usability. BASEGRAIN is a MATLAB-based software that is free to download and access by the public. In addition, there are extensive resources and tutorials on how to successfully use this method. Though the industry awareness of BASEGRAIN is not a scientific advantage of this method over AGS or PADM, it is a noteworthy feature.

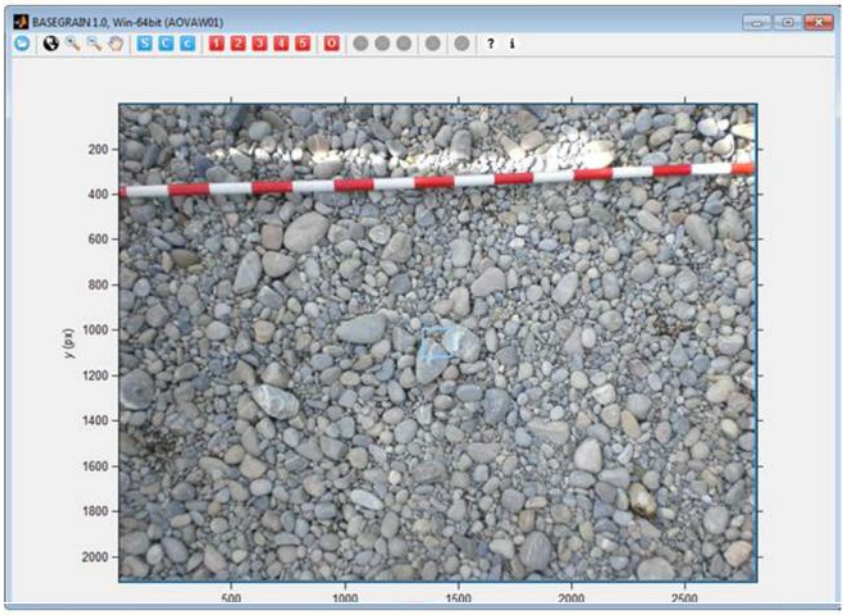

Figure 2-3. Screenshot of BASEGRAIN where a known scale (white and red pole located at the top of the image) is used to establish the image magnification. (BASEGRAIN 2013)

Since BASEGRAIN utilizes a similar image analysis procedure as AGS, this method still holds the inherent level of inaccuracy and error stemming from the procedure that was described with AGS. BASEGRAIN is also not an automatic method; there are a number of steps in the process that are user-specified. While these afford the ability to tailor BASEGRAIN for each specific application, it does slow down the computational time considerably.

The **Semisupervised Affinity Propagation Model (SAPM)** was introduced by Nie et al. (2015). SAPM is a drastically different approach to image-based grain sizing than the aforementioned methods. SAPM utilizes both image processing and machine learning techniques to determine the grain sizes of particles within a photographed soil. The model extends the fully-automated Affinity Propagation clustering algorithm of Frey and Dueck (2007) into the application of grain size distributions. The details of machine learning are beyond the scope of this chapter. In general terms, the SAPM method first processes a soil image using similar computational filtering

techniques utilized by PADM, AGS, and BASEGRAIN. Then, SAPM uses a set of *test* soil images and a set of *training* soil images. The grain size distributions of the training images are already known and are used to determine those of the larger test soil image set. The process of gathering training soil images for a variety of soil types, sizes, and colors is an arduous process – one that is not needed with the SedImaging, VisCPT, PADM, AGS, or BASEGAIN methods. Furthermore, the SAPM requires significant user-interaction, and thus requires users to have a high level of machine learning knowledge.

Chávez et al. (2015) developed **OPTGRAN-CS**, a granulometric optical method that uses stereological methods to size individual soil particles within a three-dimensional assembly. According to Chávez et al. (2015) the method "provides optical granulometry from an [Entropy-Controlled Quadratic Markov Measure Field Model] ECQMMF-based segmentation" that was developed by Rivera and Dalmau (2012). A soil assembly is photographed and analyzed by the free, downloadable QPTGRAN-CS software. The method consists of three main phases. The first phase enhances the image's contrast by histogram equalization. Then, like the PADM and AGS methods, a smoothing computing function is passed over the entire specimen image. The second phase segments the assembly into individual soil particles given user-defined parameters and creates a binary image of the soil particle edges. At this stage, users can choose to manually correct or adjust the automatic particle segmentation. Though this additional manual step increases the accuracy of the OPTGRAN-CS grain sizing, it also compromises on testing throughput. The final phase of the method is to apply the intercept-counting method of Rosiwal (1898) to size the particles in the binary image. The final result is a PSD of the soil assembly.

The greatest strength of the OPTGRAN-CS method is its flexibility. The method was tested on images of various particle sizes and colors, from cobbles and gravels down to the silt range. It

was also tested using cameras with a range of magnifications (a 15 Megapixel DSLR camera, a 5 Megapixel tablet, and a 3.2 Megapixel wireless camera phone). All three cameras yielded some success, with the highest magnification camera being able to correctly size the largest range of soil particles.

The largest limitation of the OPTGRAN-CS method is the required user involvement in both defining parameters at the start of the test, and the optional, (but recommended step), to manually adjust the automatic binary image of the soil assembly. The first point, similar to the PADM's requirement for user-defined parameters, requires (or assumes) a level of knowledge in their users to select the appropriate parameters for their specific use. Less knowledgeable users may not be aware of the (possibly negative) consequences selecting one parameter over another has on their soil assembly's outputted PSD.

The manual step of correcting the soil assembly's automatically-created binary image in the second phase of the OPTGRAN-CS method can be time-intensive. Chávez et al. (2015) provides an example where manual correction of the binary image was required. Shown in Fig. 2.3, the photographed soil assembly (Fig. 2.3[a]) was first converted to an automatically-generated binary image (Fig. 2.3[b]). Chávez et al. (2015) acknowledges that the automatic image did not correctly segment all of the soil particles. Localized examples of this are the blackened areas circled in red in Fig. 2.3(b). The manual correction of the binary image is in Fig. 2.3(c). Depending of the level of manual correction needed for a given soil image, as well as the size of the image itself, this correction process can be tedious and time-intensive. This compromises the time benefits of adopting this image-based grain sizing method over traditional testing such as sieving. A final limitation of the OPTGRAN-CS method pointed out by Chávez et al. (2015) is similar to other image-based analysis methods (including the ones used with SedImaging and the VisCPT).

Shadows, non-uniform lighting, and soils with uniform coloring are challenging to accurately size by the OPTGRAN-CS method.

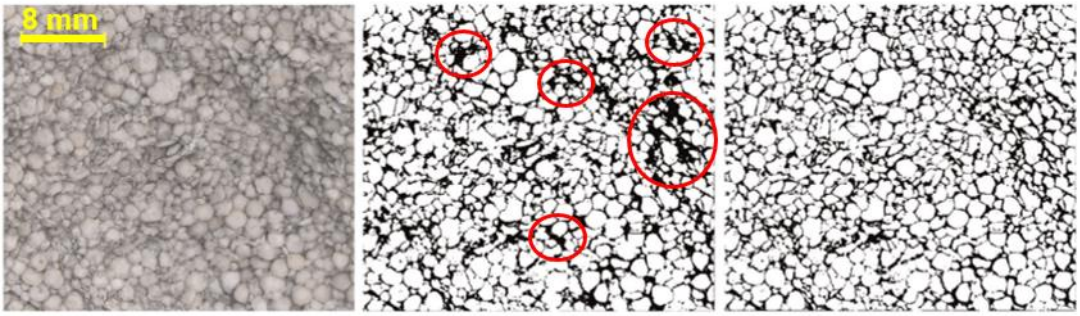

Figure 2-4. Example of necessary manual correction during the OPTGRAN-CS method. (a) Original soil image, (b) Automatically-generated soil segmentation, (c) Manually-corrected soil segmentation (Adapted from Chávez et al. 2015).

2.2 Soil assembly image-based characterization: pixel intensity spatial methods

The final two examples of image-based soil assembly characterizations are similar to the method used with SedImaging and the VisCPT. These methods do not deterministically size each individual soil particle. Instead, they use pixel intensity spatial methods to establish particle size. The first example is **Buscombe et al. (2010)**, which uses a two-dimensional spectral decomposition of a soil image to provide a statistical estimate of the mean particle size of the assembly. The method is highly adaptable. It does not require any calibration, and can be used for all cohesionless particle sizes down to a 0.1mm diameter in a variety of lighting conditions (natural and artificial lighting, direct and diffuse lighting, etc.). The system is fully automated, does not involve any user-defined parameters, and only requires the image magnification prior to an analysis. Additionally, the method can be used for images captured both on land and underwater. The method's two-dimensional special decomposition occurs in the frequency domain as opposed

to the spatial domain (where SedImaging and VisCPT image analysis methods reside). A normalization procedure also occurs in the process, which is why Buscombe et al. (2010)'s method "[removes] the dependency on calibration." However Buscombe et al. (2010) acknowledge that calibration may be necessary when dealing with soils of unique packing.

The technical procedure of the Buscombe et al. (2010) method extend beyond the scope of this chapter, but in general terms, the process utilizes a two-dimensional autocorrelation function and determines the average radius of a single fitted ellipse. This radius is linearly related to the estimated average particle size of a photographed soil assembly. The Buscombe et al. (2010) method was successfully tested on over 400 soil specimens of varying sizes, shapes, colors, and testing environments (different lighting, land, underwater etc.) Furthermore, the method was also performed on computer-generated soil bedforms using different sizes of tessellations, with similar results.

Despite its impressive list of advantages as an image-based grain sizing method, there are two main limitations of the Buscombe et al. (2010) method. The first is the high-level technical language used to describe the details of this method. A deep knowledge of both statistics and image analysis are required to understand this method's procedure to size soil particles. This could limit the range of users able to make use of this more complex method, potentially undercutting its extensive list of benefits as a non-intrusive, rapid, high-resolution grain sizing approach. The other image-based soil characterizations methods listed in Table 2.1 (including those used with SedImaging and the VisCPT) are equally rigorous and robust methods using complex computational and geotechnical knowledge to create them. Yet all of those methods, even the machine learning procedure of Nie et al. (2015)'s SAPM (Section 2.1), can be explained in approachable and attainable language. The automation and accuracy of an image-based soil

characterization method aside, the usability must also be a conscious consideration when selecting to use any of these methods.

The second limitation of the Buscombe et al. (2010) method is that only a single average particle size is assigned for an entire soil assembly image. This single value could be useful in holistic geologic characterization projects, but a complete particle size distribution for a soil assembly is required for most geotechnical, geoenvironmental, geomechanical, and related applications.

Black et al. (2014) developed an image-based soil assembly characterization method that uses a combination of first- and second-order image texture approaches to size sand and gravel river bedforms from aerial images. The first-order approaches investigate a photographed soil assembly's pixel intensity values without considering the spatial distribution of these values across the image. For example, a first-order approach of an image could be its mean, variance, or range of pixel intensity values. Alternatively, second-order approaches *do* consider the spatial distribution of pixel values across an image.

The specific second-order textural approach used by Black et al. (2014) is also utilized with the VisCPT. Both Black et al. (2014) and the VisCPT methods use various textural indices from the Spatial Gray Level Dependence Method (SGLDM) proposed by Haralick et al. (1973). Given this, the details of this method are omitted here and are reserved for Section 5.3 and Appendix B. Broadly, for the SGLDM, an image's co-occurrence matrix is calculated. This matrix is a mathematical visualization of the distribution of identical pixel intensity values across the image. From there, Haralick et al. (1973) defined equations for fourteen textural indices that characterize the shape, distribution, intensity, and other attributes of this co-occurrence matrix. Black et al. (2014) and the method used with the VisCPT correlate several of these Haralick textures to soil

particle size. Several of the same Haralick textural indices used with the VisCPT are also used in the Black et al. (2014) method.

Black et al. (2014) determined that their first-order textural approach is adequate in distinguishing between sand and gravel bedforms, while their second-order textural approach is needed for further grain size distributions of the gravel assemblies. The method was used for aerial images of soils at four testing sites along the Fraser River in British Columbia, Canada, and was calibrated using the same soils. Black et al. (2014) notes that one of the largest limitations of their method is the small, localized sample size. Given the image magnification of the aerial photographs used by Black et al. (2014), photographed sands were often sub-pixel, meaning "one pixel is an averaged measure of a population of several [sand] grains." Black et al. (2014) investigated the impact on grain sizing particles that are small enough to be influenced by this "pixel averaging effect." They compared this to sizing larger gravel particles that, instead of the "pixel average effect," are represented by "actual grain texture" in the aerial images. The camera magnifications of SedImaging and VisCPT are such that even the smallest photographed silt particles are never sub-pixel, thus eliminating this type of concern in these methods.

Chapter 3 SedImaging Systems

This chapter will describe the evolution of SedImaging, beginning from the original system of LabSed (Section 3.1) to the motivation and inception of both FieldSed (Section 3.2) and the third system, Sed360 (Section 3.3). The focus will be on the hardware of these three systems, while Chapter 4 will describe the image analysis method used with SedImaging to generate particle size distributions (PSDs) of sands. Less emphasis is placed upon the hardware of the original SedImaging system, LabSed; instead, the author's development of the FieldSed and Sed360 systems are the main focuses of Chapter 3. Example PSD results using the FieldSed are presented in this chapter, while those generated using the Sed360 are reserved for Chapter 4 as part of the discussion of the newest image analysis method. Chapter 3 also details a case history involving the FieldSed for sediment classification in the Kalamazoo River (Section 3.2.4).

***

Passages and portions of this chapter are taken from previous publications describing the FieldSed (Ventola and Hryciw 2019; Ventola et al. 2020b) and the Sed360 (Ventola and Hryciw 2022a, Ventola and Hryciw 2022b) SedImaging systems.

3.1 Original Hardware: LabSed

The original SedImaging hardware system, referred to as "LabSed", is shown in Fig. 3.1. The device consists of a water-filled 64mm x 64mm x 2134mm (2.5in x 2.5in x 7ft) square aluminum sedimentation column; a support tower for positioning and supporting the weight of the column; a system base; and a soil accumulator. The accumulator is attached to the bottom of the

sedimentation column by two quick-release clamps. The accumulator has a glass viewing window through which the soil is photographed using a digital single-lens reflex (DSLR) camera.

The SedImaging LabSed device performs best for soil particle sizes between 0.075mm (US Standard No. 200 sieve) and 2.0mm (US Standard No. 10 sieve), which encompasses the fine and medium sand range as defined by the Unified Soil Classification System. Typically, 450 ± 50g of solids are tested in a LabSed specimen. The soil is initially placed in a 455mm (18in) long cylindrical acrylic tube having an outside diameter of 64mm (2.5in) and a 6.4mm (0.25in) wall thickness. Known as the "presorter tube" (Fig. 3.2), it is used to break up soil clumps by aggressively mixing the specimen in water. The tube also provides a convenient method for releasing a soil specimen into the LabSed sedimentation column.

The presorter tube is filled between 80% and 90% with water, and a soil specimen is added. The open end of the tube is sealed with a thin rubber membrane; the membrane is pushed slightly

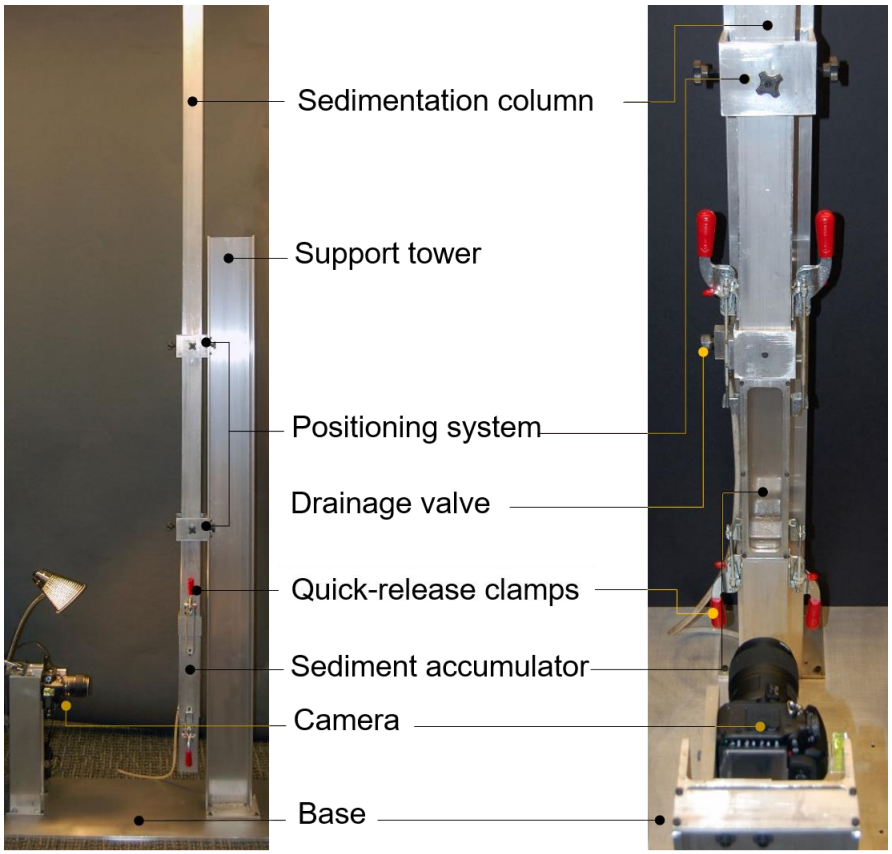

Figure 3-1. The LabSed.

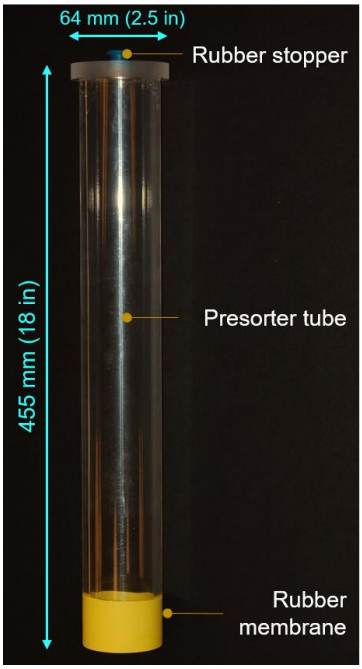

Figure 3-2. *The LabSed presorter tube.*

into the tube, thereby creating a vacuum seal (Fig. 3.3[a]). The soil-water mixture is vigorously mixed. The presorter is then inverted so that the membrane-sealed end is on the bottom, and the sand is allowed to settle atop the inwardly-curved membrane. Then the rubber membrane is slipped off of the presorter. Because of the vacuum, the soil does not fall out of the opened tube (Fig. 3.3[b]). The tube is transferred to the top of the sedimentation column (Fig. 3.3[c]) and a rubber stopper, shown in Fig. 3.2, is removed from the tube. This releases the vacuum and allows the soil-water mixture to rapidly drop into the sedimentation column. Ohm and Hryciw (2014) also discusses the presorter in detail.

The soil particles sediment through the water and settle within the sediment accumulator (Fig. 3.1), where the soil column is photographed. This photograph is analyzed using the HWT-based method (detailed in Chapter 4) to generate the soil specimen's PSD. After the specimen has been photographed, the water in the LabSed column is drained through a valve located above the

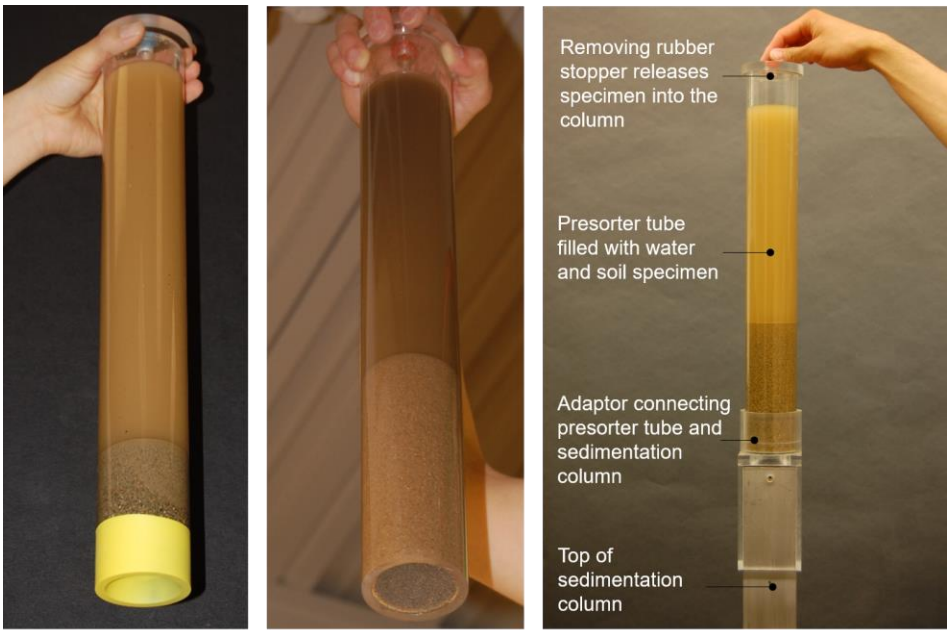

Figure 3-3. LabSed presorter tube's vacuum-release system. (a) Vacuum-sealed rubber membrane, (b) Soil specimen remains in the presorter after the membrane is removed, (c) Presorter is moved to the top of the sedimentation column and the rubber stopper is removed.

sediment accumulator (Fig. 3.1); the soil is removed from the accumulator, and the LabSed is cleaned in preparation for its next use.

3.2 FieldSed

Due to its size, large weight, and ancillary components, the LabSed is only practical for use in a laboratory setting. Therefore, a new SedImaging system known as "FieldSed" was developed in 2017 and introduced by Ventola and Hryciw (2019). FieldSed provides portable SedImaging testing at construction sites, quarries, offshore, and other locations distant from a traditional soil laboratory. FieldSed modifies the original LabSed device using reduced scale lightweight components, enabling it to be easily deployed for field applications. In addition to cost savings over traditional sieving, this field system also eliminates the time and cost associated with transporting test specimens to a laboratory. FieldSed also provides a method to determine the fines' percentage of a sand specimen (Section 3.2.2). Its portability and low cost allowed FieldSed to be the centerpiece of a large characterization program of over 100 Kalamazoo River bed sediments in 2017 (Section 3.2.4).

3.2.1 The FieldSed System

The FieldSed is shown in Fig. 3.4. The overall operation of the FieldSed is similar to that of the LabSed. The major difference between the two devices is the sedimentation column. The FieldSed replaces the sedimentation column and accumulator with one continuous 25mm x 25mm x 1830mm (1in x 1in x 6ft) square transparent acrylic tube. Secondly, the FieldSed sedimentation column is held in position by the simple bracket shown in Fig. 3.5. The column load is transferred to the ground at the base, where it is also positioned using two metal dowels shown in Fig. 3.6. The locked bracket (Fig. 3.5[b]) and dowels insure column verticality. A square rubber stopper is

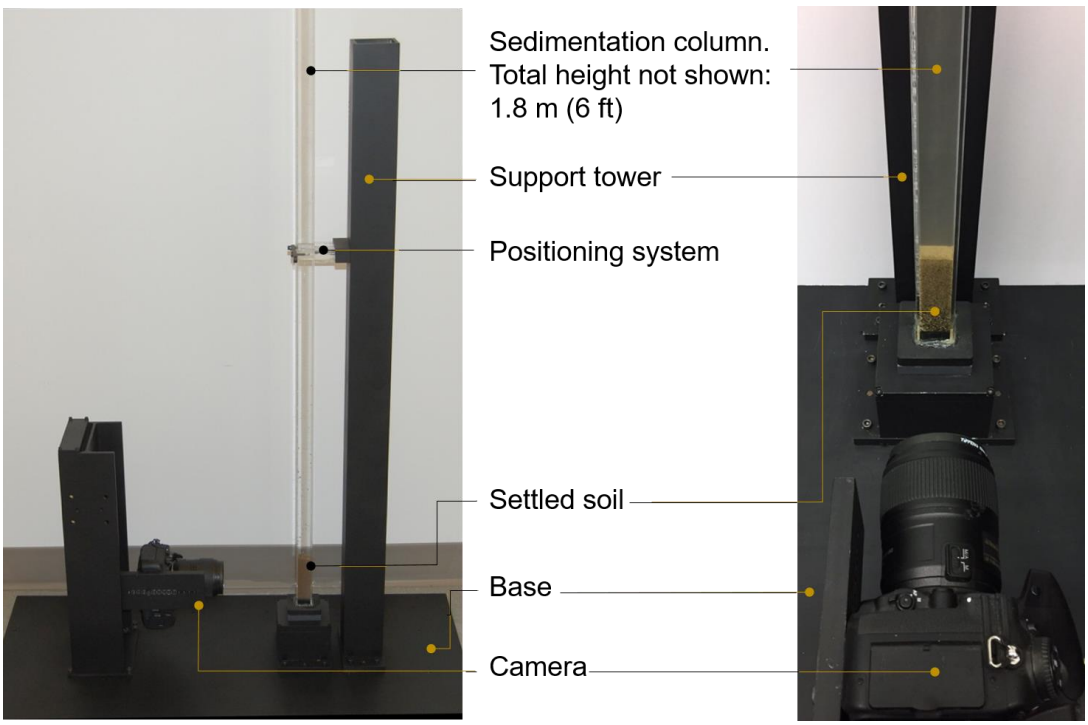

Figure 3-4. The FieldSed.

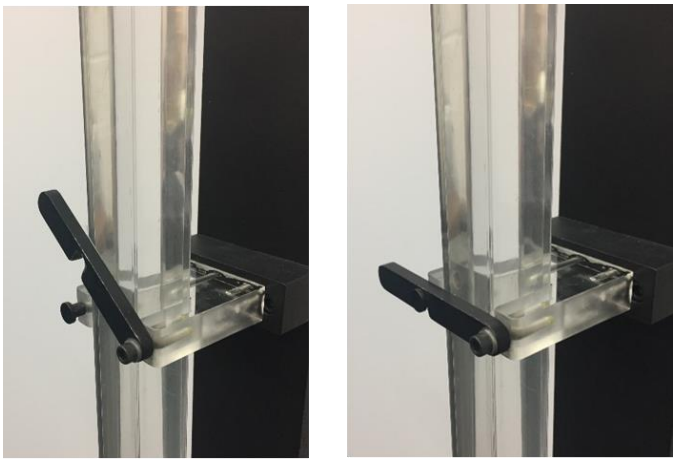

Figure 3-5. FieldSed positioning bracket. (a) Unlocked, (b) Locked.

permanently fixed inside the base of the sedimentation column (Fig. 3.6). Similar to LabSed, the FieldSed also utilizes a presorter tube. However for the FieldSed, the outside diameter of the tube

is only 25mm (1in). Figure 3.7(a) shows the FieldSed presorter placed at the top of the sedimentation column, and Fig. 3.7(b) shows the release of the presorter plug and a soil specimen's introduction into the top of the sedimentation column.

The HWT image analysis method used with the LabSed system is also used with the FieldSed. The clear acrylic sediment column and flexible positioning system of the FieldSed allow photographing all four sides of the settled soil from the same camera location. Thus, a much larger percentage of the overall soil specimen is used for image analysis. Four distinct PSD curves are generated and later combined to provide a representative PSD for the whole soil specimen.

The relatively inexpensive acrylic tubing and simple FieldSed design allow many sedimentation columns to be constructed and utilized simultaneously for parallel testing. Figure 3.8 shows 19 FieldSed columns held in a testing rack and prepared for such parallel testing. A soil

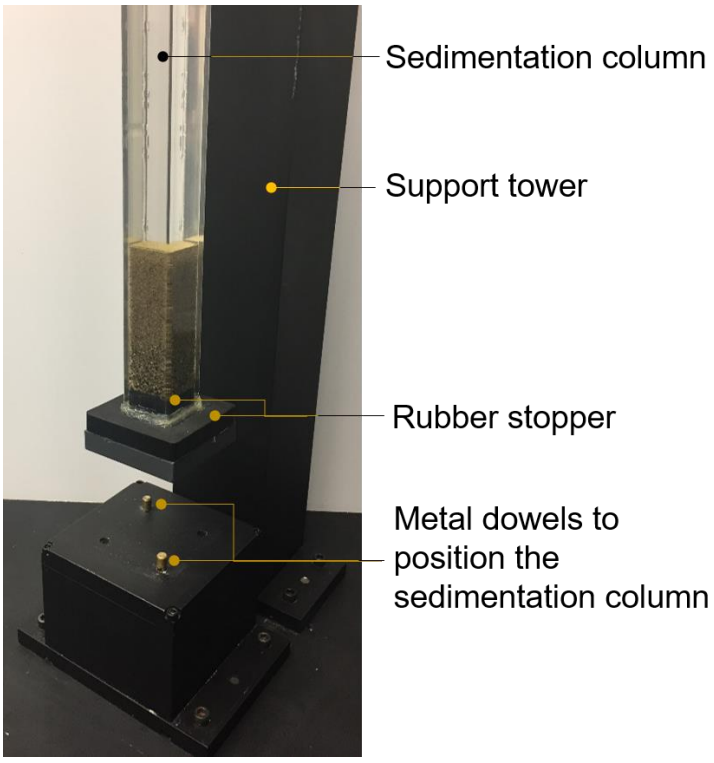

Figure 3-6. *FieldSed rubber stopper, base, and positioning dowels.*

specimen is released into each of the columns and allowed to sediment to the bottom. Later, the sedimentation columns are individually removed from the rack and placed into the FieldSed positioning system, photographed on all four sides, and returned to the rack. This parallel testing allows for quickly analyzing large numbers of specimens by eliminating the need to both wait for sedimentation to end, and to clean sedimentation columns between consecutive tests.

The small cross-section of the FieldSed sedimentation columns also allows for the use of smaller soil specimens than those required for the LabSed. While about 450g of solids are typically used in the LabSed, only about 85 ± 15g are sufficient for the FieldSed to yield reproducible results. Table 3.1 compares the salient features of the LabSed and FieldSed systems.

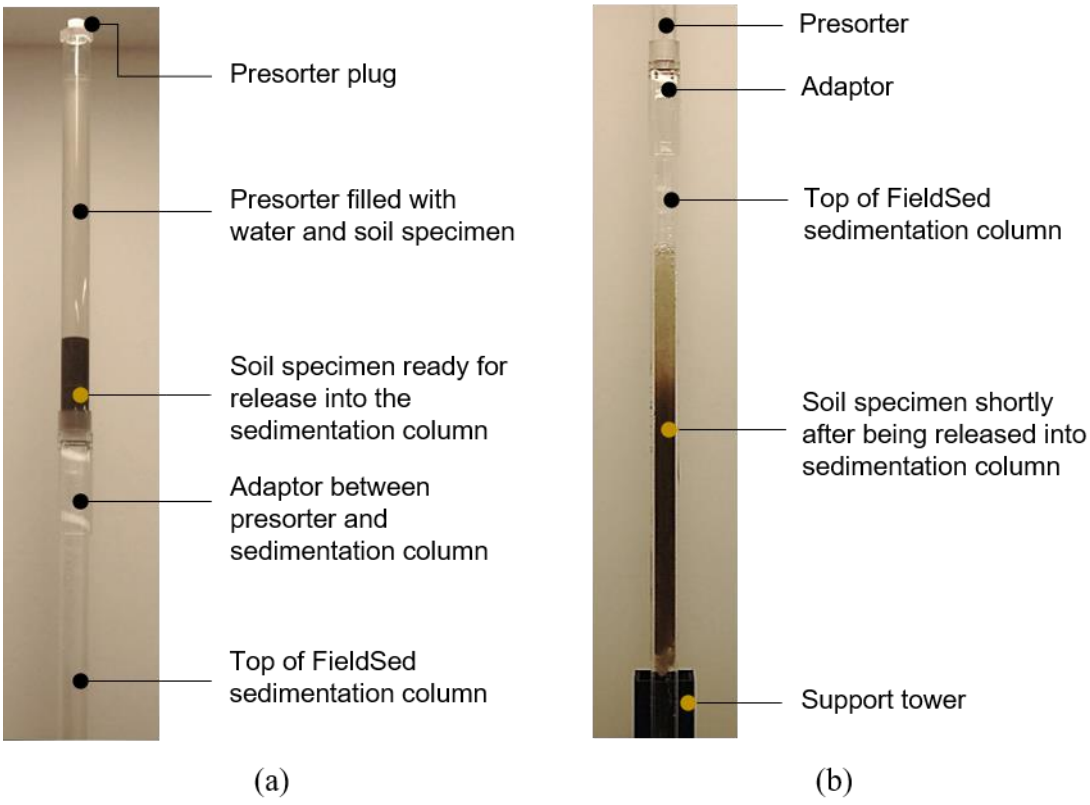

Figure 3-7. Soil specimen release from the FieldSed presorter. (a) Prior to release, (b) Several seconds after release.

Figure 3-8. FieldSed parallel testing hardware. (a) Sedimentation columns in a testing rack, (b) A technician preparing many sedimentation columns.

Table 3-1. Comparing LabSed and FieldSed systems.

Item	LabSed	FieldSed
Sediment column dimensions [mm]	64 x 64 x 2134	25 x 25 x 1830
System materials	Aluminum, glass	Acrylic
Sediment column weight [kg]	8.9	0.9
Required volume of water for each test [m^3]	9×10^{-3}	1×10^{-3}
Typical specimen weight of solids [g]	450 ± 50	85 ± 15
Field portable	No	Yes
Detachable sediment accumulator	Yes	No
Drainage port	Yes	No
Parallel testing possible	No	Yes
Number of photographed column sides	1	4
Volume percentage of specimen used for PSD [a]	2%	16%
Pre-sorting tube dimensions (length; diameter) [mm]	455; 64	455; 25

[a] Assumes an average particle size of 1.0mm

3.2.2 Specimen Prewashing

SedImaging by FieldSed works best for coarse-grained soils with particle sizes ranging from 2.0mm (No. 10 sieve opening) to 0.075mm (No. 200 sieve opening). A prewashing procedure may be used to determine the percentage of soil mass outside of this range. The prewashing

effectively removes particles larger than 2mm and smaller than 0.075mm, without specimen-drying, prior to testing with the FieldSed.

The first step of prewashing involves a visual inspection of a specimen for particles larger than 2.0mm. If the specimen does appear to have larger particles, the soil is washed over a No. 10 sieve. The material retained on the sieve is air- (or hot pan) dried and the dry weight ($W_{>No.10}$) is recorded. While the material retained on the No. 10 sieve is drying, the remainder of the specimen is transferred to the presorter. Once the soil is in the presorter, water is added to a marked height. The tube with the specimen and water is weighed (W_{pre}). Next, the presorter is sealed and the soil-water mixture is vigorously agitated for several seconds. Following agitation, the user sets the tube upright, allowing the coarser particles to begin settling. After a few moments, the tube is unsealed and the suspended fines-water mixture is carefully poured over a No. 200 sieve. The material passing the No. 200 sieve can be retained for other laboratory testing (e.g. Atterberg Limits) if desired.

Clean water is added to the presorter, and the agitation process is repeated several times until the water in the tube is observed to be relatively clear after agitation. After the final pour over the No. 200 sieve, any material retained on the sieve is carefully returned to the tube. The presorter is filled with clean water to the marked height and the weight of the tube and its contents is again recorded (W_{post}). The material that remained in the tube is the weight of the specimen portion having particles sizes between 0.075mm and 2.0mm ($W_{No.200-No.10}$). This material is then released into a FieldSed sedimentation column and, following sedimentation, is photographed. A HWT-based PSD (Chapter 4) is generated for this portion of the specimen; the distribution is later adjusted to reflect the portions of the original specimen that were retained on the No. 10 sieve

($W_{>No.10}$), and that passed the No. 200 sieve ($W_{<No.200}$). The total dry weight of the specimen ($W_{total,dry}$) is:

$$W_{total,dry} = W_{>No.10} + W_{<No.10} \tag{3.1}$$

where:

$$W_{<No.10} = \frac{G_S \times (W_{pre} - W_{tube})}{(G_S - \alpha)} \tag{3.2}$$

$$W_{No.200-No.10} = \frac{G_S \times (W_{post} - W_{tube})}{(G_S - \alpha)} \tag{3.3}$$

$$W_{<No.200} = W_{<No.10} - W_{No.200-No.10} \tag{3.4}$$

$W_{total,dry}$	=	total dry weight of the soil specimen [g]
$W_{>No.10}$	=	weight of material retained on the No. 10 sieve [g]
$W_{<No.10}$	=	weight of material passing the No. 10 sieve [g]
G_S	=	specific gravity of solids at 20°C
W_{pre}	=	weight of presorter, water, and soil specimen before agitations [g]
W_{tube}	=	weight of presorter filled just with water [g]
α	=	water temperature correction value
$W_{No.200-No.10}$	=	weight of material between the No. 200 and No. 10 sieves [g];
W_{post}	=	weight of presorter, water, and soil specimen after agitations [g]
$W_{<No.200}$	=	weight of material passing the No. 200 sieve [g]

The fines percentage of the specimen (P_{fines}), which is used for both USCS and AASHTO soil classifications, is:

$$P_{fines} = \left(\frac{W_{<No.200}}{W_{total,dry}}\right) \times 100 \tag{3.5}$$

Figure 3.9 summarizes the complete testing procedure for SedImaging by FieldSed, if prewashing is also required. It includes specimen prewashing, SedImaging via the FieldSed, and final PSD generation using the HWT-based method and prewashing results. This procedure was followed during the 2017 Kalamazoo River sediment characterization project (Section 3.2.4).

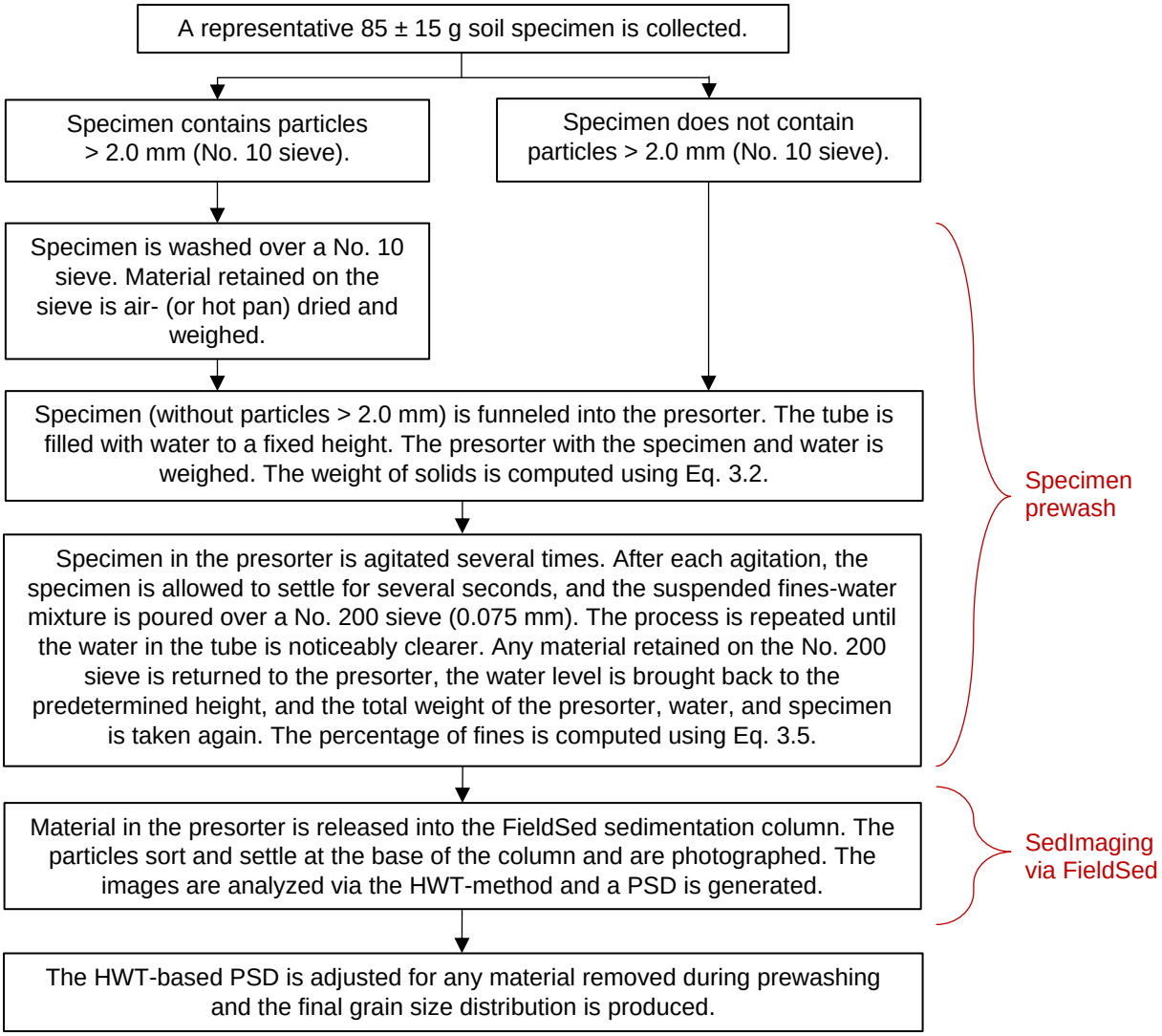

Figure 3-9. Prewashing and SedImaging by FieldSed summary design.

3.2.3 Example FieldSed Results

Figure 3.10 shows images and PSD results for two different sands photographed in the FieldSed. These results do not consider any material removed during prewashing. The specimen in Fig. 3.10(a) (Sand A) is an example where the HWT-based PSDs of the four photographed sides are nearly identical. Occasionally however, differences are observed between the four images, which warrants the development of a single combined PSD. Fig. 3.10(b) shows another example sand (Sand B) that has a larger difference between its four images. Sand B's Sides 1 and 2 contain slightly less of the coarsest particles than do Sides 3 and 4. This is reflected in Sand B's four PSDs. The PSDs are all similar in shape, but are slightly shifted horizontally from one another, with Sides 1 and 2 reporting smaller percentages of medium sand than Sides 3 and 4.

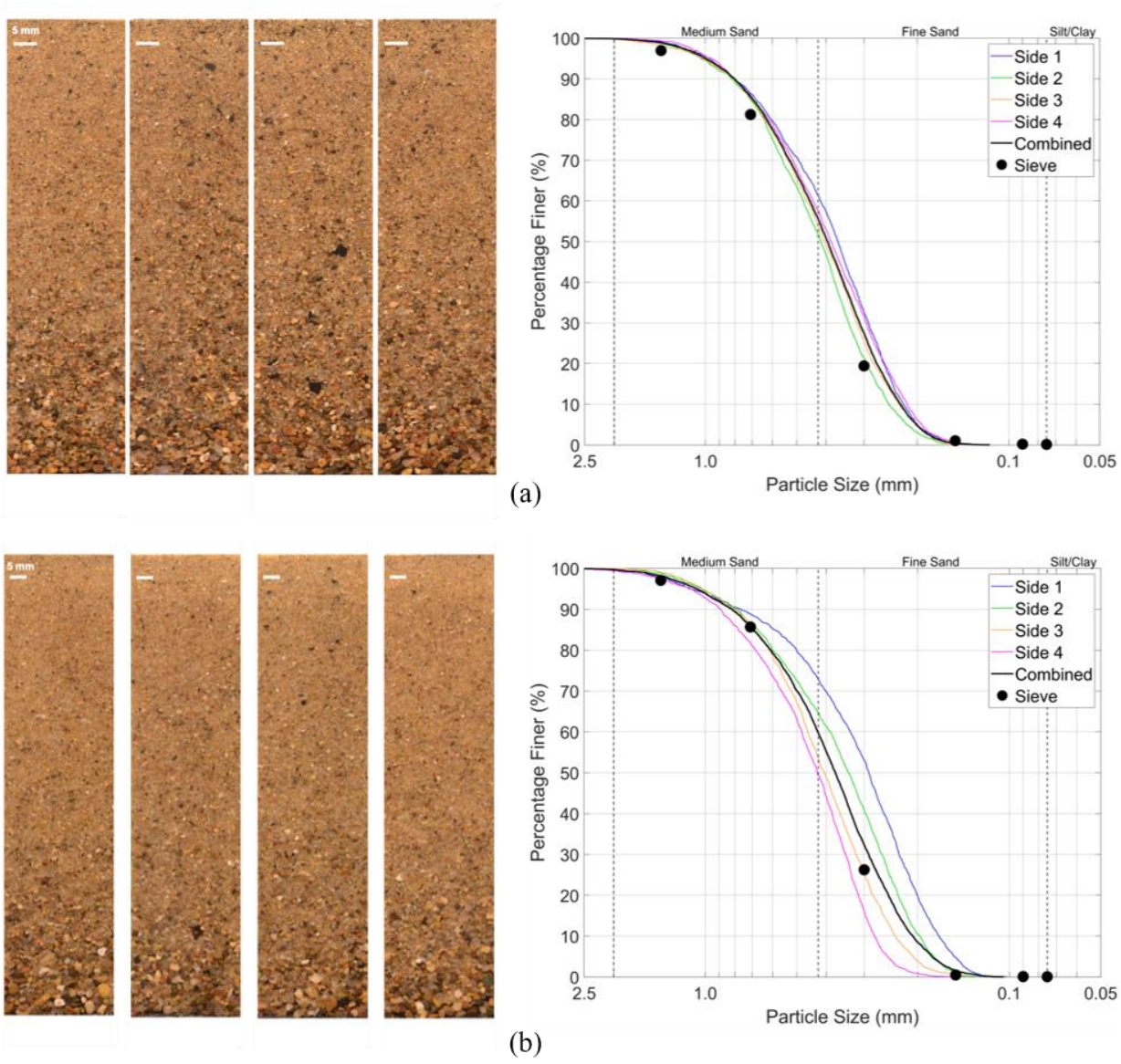

Figure 3-10. SedImaging results using the FieldSed. (a) Sand A, (b) Sand B.

For both Sand A and Sand B, the data points from all four sides are combined into one total PSD and are plotted in Figs. 3.10(a) and 3.10(b) as a thicker black line designated as “Combined”. The specimens were also sieved according to ASTM C136/C136M-19, and those results are also plotted. For both specimens, excellent agreement between the “Combined” PSD and “Sieve” is observed. Regardless of the variations between the four images of a specimen photographed in the FieldSed, combining the particle size data into one overall PSD tends to yield an accurate

representation of the specimen. Combining the four sides' PSDs into one is the standardized practice for the FieldSed.

3.2.4 Particle size distribution of Kalamazoo River sediments by FieldSed

As part of a geoenvironmental investigation of the Kalamazoo River in southwest Michigan (Fig. 3.11), river sediment samples were collected and analyzed in order to map river bedforms. In 2017, a portion of this analysis was performed using the first field application of Ohm and Hryciw's (2014) SedImaging method for particle size analysis. A field laboratory was established next to the Kalamazoo River (Fig. 3.11) to determine particle size distributions (PSDs) of over one hundred collected sediment core samples. The field laboratory was covered, but was without temperature control or an oven to dry specimens. The soils consisted mostly of fine sands with varying percentages of silt and clay. The goal of the testing program was to rapidly obtain accurate PSDs to delineate areas for more detailed subsequent mapping of fine sediment bedforms in the Kalamazoo River.

By identifying and grouping the Kalamazoo River bedforms according to grain size characteristics, more efficient follow-up stratified environmental sampling was developed. Fewer additional samples were needed in coarse bedform areas, and higher density sampling could be focused on finer-grained and transitional areas. Other field-based methods, such as cone

Figure 3-11. Kalamazoo River and this project's testing locations.

penetrometry and geophysical methods, are also available to distinguish coarse and fine bedforms. However, FieldSed was utilized in this study because it requires no additional field equipment at the sampling locations, it can be directly compared to conventional sieve and hydrometer testing, and the technology is capable of producing high resolution grain size distributions of fine and medium sands.

The field laboratory shown in Fig. 3.12 was set up by Wood Environment & Infrastructure Solutions, Inc. in a pole barn next to the Kalamazoo River in southwestern Michigan. At the field lab, 118 specimens were selected from sediment cores and analyzed using SedImaging by FieldSed. Without the need for oven-drying, the soil specimens could be tested quickly after their delivery to the field lab. Using only one to two technicians at a time, a daily average of 16 specimens were tested.

As part of the broad field testing program of the river sediments, seven samples were taken from different sediment cores for a quality control investigation. Each sample was homogenized

Figure 3-12. Field laboratory for testing the Kalamazoo River sediments.

and an approximately 85g specimen was tested in the field following the procedure outlined in Fig. 3.9. Upon imaging, the portion of the specimen tested in the FieldSed was carefully collected and sent to the Geotechnical Engineering Laboratory at the University of Michigan (UM) (see Fig. 3.11). There it was re-tested using a sister FieldSed system. This was done to evaluate the repeatability of FieldSed results obtained by different technicians under different environmental and lighting conditions. The remaining homogenized sample was also sent to UM.

Separate SedImaging tests were also performed on specimens from the untested material sent to UM. As with the specimens tested in the field lab, about 85g of each UM lab sample was tested according to the procedure in Fig. 3.9: prewashed (if necessary) and then tested by FieldSed. This second set of SedImaging tests was performed to evaluate the repeatability of the entire Fig. 3.9 testing procedure, including prewashing. The remainder of the untested material sent to UM was sieved according to ASTM C136/C136M-19. This was done to both evaluate the repeatability of prewashing, and to compare all SedImaging results by FieldSed to sieving.

Figures 3.13 through 3.19 contain the complete PSDs for the seven control specimens. These FieldSed PSDs are the combined data from the different photographed sides for each of the specimens (analogous to the "Combined" PSDs in Fig. 3.10). For each, the PSDs generated from the SedImaging's HWT image analysis method are compared to sieve data. Unlike those in Fig. 3.10, the HWT-based PSDs are now adjusted for any material removed during prewashing. The PSDs of the specimens photographed in the field are referred to as "Field" while "Field-Repeat" are the PSDs of the same specimens retested in the UM laboratory. "Lab" refers to the specimens tested fully (including prewashing) at UM. "Sieve" is the sieve data of the remaining material not tested by SedImaging that was sent to UM. Each figure also includes three photographs. The leftmost image is one of the "Field" specimen sides, the center image is one of the four "Field-Repeat" sides, and the rightmost image is one of the four sides from "Lab".

Table 3.2 summarizes various PSD characteristics including D_{60}, C_U, and the corresponding Unified Soil Classification System (USCS) group name for the seven quality control tests. The table also includes the specimen percentages that were removed by prewashing (if applicable). Using bar graphs, Fig. 3.20 compares the percentages of each specimen (according to the HWT-based PSDs or sieve data in Figs. 3.13 through 3.19) that fall within four particle size ranges: coarser than 2.0mm (coarse sand or gravel), 2.0mm to 0.425mm (medium sand), 0.425mm to 0.075mm (fine sand), and finer than 0.075mm (silt/clay).

By observation of Figs. 3.13 through 3.19, the agreement between PSD results in "Field", "Field-Repeat", "Lab", and "Sieve" tests is subjectively assessed to be excellent. Any small variations between the four data sets for each specimen can be attributed to the absence or presence of only a few of the coarsest particles, which will cause parallel offsets over the remainder of the PSD curves. For example, in Fig. 3.14 (Specimen B), the "Lab" PSD is the same shape, but lies

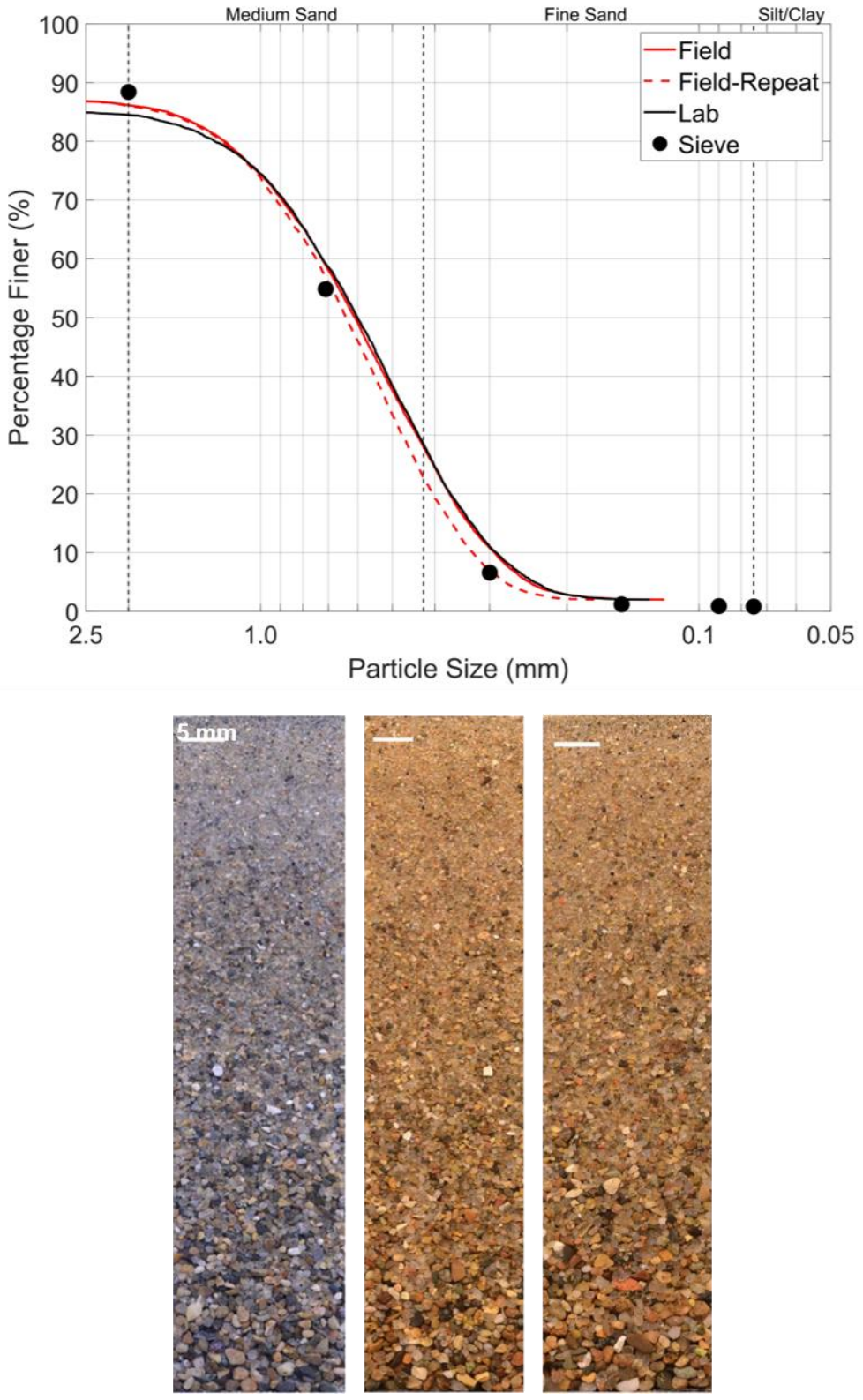

Figure 3-13. Specimen A. (Top) verification PSDs, (Bottom) Field [left], Field-Repeat [center], and Lab [right] photographed FieldSed sides.

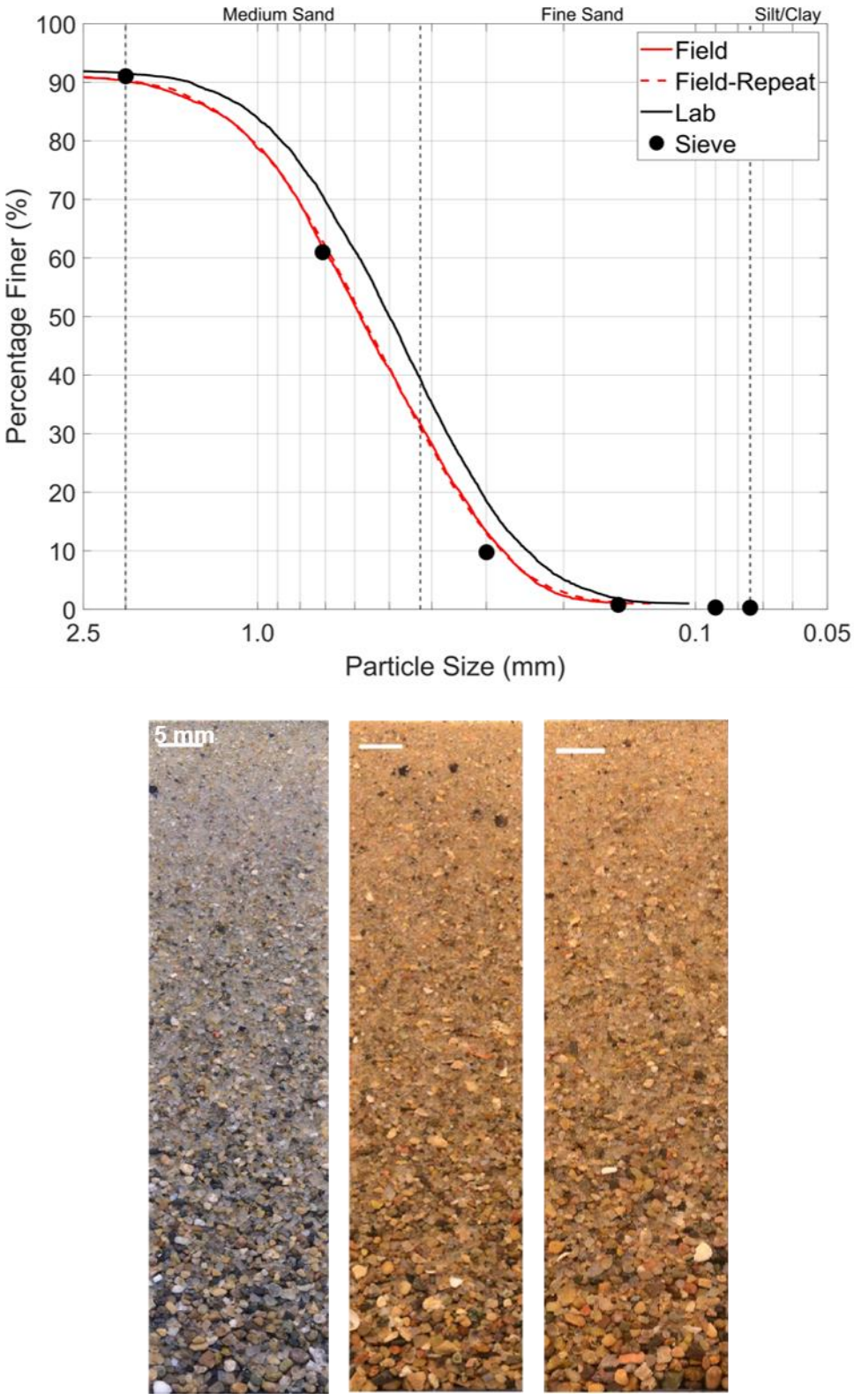

Figure 3-14. Specimen B. (Top) verification PSDs, (Bottom) Field [left], Field-Repeat [center], and Lab [right] photographed FieldSed sides.

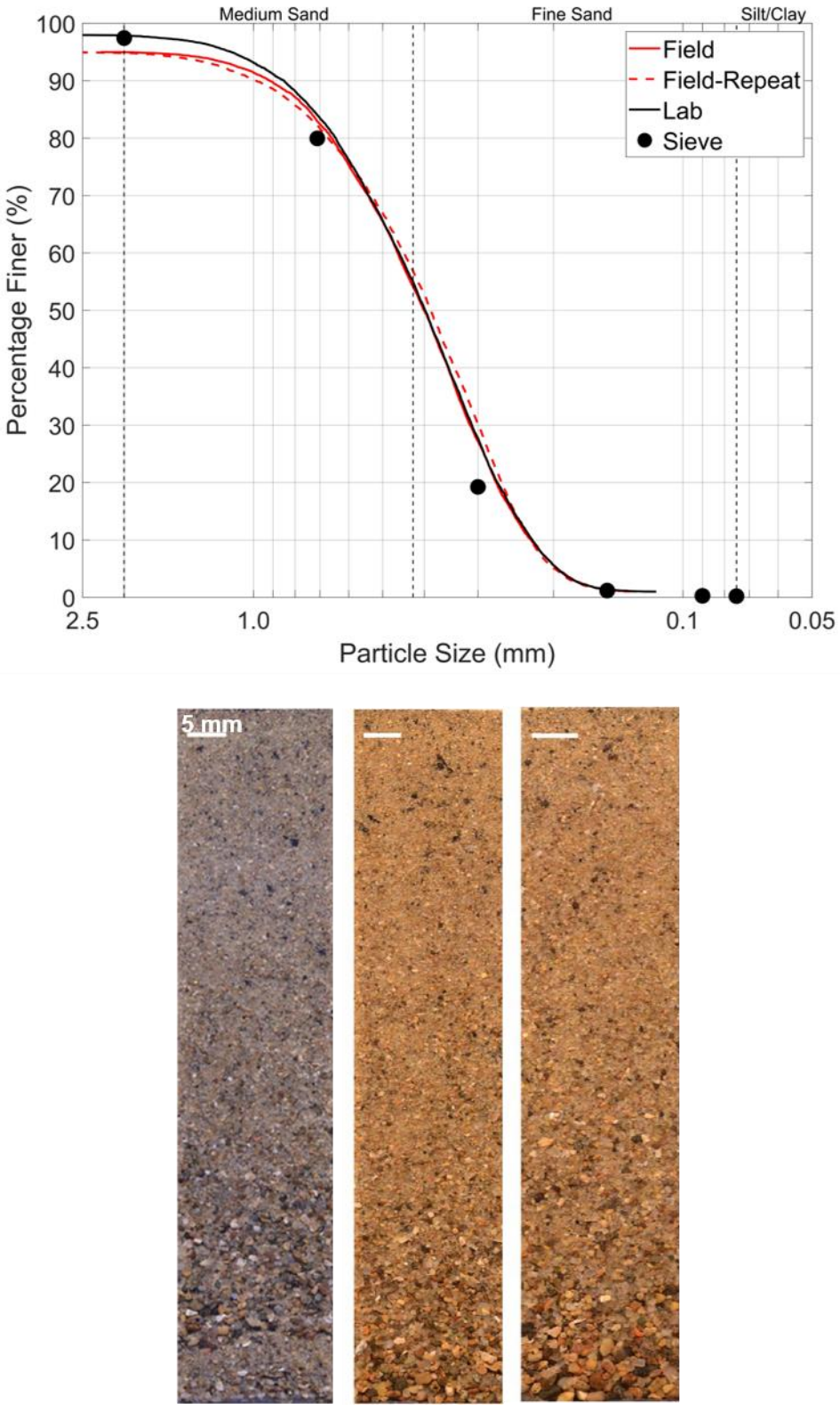

Figure 3-15. Specimen C. (Top) verification PSDs, (Bottom) Field [left], Field-Repeat [center], and Lab [right] photographed FieldSed sides.

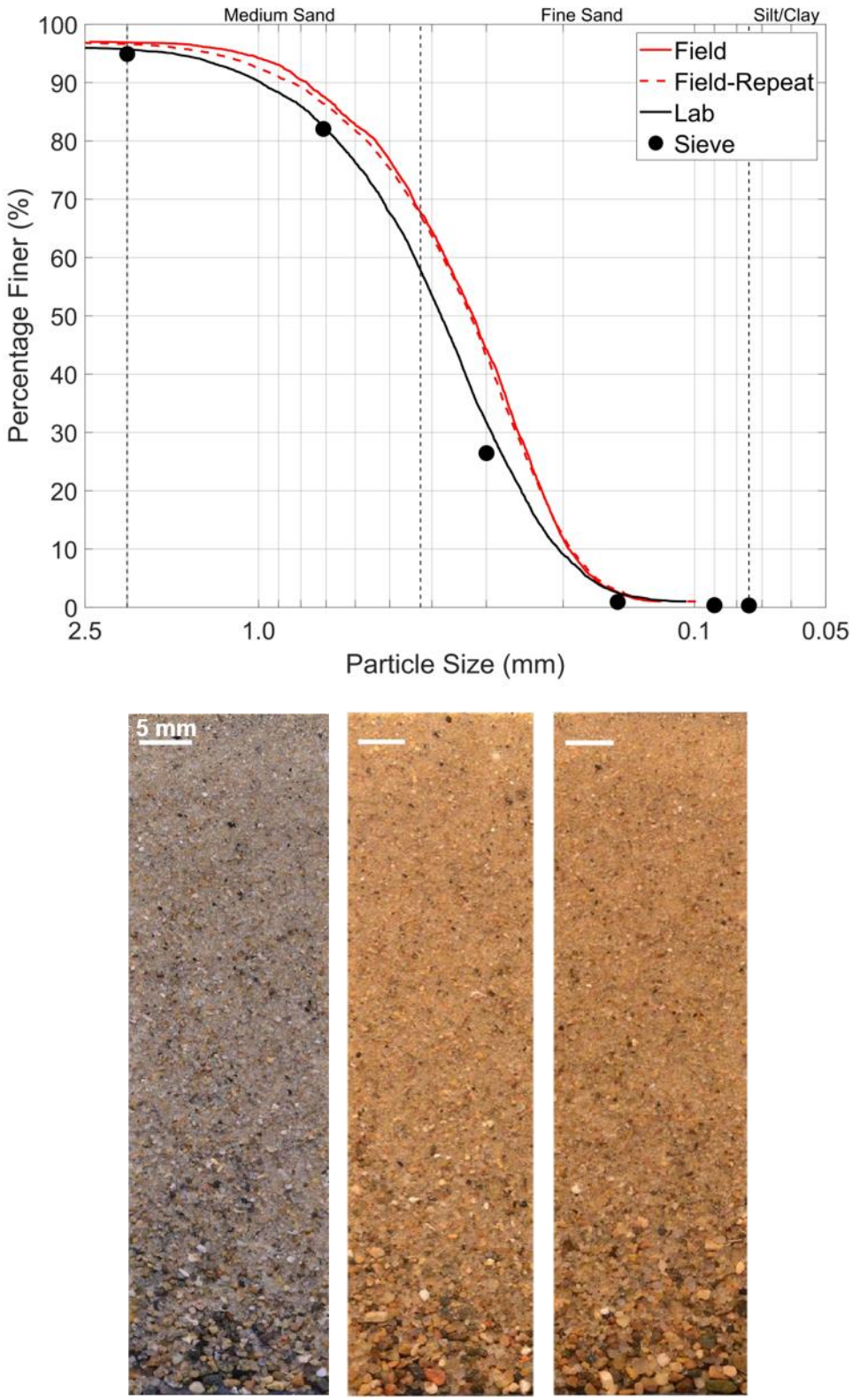

Figure 3-16. Specimen D. (Top) verification PSDs, (Bottom) Field [left], Field-Repeat [center], and Lab [right] photographed FieldSed sides.

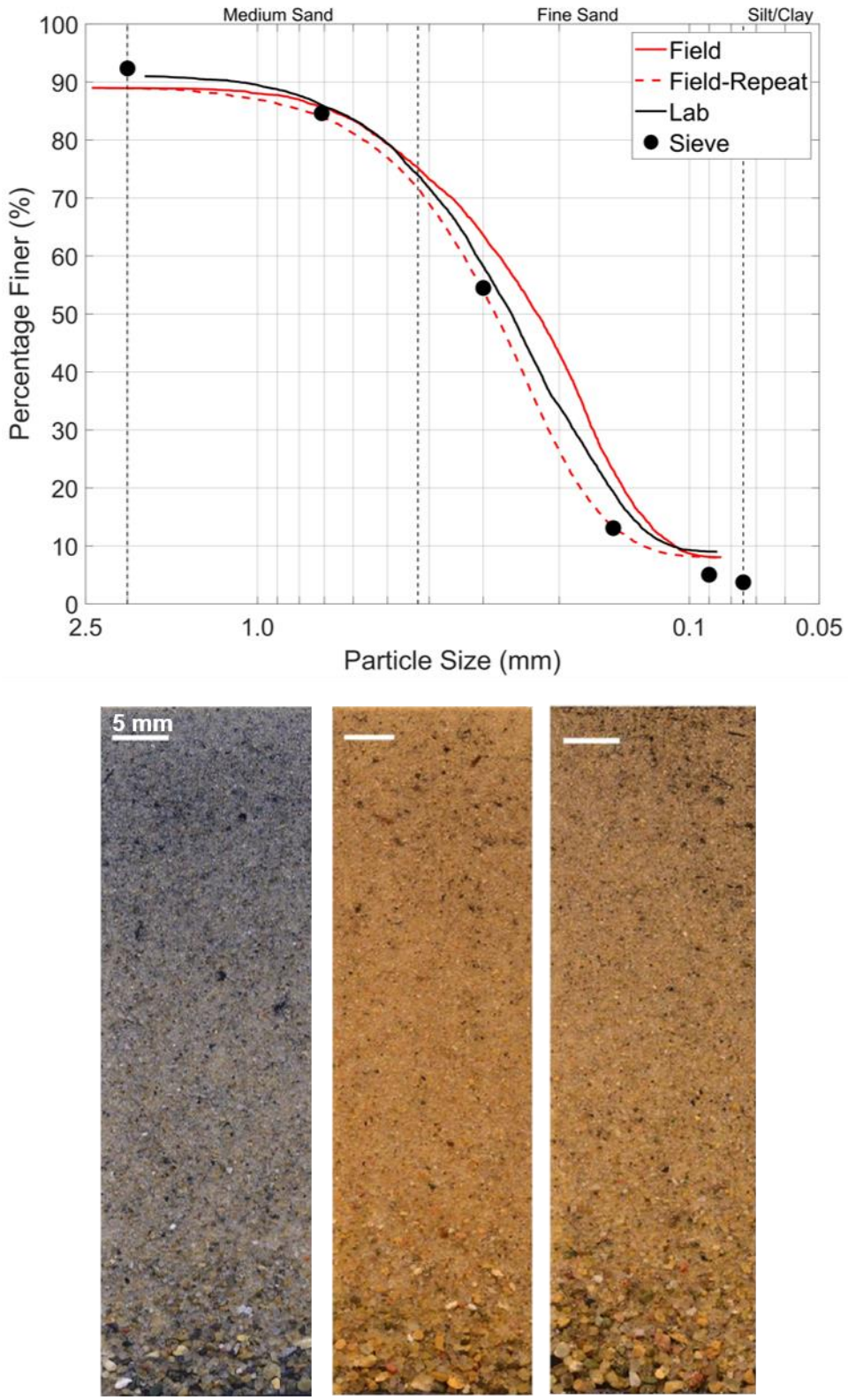

Figure 3-17. Specimen E. (Top) verification PSDs, (Bottom) Field [left], Field-Repeat [center], and Lab [right] photographed FieldSed sides.

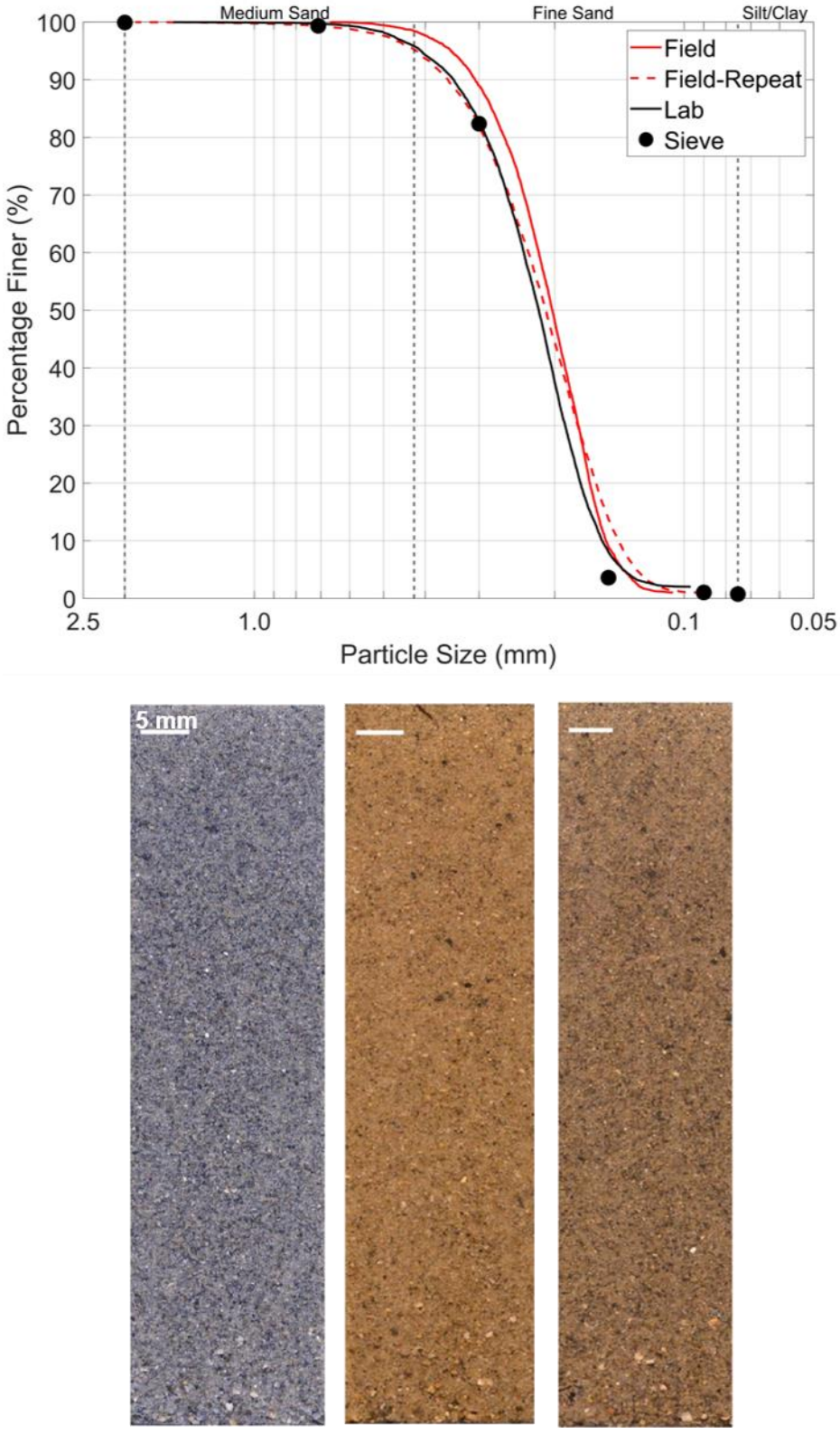

Figure 3-18. Specimen F. (Top) verification PSDs, (Bottom) Field [left], Field-Repeat [center], and Lab [right] photographed FieldSed sides.

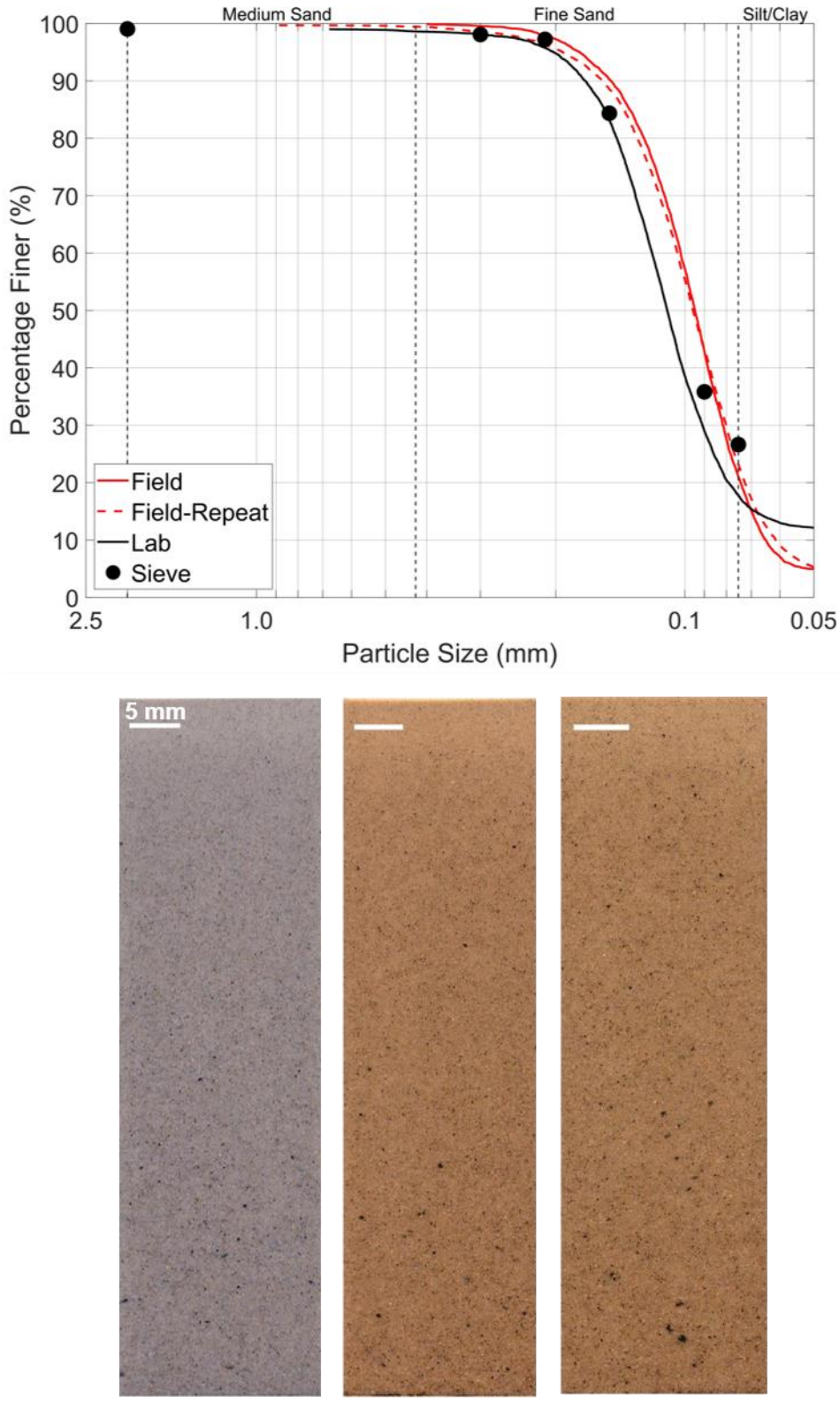

Figure 3-19. Specimen G. (Top) verification PSDs, (Bottom) Field [left], Field-Repeat [center], and Lab [right] photographed FieldSed sides.

Table 3-2. Verification testing of select Kalamazoo River specimens.

	Specimen A				Specimen B				Specimen C				Specimen D				Specimen E			
	Field	Field-Repeat	Lab	Sieve	Field	Field-Repeat	Lab	Sieve	Field	Field-Repeat	Lab	Sieve	Field	Field-Repeat	Lab	Sieve	Field	Field-Repeat	Lab	Sieve
D_{60} [mm]	0.72	0.74	0.72	0.75	0.68	0.68	0.59	0.70	0.46	0.45	0.46	0.50	0.37	0.37	0.44	0.45	0.28	0.33	0.31	0.33
D_{50} [mm]	0.60	0.63	0.60	0.63	0.58	0.58	0.50	0.59	0.40	0.39	0.40	0.43	0.33	0.33	0.38	0.40	0.22	0.28	0.26	0.28
D_{30} [mm]	0.44	0.47	0.44	0.47	0.42	0.42	0.37	0.41	0.31	0.30	0.31	0.33	0.25	0.25	0.29	0.31	0.16	0.21	0.19	0.21
D_{10} [mm]	0.29	0.32	0.29	0.33	0.28	0.28	0.24	0.30	0.23	0.23	0.23	0.24	0.19	0.19	0.21	0.22	0.11	0.14	0.11	0.13
C_U [a]	2.48	2.31	2.48	2.27	2.43	2.43	2.46	2.33	2.00	1.96	2.00	2.08	1.95	1.95	2.10	2.05	2.55	2.36	2.82	2.54
C_C [b]	0.93	0.93	0.93	0.89	0.93	0.93	0.97	0.80	0.91	0.87	0.91	0.91	0.89	0.89	0.91	0.97	0.83	0.95	1.06	1.03
USCS Soil Classification [c,d,e]	c	c	c	c	c	c	c	c	c	c	c	c	c	c	c	c	d	d	d	c
Retained on No. 10 sieve [%] [f]	13	13	15	--	9	9	8	--	5	5	2	--	3	3	4	--	11	11	9	--
Passing No. 200 sieve [%] [f]	2	2	2	--	1	1	1	--	1	1	1	--	1	1	1	--	8	8	9	--

[a] Coefficient of Uniformity, $C_u = D_{60}/D_{10}$
[b] Coefficient of Curvature, $C_c = (D_{30})^2/(D_{60} \times D_{10})$
[c] SP, poorly-graded sand
[d] SP-SM, poorly-graded sand with silt; or SP-SC, poorly-graded sand with clay
[e] SM, silty sand; SC, clayey sand; or SM-SC, silty, clayey sand
[f] Via the prewashing procedure

Table 3-2 Con't. Verification testing of select Kalamazoo River specimens.

	Specimen F				Specimen G			
	Field	Field-Repeat	Lab	Sieve	Field	Field-Repeat	Lab	Sieve
D_{60} [mm]	0.22	0.23	0.24	0.24	0.10	0.10	0.12	0.11
D_{50} [mm]	0.20	0.21	0.22	0.22	0.095	0.095	0.11	0.10
D_{30} [mm]	0.18	0.18	0.19	0.19	0.080	0.080	0.09	0.08
D_{10} [mm]	0.14	0.15	0.15	0.15	0.064	0.060	--	--
C_U [a]	1.57	1.53	1.60	1.60	1.56	1.67	--	--
C_C [b]	1.05	0.94	1.00	1.00	1.00	1.07	--	--
USCS Soil Classification [c,d,e]	c	c	c	c	e	e	e	e
Retained on No. 10 sieve [%] [f]	0	0	0	--	0	0	1	--
Passing No. 200 sieve [%] [f]	1	1	2	--	5	5	12	--

[a] Coefficient of Uniformity, $C_u = D_{60}/D_{10}$
[b] Coefficient of Curvature, $C_c = (D_{30})^2/(D_{60} \times D_{10})$
[c] SP, poorly-graded sand
[d] SP-SM, poorly-graded sand with silt; or SP-SC, poorly-graded sand with clay
[e] SM, silty sand; SC, clayey sand; or SM-SC, silty, clayey sand
[f] Via the prewashing procedure

slightly to the right of the “Field”, “Field-Repeat”, and “Sieve” PSDs. The “Lab” specimen contained slightly fewer particles with diameters larger than 1.0mm than the other specimens.

In addition to the PSDs, it is also useful to compare size distributions by specific ranges (coarse sand or gravel, medium sand, fine sand, and fines) as shown in Fig. 3.20. For example, in Specimen B, we see nearly identical percentages of the coarsest and finest particles. The only clear difference is that the “Lab” test suggested 8% more fine sand (rather than medium sand) than did the other three tests. This was caused by a slight under-sampling of the medium sand for use in the “Lab” test. The “Sieve” results agreed perfectly with the “Field” and “Field-Repeat” PSDs.

Several general observations can be made by inspection of Figs. 3.13 through 3.19 and Fig. 3.20. First, comparison of “Field” and “Field-Repeat” data confirm the repeatability of results by SedImaging using FieldSed. This means that the sorting of particles during sedimentation is both effective and repeatable. It also confirms that the particles photographed on the four sides of the column are representative of the material in the interior that is not in camera view. These tests further illustrate the insensitivity of the FieldSed results to environmental changes and specifically, differences in ambient lighting. As seen in the specimen photos in Figs. 3.13 through 3.19, the “Field” specimens were photographed in natural light, whereas the “Field-Repeat” and “Lab” were photographed under overhead fluorescent lighting. The final PSDs of these three tests were not impacted by the different lighting conditions.

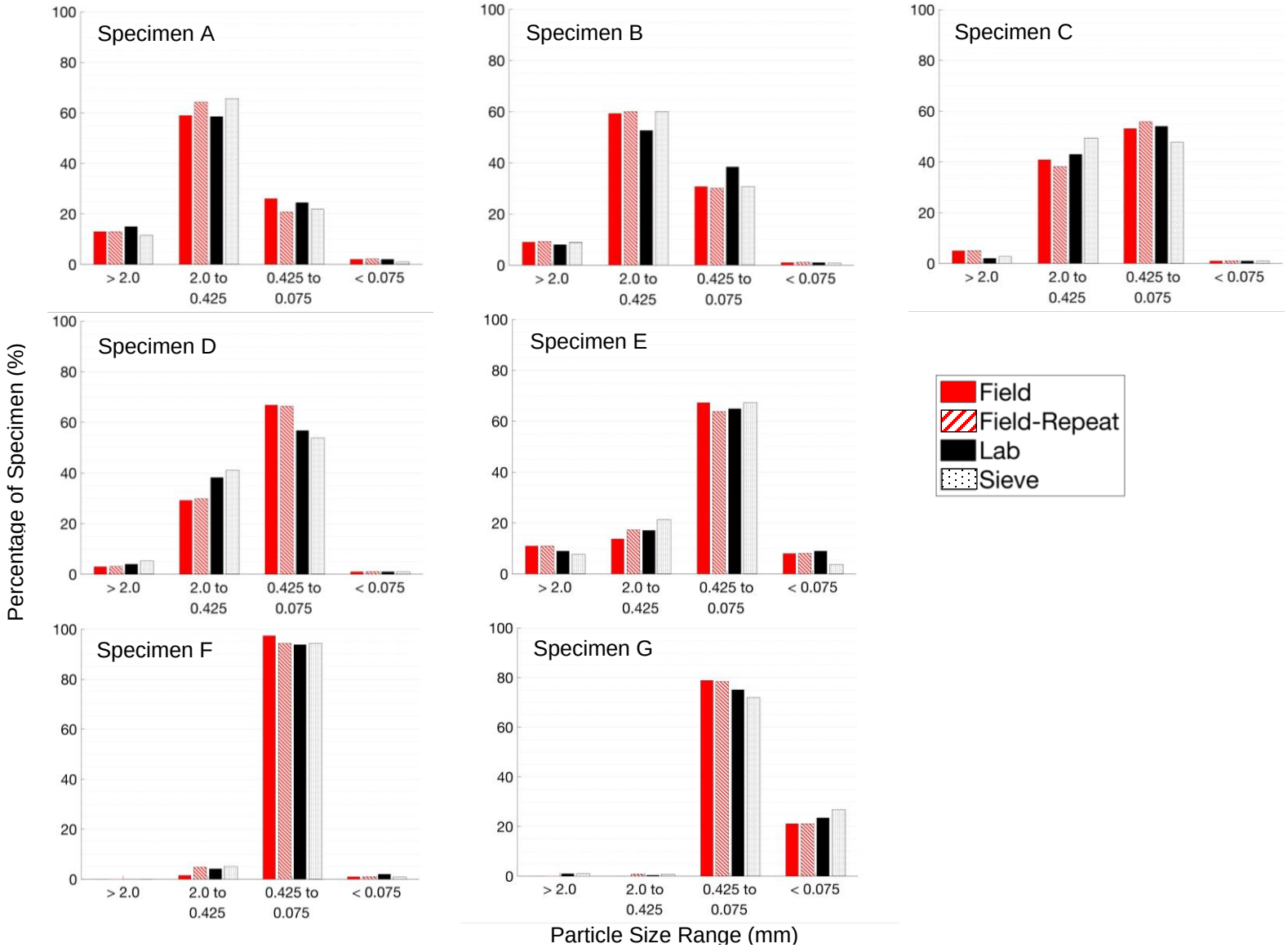

Figure 3-20. Particle size distributions by size ranges for quality control Specimens A through G.

Secondly, the HWT-generated PSDs, once adjusted for material removed by prewashing, show strong correlation with traditional sieve results. This confirms the accuracy of the sample-splitting procedures used by field technicians and, more importantly, of the prewashing method itself. The figures confirm that prewashing does a very good job of removing the out-of-range sized particles from the specimens prior to FieldSed testing.

The results for Specimen G (Fig. 3.19) are noteworthy, as this material contained more fines than the other six specimens. According to Table 3.2, the field technicians removed only 5% fines from their sample by prewashing. By contrast, 12% fines were removed in the "Lab" specimen. In the "Field", "Field-Repeat", and "Lab" FieldSed photographs, the HWT-based image analysis reported additional fines in the specimens that were not removed during both prewashings.

Although there was a significant difference in the amount of fines removed during prewashing between the field and at UM, when the corresponding HWT-based PSDs were appropriately adjusted, the results were similar. The final HWT-based PSDs more closely match the sieve data. This success is attributed to the fact that the HWT method (when used on images having sufficient magnification), will detect silt particles. Despite this, it is important to note that prewashing specimens is still an important step with SedImaging by FieldSed. The prewashing removes the vast majority of fines in a specimen, especially clay, thus reducing the settling time required during its release into the FieldSed sedimentation column. While it may be concluded that the FieldSed procedure somewhat compensates for incomplete prewashing, more research is needed to test the particle size limits of the FieldSed analysis. This quality control investigation was an early indication that silty sands and possibly sandy silts may be characterized by SedImaging using FieldSed.

The FieldSed and HWT results may also be immune to some abnormalities that may arise during sedimentation. In the "Field" test of Specimen C (Fig. 3.15) the soil particles appear to have been deposited in two stages. This was attributed to an inadvertently step-wise release of soil from the presorter tube. As a result, instead of the larger particles continuously grading to smaller particles over the full specimen height, some of the smaller particles are located beneath larger ones, as observed in Fig. 3.15. This was an extremely rare occurrence in the Kalamazoo River FieldSed testing program but is mentioned here because it happened to occur in one of the control tests. Despite this unusual abnormality, the final "Field" HWT-based PSD for Specimen C was in excellent agreement with the other PSDs.

3.3 Sed360

As noted throughout Section 3.2, SedImaging via FieldSed furthered the already established advantages of LabSed over sieving. However, FieldSed still requires users to manually rotate the sedimentation column to photograph each of its four sides. The PSDs determined for each side has to be combined to produce a single PSD representative of the entire specimen. The square-cross section of the extruded acrylic tubing also causes visual distortion at the four corners, requiring users to crop out portions of the FieldSed images prior to image analysis.

In response, the Sed360 SedImaging system was developed by Ventola and Hryciw (2022a). The new Sed360 system replaces the square tubing of the FieldSed with a circular cross-section sedimentation column that sits atop a rotating stage. This new system captures images of the sedimented cylindrical soil specimen on the rotating stage. Thus, instead of taking four separate images (like FieldSed), the Sed360 is automated to take many more images of the settled soil assembly as it rotates. Narrow vertical strips from each images is extracted and stitched into one large seamless "unwrapped cylinder" image of the specimen surface. This stitched image is

analyzed to determine the specimen's PSD. This automation increases the testing efficiency of SedImaging by reducing required user intervention during a test, increases the accuracy of the image analysis results by including more of a specimen's soil particles in the analysis, and it has also lead to the expansion of the soil particle size (diameter) range eligible for SedImaging testing by more than a factor of two. For the first time with any SedImaging system, the range of testable soil particle sizes in the Sed360 includes the entire range of sands, from 4.75mm to 0.075mm (between US Standard sieves No. 4 and No. 200) per the Unified Soil Classification System. The prewashing method described in Section 3.2.2 can also be used with the Sed360 to determine the fines and gravel percentages of a sand specimen tested in the Sed360.

3.3.1 The Sed360 system

The Sed360 system, shown in Fig. 3.21, consists of a 1.8m (6ft) long clear acrylic sedimentation column with an inside diameter of 25.4mm (1in) and a 3.2mm (1/8in) wall thickness. The column is held in place by a support tower. A positioning bracket mounted on the support tower (Fig. 3.21[a]) ensures perfect verticality of the column, while allowing it to rotate. The split-piece bracket and the bracket latch (Fig. 3.22) were designed to facilitate easy removal and replacement of one sedimentation column by another for rapid testing of consecutive

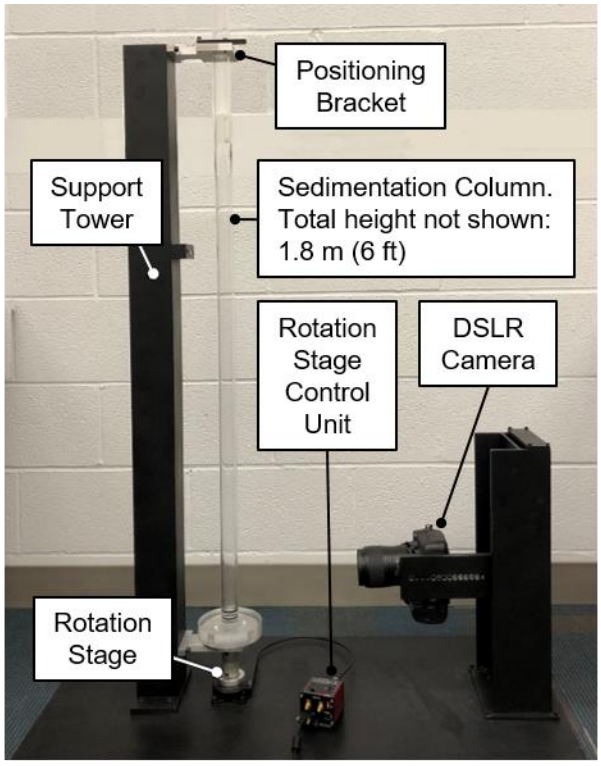

(a)

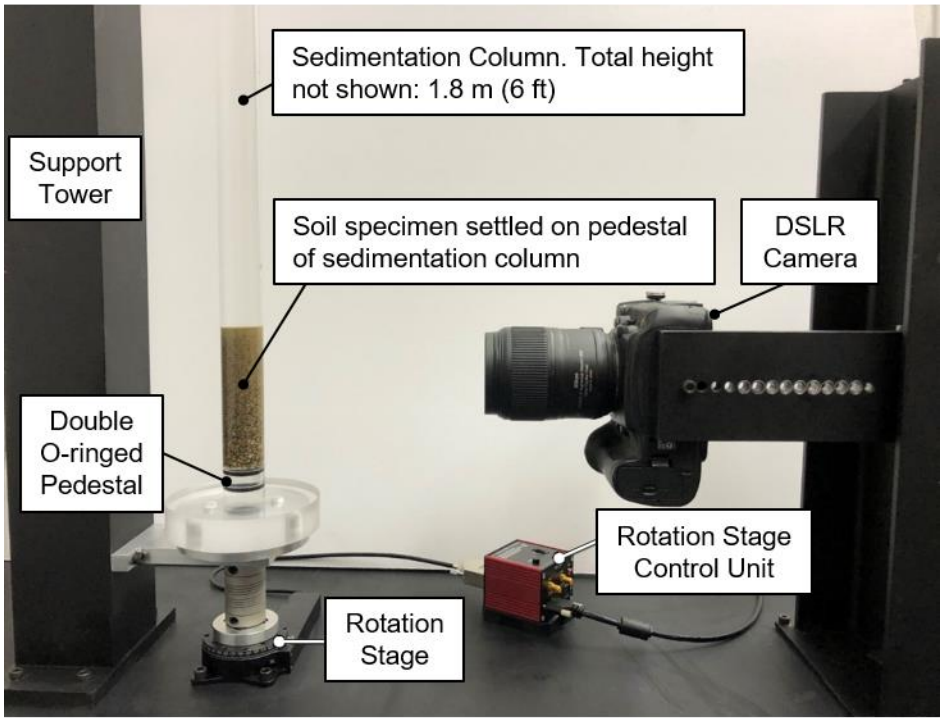

(b)

Figure 3-21. The Sed360. (a) Full view, (b) Detailed view of bottom.

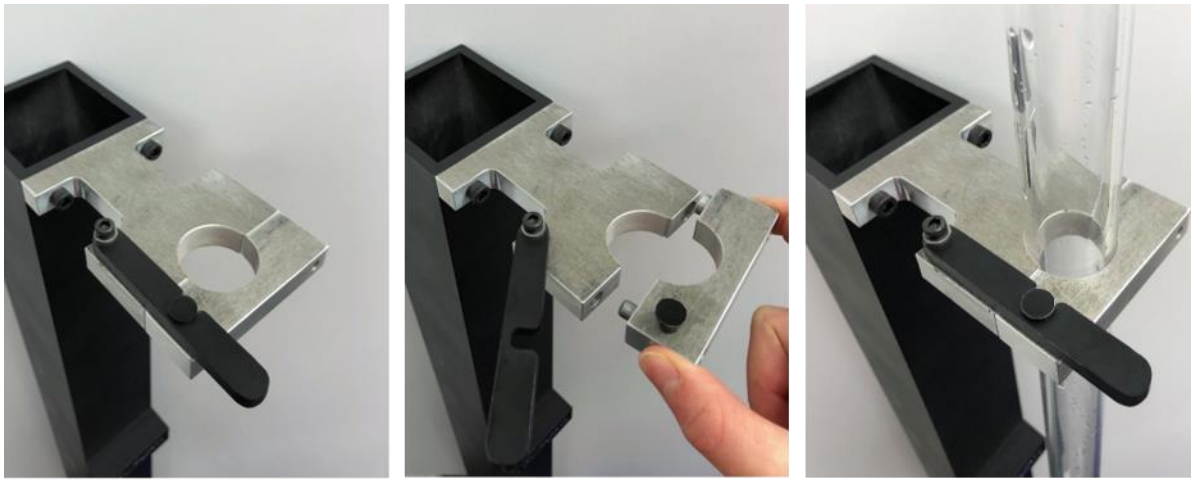

Figure 3-22. Sed360 positioning bracket. (a) Closed, (b) Opened, (c) Sedimentation column inserted.

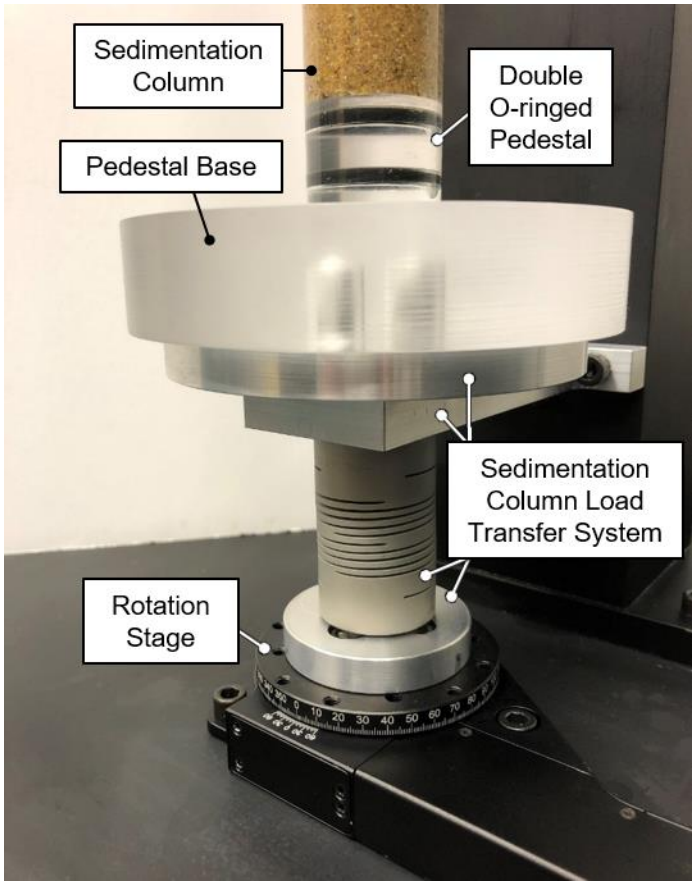

Figure 3-23. Sed360 pedestal, load transfer system, and rotation stage.

specimens. The sedimentation column is open on its top end, and fitted with a removable double O-ringed acrylic pedestal on the bottom (Fig. 3.23). Removal of the pedestal allows for rapid clean up after testing. The sedimentation column sits atop a Thorlabs motorized precision rotation stage (Fig. 3.23). Users can set the range and speed of rotation.

Figure 3.23 also shows the Sed360's load transfer system. The Thorlabs rotation stage has a load capacity of 15N (1.5kg, 3.4lb). The weight of the Sed360 hardware plus soil and water in the column exceeds this capacity. Therefore, a system was designed to transfer the weight of the sedimentation column and its contents from the stage to the support tower while still allowing the column to rotate freely. Figure 3.24 details the hardware components of the load support system.

A drive block (Fig. 3.24[a]) is screwed into the rotation stage. A short central shaft protrudes up from the drive block where it is firmly locked into the lower section of a flexible shaft coupling (Fig. 3.24[b]). The coupling is used to adjust for any small longitudinal misalignment between the rotation stage and the parts of the load support system above it. The bearing block in Fig. 3.24(c) is secured to the system's support tower. A stainless steel ball bearing bushing is press-fitted into the bearing block (Fig. 3.24[c]). Figure 3.24(d) shows a rotation platform which sits on the bearing block. The rotation platform has a central aluminum shaft (not shown in Fig. 3.24) permanently affixed to the underside of the platform. This shaft slips through the ball bearing bushing and is held tightly in the upper section of the flexible shaft coupling. Thus, the shaft and the platform rotate with the rotating stage, drive block, and flexible coupling. Lastly, the sedimentation column and its pedestal base sit on the rotation platform. Two rigid positioning dowels project upward from the rotation platform (Fig. 3.24[d]). They fit snugly into the removable pedestal base, ensuring accurate and consistent positioning of the sedimentation column for image capture.

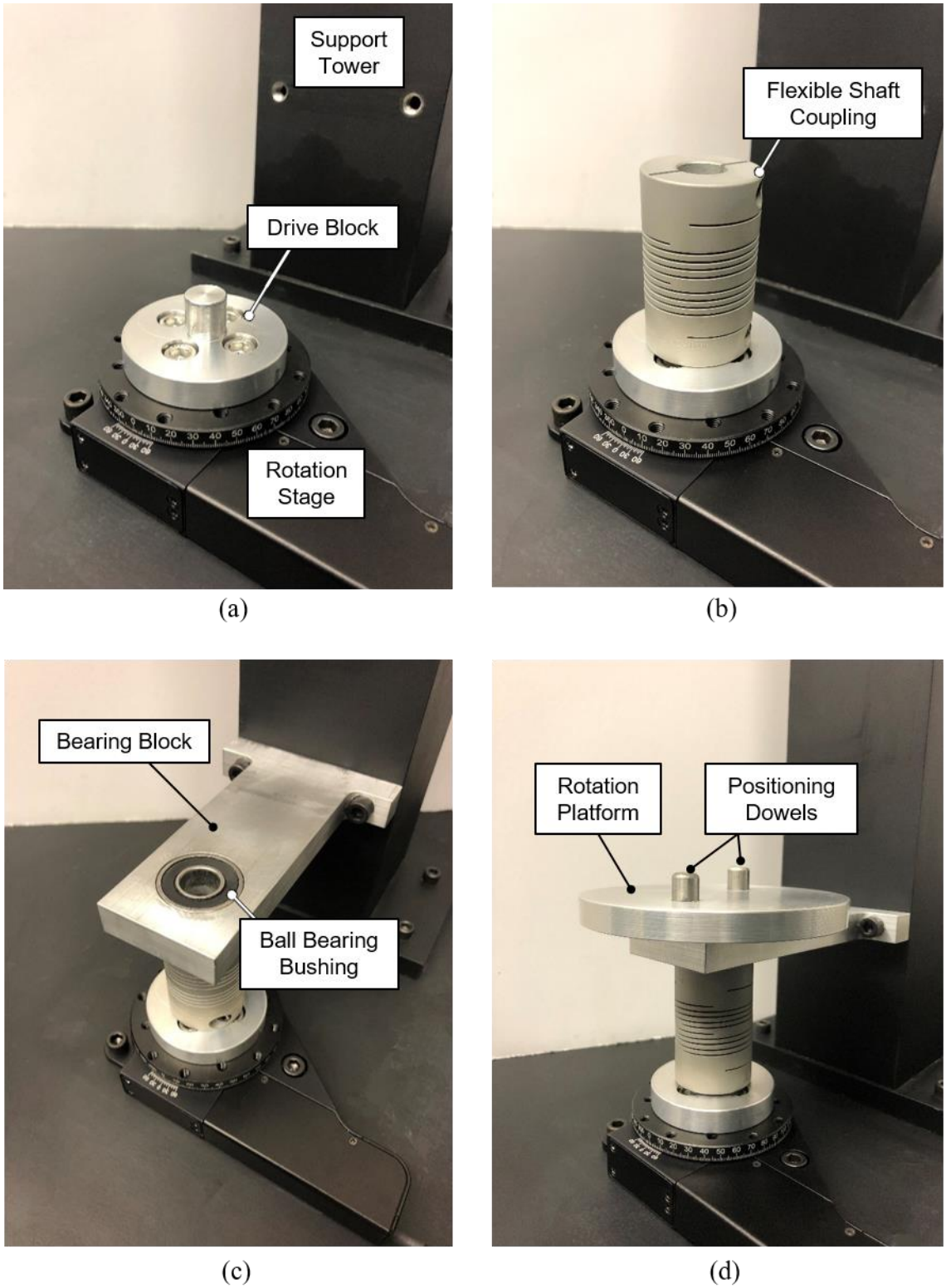

Figure 3-24. Sed360 load transfer system. (a) Drive block, (b) Flexible shaft coupling, (c) Bearing block, (d) Rotation platform.

The final piece of hardware of the Sed360 system is the presorter tube. It is a 457mm (18in) long clear acrylic tube having an inside diameter of 22.2mm (7/8in) and a 1.6mm (1/16in) wall thickness. Like the sedimentation column, the tube has one open end while the other is closed by a rubber plug. The presorter is used to instantaneously release a soil specimen into the top of the sedimentation column. The tube is also used to break up any particle clumps within a soil specimen prior to release into the column. Finally, the presorter tube can be used (as applicable) in the prewashing procedure (Section 3.2.2) to quantify and remove gravel and fines from a soil specimen.

3.3.2 Performing a Sed360 test

There are four stages in a Sed360 test. The first stage involves preparing a soil specimen and releasing it into the Sed360 system. The next set of steps is to automatically capture images of the settled soil. The third stage is automatically processing the captured images into a single "unwrapped cylinder" image, and the fourth stage is the analysis of the unwrapped image to generate the soil's PSD.

Stage 1. Introducing a Soil Specimen into the Sed360 System

To begin the Sed360 test, the sedimentation column is filled with water. Next, an 85 ± 15g soil specimen is funneled into the open end of the presorter tube. Water is added to the presorter until the tube is around 80 to 90 percent full. Next, the open end of the tube is covered by a rubber membrane. A vacuum seal is created by gently pressing the membrane into the tube while stretching it over the outside of the tube. Once sealed, the presorter and its contents are vigorously agitated to break up any soil clumps in the specimen. The tube is then inverted so the end with the rubber membrane is on the bottom and soil particles begin to settle atop the rubber membrane. Next, the membrane is slipped off. Due to the vacuum, the soil specimen and water remain inside

the tube even with the membrane removed. This allows the presorter tube to be cleanly transported to the top of the sedimentation column. A small adaptor is used to align and mate the open end of the presorter to the top of the sedimentation column. The rubber plug is removed, releasing the vacuum. The soil and water in the presorter immediately fall into the sedimentation column, and the soil particles begin to settle and sort by size.

The largest particles in the soil specimen naturally settle at the base of the sedimentation column first, followed by progressively finer particles. The amount of time required for the entire soil specimen to settle will vary depending on the soil's gradation, but most well-graded sand specimens will settle in less than 10 minutes, with clean, poorly-graded medium sands settling in under five. Once the entire specimen has settled, image capture using the rotation stage can commence.

Stage 2. Sed360 Image Capture

The image capture is fully automated. The Thorlabs precision stage is controlled by a computer where users set the rotation speed and range. For the current Sed360 test, the stage is programmed to rotate at a speed of 0.8°/s. A full 360° rotation takes 7.5 minutes. The rotation speed was conservatively selected to assure that there would be precise image stitching and no image blurring. While the stage is rotating, the camera is automatically capturing images of the soil. There is a five-second pause between photographs; with the current stage rotation speed, this corresponds to a soil image every four degrees, totaling 90 images captured for the full rotation. After the stage has rotated 360°, the sedimentation column is detached from the positioning system, and the column's pedestal base (Fig. 3.23) is removed for quick cleanup.

A parametric analysis later revealed that a rotation speed of 1.5°/s paired with a one-second pause between photographs can be used to produce the same results as those by the slower

rotation (0.8°/s). Using a rotation speed of 1.5°/s reduces the total rotation and image capture time to four minutes. Henceforth, the faster rotation time of 1.5°/s will be utilized in all Sed360 testing. All data photographed by the Sed360 presented here use the older rotation speed of 0.8°/s.

Stage 3. Image Processing

The 90 photographs collected during stage rotation are stitched to form an "unwrapped cylinder" of the settled soil. The image stitching is fully automated. Figure 3.25 illustrates the process. For each of the 90 captured images, only a 64 pixel-wide portion from the center of the photographed sedimentation column is utilized. The 64-pixel width of each stitched image was selected based on the diameter of the sedimentation column and the camera magnification. This thin strip of each image is taken from the portion of the sedimentation column that is normal to the axis of the camera lens (i.e. there is no particle distortion due to the curve of the sedimentation column). Therefore, when the 64-pixel widths of consecutive images are automatically stitched together, there is no image distortion (particle shortening or elongation).

The physical distance of this 64-pixel width is approximately 1.3mm (0.05in). Once all the image "slices" are extracted, they are ordered sequentially to begin forming the stitched image. A final step crops the widths of the slices (as needed) to ensure adjacent slices are perfectly aligned. The cropping involves comparing the columns of pixel grayscale intensity values of one slice to those of the next consecutive slice, and removing the pixel columns of the first slice that are also present in the later slice. This final step is needed to account for any minor fluctuations in camera shutter speed or elapsed time between successive image captures. Figure 3.26 shows the unwrapped image for an example soil that contains soil particles from the entire sand range (coarse, medium, and fine sand). The stitched image of the unwrapped cylinder is now ready for PSD analysis.

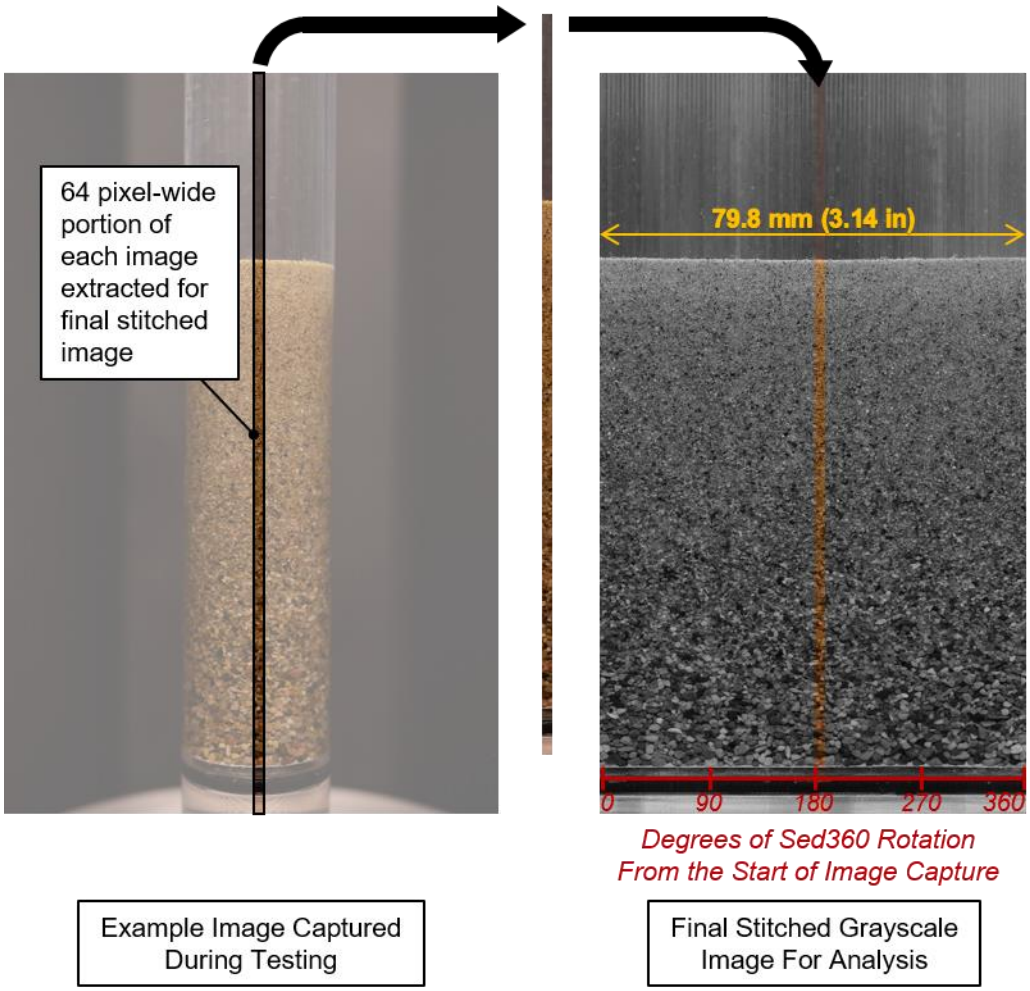

Figure 3-25. Image stitching of the Sed360 system.

Figure 3-26. Unwrapped cylinder image of example sand tested with the Sed360 system.

Stage 4. PSD Determination Using Haar Wavelet Transformation

With the expanded range of testable soil particle sizes afforded by the new Sed360, the accuracy of the original HWT-based analysis method used with the LabSed and FieldSed systems required reexamination. As will be discussed in Section 4.2.2, an autoadaptive HWT image analysis approach was developed. Despite it being developed after the fabrication of the Sed360, this updated analysis method can be used for any of the other SedImaging systems. This new method also relies on the same HWT-based image analysis fundamentals as the original analysis approach. The details of both of these methods, as well as example Sed360 PSD results will be reserved for Chapter 4.

3.3.3 Sed360 specimen utilization in the image analysis

For typical 85g sand specimens tested in the Sed360, such as that in Fig. 3.26, the percentage of the specimen's total soil particles that are observed at the sedimentation column's periphery (and photographed by the Sed360) is between approximately 10% and 20%. This percentage will be larger for coarser sand particles than for finer ones. There has not been a direct verification that the soil particles in the interior of the column at a given elevation are of the same size as those at the periphery. However, with excellent agreement between Sed360 and sieve results (deferred to Chapter 4) as well as in earlier reported SedImaging comparisons (Figs. 3.10 and 3.13 through 3.19, Hryciw et al. 2015, Ohm and Hryciw 2014, Ventola and Hryciw 2019, and Ventola et al. 2020b), which also reported strong agreement, such a verification has essentially been performed. Moreover, visual observation of particle settling confirms a mostly horizontal settling front, which, in addition to the Sed360-sieve agreement, confirms that soil particles at the outer edge of the sedimentation column are of similar size to those in the interior of the column at the same elevation.

3.3.4 Summary of Sed360 improvements over previous SedImaging systems

The advantages of FieldSed over sieving as described in Section 3.2 and by Ventola et al. (2020b) and Ventola and Hryciw (2019) also hold for the Sed360: simple hardware, portability, rapid testing, no need to oven-dry specimens prior to testing, low noise, and the ability to set up many sedimentation columns for parallel testing of specimens. However, the Sed360 has its additional advantages. First, the new circular column atop a rotation stage allows for test automation; during image capture, lab technicians can attend to other tasks. Secondly, the removable circular double O-ringed pedestal of the Sed360 provides a better seal and facilitates rapid cleaning of the system. As mentioned previously, all of the particles at the periphery of the

specimen are utilized for PSD determination. Lastly, but maybe most importantly, the continuous unwrapped cylinder image has expanded the testable soil particle size range of SedImaging to now include the entire sand range (4.75mm to 0.075mm; between US Standard sieves No. 4 and No. 200). This last improvement will be further emphasized in Section 4.2 as part of the discussion of the autoadaptive HWT-based image analysis method.

3.4 Chapter Summary

This chapter documented the evolution of SedImaging. It began by introducing the original SedImaging system, the LabSed, while detailing the overall procedure of testing a soil by this method. Next, the second SedImaging system, the FieldSed, was presented. The FieldSed is a field-portable device with low-cost hardware and is ideal for testing a large number of soil specimens with parallel testing hardware (Fig. 3.8). Generating a coarse-grained soil's particle size distribution (PSD) by FieldSed is nearly identical as doing so by LabSed. However there are several key differences between the LabSed and FieldSed; these differences were discussed in Section 3.2.1, with the largest differences between the two systems listed in Table 3.1. With the advent of the FieldSed, a prewashing procedure was developed. Detailed in Section 3.2.2, this procedure is used before testing in the FieldSed in order to cleanly and quickly remove soil particles in a specimen that fall outside of the testable particle size range for the FieldSed. The prewashing procedure determines a soil's percentage of gravels and fines (by weight). The FieldSed was the centerpiece of a large-scale soil characterization project of Kalamazoo River sediments. This project was the focus of Section 3.2.4. Using the prewashing procedure, the FieldSed was used to generate PSDs of over 100 Kalamazoo River sediments. Seven of the river sediments were part of a quality control investigation that showed excellent agreement between FieldSed and sieving PSDs, as well as reproducibility of the prewashing procedure.

Chapter 3 concluded with the third SedImaging system, the Sed360. The Sed360 transforms SedImaging into a near fully automated test. The introduction of a precision rotation stage with the Sed360 eliminates the need for user-intervention during image capture. The Sed360 has also successfully expanded the range of testable soil particles by SedImaging to include the entire sand range (as defined by the Unified Soil Classification System). The four stages of performing a Sed360 test were detailed in Section 3.3.2. An example of the final image of a soil specimen tested in the Sed360 was presented in Fig. 3.26. Example Sed360 PSDs and how they compare to sieving are part of Chapter 4's discussion of the current autoadaptive HWT-based method. Lastly, the Sed360 was compared to the LabSed and FieldSed in Section 3.3.4.

Chapter 4 Haar Wavelet Transform (HWT)-Based Image Analysis

The focus of this chapter is the image analysis method used with the SedImaging systems. Section 4.1 describes the original analysis method used with LabSed and FieldSed. The development of the Sed360 (Section 3.3) led to the expansion of testable soils by SedImaging which became the impetus for a new image analysis method. The new method (Section 4.2) is an autoadaptive approach that expands upon the functions of the original analysis method. In doing so, sands with a range of gradations and mixes can now be accurately tested with SedImaging. (This new analysis method, though created only after the fabrication of the Sed360, can be used with all three SedImaging systems.) Example PSDs of sands tested in the Sed360 and analyzed with the new image analysis method are presented in Section 4.2.3.

***

Passages and portions of this chapter are taken from previous publications (Ventola and Hryciw 2019; Ventola et al. 2020b, Ventola and Hryciw 2022a, and Ventola and Hryciw 2022b).

4.1 Original HWT-based image analysis for SedImaging

Some image-based, three-dimensional particle assembly analysis methods, including the method used with SedImaging, do not size soil particles individually. Instead, they determine a soil's PSD statistically by analyzing the spatial distribution of pixel color or grayscale intensities of the photographed soil assembly. Individual soil particles are not counted or analyzed using these spatial methods. These statistical spatial methods eliminate the need for user-defined thresholds for deterministic segmentation analysis, and are less computationally-intensive than deterministic

approaches.

To determine a soil's PSD with SedImaging, an image analysis method based on the mathematical Haar Wavelet Transform (HWT) (Haar 1910) is utilized. Figure 4.1 shows a 20 by 16 square grid superimposed over a sedimented Sed360 specimen that contains only medium and fine sand particles (i.e. the allowable range of testable soil sizes for the original HWT-based analysis method). Each square area in Fig. 4.1 is analyzed and will contribute one data point to the PSD. Thus, the image in Fig. 4.1 will contribute 20 x 16 = 320 data points to the PSD.

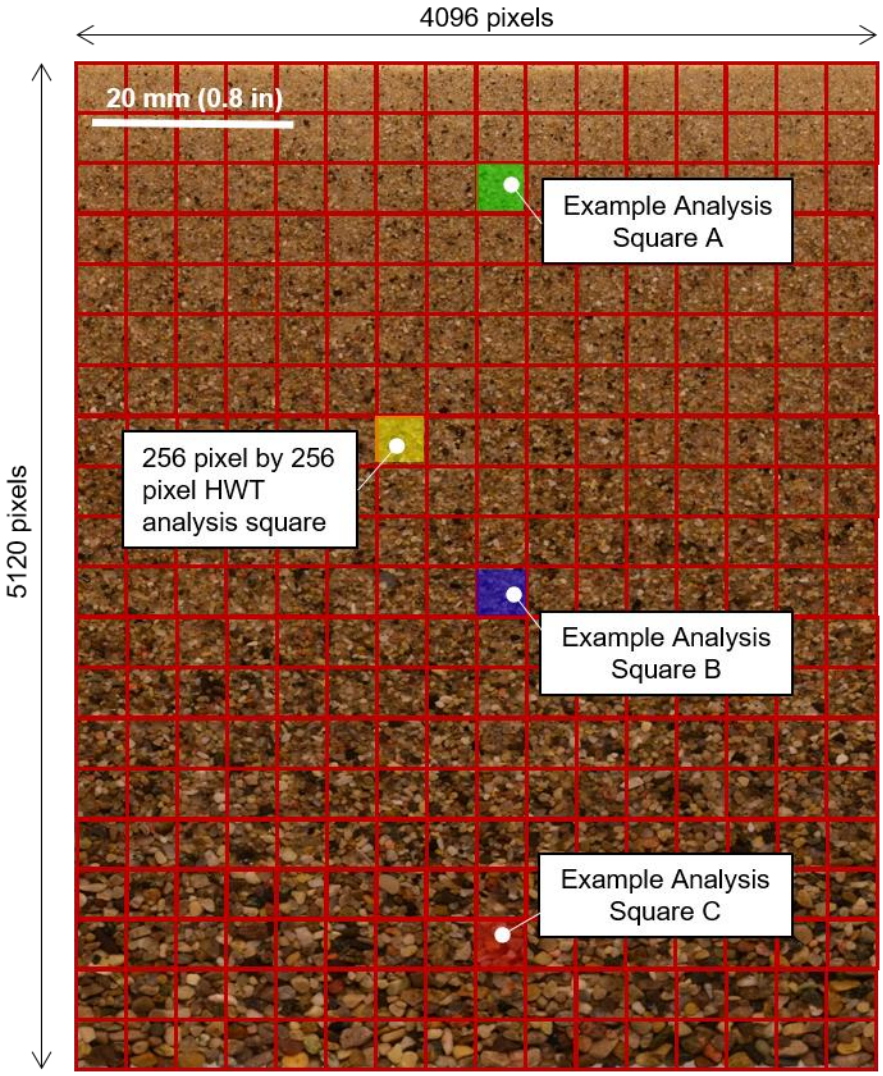

Figure 4-1. HWT analysis squares for a Sed360 soil specimen.

For the HWT, each analysis square must be 2^n pixels by 2^n pixels in size where n is typically seven or eight. The squares in Fig. 4.1 are 2^8 (256) pixels by 2^8 (256) pixels in size. With SedImaging, since sedimentation through water sorts a soil specimen by particle size, each of the HWT analysis squares contains particles of approximately the same size. The relative uniformity of particle sizes within each analysis square is important to the analysis.

For each analysis square, an "Energy" (E) is computed at n "*decomposition levels*" (DL). At the first decomposition level, E_1 reflects the magnitude of the difference in grayscale values of adjacent pixels throughout the analysis square. The greater the difference, the larger the E_1. At the second DL, E_2 reflects the difference between average grayscale values of adjacent 2 x 2 pix^2 subareas throughout the analysis square. At the third decomposition, E_3 is a measure of the difference of average grayscale values between adjacent 4 x 4 pix^2 subareas, and so on. At the last decomposition level (regardless of n), E_n quantifies the difference in grayscale values between the four quadrants of the analysis square.

To mathematically define E, at each DL, four values are computed for each 2 x 2 subarea of the analysis square. (The pixel dimensions of these subareas change depending on the DL.) Described by Hryciw et al. (2015), these four values are

"1. The approximation: twice the average of [the] four grayscale values;

2. The average difference in grayscale [values] between the two rows;

3. The average difference in grayscale [values] between the two columns; and

4. The average difference in grayscale [values] between the two diagonals."

At each decomposition level i (i = 1,2,…n), these four values are collected from all of the 2 x 2 subareas to form four new matrices A_i, H_i, V_i, and D_i respectively (e.g. H_i is a matrix that contains "the average difference in grayscale [values] between the two rows" and V_i is a matrix

that contains “the average difference in grayscale [values] between the two columns” (Hryciw et al. 2015)). The Energies of matrices H_i, V_i, and D_i (E_H, E_V, and E_D) are calculated and summed to compute E_i for each *DL*. The *E* of a matrix is the sum of the squares of the matrix’s elements. For example, for a small 4 x 4 pix^2 image, if H_1 is

$$H_1 = \begin{bmatrix} 2 & 5 \\ 1 & 7 \end{bmatrix}$$

then the energy of H_1, represented as E_{H1}, is

$$E_{H1} = 2^2 + 5^2 + 1^2 + 7^2 = 79 \quad Ans.$$

The *E* of each DL_i, (E_i) is

$$E_i = \sum E_{Hi} + \sum E_{Vi} + \sum E_{Di} \tag{4.1}$$

For each analysis area, the energy of every *DL* is calculated. The distribution of *E* across the *DL*s is of interest. Figure 4.2 shows the Energies (Eq. 4.1) at eight decomposition levels for three example analysis squares marked in Fig. 4.1.

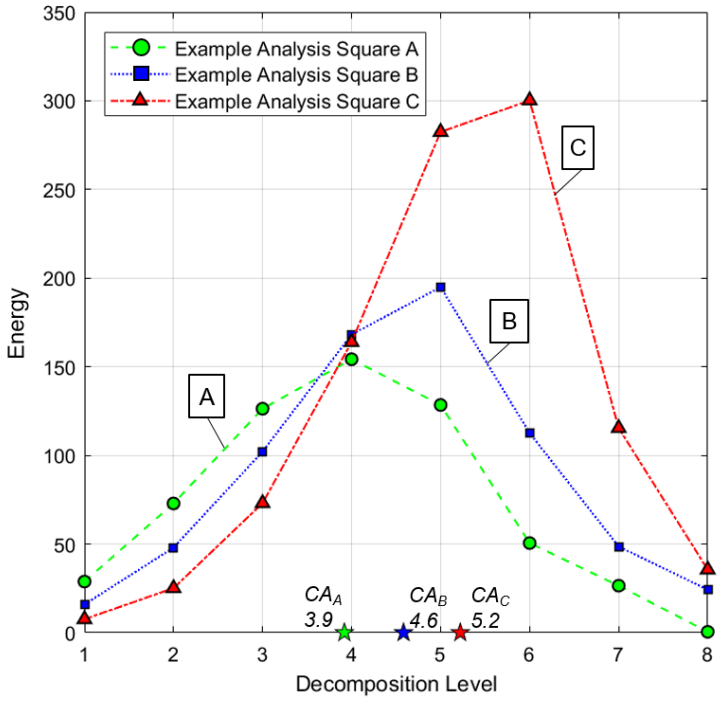

Figure 4-2. Energy curves of three example HWT analysis squares from Fig. 4.1.

Many sands are composed of multicolored grains, or at least different shades of the same color. The important benefit of this is that an analysis area's *E* will be largest at the *DL* at which the pixel area of "grayscale averaging" approximately coincides with the size of the soil particles within the analysis square. This point is illustrated in Fig. 4.3, which shows the distribution of *E* by *DL* (Fig. 4.3[a]) for an example analysis square (not one of the squares in Fig. 4.1). Also shown in Fig. 4.3 are the grids corresponding to the grayscale averaging areas at the 5^{th} (16 x 16 pix^2) (Fig. 4.3[b]), 6^{th} (32 x 32 pix^2) (Fig. 4.3[c]), and 7^{th} (64 x 64 pix^2) (Fig. 4.3[d]) *DL*s. To the right of each of the three gridded analysis squares, pixel values have been replaced with each area's average grayscale. As compared to the 5^{th} and 7^{th} *DL*s, the differences in average grayscale values of adjacent grid areas is more pronounced at the 6^{th} *DL*. Thus, the *E* is greatest around the 6^{th} *DL*. By visual observation of Fig. 4.3, the particle size is best approximated by the size of the grid at the 6^{th} level, where *E* is largest.

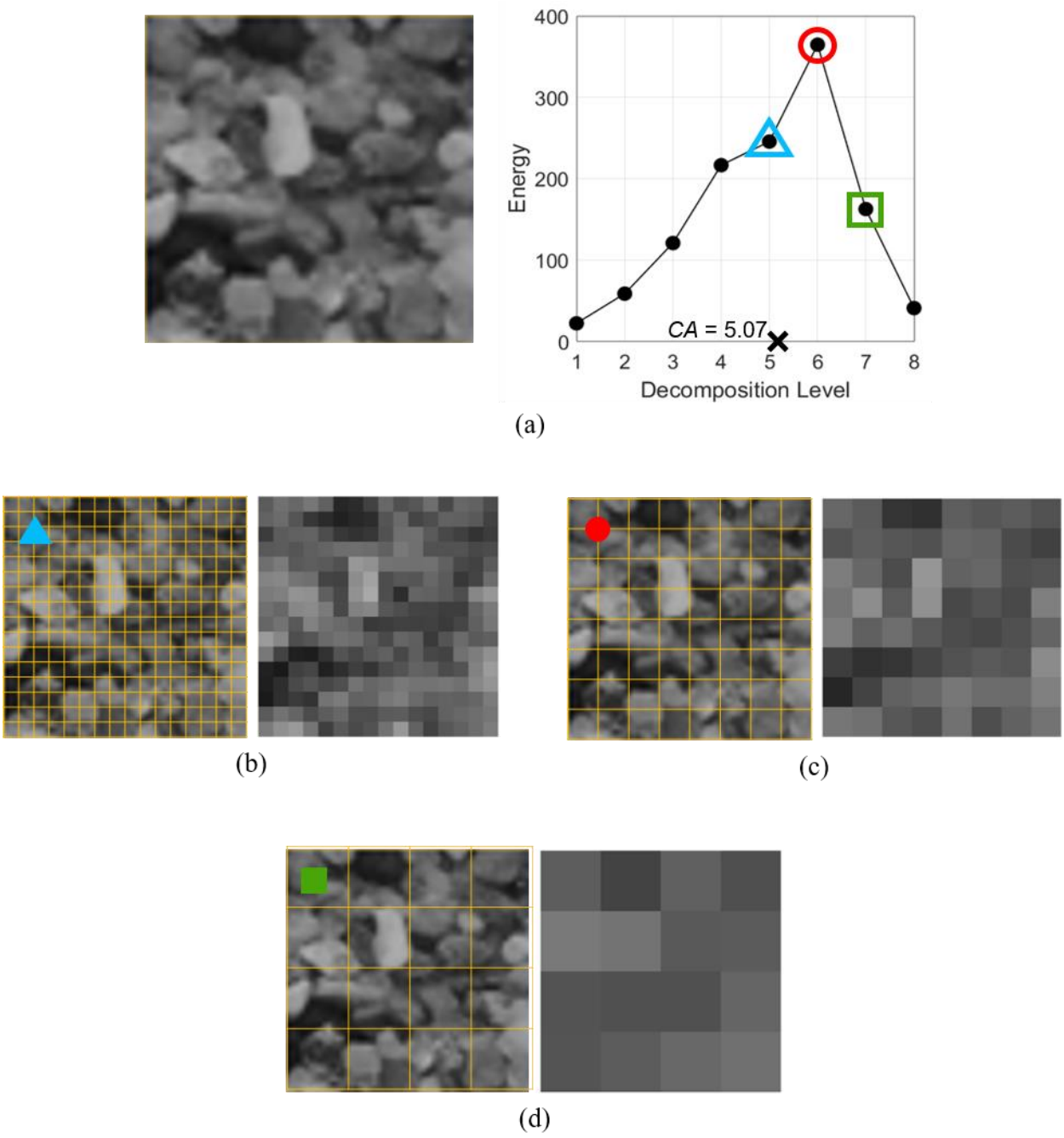

Figure 4-3. Example of the HWT method used with SedImaging. (a)Analysis area and corresponding Energy versus decomposition level plot, (b) grayscale averaging areas for the 5th, (c) 6th, and (d) 7th decomposition levels.

At a fixed image magnification, Energy distributions shift to the right (to higher *DL*s) with increasing particle size. This is observed in the three example analysis areas and their corresponding energy curves in Fig. 4.2. Shin and Hryciw (2004) observed that the centroid of the area (*CA*) under the *E* vs. *DL* plot correlated very well with the size of particles in the analysis square (where particle size is defined by sieve opening). The *CA* for Example Analysis Squares A, B, and C in Fig. 4.2 are 3.9, 4.6, and 5.2 respectively (and 5.07 for the separate example in Fig. 4.3). A calibration curve between *CA* and the *Pixels per Particle Diameter* (*PPD*) was established by Hryciw et al. (2009). This calibration curve is plotted in Fig. 4.4 and given by the equation:

$$PPD = \left(\frac{CA}{2.4}\right)^{5.1} \tag{4.2}$$

The *CA* values for the three Fig. 4.1 analysis squares and their corresponding *PPD*s are also shown in Fig. 4.4.

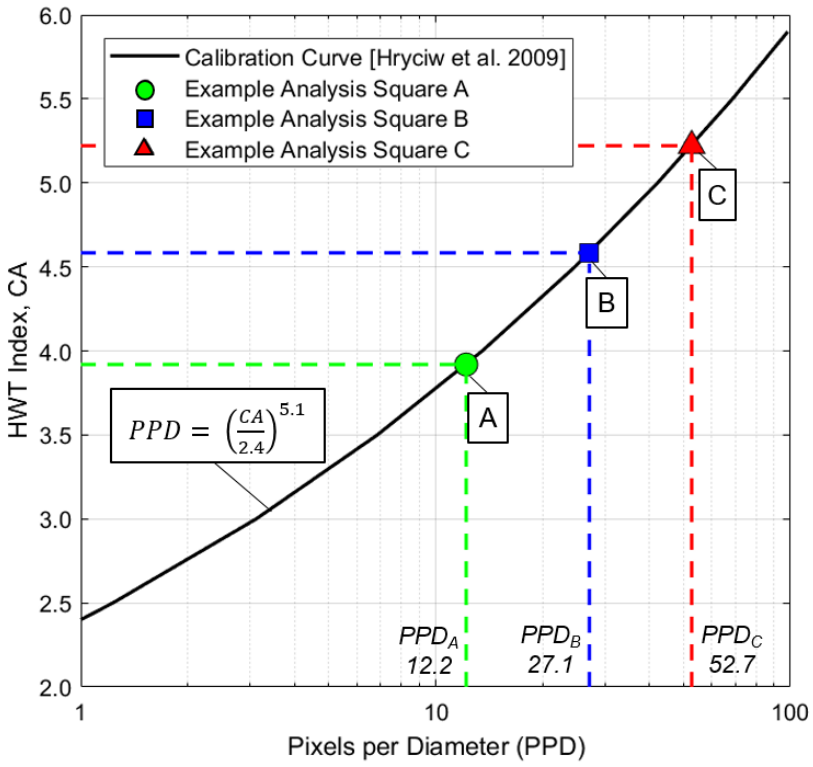

Figure 4-4. HWT calibration results for three example HWT analysis squares from Fig. 4.1.

The HWT analysis is repeated for all of the analysis squares shown in Fig. 4.1, the *CA* values are computed, and the corresponding *PPD*s are found. The *PPD* values are converted to particle sizes (d) from the known image magnification (MAG) in pixels/mm according to Eq. 4.3

$$d = \frac{PPD}{MAG} \tag{4.3}$$

Hryciw and Jung (2008) showed that void ratio variations in the sedimented soil specimens are very small. As such, each analysis square represents an equal fraction of the specimen's volume of solids. Thus, the particle sizes are ranked from largest to smallest and plotted in Fig. 4.5. The points corresponding to the three Fig. 4.1 example analysis squares are identified in the figure.

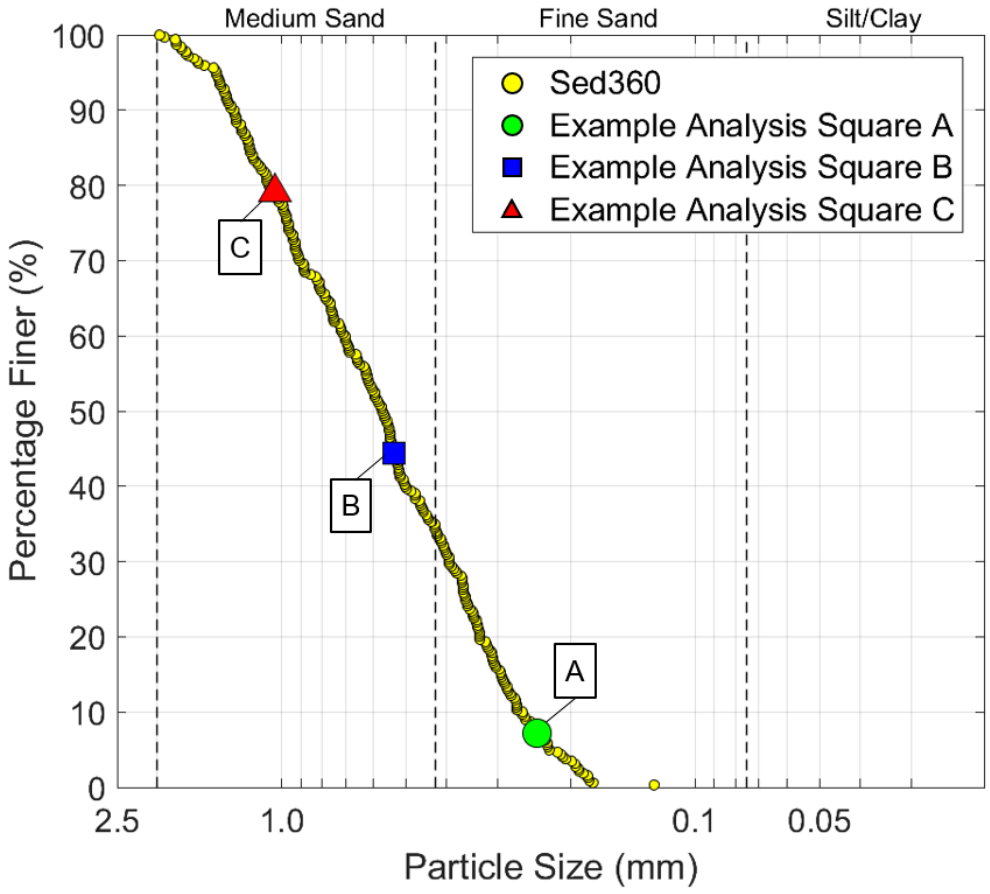

Figure 4-5. Sed360 PSD results from Fig. 4.1 highlighting three example HWT analysis squares

4.2 Advancements to SedImaging's HWT-based image analysis method

With the expanded range of testable soil particle sizes afforded by the Sed360 (Section 3.3), the accuracy of the original HWT-based analysis method required reexamination. From this, two significant issues were revealed: (1) the original *PPD-CA* calibration (Eq. 4.2) required an update (Section 4.2.1), and (2) using a fixed HWT analysis area size (regardless of the area's pixel dimensions) to evaluate an entire soil specimen yields inaccurate PSDs (Section 4.2.2). These two issues motivated development of the new, autoadaptive HWT image analysis approach described herein.

4.2.1 The New PPD-CA *calibration*

The original *PPD-CA* calibration (Eq. 4.2) was developed using older camera technology and a narrower particle size range (medium and fine sands only). Values of *PPD* ranged only between 2 and 60. With new Sed360 hardware (Section 3.3) and the expanded particle size range, *PPD*s can now range to above 200. This warranted an investigation into how well Eq. 4.2 fits data at these much higher *PPD*s. To perform this recalibration, sand particles were sieved into 11 narrow size ranges as listed in Table 4.1. The sand is a glacio-fluvial material referred to as "2NS" by the Michigan Department of Transportation (MDOT 2010).

The *CA* values for the 504 analysis squares listed in Table 4.1 are plotted versus the corresponding mid-*PPD* values in Fig. 4.6. Equation 4.2 (solid red line) remains a good fit for *PPD*s of 4.1, 5.9, and 8.9. However, at higher *PPD*s, the calibration points are better fitted by

$$PPD = 2.5^{(CA-1.15)} \tag{4.4}$$

Table 4-1. 2NS sand ranges for Sed360 calibration testing.

Size Range No.	Sieve Range	Size Range [mm]	Corresponding *PPD* Range [a]	Mid *PPD*	Number of analysis squares (i.e. data points in Fig. 4.6)
1	No. 4 to No. 5	4.75 – 4.00	233.2 – 196.4	214.8	42
2	No. 5 to No. 6	4.00 – 3.35	196.4 – 164.5	180.5	46
3	No. 7 to No. 8	2.80 – 2.36	137.5 – 115.9	126.7	45
4	No. 10 to No. 12	2.00 – 1.70	98.2 – 83.5	90.8	35
5	No. 14 to No. 18	1.40 – 1.00	68.7 – 49.1	58.9	28
6	No. 20 to No. 25	0.85 – 0.71	41.7 – 34.9	38.3	30
7	No. 30 to No. 35	0.60 – 0.50	29.5 – 24.6	27.0	22
8	No. 40 to No. 50	0.425 – 0.300	20.9 – 14.7	17.8	72
9	No. 70 to No. 100	0.212 – 0.150	10.4 – 7.4	8.9	66
10	No. 100 to No. 170	0.150 – 0.090	7.4 – 4.4	5.9	80
11	No. 170 to No. 200	0.090 – 0.075	4.4 – 3.7	4.1	38
					Σ 504

[a] Image magnification = 49.1 pix/mm.

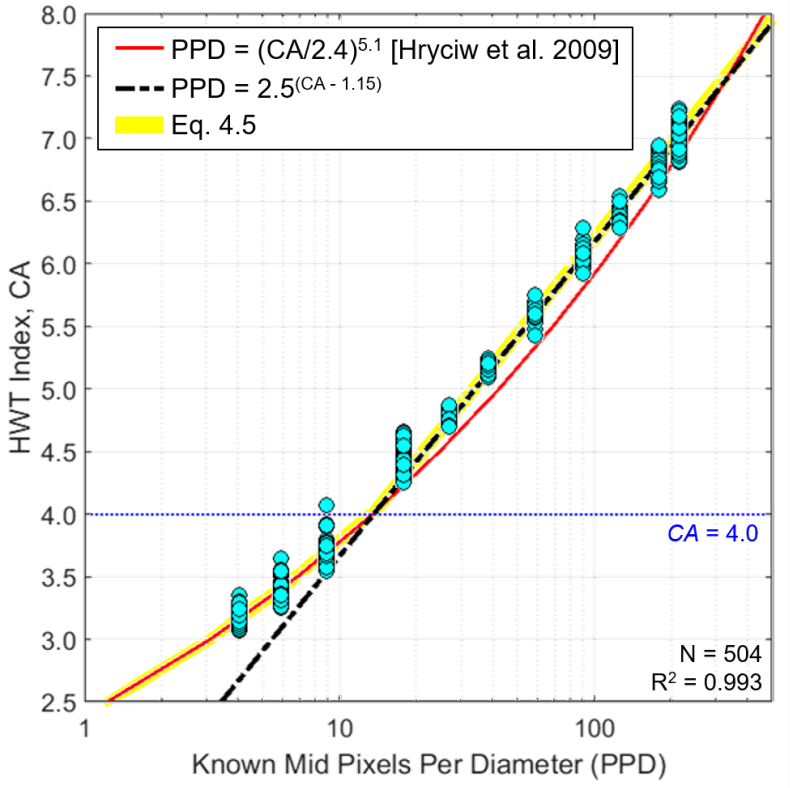

Figure 4-6. PPD-CA *calibration using the Sed360 data from Table 4.1.*

Equation 4.4 is a straight line in the semi-log scale of Fig. 4.6. This equation was obtained by fitting the data above *PPD* =15 to maximize the coefficient of determination, R^2. Hryciw et al. (2014) anticipated that when camera technology advances to higher resolutions, the *PPD-CA* calibration would be linear of the form given by Eq. 4.4. At the same time, there is good reason for the flattening of the curve below *PPD* ≈ 15. When *PPD*s are low, the *E* values are high at low *DL*s. Because there is no data below *DL* = 1, the "*E* curves" are truncated at the 1st decomposition level. This results in an increasing compression of *CA* values as *PPD* moves downward from about 15 (i.e. *CA* ≈ 4).

Ideally, a single equation would fit the entire *PPD* range, but at the present time, this would require a drastic change to image acquisition. Camera magnifications would have to be increased so that *PPD*s are always greater than 15. In other words, the finest (0.075mm) sand particles would require *PPD* = 15. This in turn would require a camera magnification of 200pixels/mm (about four times the current magnification). Unfortunately, this would decrease a camera's field of view so much that several photos in the vertical direction would be needed, possibly at different camera magnifications, to photograph an entire soil specimen. Such complexity would make Sed360 testing cumbersome. Therefore, to maintain the simplicity of the Sed360 hardware (as well as the analysis) the author recommends using the following piecewise *PPD-CA* calibration:

$$PPD = \begin{cases} \left(\frac{CA}{2.4}\right)^{5.1} & if\ CA \leq 4.0 \\ 2.5^{(CA-1.15)} & if\ CA > 4.0 \end{cases} \tag{4.5}$$

Equation 4.5 is highlighted in yellow in Fig. 4.6. The R^2 value of Eq. 4.5 for the calibration data is 0.993. Equation 4.5 is used for obtaining all of the HWT-based PSD results presented in Section 4.2.3.

4.2.2 Autoadaptive HWT-based image analysis for SedImaging

While the establishment of Eq. 4.5 is crucial to accurately characterize the expanded particle size range in the Sed360, the greater improvement to the original HWT-based analysis method stems from the need for autoadaptive determination of the HWT analysis square sizes. To illustrate this need, Fig. 4.7(a) presents a Sed360 specimen that contains coarse, medium, and fine sand particles. Figure 4.7(b) plots this specimen's PSDs. This image was analyzed using the original HWT-based method (Section 4.1), but with Eq. 4.5 instead of Eq. 4.2, four separate times. Each time, a single HWT analysis square size was used for the entire image. Sieving results following ASTM C136/C136M-19 (ASTM 2019) are also in Fig. 4.7(b) (as red square data points).

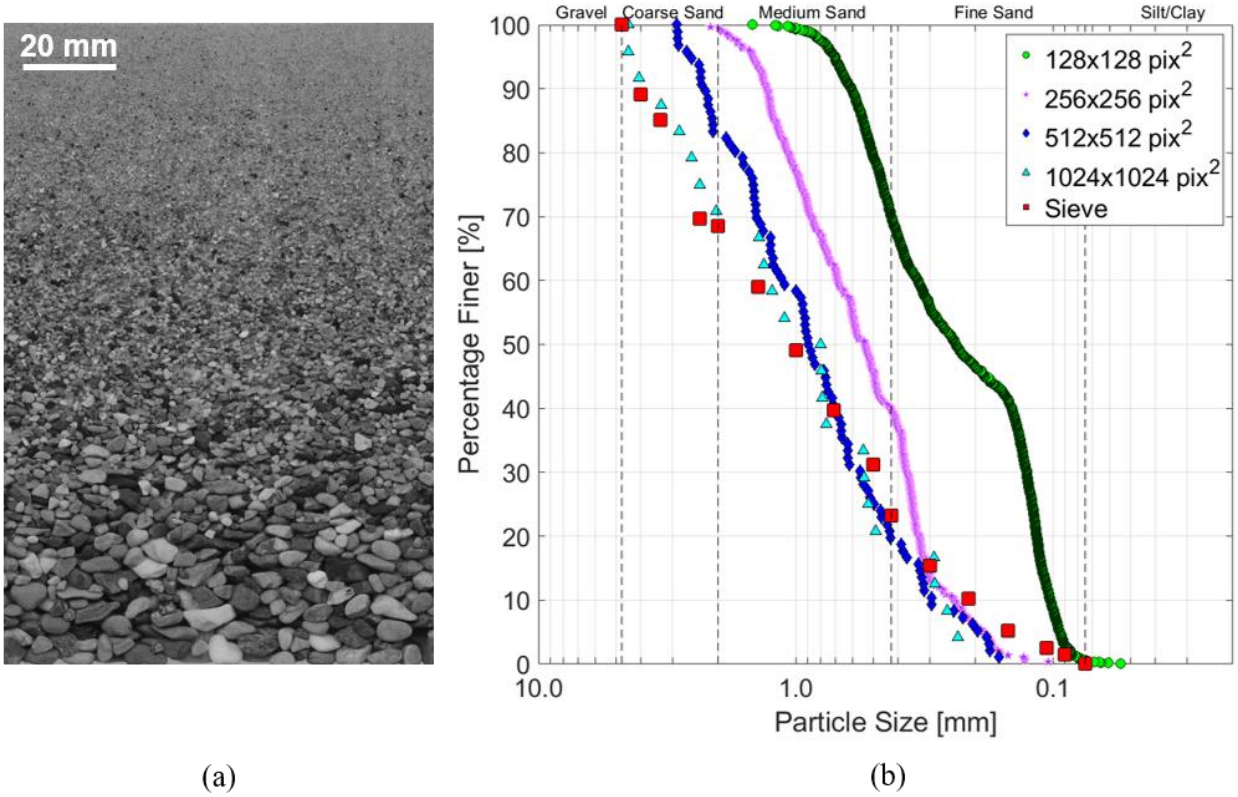

Figure 4-7. Analyzing the same sand specimen image using different sizes of HWT analysis squares. (A) Sand in Sed360, (b) PSD results.

Figure 4.7 reveals that none of the four PSDs using uni-sized analysis squares matches the full range of sieve-based results. Only the PSD using 1024 x 1024 pix^2 analysis squares correctly sizes the coarse sand. Conversely, only the 128 x 128 pix^2 analysis squares correctly size the finest sand. Figure 4.7 confirms that variable analysis area sizes are needed to correctly characterize specimens containing particles over the full spectrum of sand sizes; larger squares should be used for coarser sand, and smaller squares for finer sand. In response to these findings, a procedure was developed that autoadaptively select the sizes of the analysis squares to suit the various particle sizes.

The great majority of *E*-distributions follow a pattern as shown in Fig. 4.8 (and Figs. 4.2 and 4.3). These ideal distributions display low *E* at low *DL*s, gradually rise with increasing *DL*, and steepen and peak at the midrange-*DL*s. The *E* then monotonically decreases back to low levels at the highest *DL*s. When a distribution follows this quasi-parabolic pattern, particle sizes determined by Eq. 4.5 will be accurate and reliable. *E*-distributions such as those in Figs. 4.2, 4.3, and 4.8 are deemed "acceptable".

On occasion, an *E*-distribution does not follow an acceptable pattern. In such cases, Eq. 4.5 does not yield an accurate *PPD*. Figure 4.9 shows examples of such undesirable *E*-distributions. In Fig. 4.9(a) the analysis square is too small for the particle size and thus, the *E*-distribution fails

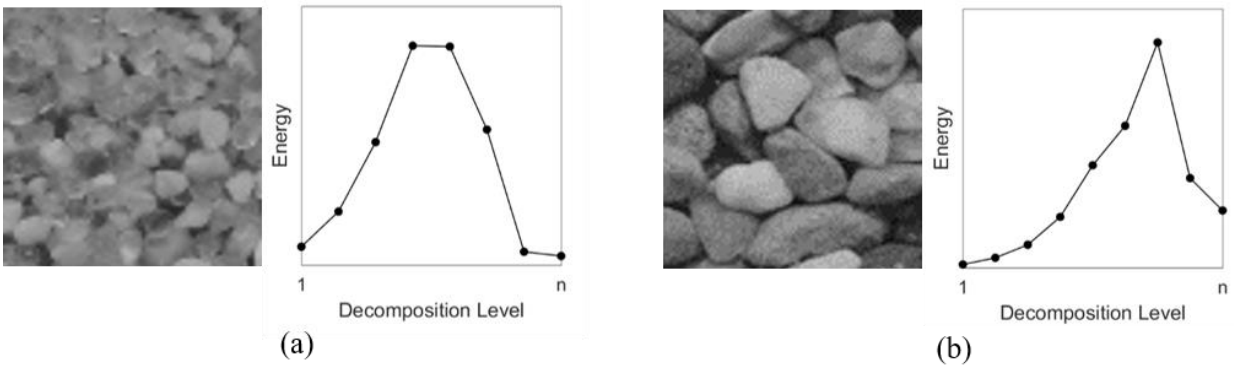

Figure 4-8. Examples of analysis squares with "acceptable" E*-distributions. (a) Analysis square containing smaller particles, and (b) Square containing larger particles.*

to decrease at high *DL*s. This truncation of the *E*-distribution results in an inappropriately low *CA* value and the underestimation of *PPD* by Eq. 4.5. A similar, although less pronounced underestimation of *CA* can also occur for an *E*-distribution that peaks at the second largest *DL*. In this case (not shown in Fig. 4.9), the analysis square is still too small, and should not be used.

The analysis square in Fig. 4.9(b) is too large because it contains particles with a wide range of sizes. Larger sand particles are at the bottom of the square, with progressively finer sand above. The corresponding *E*-distribution peaks around *DL* = 5 to 6 before decreasing. However because of the wide range of soil particle sizes in the analysis square, the energy distribution begins

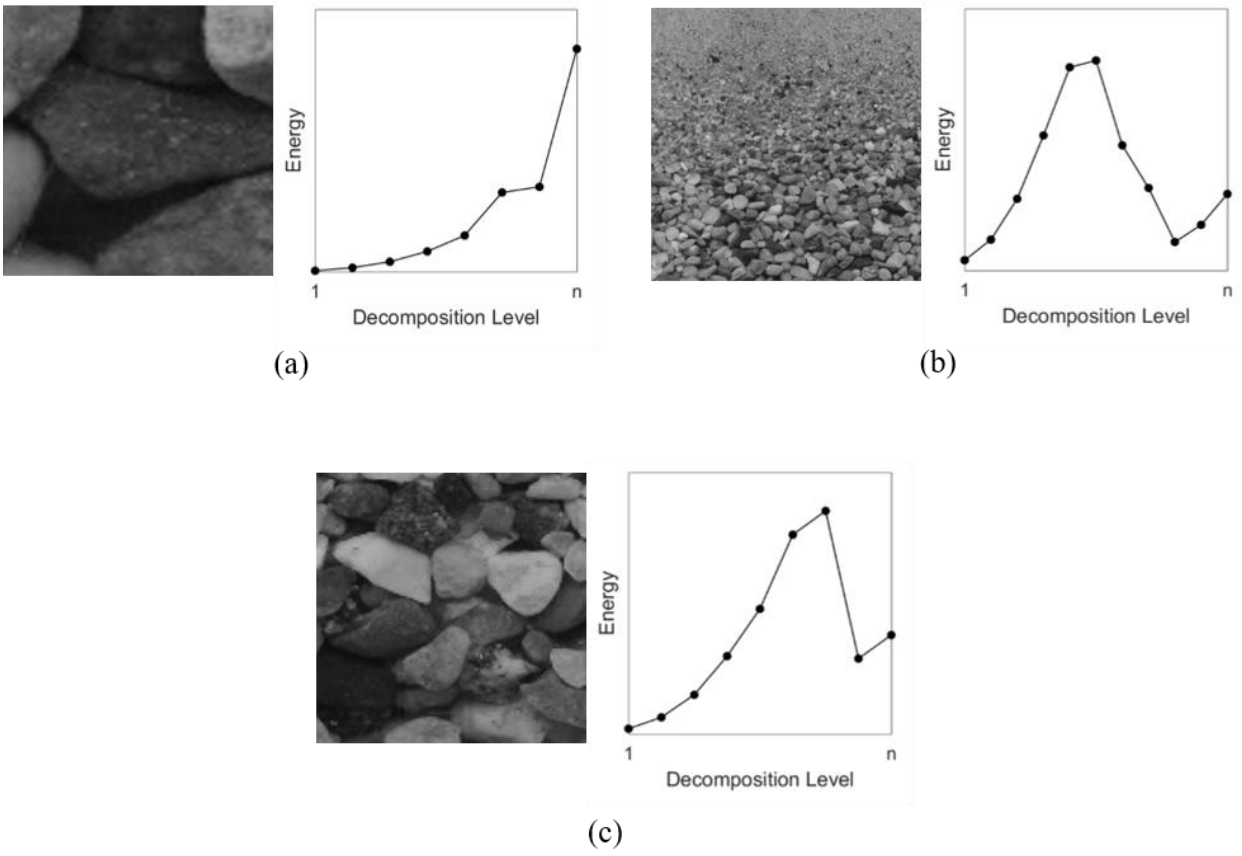

Figure 4-9. Examples of analysis squares with "unacceptable" E-*distributions. (a) HWT analysis square is too small relative to the soil particles, (b) Range of particle sizes is too large and (c) Energy curve impacted by particle coloring.*

to increase again at *DL = n-1* and *n*. The reason for this *E* increase is that at *DL = n-1* and *n*, large areas of averaged grayscale values are being compared to other large areas of averaged grayscales. When particles of greatly different sizes are contained within compared areas, the averaged grayscale values can differ enough to cause the increases in *E* at these higher *DL*s.

Another example of unusual features impacting the *E*-distribution is shown in Fig. 4.9(c). Like the *E*-distribution in Fig. 4.9(b), the one in Fig. 4.9(c) also increases at the final decomposition level, *n*. Here, the *E* increase is caused by the proximity of similarly colored particles. Three large light-colored particles in Fig. 4.9(c) occupy almost 50% of the top half of this analysis square. Moreover, the bottom left quadrant of Fig. 4.9(c) contains a very dark particle. Because of the

large areas of high contrasting grayscale values and their location within the analysis square, the *E* at the final *DL* jumps up. This upturn in *E* at the last *DL* shifts *CA* to the right and causes an overestimation of particle size.

It is important to emphasize that while the *E*-distributions in Figs. 4.9(b) and 4.9(c) are both "unacceptable", the causes of the undesirable increasing *E* at the highest *DL*s is different. In Fig. 4.9(b), the analysis square contains a range of particle sizes that is too large. The size of the analysis square in Fig. 4.9(c) is actually "acceptable"; it contains particles of about the same size (i.e. the square is not too big) and it also contains enough soil particles (i.e. the square is sufficiently large). Instead, the "unacceptability" in this case is due to the happenstance proximity of certain-colored soil particles. While Figs. 4.9(b) and 4.9(c) have similarly shaped "unacceptable" *E*-distributions, the autoadaptive analysis square sizing method uses different procedures for addressing these two situations.

A final cause of "unacceptable" energy distributions is uneven particle illumination across an analysis area. One would see a similar increase in *E* at the highest *DL*s like those in Figs. 4.9(b) and 4.9(c) if an analysis square had uneven lighting. For example, if the upper half of the HWT square had more illumination than the bottom, the *E* at the final *DL* (which compares the average grayscale values of the square's four quadrants) would increase. The *CA* value from a HWT energy distribution that is impacted by such global characteristics would be skewed high. Using a *CA* value from this type of *E*-distribution in Eq. 4.5 would oversize the analysis square's particles. Appendix A summarizes the research on the effects of uneven lighting on the shape of HWT energy distributions that lead to these conclusions. This research was conducted with soil images photographed in the FieldSed. Based on the results from this research, the effects of uneven

lighting on HWT results have been reduced with the Sed360 and the autoadaptive HWT-based analysis method.

Basic Principles of the Autoadaptive HWT-Based Image Analysis Method

The autoadaptive analysis square sizing is predicated on four principles:

(a) It is a reasonable assumption that soil particles of the same size are located at the same elevation of a sorted Sed360 specimen. Therefore, the *E*-distributions of all analysis squares at the common elevation are collectively used for the selection of the analysis area size. The same square size is then assigned for a given elevation across the entire width of the image.

(b) The distinctions between "acceptable" and "unacceptable" *E*-distributions discussed with Figs. 4.8 and 4.9 are utilized by the autoadaptive procedure. Acceptable *E*-distributions are used "as is" while unacceptable distributions are used after being adjusted. The adjustment procedure is discussed in "Procedure" within this Section.

(c) Larger analysis squares are preferred for larger particle sizes because larger analysis squares can be decomposed to more (higher) levels, and thus, the *E*-distribution is less likely to be truncated at $DL = n$. With less truncation, the computed *CA* will yield a more reliable *PPD* by Eq. 4.5.

(d) Despite the preference for larger analysis squares as noted in the third principle, the smallest "acceptable" analysis squares are used for better resolution of particle sizes. Even if a larger analysis square yields an "acceptable" *E*-distribution, the *E*-distributions of the contained smaller analysis areas are investigated for acceptability before final selection of an analysis square size.

Figure 4.10 illustrates principle (d). Here, a 2048 x 2048 pix^2 analysis area contains coarse sand particles. Based on the discussion of "acceptable" *E*-distributions with Fig. 4.8, the *E*-distribution for this large 2048 x 2048 pix^2 area is "acceptable". It exhibits a peak at one of the mid-range *DL*s and *E* is low at the upper levels. Using Eq. 4.5 with the known camera magnification and Eq. 4.3, the size of this area's particles is found to be D = 3.29mm. When the square is quartered, the 1024 x 1024 pix^2 areas reveal four *E*-distributions that are also "acceptable". The top two 1024 x 1024 pix^2 areas yield particle sizes of 2.79mm and 2.75mm which, as expected, are smaller than the one determined for the entire 2048 x 2048 pix^2 area. The bottom two 1024 x 1024 pix^2 areas yield larger particle sizes of 3.58mm and 4.11mm. The size difference between particles in the top and bottom halves of the 2048 x 2048 pix^2 area is visible by eye in Fig. 4.10. While the 2048 x 2048 pix^2 analysis area's *E*-distribution was "acceptable", using the smaller (and also acceptable) 1024 x 1024 pix^2 areas leads to more accurate particle sizing.

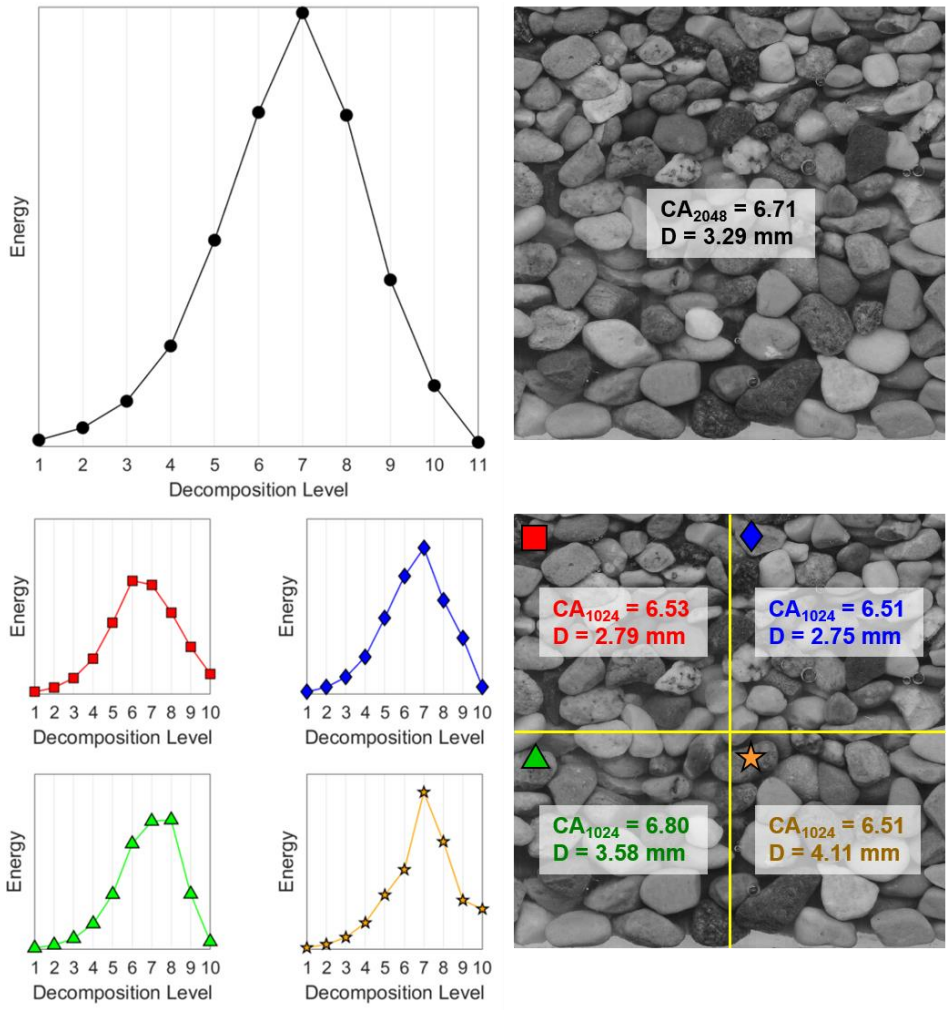

Figure 4-10. Example illustrating guiding principle (d) of the autoadaptive sizing method of HTW analysis squares.

Procedure for the Autoadaptive HWT-Based Image Analysis Method

After a Sed360 soil specimen is sedimented, photographed, and "unwrapped", it is ready to be analyzed according to the autoadaptive analysis square sizing procedure:

(1) The entire soil specimen is first discretized into 2048 x 2048 pix^2, then 1024 x 1024 pix^2, 512 x 512 pix^2, 256 x 256 pix^2, and finally,128 x 128 pix^2 HWT analysis squares.

(2) The *E*-distributions are computed for all of the analysis squares. When the *E*-distribution takes an upward turn at high *DL*s, the *E* values at the high *DL*s are set to zero. This same zeroing of *E* at high *DL*s was performed during the calibration that produced Eq. 4.5.

(3) Selection of the appropriate size of analysis squares is determined using the flow chart in Fig. 4.11. The investigation begins with the largest analysis square size of 2048 x 2048 pix^2. Analysis starts with the lowest row of 2048 x 2048 pix^2 analysis squares in the image and progresses upward. With each new 2048 x 2048 pix^2 row, Fig. 4.11 is used from "Start". The smallest allowable analysis square size anywhere in the image is set at 128 x 128 pix^2.

(4) Using the appropriate analysis square sizes determined by Fig. 4.11, the *CA* values for all of the areas are computed. Equation 4.5 converts the *CA* values to *PPD*, and with the known camera magnification and Eq. 4.3, the actual particle size representing each analysis square is computed.

(5) Since analysis squares have varying sizes, the particle sizes are weighted by the size of the analysis squares when developing the PSD.

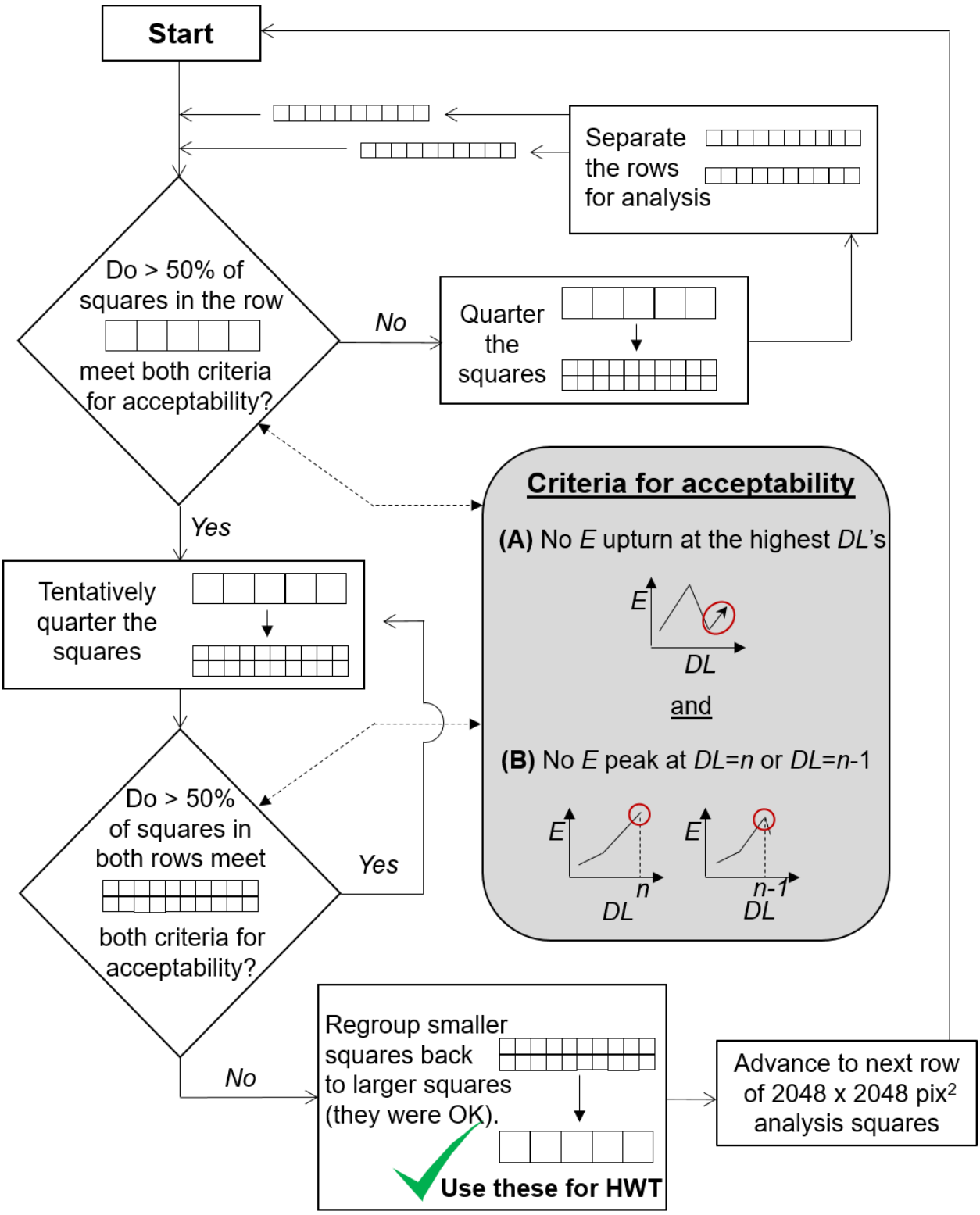

Figure 4-11. Flow chart followed in Step 3 of the autoadaptive HWT analysis square sizing method.

4.2.3 Sed360 PSD results using the autoadaptive HWT-based analysis method

Five soil specimens were tested in the Sed360 using the autoadaptive analysis square sizing method. The stitched "unwrapped" views of these specimens are in Fig. 4.12. The specimens contain varying amounts of coarse (4.75mm to 2mm), medium (2mm to 0.425mm), and fine sand (0.425mm to 0.075mm). The exception is Specimen B, which contains only coarse and fine sand. The same 2NS parent soil was used for all five engineered specimens so that the study would focus only on the performance of the autoadaptive method on different size gradations, rather than on different soil types.

Figures 4.13 through 4.17 show the grayscale images of the five specimens. Overlaying each of these images is a grid showing the autoadaptively selected analysis squares. All five specimens required analysis squares ranging from 128 x 128 pix^2 to 1024 x 1024 pix^2. Although 2048 x 2048 pix^2 areas were the starting point in all five cases, no such large analysis area was found to be appropriate. The resulting PSDs are also plotted in Figs. 4.13 through 4.17 with comparisons to sieving results. Table 4.2 summaries the PSD-derived parameters (D_{60}, C_u etc.). To emphasize the benefit of the autoadaptive method, Table 4.2 also lists the PSD parameters obtained by using the older approach of uni-sized analysis squares, in this case, only 256 x 256 pix^2. The 256 x 256 pix^2 results are clearly inferior to the autoadaptive results and therefore, are not plotted in Figs. 4.13 through 4.17, and will not be further discussed.

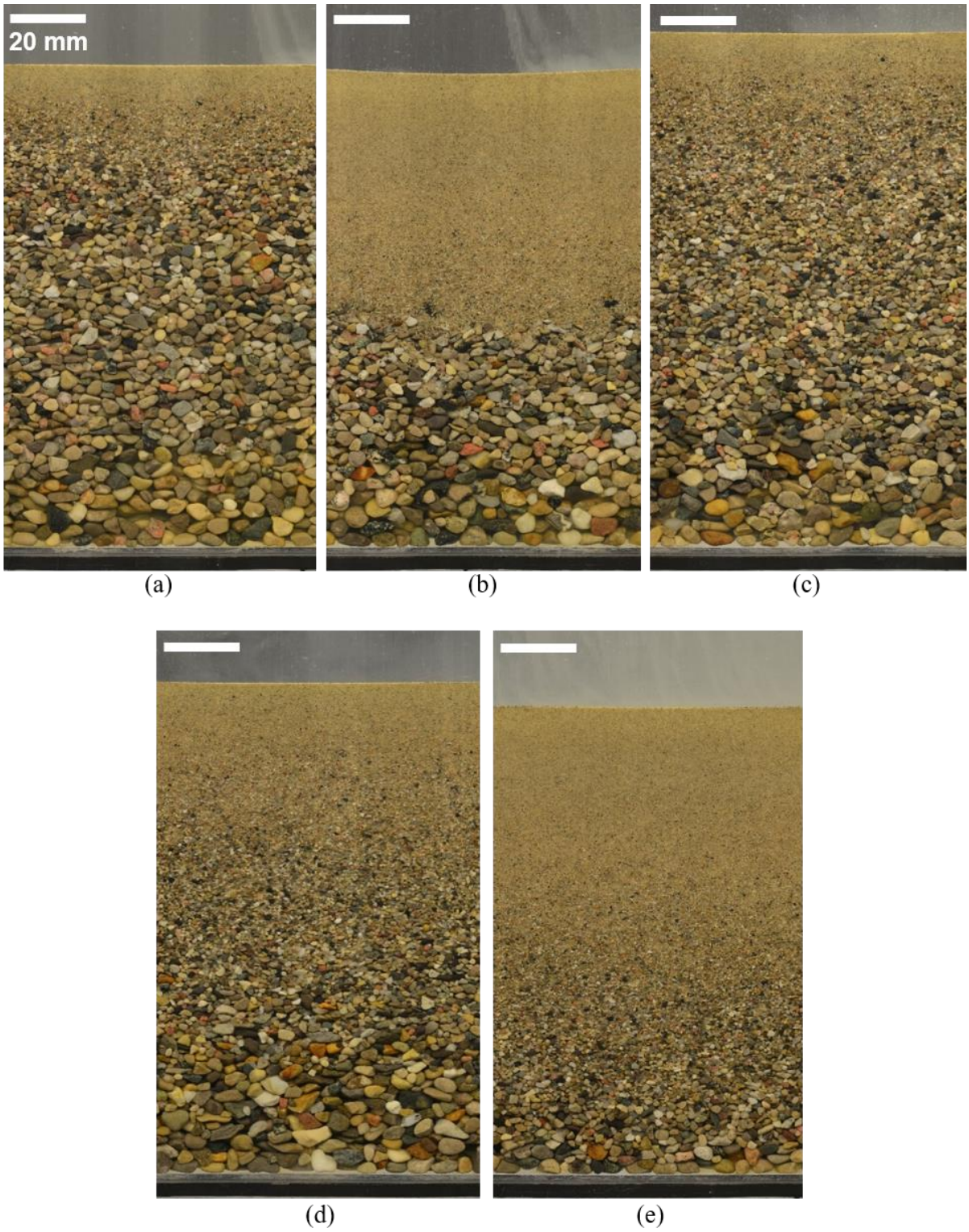

Figure 4-12. Sed360 sand specimens containing various size percentages per sieve analysis (coarse/medium/fine sands): (a) 67/23/10, (b) 50/0/50, (c) 37/51/12, (d) 31/46/23, and (e) 10/40/50.

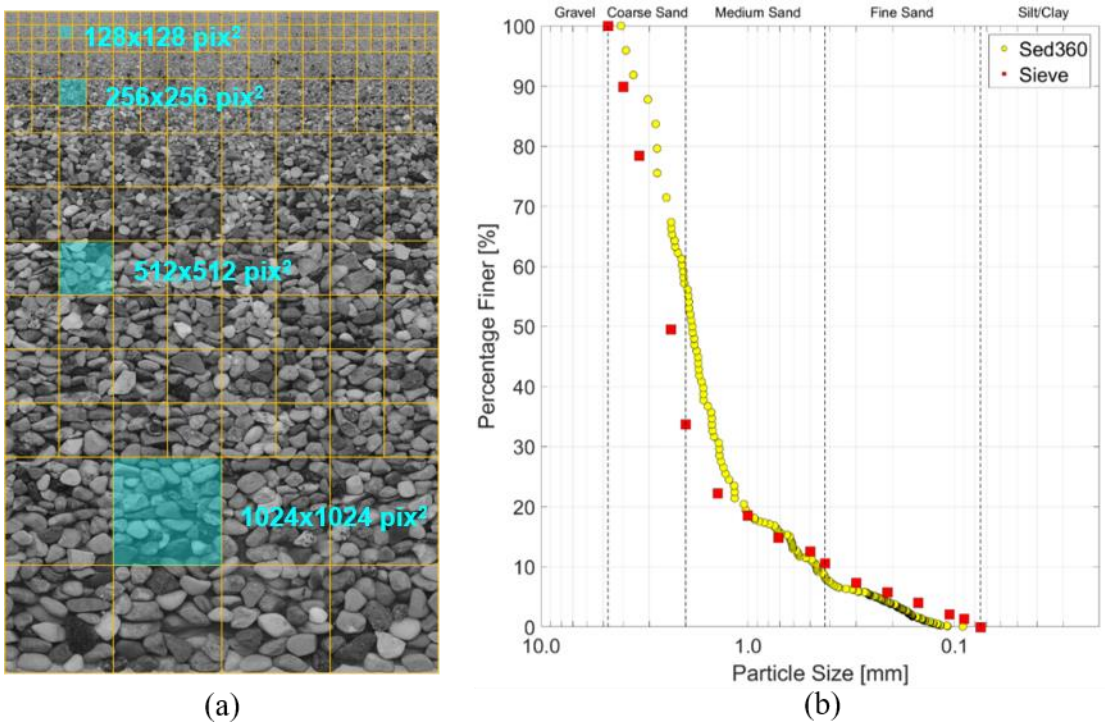

Figure 4-13. Sed360 Results for Specimen A. (a) Autoadaptively determined analysis squares used to generate the HWT-based PSD, (b) PSD results.

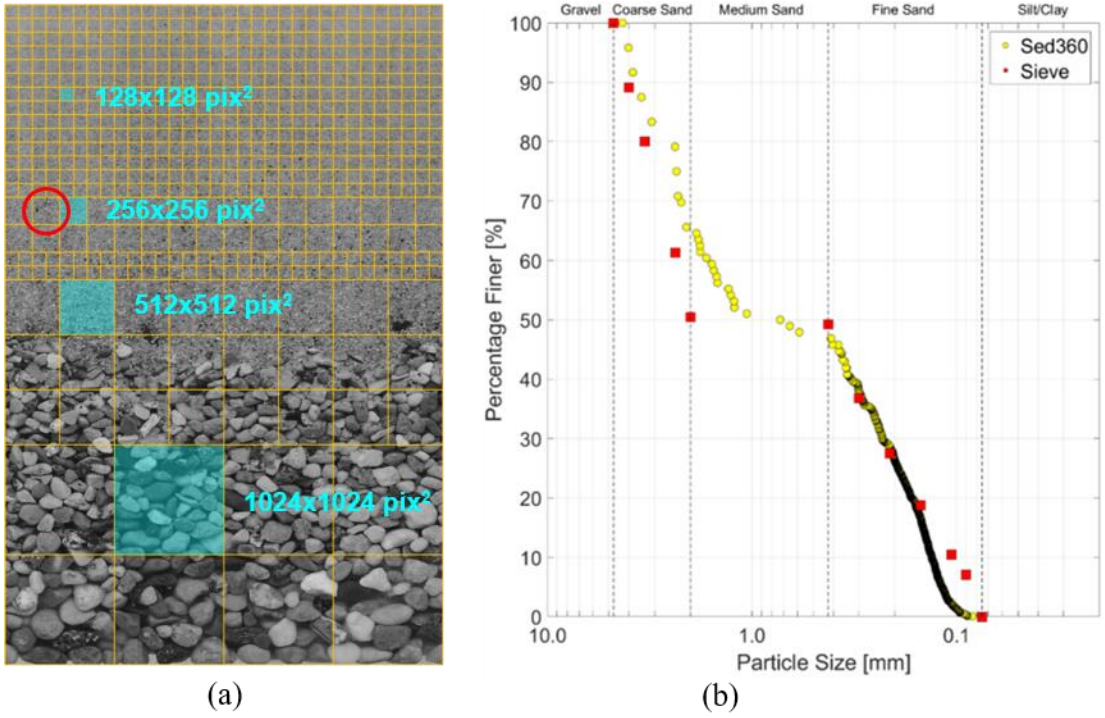

Figure 4-14. Sed360 Results for Specimen B. (a) Autoadaptively determined analysis squares used to generate the HWT-based PSD, (b) PSD results.

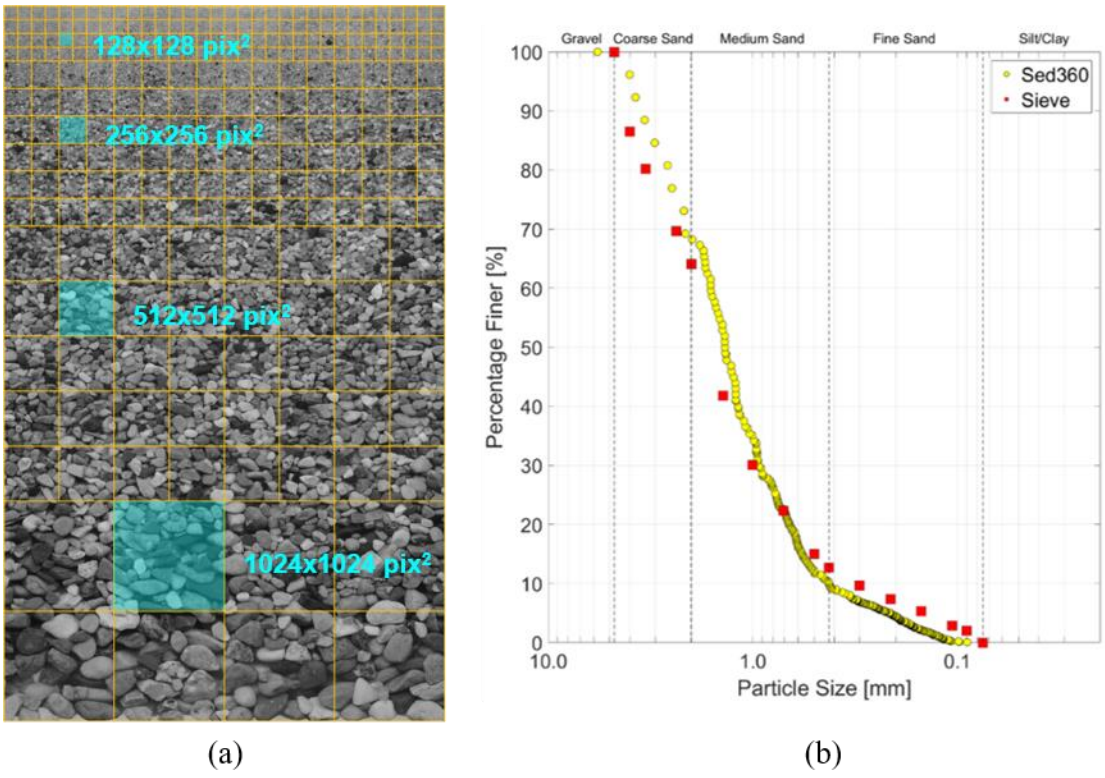

Figure 4-15. Sed360 Results for Specimen C. (a) Autoadaptively determined analysis squares used to generate the HWT-based PSD, (b) PSD results.

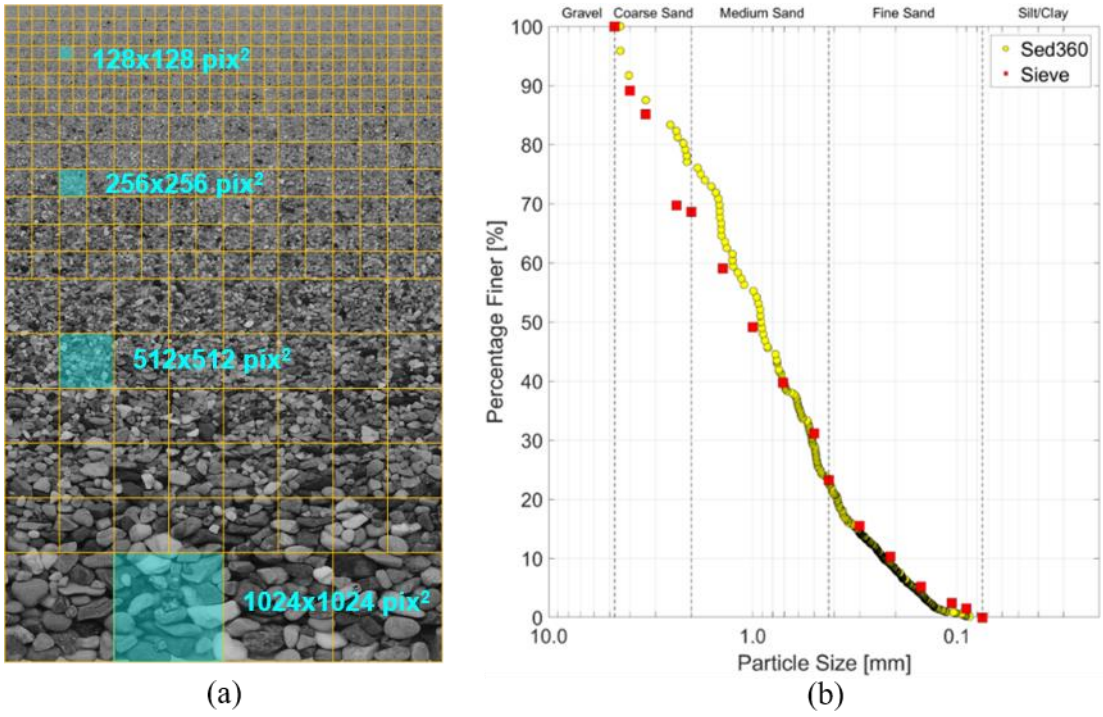

Figure 4-16. Sed360 Results for Specimen D. (a) Autoadaptively determined analysis squares used to generate the HWT-based PSD, (b) PSD results.

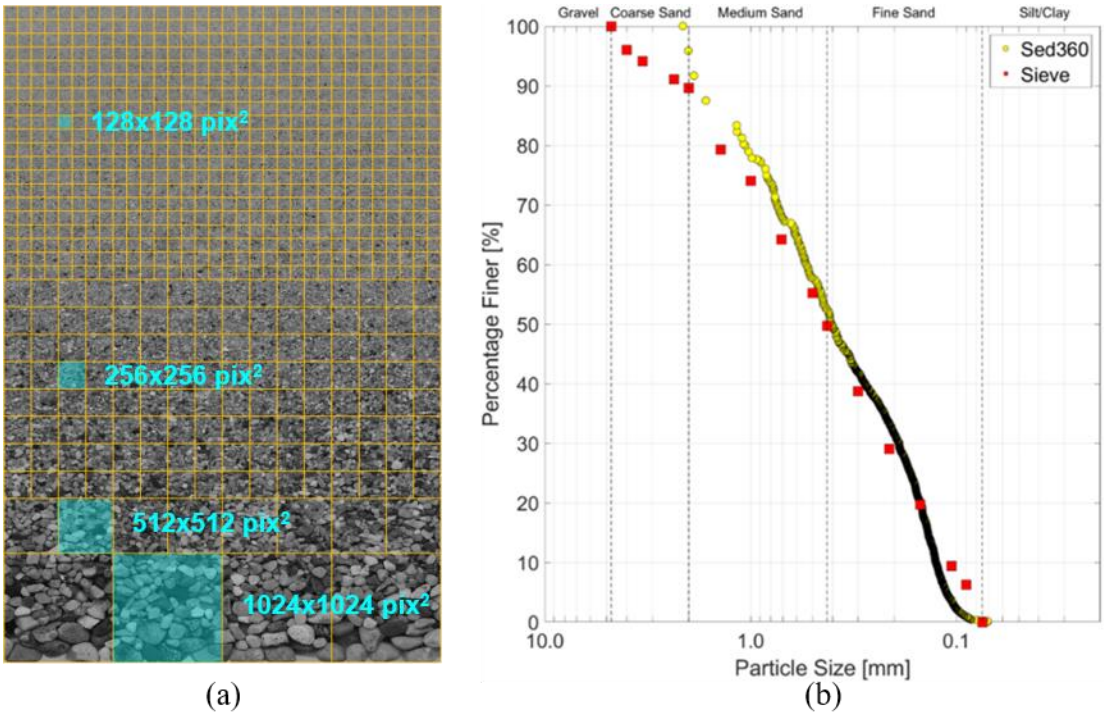

Figure 4-17. Sed360 Results for Specimen E. (a) Autoadaptively determined analysis squares used to generate the HWT-based PSD, (b) PSD results.

Table 4-2. Details and results of the five sands tested in the Sed360.

Item	Specimen A			Specimen B			Specimen C			Specimen D			Specimen E		
	Sed360		Sieve	Sed360		Sieve	Sed360		Sieve	Sed360		Sieve	Sed360		Sieve
	256 [a]	Auto [b]		256 [a]	Auto [b]		256 [a]	Auto [b]		256 [a]	Auto [b]		256 [a]	Auto [b]	
Specimen Size [g]	96.8			93.0			100.3			97.8			91.4		
Coarse Sand [%]	2	44	67	1	35	50	2	31	37	1	24	31	0	8	10
Medium Sand [%]	56	48	23	23	17	0	68	59	51	59	53	46	42	42	40
Fine Sand [%]	42	8	10	76	48	50	30	10	12	40	23	23	58	50	50
D_{60} [mm]	0.88	2.10	2.60	0.34	1.70	2.20	0.90	1.80	1.90	0.70	1.40	1.50	0.43	0.54	0.60
D_{30} [mm]	0.36	1.40	1.80	0.23	0.23	0.23	0.42	0.96	1.00	0.38	0.50	0.50	0.21	0.20	0.21
D_{10} [mm]	0.31	0.45	0.40	0.16	0.13	0.10	0.31	0.43	0.30	0.24	0.22	0.21	0.14	0.12	0.10
C_u [c]	2.8	4.7	6.5	2.1	13.1	22.0	2.9	4.2	6.3	2.9	6.4	7.1	3.1	4.5	6.0
C_c [d]	0.5	2.1	3.1	1.0	0.2	0.2	0.6	1.2	1.8	0.9	0.8	0.8	0.7	0.6	0.7

[a] Using a fixed HWT analysis area size of 256 pixel by 256 pixel
[b] Using the autoadaptive HWT analysis area sizing procedure from Fig. 4.11
[c] Coefficient of Uniformity, $C_u = D_{60}/D_{10}$
[d] Coefficient of Curvature, $C_c = (D_{30})^2/(D_{60} \times D_{10})$

As seen in Figs. 4.13 through 4.17, for all five of the sand specimens, the coarsest sand particles that were first to settle at the base of the sedimentation column require larger HWT analysis squares; as finer sand particles settle overtop larger ones, progressively smaller analysis squares were automatically adopted. Because of the different analysis square sizes, the coarser portions of the sands' Sed360 PSDs contain fewer data points while the finer sand portions of the PSDs have more points. Naturally, for the specimens with greater percentages of coarse sand (Specimens A, B, and C), more of the larger (1024 x 1024 pix^2 and 512 x 512 pix^2) analysis squares were employed than for the specimens with more fine sand (Specimens D and E). These trends are visualized in the stacked bar graphs in Fig. 4.18. About 50% of Specimens B and E are fine sand, which is reflected in the high number of the smallest analysis square (128 x 128 pix^2) being employed for these two specimens.

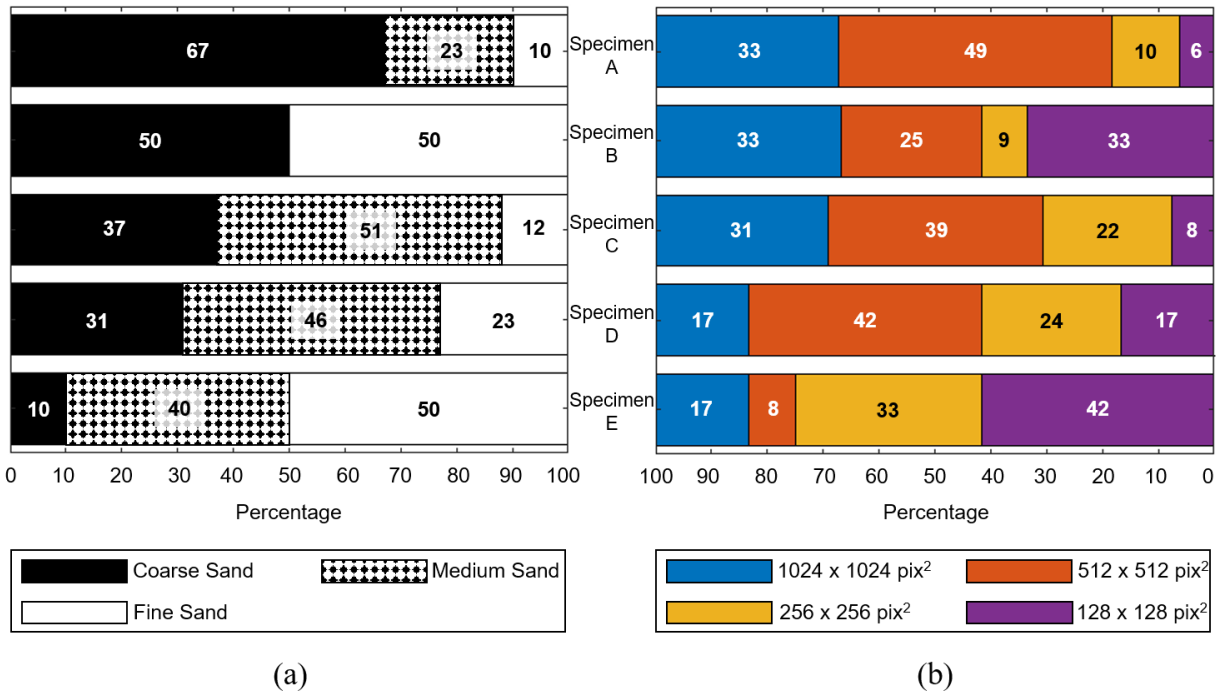

Figure 4-18. Composition breakdown of the five specimens by percent. (a) Sand type percentages within each specimen according to sieve results, and (b) percentage of the specimen images analyzed using each of the autoadaptively-selected HWT square sizes.

Overall there is very good agreement between the autoadaptive Sed360 PSD and the sieving results for all five sand specimens. In all five cases, the percentages of fine sand by the autoadaptive method and by sieving (see Table 4.2) are virtually identical. This excellent agreement is also seen in Figs. 4.13 through 4.17 where at 0.425mm, the Sed360 and sieving curves coincide. However, at the rightmost ends of the PSD curves, the autoadaptive Sed360 typically undersizes the smallest particles. This could be due to small errors in the manual cropping of Sed360 images. Or, ambient light may be illuminating the tops of the soil specimens, thus making the top row of analysis areas appear to contain larger particles than they actually are. Future research can address this relatively minor issue.

Specimen B Discussion

The gap-graded Specimen B (Fig. 4.14[a]) illustrates an important success of the autoadaptive method. Specimens A, C, D, and E have a continuous and uninterrupted flow of larger HWT analysis squares from the bottom of the images to progressively smaller squares moving up the image. By contrast, in the middle of Specimen B near the interface between coarse and fine sand, 512 x 512 pix^2 analysis squares were adopted. Above them there is an immediate jump to 128 x 128 pix^2 areas. This is a logical and expected result for a gap-graded sand. More interestingly, above the row of smaller squares, larger 256 x 256 pix^2 squares were selected by the autoadaptive procedure. Here, the small sand particles dictate the use of the smallest squares (128 x 128 pix^2), but various locations of different particle colors necessitated two rows of larger squares (256 x 256 pix^2) above the two rows of smaller squares. Had smaller analysis squares been used in this region, clustered black particles within the lighter colored sand could lead to undesired upturns in *E*-distributions at the highest *DL*s. The autoadaptive procedure eliminates this problem by effectively "diluting" these localized effects over larger 256 x 256 pix^2 areas.

To illustrate this further, one of the 256 x 256 pix^2 analysis squares in this region, circled in red in Fig. 4.14(a), contains a cluster of black particles in its upper left quadrant. Figure 4.19 includes the *E*-distribution for this 256 x 256 pix^2 analysis square as well as for the four corresponding 128 x 128 pix^2 squares. The 256 x 256 pix^2 analysis square yields an ordinary *E*-distribution that has one peak at the fourth decomposition level and no undesired *E* upturns at its upper *DL*s. However, the square's upper left 128 x 128 pix^2 quadrant, which contains the aforementioned cluster of black particles in the lower 1/8th of the area, *E* peaks at the second to last *DL*, as it should based on the fundamental HWT mathematics (Section 4.1). Even though there is no upturn in *E*, *CA* will be somewhat high due to the large *E* at *DL*=n-1.

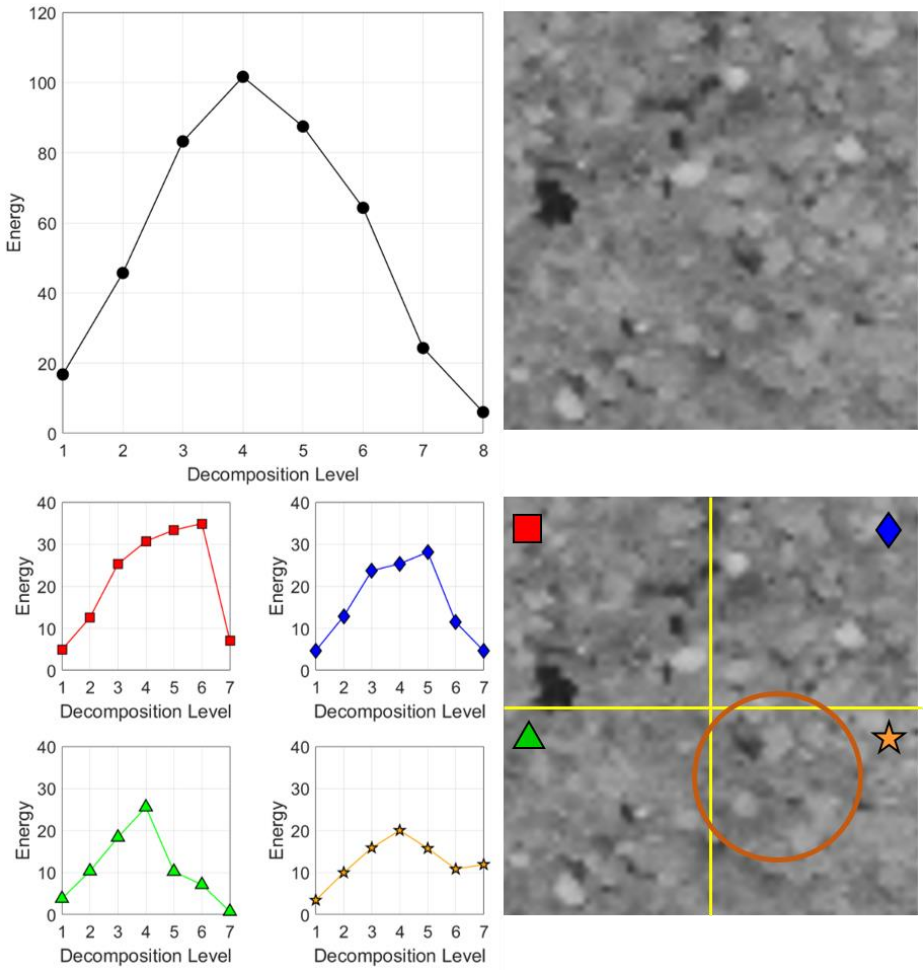

Figure 4-19. A Specimen B 256 x 256 pix^2 analysis square and its corresponding 128 x 128 pix^2 quadrants.

The lower right 128 x 128 pix^2 of the original 256 x 256 pix^2 illustrates another effect. Here we observe a very light cluster in the lower right quadrant and a spattering of darker particles (circled in Fig. 4.19) in the upper left quadrant. This causes the upturn in *E* at the final *DL*. As previously discussed, an *E*-distribution that upturns at the final few *DL*s (as the *E* for this 128 x 128 pix^2 area does), skews *CA* higher. The autoadaptive analysis area sizing procedure does not allow this to affect the PSD; because of this and similar 128 x 128 pix^2 squares throughout these two rows of 128 x 128 pix^2 areas (Fig. 4.14[a]), the larger 256 x 256 pix^2 analysis squares were instead adopted to represent this region for determining Specimen B's Sed360 PSD.

To explain why the Sed360 PSD reports 17% medium sand in Specimen B when the mix was created with only coarse and fine sand, the three rows of 512 x 512 pix^2 analysis squares in Fig. 4.14(a) are examined. These three rows are located at the interface between the fine and coarse sand. The top one of these rows contains mostly fine sand, with only several particles of coarse sand visible in a few of the analysis squares. The bottom row contains mostly coarse sand with a few pockets of visible fine sand. The middle row contains variable amounts of fine and coarse sand. In Fig. 4.20, the data points in the Sed360 PSD are color-coded to the analysis squares in the three rows.

As expected, the analysis squares that appear to contain only fine sand (the green-colored squares in Fig. 4.20) yield particle size values (the green circle data points in Fig. 4.20) that fall within the fine sand range of the Sed360 PSD. Similarly, the analysis squares that appear to contain only coarse sand (the pink squares) have particle sizes (the pink circle data points) that are within or very near the coarse sand range of the PSD.

The remaining areas in these three rows of analysis squares (the brown, cyan, and dark blue squares) correspond to the PSD data points that plot within the medium sand range. The three sets

contain various proportions of fine and coarse sand. The brown areas contain mostly fine sand with a few coarse sand pieces. Thus, the corresponding brown PSD data points lie at the finer end of the medium sand size range. The dark blue squares contain mostly coarse sand with a few small clusters of fine sand, which explains why the dark blue Sed360 PSD data points lie in the coarser end of the medium size range. Lastly, the cyan areas are those that contain a more even mix of coarse and fine sand. As such, their points lie closer to the middle of the medium sand range. The HWT-based particle sizes for the brown, cyan, and dark blue analysis squares are essentially providing a weighted average for the varying amounts of coarse and fine sands in these areas. In doing so, the Sed360 PSD erroneously concludes that there is medium-sized sand in Specimen B.

It is worth noting that Specimen B was intentionally engineered to test the limits of the Sed360 for a severely gap-graded sand. With particles between 2.0mm and 0.425mm entirely absent from this specimen, penetration of the pores in the coarse sand by fine sand particles was guaranteed. A naturally-occurring gap-graded sand would typically not have such a wide range of particles sizes missing entirely. Even small amounts of medium-sized particles would create a sand filter that would limit the pore “clogging”. Better agreement should therefore be expected between the Sed360 and sieve PSDs for naturally-occurring gap-graded sands.

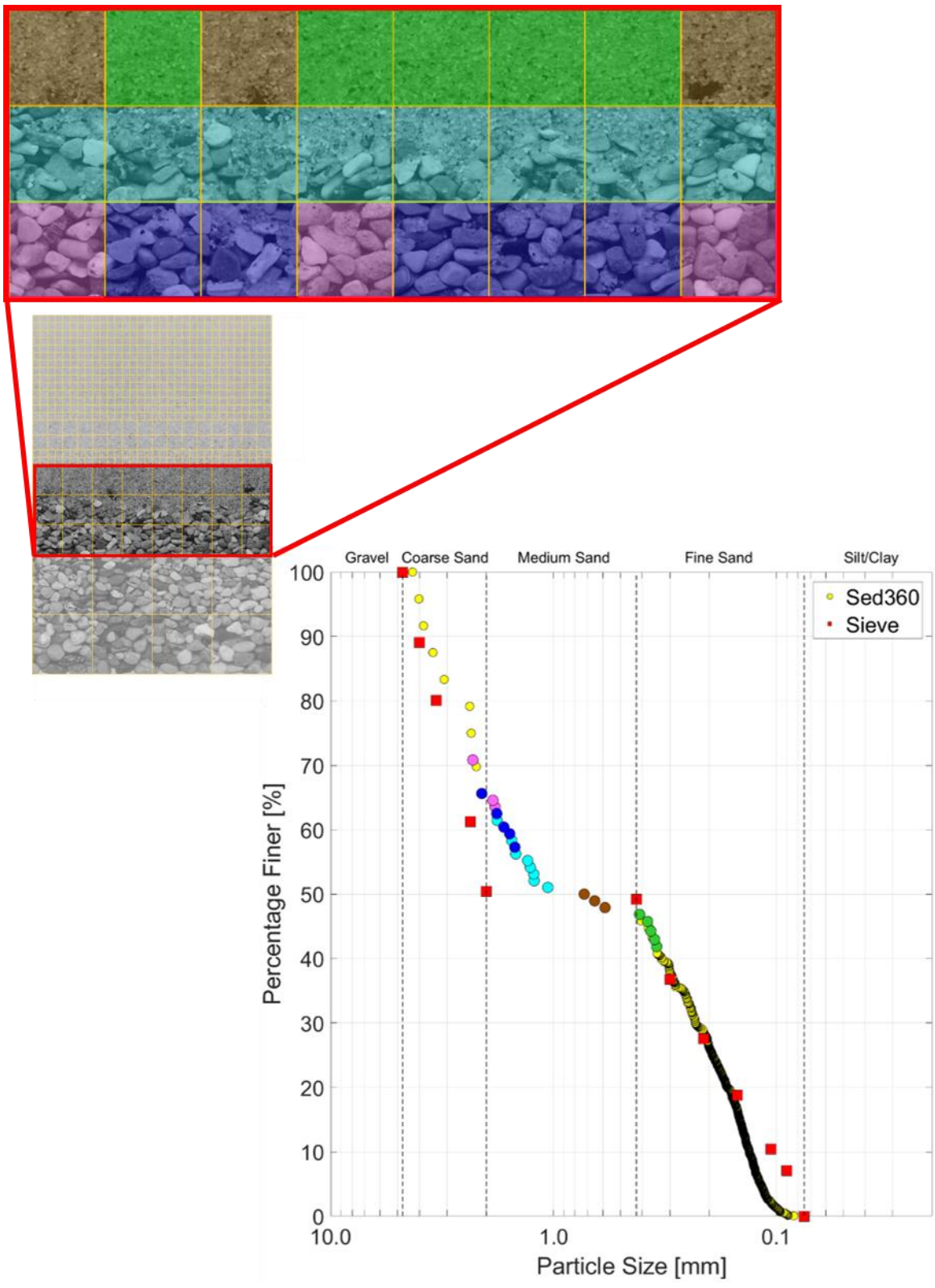

Figure 4-20. Investigating the HWT analysis squares at the coarse and fine sand interface in Specimen B.

Specimen E Discussion

At the coarse end of the PSDs, the autoadaptive Sed360 method seems to undersize particles slightly. This is most evident and pronounced in Specimen E, shown in Fig. 4.17. To understand why this occurs, Specimen E's row of 1024 x 1024 pix^2 analysis squares in Fig. 4.17(a) is examined. There are not enough coarse sand particles to fully fill up these four large analysis areas; the coarse sand particles fill only the bottom half of these 1024 x 1024 pix^2 squares while finer sand particles fill the top half of this row of analysis squares. The HWT results for these squares are like that in the Fig. 4.10 example. In both instances, for an analysis areas that contains a range of particle sizes, the HWT-determined particle size is smaller than the largest particles in the area, but larger than the finest particles. The possible solution to this in Fig. 4.10 was to quarter the larger analysis square. This yielded four HWT-based particle sizes that more accurately represented the particles in the specimen. However using smaller areas for the coarse sand particles in Specimen E is not feasible, and ultimately the reason why the Sed360 PSD undersizes the coarse sand portion of the specimen.

To illustrate, Fig. 4.21 examines the eight energy curves for the 512 x 512 pix^2 analysis squares located in the bottom half of Specimen E's 1024 x 1024 pix^2 areas. As reflected in their energy curves, these areas are too small relative to the size of the coarse sand. Four of the energy curves violate the rules of the current autoadaptive HWT analysis area sizing procedure detailed earlier. Energy curves 3 and 8 have increasing energy values at the final decomposition level, while curves 2 and 7 peak at the second to last decomposition level. Per the autoadaptive rules, these four energy curves should have their *E*s at the upper *DL*s set to zero. However, since 50% of this row of 512 x 512 pix^2 analysis squares are "corrected", the HWT-based method does not use these smaller areas, and is therefore forced to use the larger 1024 x 1024 pix^2 squares. The 512 x 512

pix^2 analysis squares are too small to correctly size the coarse sand in Specimen E, yet there is not enough coarse sand in this specimen to be accurately detected by the HWT method in the larger 1024 x 1024 pix^2 squares. One solution to this problem is to use a larger overall specimen size, but other remedies may exist that can be explored in the future.

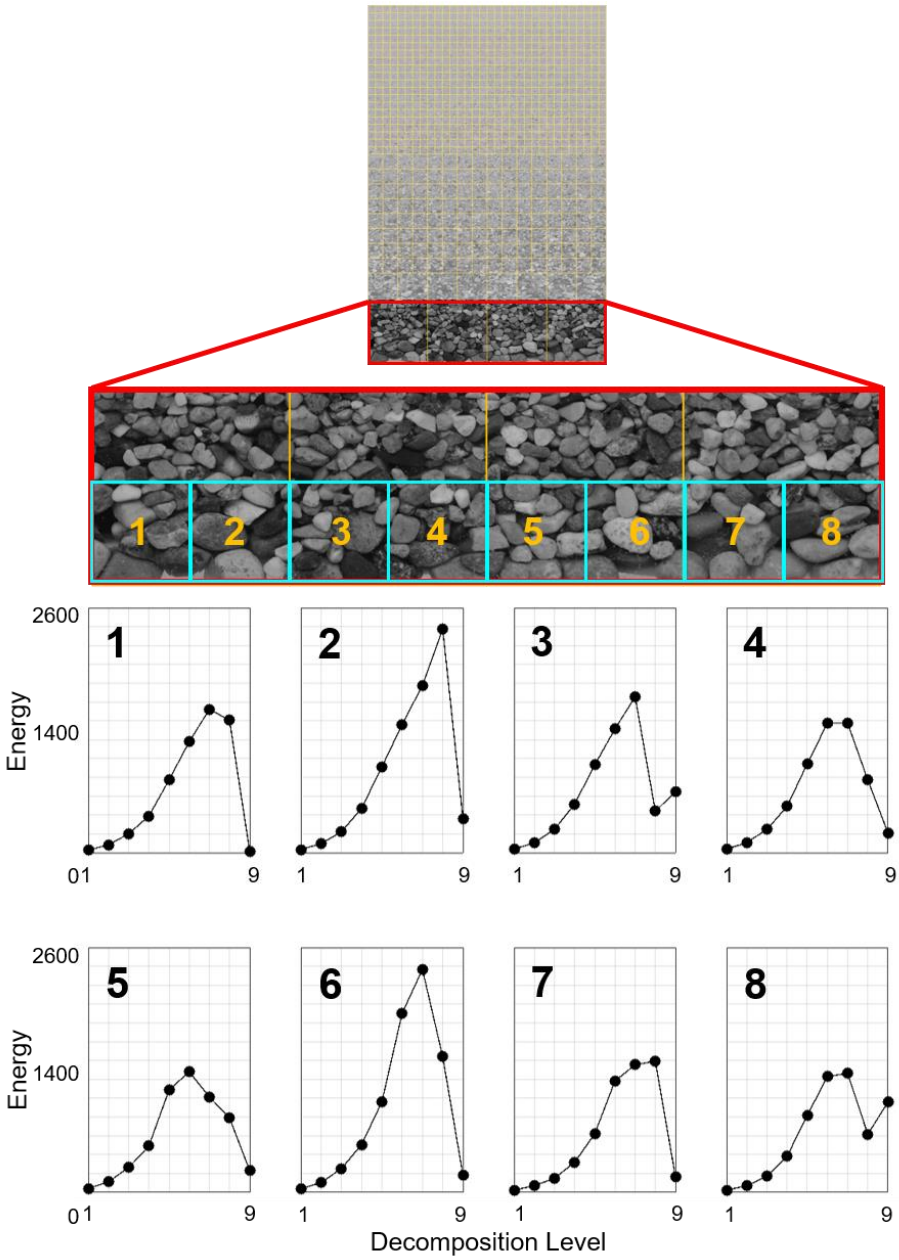

Figure 4-21. Invalid 512 x 512 pix^2 energy curves leads to an undersizing of the Specimen E's coarse sand.

4.3 Chapter Summary

Chapter 4 focused on the image analysis method used with all three SedImaging systems. This method was referred to throughout this chapter as the "HWT-based method." Soils tested by LabSed and FieldSed were analyzed by the original HWT-based method. A detailed description of the original method was provided in Section 4.1. To aid this description, example HWT-based results for a sand tested by SedImaging were shown in Figs. 4.1, 4.2, 4.4, and 4.5. The two main parameters of the HWT-based method, *CA* and *PPD*, were introduced here. The original sieve-defined calibration curve relating *CA* and *PPD* was given in Eq. 4.2. Using this with Eq. 4.3, the size of the soil particles in an analyzed image are determined and a soil's final PSD is created.

The expanded soil particle size range for SedImaging that was made possible by the Sed360 required a re-calibration of the original *PPD-CA* equation (Eq. 4.2). Narrow ranges of known soil particle sizes were photographed with the Sed360. These ranges were listed in Table 4.1. Using these images, a new piecewise *PPD-CA* calibration curve was defined in Eq. 4.5 and shown in Fig. 4.6. Equation 4.5 was necessary to accurately size the coarse sand particles that can now be tested with SedImaging via the Sed360.

In addition to Eq. 4.5, the original HWT-based method was redesigned to automatically (and continually) adapt its procedure to accurately size the different particles throughout a soil assembly image. This autoadaptive image analysis method was described in Section 4.2.2 and presented as a flow chart in Fig. 4.11.

Using both Eq. 4.5 and the autoadaptive HWT-based method, five soil specimens were tested with the Sed360 and were the focus of Section 4.2.3. The specimens were all formed from the same parent soil, but all had different gradations, with one soil being a gap-graded mix. The five sands were presented in Fig. 4.12. Their PSDs were determined using the autoadaptive HWT-

based method and were compared to sieving with overall very good agreement. These comparisons were shown in Figs. 4.13 through 4.17 and also presented in Table 4.2. This chapter concluded with several discussions of unique results of the autoadaptive HWT-based method for two of the sand specimens.

Chapter 5 Vision Cone Penetrometer (VisCPT)

This chapter begins by discussing the evolution of the VisCPT hardware. Section 5.1 briefly describes the first and second generation VisCPTs, while Section 5.2 focused on the latest third generation VisCPT. A prototype of the third generation system (Section 5.2.1) was fabricated by ConeTec Investigations Ltd. and was extensively used as part of several benchtop-testing calibration projects. During these, the original image analysis method utilized with the earlier VisCPTs, the Haralick Spatial Gray Level Dependence Method (SGLDM) (Section 5.3), was used to analyze images captured by the prototype (Section 5.4.1). The Haar Wavelet Transform (HWT)-based method that has mainly been used with SedImaging (Chapters 3 and 4) was also used to analyze VisCPT images (Section 5.4.2). In doing so, ongoing research (Section 5.4.3) is exploring ways to utilize both of these analysis methods to expand the application and accuracy of both the VisCPT and SedImaging systems.

***

Passages and portions of this chapter are taken from a previous publication that introduced the third generation VisCPT prototype (Ventola et al. 2020a).

5.1 First and Second Generation VisCPT Hardware Systems

The original VisCPT shown in Fig. 5.1 (top) was developed by Raschke and Hryciw (1997). It equipped a traditional CPT device with two black and white charge coupled device (CCD) cameras. The camera closer to the penetrometer tip captured lower-magnification images, while the second camera captured higher-magnification images. The lower-magnification

camera's field of view was 14mm (vertical), while the higher-magnification's was 2mm (vertical). Both cameras had a resolution of only 768 pixels by 494 pixels. The second generation VisCPT (Shin 2005), shown in Fig. 5.1 (bottom), replaced the two previous cameras with one micro digital color CCD camera. The device consisted of an electronic piezocone and a vision module containing the camera. The camera captured images with a 720 x 480 pix^2 resolution and a 10mm field of view (vertical).

One undesirable design feature of the first two generations of the VisCPT was the diameter difference between the piezocone and the vision module. The piezocone has a diameter of 36mm (1.4in), while the vision modules have larger diameters of 51mm (2.0in) (first generation) and 47mm (1.9in) (second generation). The larger diameters for the VisCPT vision modules were necessary to house the internal video components that were commercially available at the time of fabricating these systems.

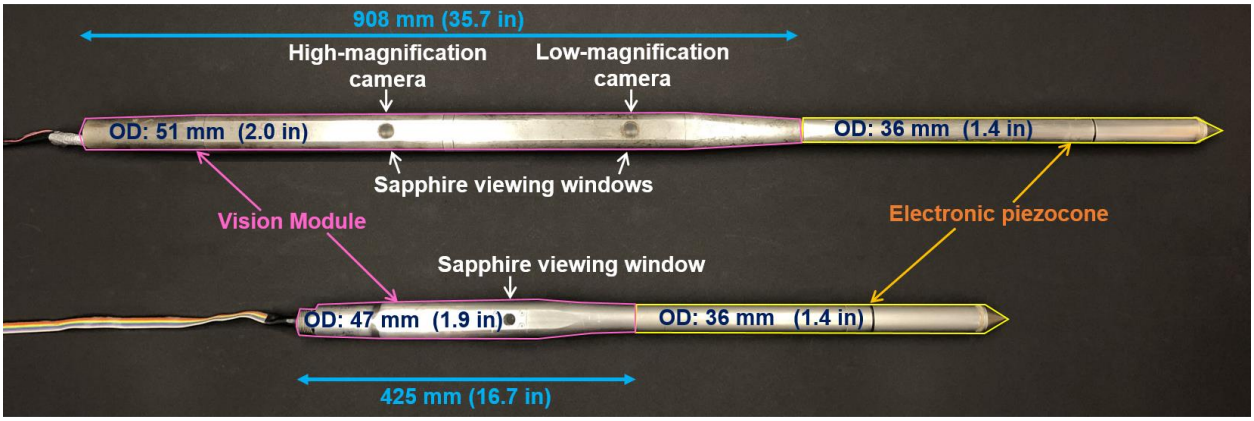

Figure 5-1. Earlier Vision Cone Penetrometers (VisCPTs). Top: First generation VisCPT (1997), Bottom: Second generation VisCPT (2005).

5.2 Third Generation VisCPT Hardware System

The introduction of smaller, board-based microcameras warranted a redesign of the VisCPT with the intent to reduce or eliminate the diameter differences between the various components of the system. First, a prototype of the third generation VisCPT (Section 5.2.1) was fabricated in 2019 by ConeTec and used for several benchtop calibration testing projects (Section 5.4). The purpose of this testing was to determine if the original image analysis method (Section 5.3) used with the previous VisCPT generations was still an effective tool given the updated camera technology in the third generation system. It was also an opportunity to explore, the use of the Haar Wavelet Transform (HWT)-based image analysis method (Chapter 4) with the VisCPT system. After promising results of this testing, the third generation VisCPT was fabricated (Section 5.2.2) and is prepared to be used in upcoming calibration chamber testing as part of a larger in-situ project for thin layer soil detection by VisCPT (Section 6.2).

5.2.1 3D-Printed Prototype for Benchtop Calibration Testing

The third generation VisCPT camera module contains a high-speed digital interface. This allows high-resolution images to be transmitted quickly enough to be viewed in real time and be stored for later analysis. The interface uses a differential cable and an error correcting protocol to guarantee transmission. The highest resolution soil images are transmitted with the cone stationary using lossless compression. Lower resolution images are transmitted and stored with each depth pulse allowing less detailed analysis in real time. The camera itself has a long focal length and views the soil using a right-angled mirror through a sapphire viewing window. The long focal length enables the camera to view the passing soil with a small angle of view, therefore minimizing fisheye effects in the captured images. Careful control of lighting and aperture keep the image in

focus even when thermal expansion and contraction of the physical components change the optical path. This also keeps soil in focus even if the viewing window is not in direct contact with the soil. A 3D-printed prototype of the third generation VisCPT was built in 2019 and used as part of a benchtop calibration testing program. The prototype is shown in Fig. 5.2(a); a cross-section schematic is illustrated in Fig. 5.2(b). The prototype has an octagonal cross-section, with a 15.9mm (0.63in)-diameter sapphire viewing window centered on one of the flat sides. One end of the prototype connects to a 15cm^2 (2.3in^2) electronic CPT piezocone. The other end connects to a CPT rod. An e-Con Systems See3CAM_80 13 Megapixel UVC USB camera is used. This camera has a resolution of 13 Megapixels, which is almost 38 times greater than that of the second generation VisCPT.

Figure 5.3 shows images captured with the VisCPT prototype. The 4208 x 3120 pix^2 images are of various dry soil particle sizes from the same parent 2NS sand (MDOT 2010). As seen in Fig. 5.3(d), which depicts silt material photographed with the VisCPT, this system's high-resolution camera enables characterization of soils into the silt range (Section 5.4). An area of the prototype's viewing window (the upper left region) has localized uneven illumination, casting shadows over the photographed soil particles. Though undesirable, this is a byproduct of the vision module's internal dimensions, which restrict the placement of the system's camera and illumination board. In response, only portions of the viewing window with uniform illumination were extracted for use in the calibration testing.

For benchtop calibration testing, the VisCPT prototype was connected to a BK Precision 1735A DC power supply that controlled the illumination of the soil through the sapphire window. Figure 5.4 shows the benchtop calibration testing set up. Details and results of the testing using the prototype are presented in Section 5.4.

(a)

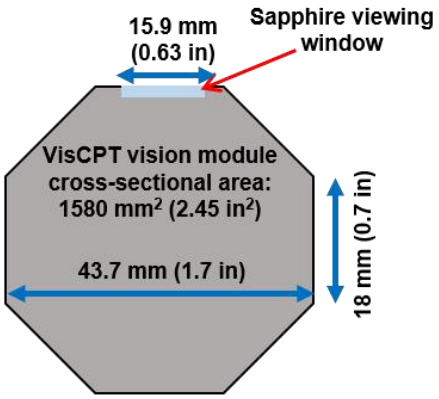

(b)

Figure 5-2. 3D-printed prototype of the third generation VisCPT vision module. (a) Vision module, (b) Schematic of the module's cross-section.

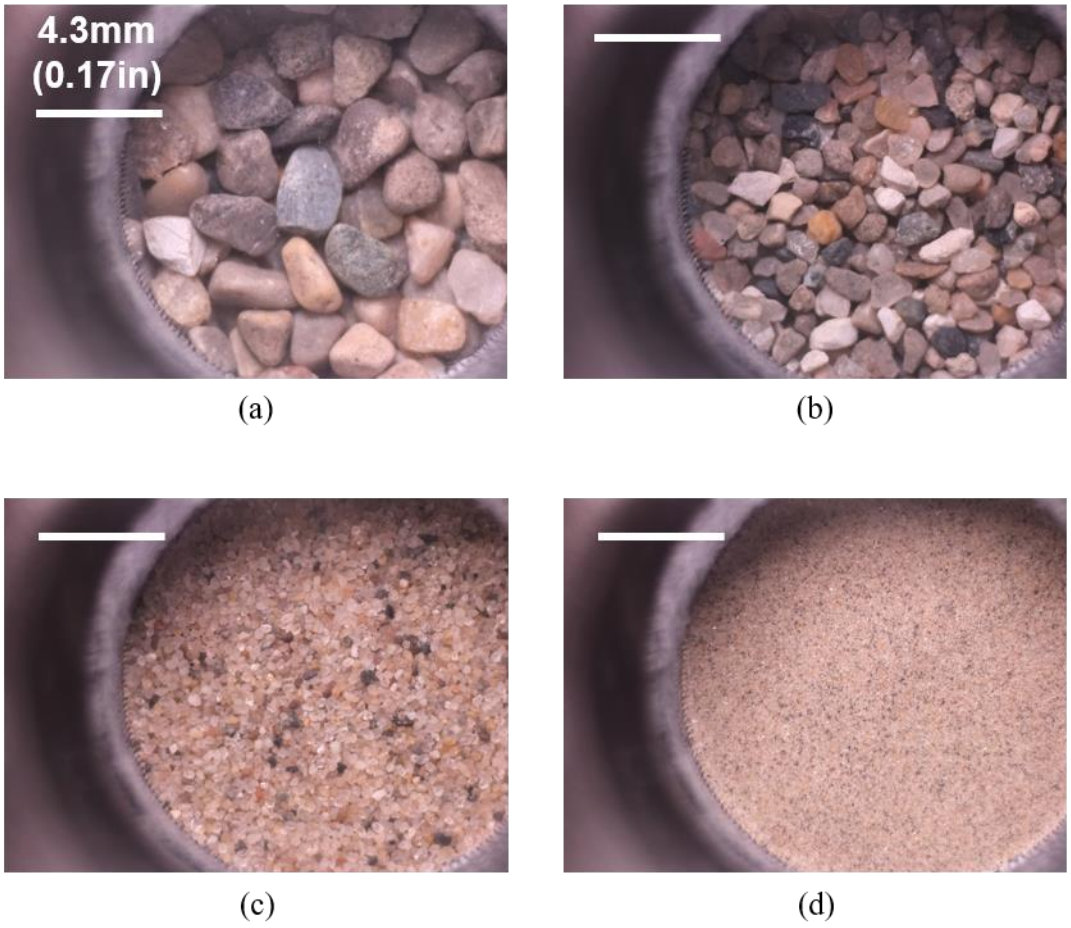

Figure 5-3. Images of 2NS sand captured with the VisCPT prototype. Midpoint particle sizes of (a) medium sand, 1.85mm, (b) medium sand, 0.86mm, (c) fine sand, 0.256mm, (d) silt, 0.046mm.

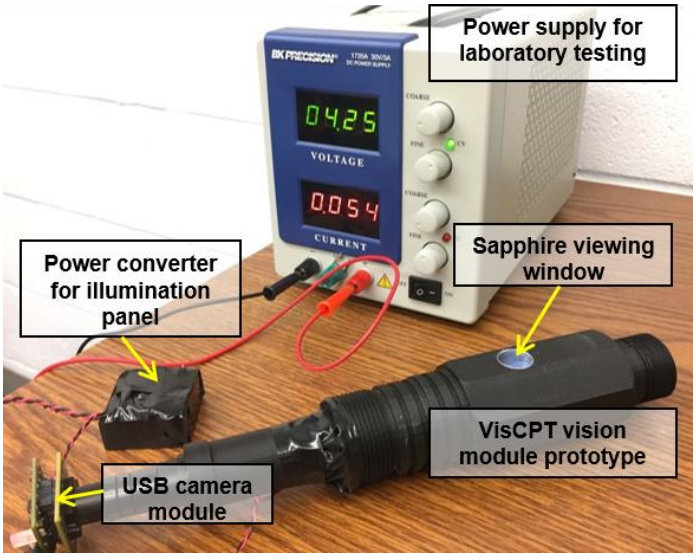

Figure 5-4. Benchtop calibration testing setup using the VisCPT prototype.

5.2.2 Third Generation VisCPT for Calibration Chamber Testing

After conducting the benchtop calibration testing (Section 5.4) with the 3D-printed prototype, ConeTec fabricated the third generation VisCPT in 2022 in preparation for use in forthcoming calibration chamber testing (Section 6.2). This new VisCPT is shown in Fig. 5.5. The VisCPT's camera and illumination board are housed directly "upstream" of the vision module in the hardware housing unit. Standard 10cm^2 (1.6in^2) CPT rods (not shown in Fig. 5.5) can be connected to this housing unit. A non-functioning 15cm^2 (2.3in^2) CPT cone tip is attached at the opposite end of the vision module. This cone tip does not have electronic piezocone capabilities; a separate CPT system with a piezocone will be used for the aforementioned calibration chamber testing. Attaching an electric piezocone to the VisCPT in Fig. 5.5 is possible for future field testing applications. The vision module, hardware housing unit, and cone tip in Fig. 5.5 all have the same outer diameter as a standard 15cm^2 (2.3in^2) CPT cone tip (44mm, 1.8in). This uniformity across the entire VisCPT was not possible with the first and second generation systems.

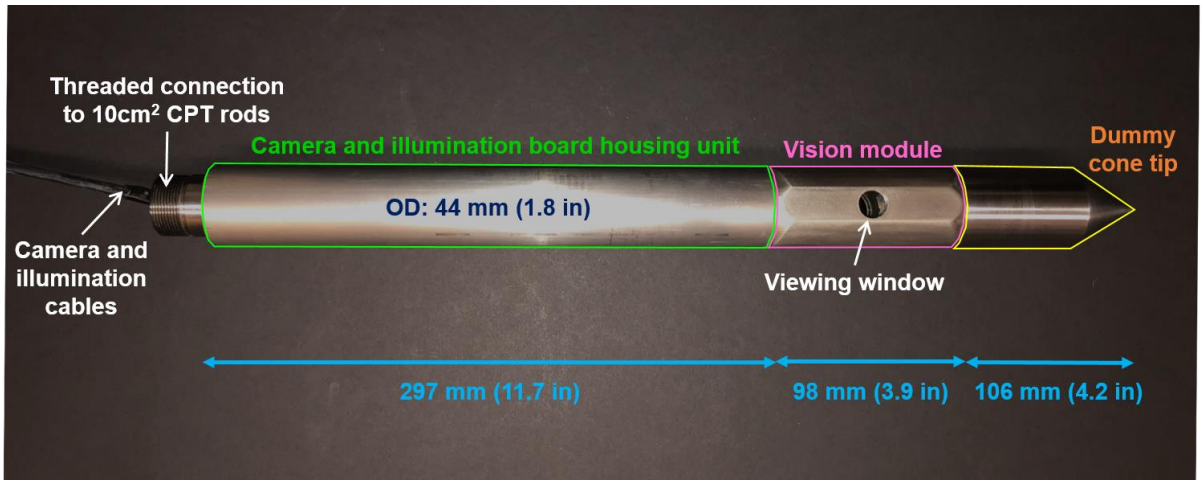

Figure 5-5. Third generation VisCPT.

The cross-section of the vision module is no longer an octagon like its earlier prototype. Instead, the module's cross-section is nearly circular with two flattened sides that are located 180° relative to one another. The 15.9mm- (0.63in) diameter viewing window is set within one of these flattened sides. The other flattened side (not shown in Fig. 5.5) allows for the VisCPT to be positioned horizontally on a table or other flat surface for ex-situ testing. The transition areas between the rounded and flattened portions of the vision module have been smoothed to reduce any impact the changing cross-section shapes may have on the surrounding soil as the VisCPT advances through soil strata. Two of these transition areas on the vision module are circled with a dashed line in Fig. 5.6.

The e-Con Systems See3CAM_80 13 Megapixel UVC USB camera from the third generation VisCPT prototype has been replaced with an even higher resolution, Ximea MU181CR-ON 18 Megapixel USB3 camera. The same BK Precision 1735A DC power supply from the prototype is still used to power the illumination board in this system. Figure 5.7 shows six images (all with an image size of 4896 x 3680 pix^2) of different dry sands and a moist red clay photographed with the third generation VisCPT. For comparison, Figs. 5.7(a) through 5.7(d) are the same 2NS particle sizes as the prototype images from Fig. 5.3. Figures 5.7(e) and 5.7(f) are the clay and sand that will be used in the forthcoming VisCPT calibration chamber testing.

Images captured with this VisCPT have a magnification of 247.1pix/mm. Unlike the prototype, nearly the entire viewing window is visible in images captured by this VisCPT. This allows for more of the viewable soil to be utilized for image analysis. Furthermore, the severe shadow in the prototype images in Fig. 5.3 is no longer present in those in Fig. 5.7. However, the hardware constraints of this VisCPT still creates some uneven illumination throughout the viewing

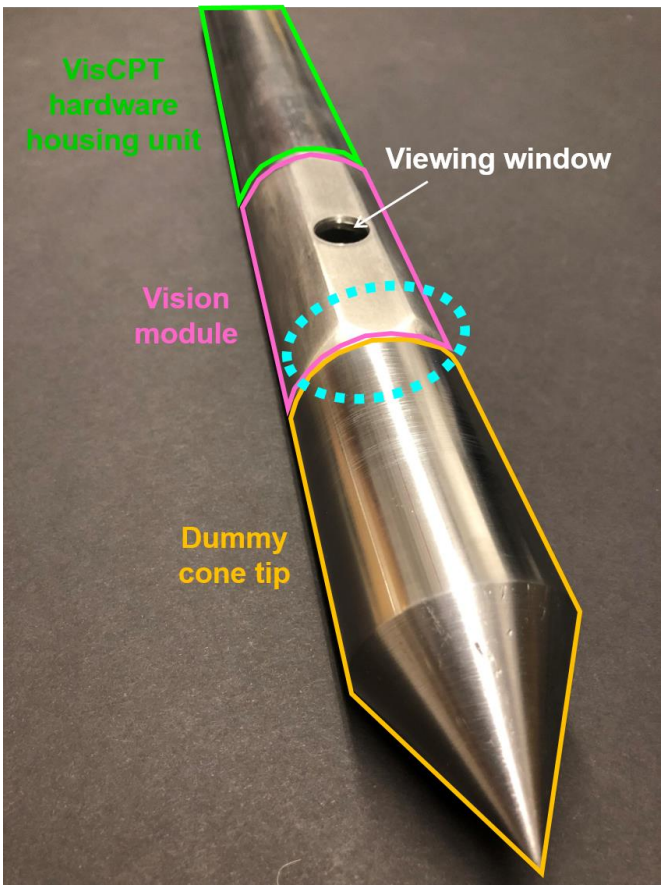

Figure 5-6. Smoothed transition areas in the VisCPT's vision module.

window. As seen in the images in Fig. 5.7, there is a localized region in the center of the viewing window that is slightly brighter than the rest of the image. While this is still undesirable, (the uneven illumination will erroneously impact the image analysis results since they, as will be discussed in Section 5.3, are based on an image's distribution of pixel grayscale intensity values) the uneven illumination in this VisCPT is reduced from that of the prototype. Future research will focus on post-processing methods to properly address this uneven illumination.

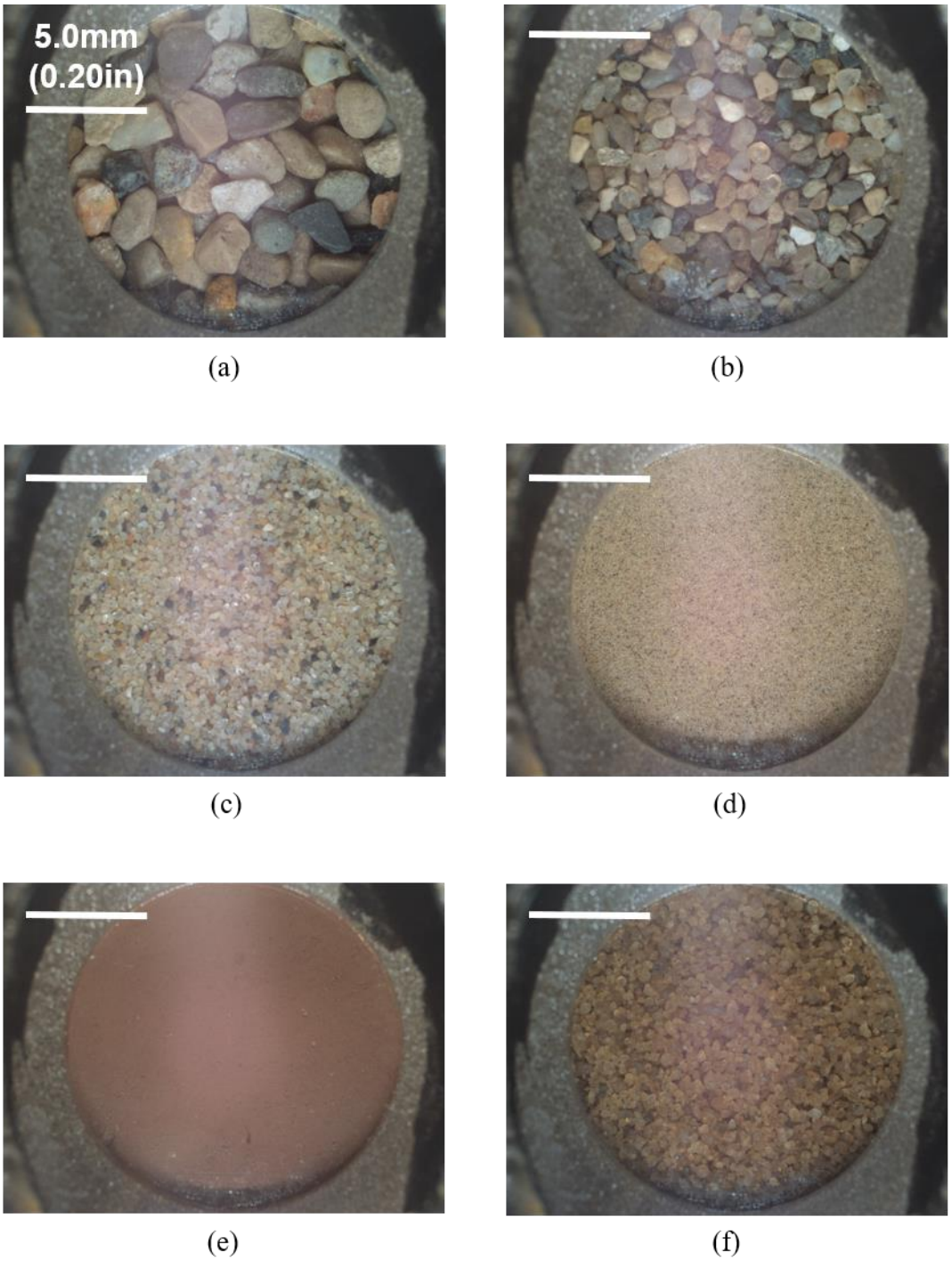

Figure 5-7. Images of soils captured with the third generation VisCPT. Midpoint particle sizes of the sands (a) 2NS medium sand, 1.85mm, (b) 2NS medium sand, 0.86mm, (c) 2NS fine sand, 0.256mm, (d) 2NS silt, 0.046mm, (e) Red clay, (f) Sand used in upcoming calibration chamber testing.

5.3 Haralick Spatial Gray Level Dependence Method (SGLDM) Image Analysis

Images captured with the VisCPT are analyzed using the Spatial Gray Level Dependence Method (SGLDM) proposed by Haralick et al. (1973). The SGLDM defines 14 textural indices based on various spatial distributions of grayscale pixel intensity values of an image. These indices are a single numerical value corresponding to different textural characteristics of an image. An image of any dimension (square or not) can be analyzed with the Haralick SGLDM method. Appendix B provides a brief overview of the mathematical definitions of the selected Haralick textural indices used with the VisCPT.

Ghalib et al. (1998) and Ghalib et al. (2000) determined that three of the textural indices "Energy", "Contrast", and "Local Homogeneity" were most useful for delineating soil layers in (first and second generation) VisCPT data. This Energy textural index is not to be confused with the Energy from the HWT-based method described in Chapter 4; these two Energies are entirely different and have different mathematical definitions. Ghalib et al. (2000) plotted Energy, Contrast, and Local Homogeneity textural indices alongside traditional CPT tip resistance, side friction, and pore pressure logs. The Haralick textural index profiles are used to identify thin soil layers and lenses that are often undetected by the CPT. Appendix C provides results of a case history comparing CPT and textural index soil profile logs for a testing location in California.

The Energy textural index is defined as the global homogeneity of an image (Ghalib et al. 2000). The Energy index increases when an image contains increasingly larger clusters of similar grayscale values. In the application of the VisCPT, such clustering would occur for finer-grained materials, such as clay or silt layers. For example, the clay in Fig. 5.7(e) would be expected to have a higher Energy than the medium sand in Fig. 5.7(c). Contrast is the measure of any local variations in grayscale values within an image (Ghalib et al. 2000). It is highly sensitive to boundaries

between soil particles or open cracks; Contrast drops significantly for finer-grained materials. A profile log of Contrast contains a large amount of noise due to the sensitivity of this index to said boundaries. A Local Homogeneity profile log is virtually a mirror-image of a corresponding Contrast log, but with much less boundary sensitivity (and therefore less noise). For example, when a Contrast log reaches a minimum value for clay layers, the Local Homogeneity log will peak at a maximum value. Figure 5.8 plots these three textural indices for a profile of known soil types.

In Fig. 5.8, all three indices can accurately detect the two thin (1 to 3cm thick) clay layers located between 0.4 and 0.6m distance, with the Energy profile most clearly detecting these layers. The Contrast and Local Homogeneity profiles both distinguish the different sand layers between the 0.0 and 0.2m and 0.6 and 0.8m distances, but as previously mentioned, the Local Homogeneity profile contains less noise than the Contrast profile. The Energy profile does not clearly distinguish between these sand layers. Since the Contrast and Local Homogeneity index logs can distinguish similar soil profile features, and higher noise is present within the Contrast data, Ghalib (2001) concludes that only using Energy and Local Homogeneity indices are necessary for the VisCPT. As will be discussed in Section 5.4, these two textural indices, as well as several others, formed the basis of a portion of the benchtop calibration testing with the third generation VisCPT prototype.

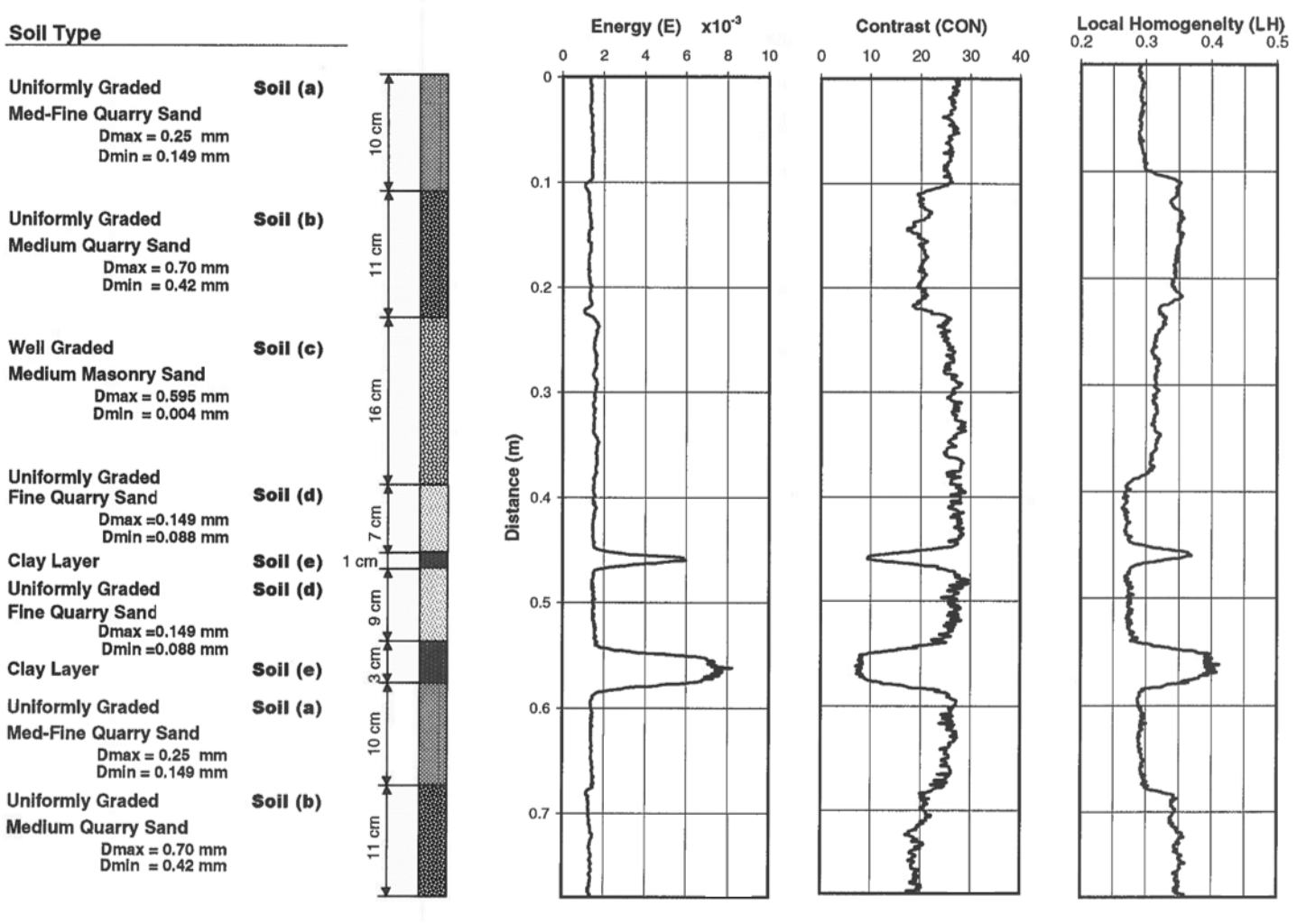

Figure 5-8. Profile logs for Energy, Contrast, and Local Homogeneity Haralick texture indices of a known soil profile (Ghalib et al. 2000).

5.4 Benchtop calibration testing with the third generation VisCPT prototype

Two benchtop calibration testing projects were conducted with the VisCPT prototype. The first one (Sections 5.4.1 and 5.4.2) only involved 2NS sand. Both the SGLDM and HWT-based analysis methods were used to analyze these 2NS images. After this work yielded promising results, the benchtop testing was expanded for the second project (Section 5.4.3), which used these same image analysis methods for different soils beyond 2NS. The work for this second project is ongoing, but the preliminary results merit a discussion that begins in Section 5.4.3 and continues within Section 6.2.

5.4.1 Haralick SGLDM analysis of VisCPT images

The advent of the third generation VisCPT warranted a re-evaluation of the original SGLDM image analysis method. As noted in Section 5.2, this testing occurred using the VisCPT prototype in Fig. 5.2 with the benchtop setup in Fig. 5.4. The voltage from the system's power supply was varied to study the effect of image brightness on the textural indices. To determine the appropriate voltage, dry 2NS soil particles of different size ranges were photographed at a series of voltages. Table 5.1 summarizes the different particle sizes selected for use in this calibration research. All soil images were captured at the same camera magnification (246.6pix/mm) and with the same camera settings (e.g. sharpness, white balance, exposure, etc.). Five different images for each size range were captured; a total of 40 unique soil images at each voltage were obtained. Nine different voltages ranging from 3.75 Volts to 7.00 Volts were analyzed. Through a comparison (not detailed here) of voltages/illuminations and the resulting textural indices, 4.25 Volts was determined to provide the ideal illumination for this investigation.

Table 5-1. 2NS sand particle size ranges used in VisCPT benchtop calibrations testing.

Sample	Sieve Size Range [a]	Particle Size Range [mm] (Midpoint)	Midpoint *PPD* [b] [pix]
a	No. 10 – No. 12	2.0 – 1.7 (1.85)	456.2
b	No. 18 – No. 25	1.00 – 0.71 (0.86)	210.8
c	No. 30 – No. 35	0.6 – 0.5 (0.55)	135.6
d	No. 50 – No. 70	0.300 – 0.212 (0.256)	63.1
e	No. 70 – No. 100	0.212 – 0.150 (0.181)	44.6
f	No. 100 – No. 170	0.15 – 0.09 (0.12)	29.6
g	No. 200 – No. 270	0.075 – 0.053 (0.064)	15.8
h	No. 270 – No. 400	0.053 – 0.038 (0.046)	11.2

[a] Sieve size ranges were gathered in accordance with ASTM (2019) C136/C136M-19
[b] Pixels per particle diameter, *PPD*, can be determined by rearranging Eq. 4.3 in Section 4.1 using a particle size range's midpoint and the known VisCPT magnification of 246.6pix/mm

Figure 5.9 shows one of the five soil images captured for each of the Table 5.1 size ranges using a VisCPT illumination of 4.25 Volts. The images in Fig. 5.9 are 2048 x 2048 pix^2 and were gathered from a fixed region of the VisCPT viewing window with uniform illumination. Even though the Haralick SGLDM image analysis method can be used for non-square images, this image size was selected so that the same exact images could also be analyzed with the HWT-based method, which Section 4.1 notes requires 2^n x 2^n pix^2 (n = 1,2,3...) analysis area sizes.

Five Haralick textural indices: Contrast, Correlation, (Local) Homogeneity, Variance, and Energy were computed for the 40 images of various-sized soil particles from Table 5.1 and Fig. 5.9. In Fig. 5.10, the Haralick textural indices are plotted versus the known midpoint *PPD* value for each image. (As noted in footnote *b* of Table 5.1, this *PPD* is the same as that defined in Eq. 4.3 in Section 4.1). Contrast (Fig. 5.10[a]), Correlation (Fig. 5.10[b]), Homogeneity (Fig. 5.10[c]), and Variance (Fig. 5.10[d]) all exhibit clear trends with *PPD*; Contrast has an inverse relationship with *PPD*, while Correlation, Homogeneity, and Variance all have direct relationships with *PPD*. Furthermore, there is very high reproducibility between the five different soil images taken at each *PPD*. Figure 5.10 shows that Contrast, Correlation, Homogeneity, and Variance are promising

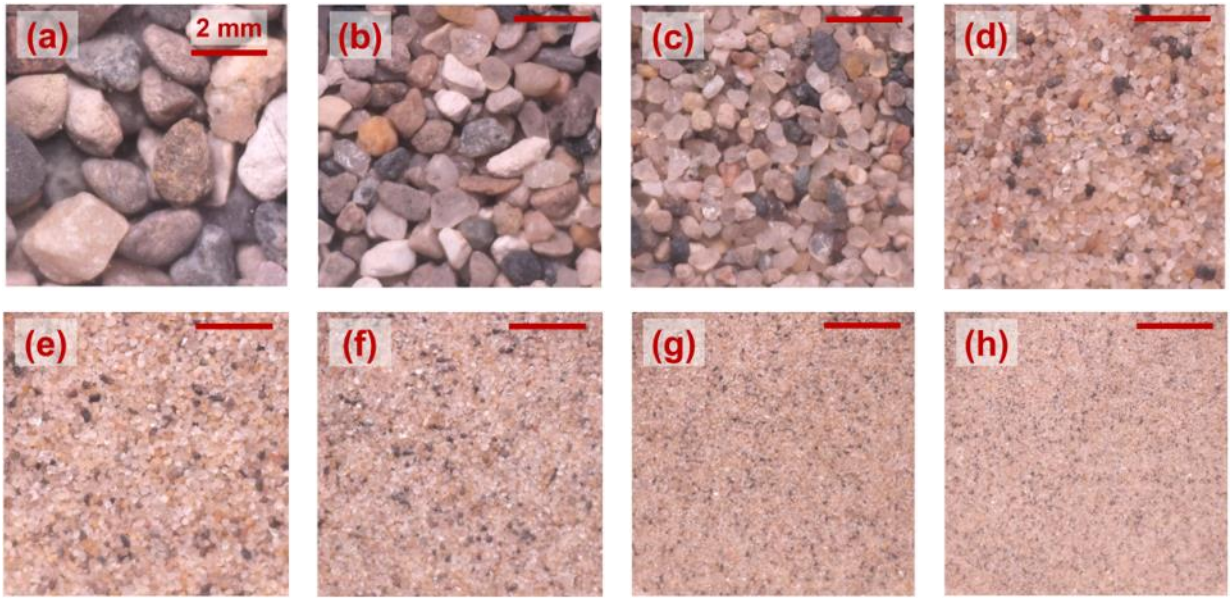

Figure 5-9. Photos of each 2NS sieve size range from Table 5.1.

textural indices that will eventually be used to characterize particles over a size range spanning nearly two orders of magnitude, from the silt range to medium sand.

In contrast to the other indices, Energy (Fig. 5.10[e]) appears to have no correlation with *PPD*. Unlike the conclusions reached by Ghalib (2000), it appears that Energy cannot be used to determine soil particle sizes. The reason for the discrepancy between Fig. 5.10(e) and Ghalib (2000) possibly lies in the VisCPT camera magnification. Ghalib (2000) was using the earlier generations of the VisCPT, which utilized significantly lower magnification cameras. As such, Ghalib was reporting *PPD* values for sands between 1 and 30 pixels; the *PPD* values reported with the third generation VisCPT prototype range between 10 and 500 pixels Therefore, the correlation Ghalib (2000) reported between Energy and *PPD* is not appropriate for the larger *PPD*s shown in Fig. 5.10.

With the exception of Energy, four of the textural indices in the Haralick SGLDM image analysis method from this VisCPT calibration work were shown as promising methods for

determining soil particle sizes from the silt range to medium sand. Using these four indices (as well as potentially the HWT-based analysis method in Section 5.4.2), the Haralick SGLDM will be used with the third generation VisCPT (Fig. 5.5) in an upcoming calibration chamber application. Formal correlations between these Haralick textural indices and *PPD* can also be established. Section 5.4.3 also explores the use of these indices for testing other soils beyond 2NS.

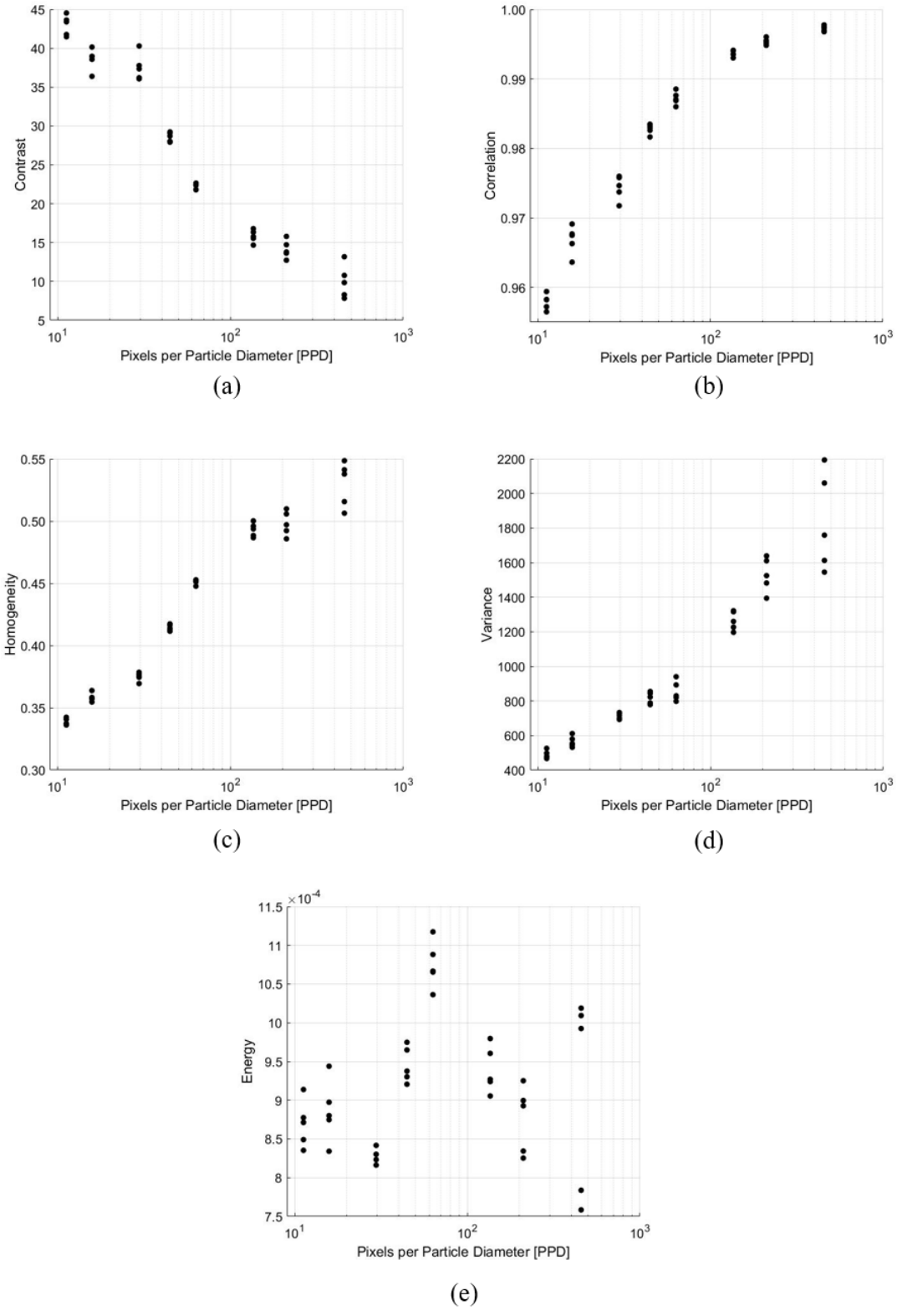

*Figure 5-10. Haralick textural indices versus Pixels per Particle Diameter (*PPD*) as part of the VisCPT benchtop calibration testing for 2NS sand. (a) Contrast, (b) Correlation, (c) Homogeneity, (d) Variance, (e) Energy.*

5.4.2 HWT-based image analysis of VisCPT images

The increased camera resolution of the third generation VisCPT prototype enabled an opportunity to analyze VisCPT images using the Haar Wavelet Transform (HWT)-based method. Already proven as a powerful analysis tool when paired with SedImaging (Chapters 3 and 4), the HWT-based method may yield similar success when used with this VisCPT. The HWT-based results may be used to supplement, refine, or confirm those from the Haralick SGLDM textural indices. The HWT-based method may also be useful in delineating between different soil types tested with the VisCPT. The foundational research for this was part of the calibration work performed with the VisCPT prototype.

The same 40 images used to compute the Haralick textural indices in Section 5.4.1 and Fig. 5.10 were also analyzed with the HWT-based analysis method. The 40 wavelet indices, *CA*, (defined in Section 4.1) are plotted versus the soil particles' known midpoint *PPD*s in Fig. 5.11. For each image, the entire 2048 x 2048 pix^2 image was used as a single HWT analysis area (i.e. smaller 1024 x 1024 pix^2, or 512 x 512 pix^2 etc. analysis areas were not part of this investigation). There is a well-defined positive correlation between *CA* and *PPD*. A best-fit line ($R^2 = 0.933$) for the data is

$$PPD = 10^{\left(\frac{CA}{2.2} - 1\right)} \tag{5.1}$$

Equation 5.1 is plotted in Fig. 5.11 as a solid red line. For comparison, the updated *PPD-CA* equation used with SedImaging and the Sed360 (Eq. 4.5) is also plotted in the figure, as a dashed black line.

As seen in Fig. 5.11, despite both being empirically-fitted equations for 2NS and analyzed by the same HWT-based method, Eqs. 5.1 and 4.5 are not identical. Initially the cause of this

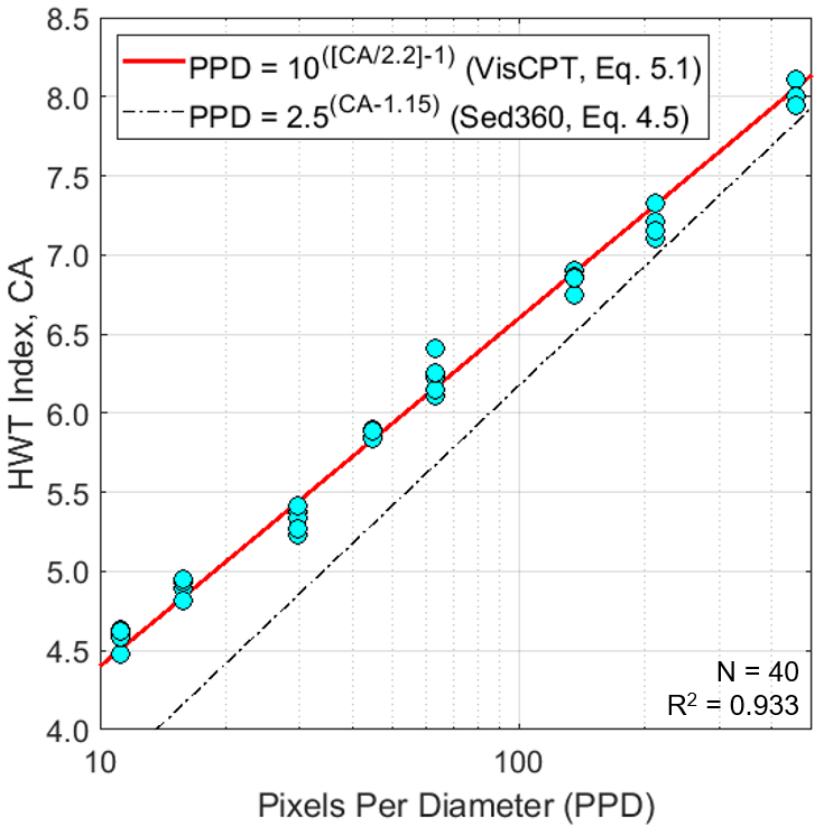

Figure 5-11. CA *versus* PPD *for 2NS particles photographed with the VisCPT prototype.*

discrepancy was thought to involve the environmental differences between VisCPT (Eq. 5.1) and Sed360 (Eq. 4.5) images. Though these effects do impact the two calibration equations, they do so minimally and do not fully explain the equation differences. The larger source of this difference is an intriguing new discovery of the HWT-based analysis method and will be explored further in future research (Section 6.2).

The 2NS particles photographed with the VisCPT prototype are dry, while those in the Sed360 are saturated. The VisCPT particles are illuminated by the system's direct, LED illumination board, while those in the Sed360 are illuminated by overhead fluorescent laboratory lights. As such, the same soil particle photographed in these lighting systems *would* have two

different grayscale pixel intensity distributions across its surface. The particle orientation for the Sed360 and the benchtop VisCPT testing may also be distinct.

While these environmental differences do affect the pixel grayscale intensity distributions of the 2NS images, they do not fully account for the difference between Eqs. 5.1 and 4.5. The larger source of the difference relates to the two systems' camera magnifications. The VisCPT images have a magnification (246.6pix/mm) that is over five times larger than those captured with the Sed360 (49.1pix/mm). To determine the impact of these different magnifications on the *CA-PPD* data, the VisCPT images were downscaled to more closely match the Sed360 magnification. The VisCPT *PPD* values were adjusted and the *CA* values recalculated. The adjusted VisCPT 2NS data is plotted in Fig. 5.12 as yellow triangle data points. The original VisCPT data, as well as Eqs. 5.1 and 4.5 are plotted again in Fig. 5.12. The adjusted VisCPT data falls very close to the Sed360 *PPD-CA* piecewise calibration curve. The differences between the adjusted VisCPT data in Fig. 5.12 and Eq. 4.5 are now possibly due to the aforementioned environmental differences between VisCPT and SedImaging image capture.

The results in Fig. 5.12 are revelatory. They show that the HWT-based analysis method, specifically *CA*, is a function of camera magnification. This discovery was only possible by analyzing VisCPT images using the HWT-based method. Previous to this, only SedImaging soil images were analyzed. Between the three SedImaging systems, camera magnification has changed very little (between 10 and 30pix/mm). Therefore, any effects of the different SedImaging magnifications on *CA* values were less detectable. Future research (Section 6.2) will be dedicated to investigating the relationship between *CA* and camera magnification. It may be possible to eliminate the need for Eqns. 4.5 and 5.1 and instead have a single *PPD-CA* equation that contains

an additional parameter that varies with camera magnification. This would streamline the adaptability of the HWT-based method for various cameras and testing systems.

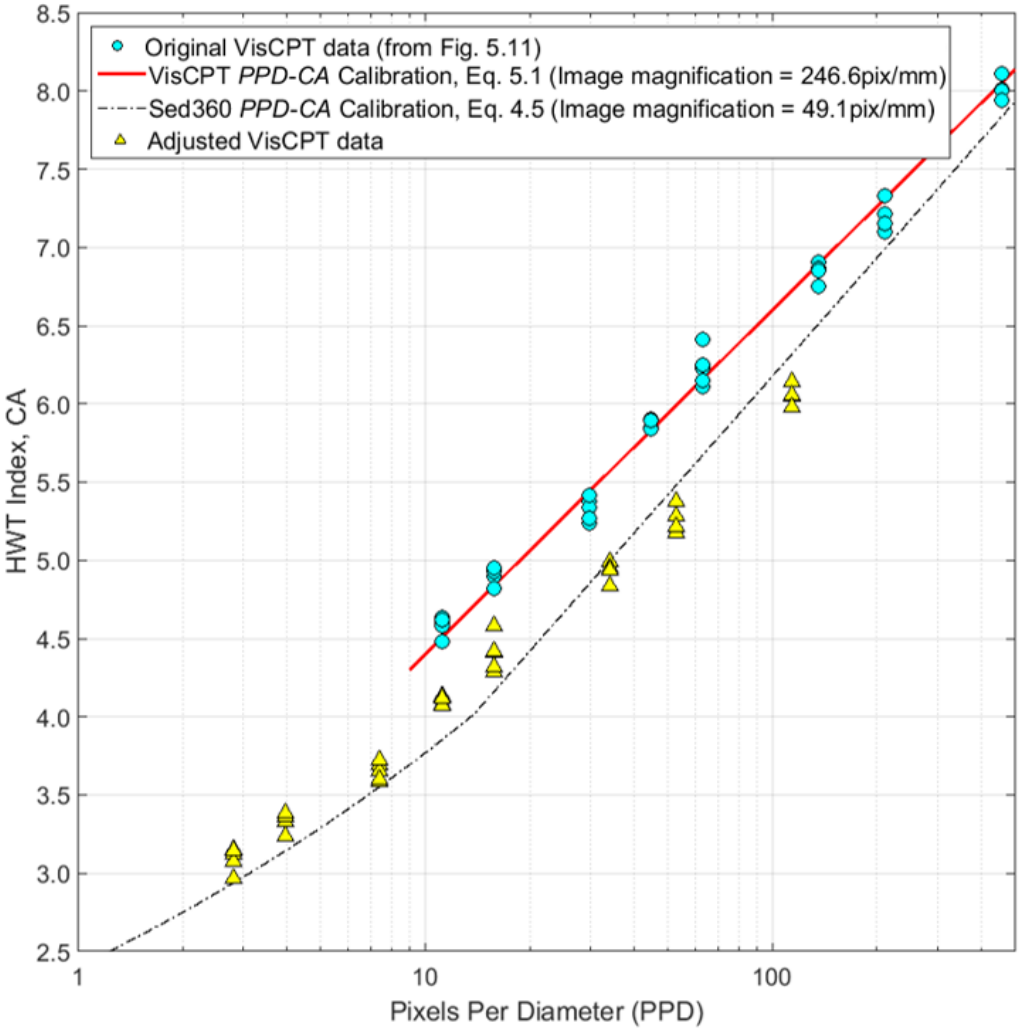

Figure 5-12. Adjusted VisCPT 2NS CA-PPD *data compared to the Sed360's Eq. 4.5.*

5.4.3 Soil differentiation by the SGLDM and HWT-based method

Well-defined trends between *CA* and *PPD* in Figs. 5.11 and 4.6, and the high coefficients of determinations (R^2) for both Eq. 5.1 (0.933) and Eq. 4.5 (0.993) support the use of the HWT-based method for determining soil particle size for both SedImaging and VisCPT images. The

strong trends between the Haralick textural indices and *PPD* presented in Fig. 5.10 are similarly promising. However both investigations have been constricted to 2NS (or similarly-looking) sand.

Thus, preliminary research has been conducted using the VisCPT prototype with the SGLDM and HWT-based analysis methods with the goal to differentiate and accurately characterize different soils beyond 2NS. Research will be conducted on how these two image analysis methods can be used concurrently or sequentially to characterize different soils, thereby widely expanding the application of these methods. Though this research with the prototype is only preliminary and requires additional calibration (potentially involving machine learning) the work that has already been conducted is still noteworthy, and is presented here. Lastly, though this research was performed using VisCPT images, the findings of this work can also be applied to SedImaging testing.

For this investigation, eight different dry soils (including 2NS from previous studies) were photographed with the VisCPT prototype. The soils contained particles of various sizes, colors, transparency, and shapes. The soils were sieved into narrow size ranges and photographed with the prototype under constant illumination and camera settings. Unlike the VisCPT images from Sections 5.4.1 and 5.4.2 which were only of 2NS particles, the illumination here was lowered to 4.0V. This was necessary to reduce image washout for the white-colored soils in this investigation.

There were nine sieve ranges, varying from medium sand retained between the No. 10 and No. 12 sieves (sieve openings 2.0mm to 1.7mm) down to silt material retained between the No. 270 and No. 400 sieves (sieve openings 0.053mm to 0.038mm). Figure 5.13 shows one of the 4208 x 3120 pix^2 VisCPT image for the eight different soils and their applicable sieve ranges. The known midpoint *PPD* value for each of the nine sieve size ranges is also included in the figure.

As seen in Fig. 5.13, 2NS contains soil particles in all of the sieve ranges, while the Nevada soil only contains fine sand particles. Costa Rica and Treasure Island soils contain fine sand and silt. The Upper Peninsula soil only contains silt material, Scotts Valley and Nesika Beach contains fine and medium sand, and Ottawa soil only contains medium sand particles. The Costa Rica sand contain mostly dark brown and black particles, and the Nesika Beach sand contains a more even mix of black and white particles. The Upper Peninsula and Treasure Island soils are similar to 2NS in their heterogeneous mix of soil colors, though the Upper Peninsula material has an overall slightly reddish hue to its particles. Lastly, Scotts Valley and Ottawa sands contain mostly white and translucent particles, while the Nevada contains nearly fully white, opaque particles. As a collection, the eight soils represent an expansive range of soil particle types.

For each of the soils and their sieved particle size ranges, four or five different images were captured by the prototype. Just like those in Fig. 5.9, 2048 x 2048 pix^2 images from a fixed region of the VisCPT viewing window with uniform illumination were used from each photograph. These images were analyzed with the HWT-based image analysis method using a single 2048 x 2048 pix^2 analysis area. The computed *CA* values from the HWT-based method are plotted versus the known midpoint *PPD* values for all eight soils in Fig. 5.14.

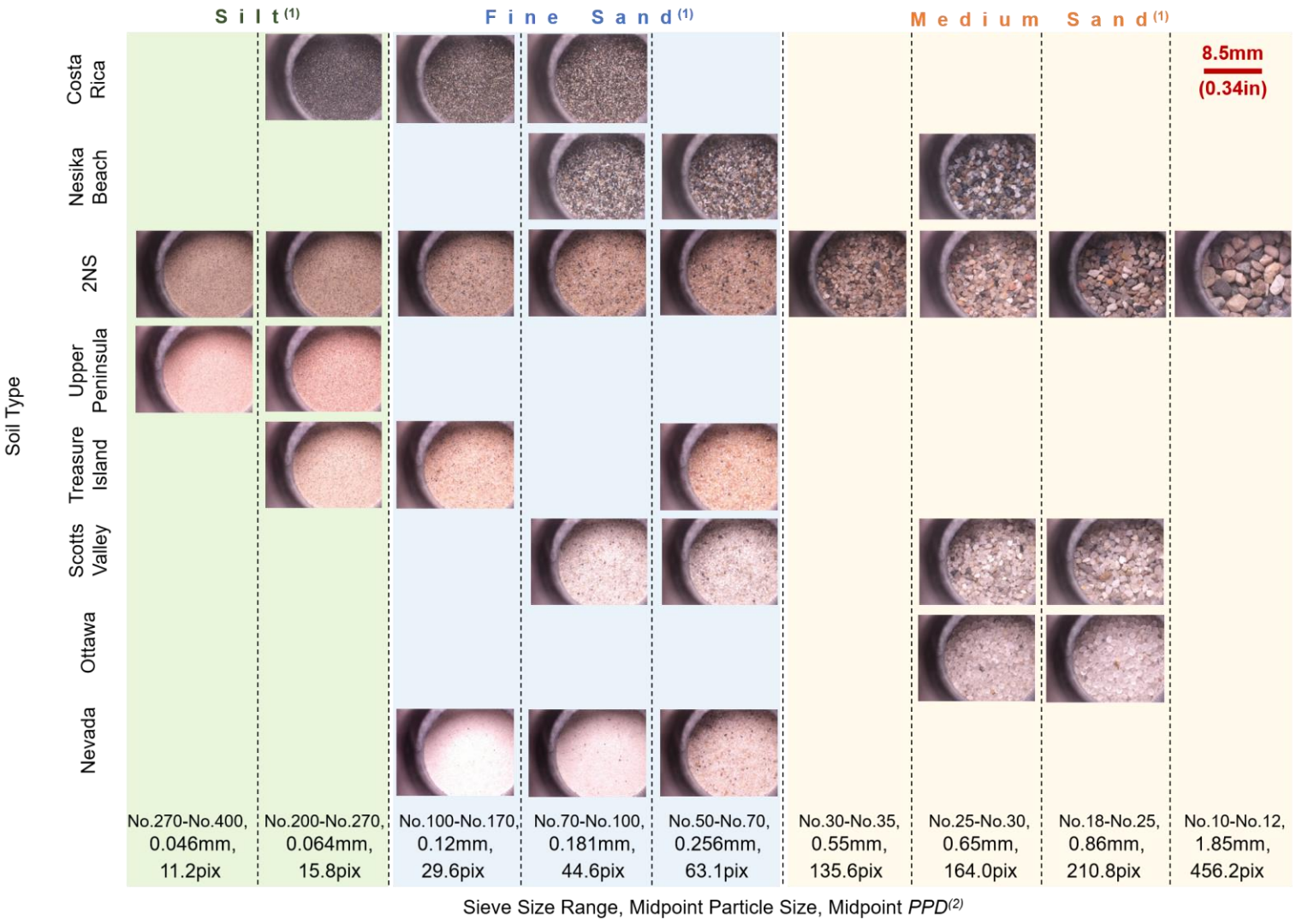

Figure 5-13. Testing different soils with the VisCPT prototype.

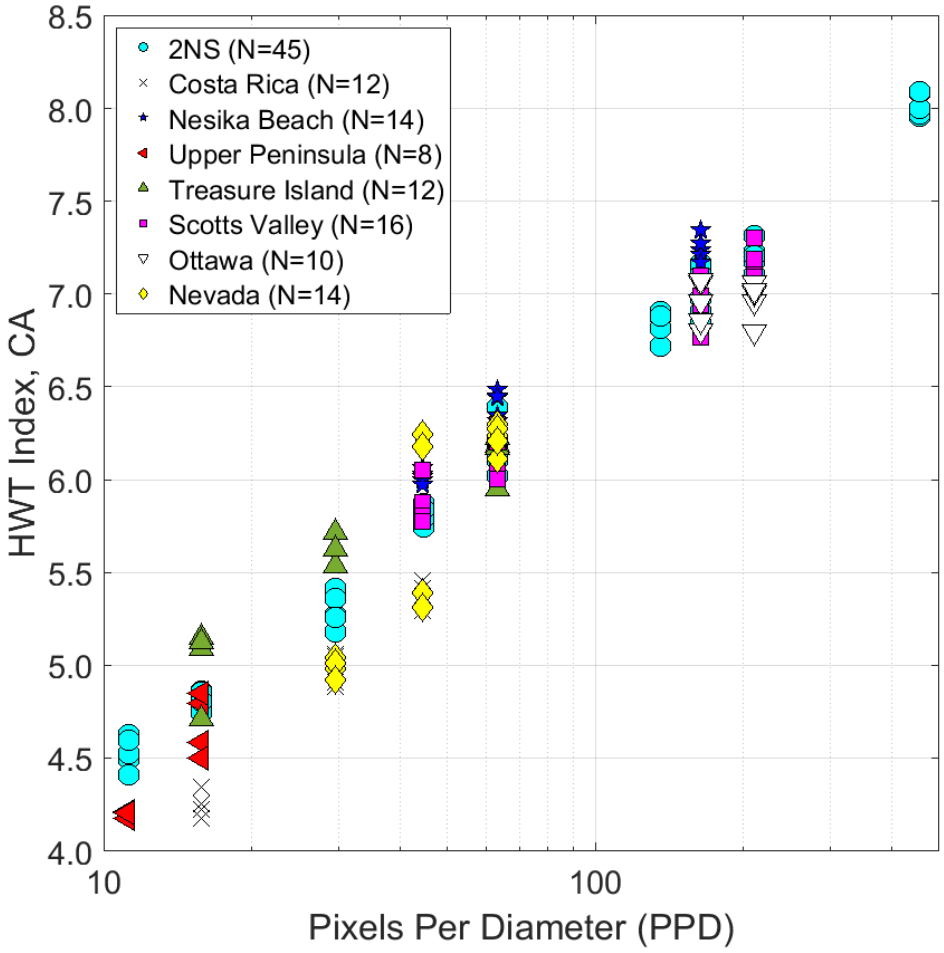

Figure 5-14. CA *versus* PPD *results for different soils tested with the VisCPT.*

All eight soils have a visible, direct *CA-PPD* trend. However, the empirical constants needed to fit these trend lines are different. An empirical best-fit line was calculated for each soil, except for the Upper Peninsula and Ottawa sands since those sands only contained two sieve size ranges of data. These best-fit lines (without the data points) are plotted in Fig. 5.15. The R^2 value for each of the soils' best-fit line is listed in the figure's legend. Appendix D includes separate figures for each of the eight soils (including the Upper Peninsular and Ottawa sands) that plot the *CA-PPD* data points with their corresponding best-fit trend line. The trend line for 2NS in Fig. 5.15 is different from (though virtually identical to) Eq. 5.1 for the 2NS data in Fig. 5.11 (Section

5.4.2). Though these sets of data are both dry 2NS particles, a different VisCPT illumination level was used for each (4.25V versus 4.0V). An additional particle size range (particles retained between the No. 25 and No. 30 sieves) was also added for this later work. Therefore, these two data sets of 2NS particles are independent from one another. Appendix E includes a plot comparing these near identical, yet independent data sets and trend lines of 2NS photographed at the two different illuminations.

With the exception of the Nevada sand, all of the trend lines in Fig. 5.15 have similar slopes, but at different heights in the *CA-PPD* space. Furthermore, 2NS, Treasure Island, and Scotts Valley sands have nearly identical slopes and locations. As seen in the images in Fig. 5.13,

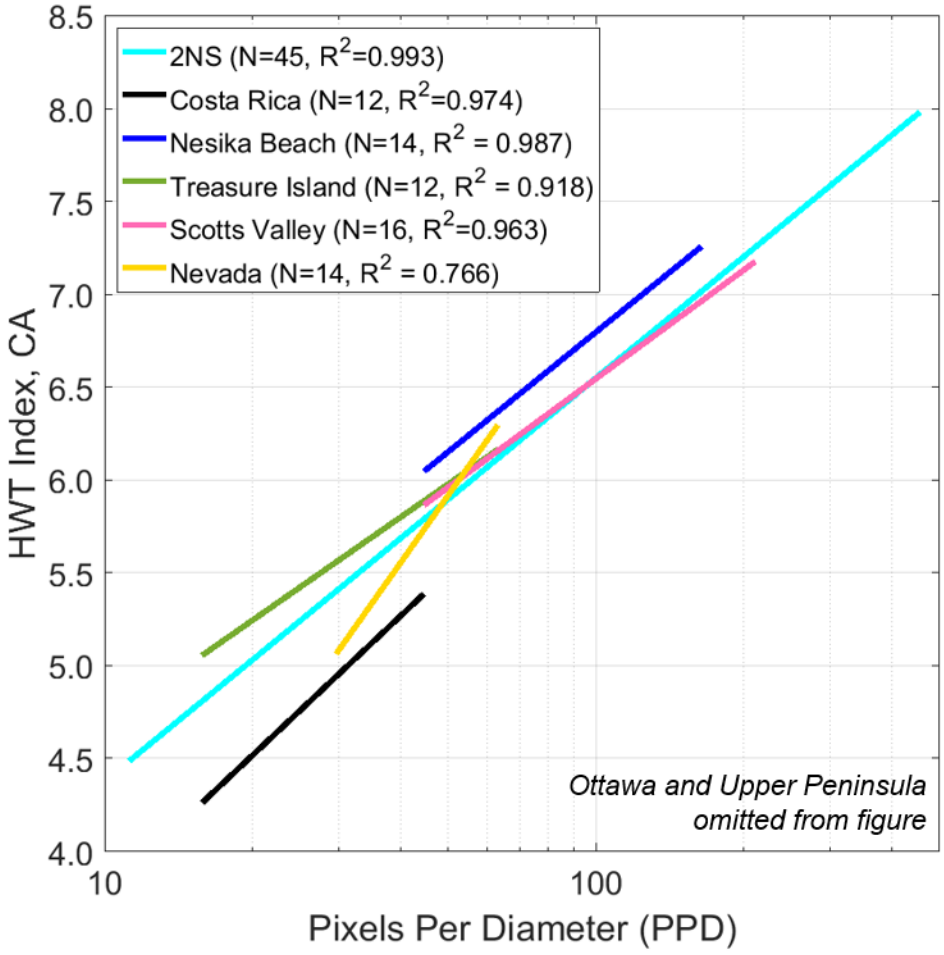

Figure 5-15. Empirical CA-PPD *trend lines of the soils from Figs. 5.13 and 5.14.*

a reassessment of Nevada sand photographed at an even lower illumination may be necessary since at the current 4.0V illumination, particle washout may still be occurring. This could explain this sand's unusually high slope in Fig. 5.14, and its low R^2 and unique best-fit line in Fig. 5.15. Future research will explore the reevaluation of Nevada sand.

The Fig. 5.15 trend lines (barring Nevada sand) support a future approach where instead of using a single *PPD-CA* equation like Eqs. 4.5 and 5.1, a family of *PPD-CA* equations can be available to determine the particle size(s) for a soil tested with either VisCPT or SedImaging. The specific *PPD-CA* equation would be selected for a given soil based upon some identifier. The

identifier could be something as simple as the average grayscale value of an image of that soil. More likely, the identifier (or identifiers) would be more complex, such as one (or more) of the Haralick textural indices discussed in Sections 5.3 and 5.4.1. To this final point, the same 2048 x 2048 pix^2 images of the eight soils in Fig. 5.13 were analyzed by the SGLDM.

Figures 5.16 through 5.20 plot the results of the same five Haralick textural indices from Section 5.4.1 for the eight different soils. The indices are plotted versus the known midpoint *PPD* value for each image. The data in these figures continue to be analyzed and will be part of ongoing research (Section 6.2), yet initial observations yield some promising avenues of investigations.

As a hypothetical example, Section 5.4.1 notes that the Energy index (Fig. 5.20) did not appear to have any discernable direct or indirect trend with the *PPD*s for 2NS. Additionally, 2NS, Treasure Island, and Scotts Valley soils (the same three soils with the most similar best-fit *CA-PPD* lines in Fig. 5.15) all have Energy values that are consistently localized near 10^{-3}, regardless of *PPD*. The remaining soils' Energy values do not always lie so close to 10^{-3}, if at all (e.g. Ottawa, Costa Rica, and Nevada). If an unknown soil was photographed using either VisCPT or

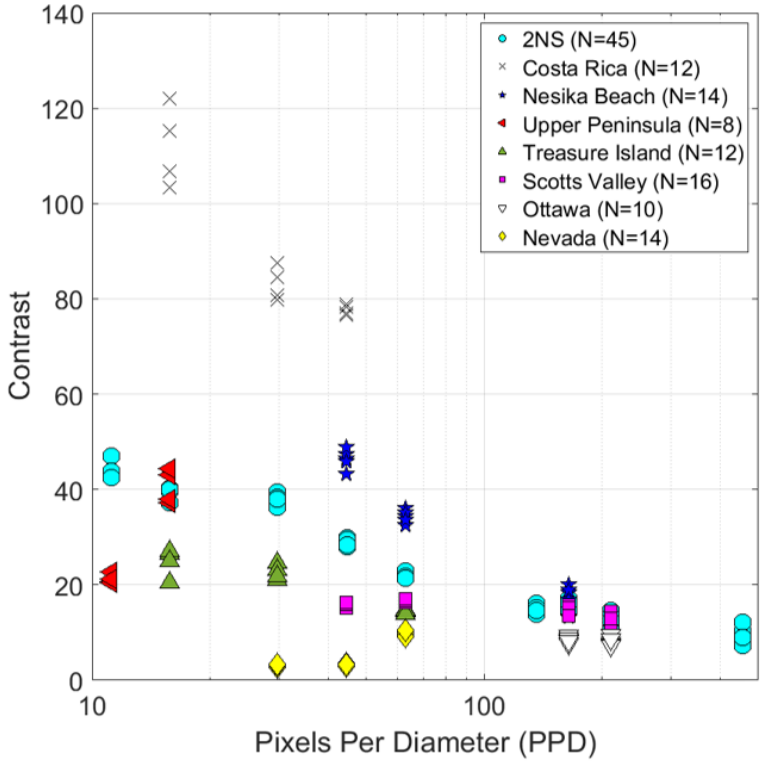

Figure 5-16. Contrast vs. PPD *for various soils.*

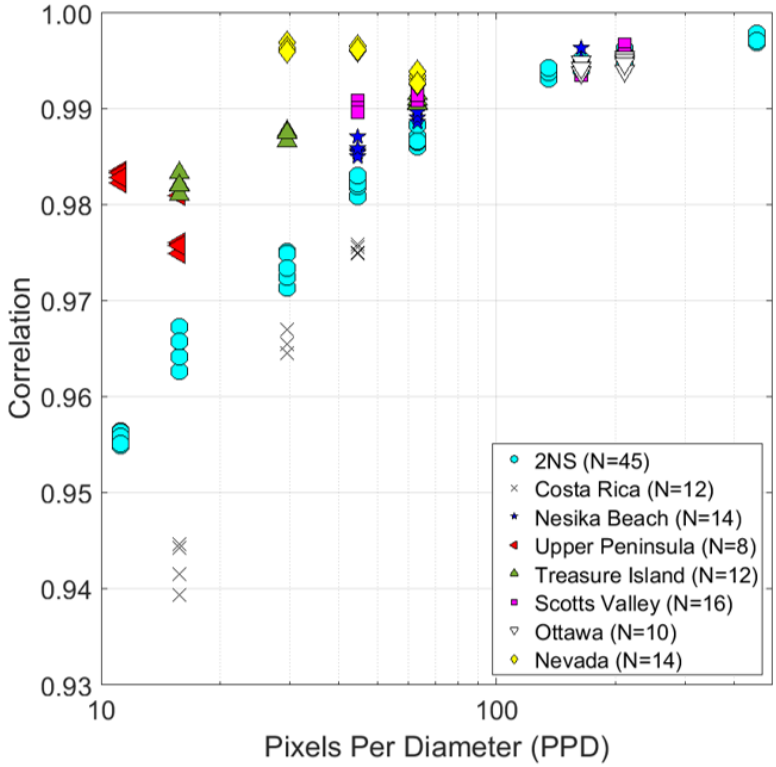

Figure 5-17. Correlation vs. PPD *for various soils.*

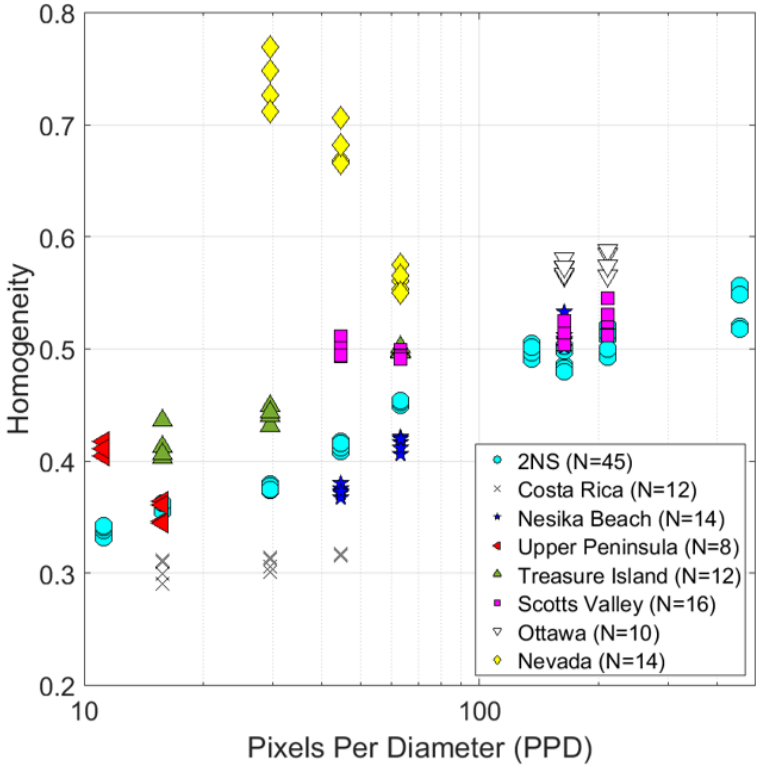

Figure 5-18. Homogeneity vs. PPD *for various soils.*

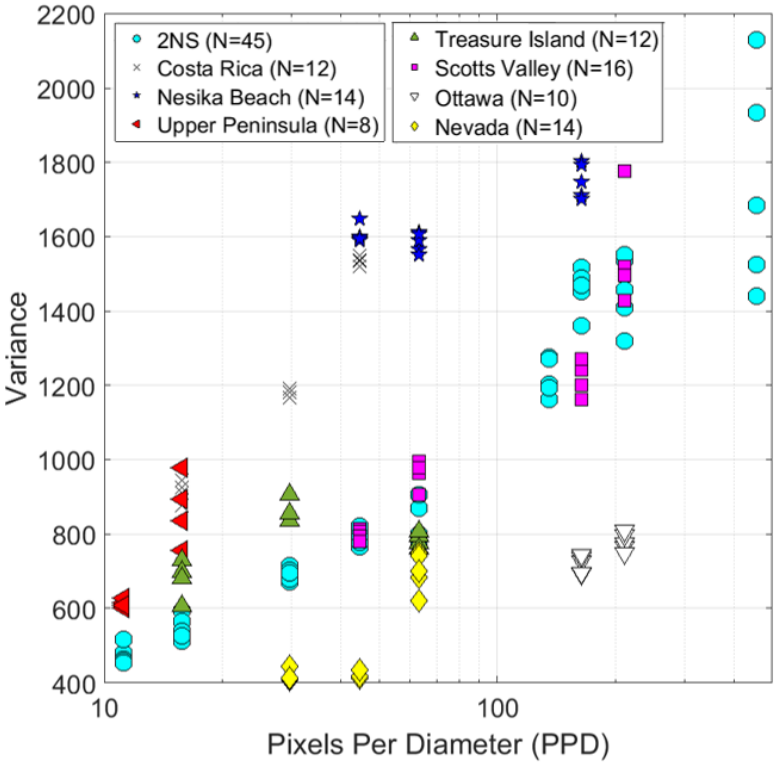

Figure 5-19. Variance vs. PPD *for various soils.*

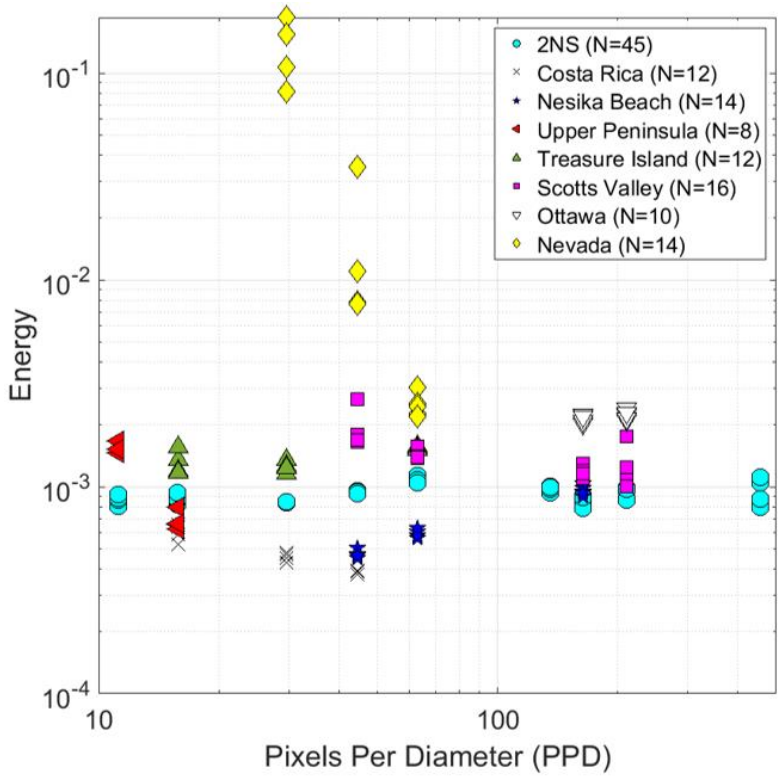

Figure 5-20. Energy vs. PPD *for various soils.*

SedImaging, and its Haralick textural Energy index was 10^{-3}, then the soil may possibly be similar in composition to 2NS, Treasure Island, or Scotts Valley sands. Therefore, the specific *PPD-CA* equation that was fitted for these three calibration soils could then be applied to the example unknown soil, to yield an accurate soil PSD.

Though formally unsubstantiated, this example illustrates the ongoing work of using the HWT-based analysis method in conjunction with the SGLDM textural indices to further expand the application and accuracy of both the VisCPT and SedImaging systems. Section 6.2 details the implications of such research with greater impact.

5.5 Chapter Summary

Chapter 5 detailed the hardware advancements of the VisCPT, as well as the image analysis methods used with this system. The first and second generation VisCPTs were shown in Fig. 5.1. The prototype of the third generation was fabricated by ConeTec Investigations Ltd. in 2019 and was shown in Fig. 5.2 within Section 5.2.1. Later, the third generation VisCPT (Figs. 5.5 and 5.6) was constructed in 2022 and was discussed in Section 5.2.2. This device will be used in upcoming calibration chamber testing (Section 6.2). The focus of Section 5.3 was the image analysis that was historically the main method to characterize soils photographed by the earlier VisCPTs. This approach uses several of the textural indices from the Spatial Gray Level Dependence Method (SGLDM) proposed by Haralick et al. (1973). Using these textural indices, the VisCPT can detect thin soil layers that are often missed in CPT soil profiles. Figure 5.8 showed an example soil profile illustrating this.

Section 5.4 discussed the benchtop calibration testing performed with the third generation VisCPT prototype. This testing consisted of several parts. In Section 5.4.1, narrow particle size ranges of the same sand were photographed by the prototype VisCPT. Information for all of the size ranges was included in Table 5.1, and sample images of each size range were shown in Fig. 5.9. These images were analyzed by five of the Haralick textural indices and plotted in Fig. 5.10. Several of the indices were shown to be promising methods for determining soil particle sizes from the silt range to medium sand.

The second benchtop research area was presented in Section 5.4.2. It involved analyzing the same soil images from Section 5.4.1, but now using the HWT-based method. This research revealed several conclusions, the most unexpected being that the *PPD-CA* calibration is a function of camera magnification. This topic will be prioritized in future research.

The final focus area involving the VisCPT prototype was detailed in Section 5.4.3. Eight different soils with various particle size ranges were photographed using the VisCPT. Example images of the soils were included in Fig. 5.13. These images were analyzed with both the Haralick textural indices and the HWT-based method. The goal of this exploratory research is to see how these two image analysis methods can be used together to delineate different soil types. If successful, this could be applied to VisCPT and SedImaging to broaden the applications of both systems in the future.

Chapter 6 Summary and Future Recommendations

Sieving is the traditional method of determining a coarse-grained soil's particle size distribution (PSD). A PSD is used to classify a soil and provide an initial estimate for soil properties and behaviors. As such, sieving is a laboratory procedure widely used throughout civil and environmental engineering, earth sciences, and related industries. Despite its broad application, sieving is not without its disadvantages. Sieving has been well documented as time- and energy-intensive, disruptive, and costly.

In response, image-based soil analysis methods have been developed as alternatives to sieving. These methods are repeatable, rapid, clean, non-disruptive, and often low-cost and semi- or fully-automated. One of these methods was developed by Ohm and Hryciw (2014) and is called SedImaging. To determine a sand's PSD using SedImaging, a soil specimen sediments through a column of water. The soil particles will naturally sort by size, with larger soil particles sedimenting through the water faster than finer particles. Therefore the sedimented soil assembly that settles at the base of the water column is sorted by size: larger soil particles at the base of the assembly and finer soil settling overtop. Once fully sedimented, the soil assembly is photographed. The image is analyzed using a method based on the Haar (1910) mathematical Wavelet Transform (HWT). In this image analysis, a sieve-defined calibration is used to generate the soil's PSD. The original SedImaging system developed by Ohm and Hryciw (2014) holds many benefits over sieving (Ohm et al. 2013 and Chapter 3 of this dissertation). However the original SedImaging system also has its own limitations, namely the system's limited range of testable soil particle sizes, its non-portability, and its non-automated testing procedure. As a result, the author created two newer

SedImaging systems, the FieldSed and the Sed360. These two systems hold the same benefits as the original SedImaging system over sieving, as well as their own additional benefits (Table 1.2 and Chapter 3). These added advantages of FieldSed and Sed360 have cemented SedImaging as a rapid and accurate alternative to sieving for a wide range of coarse-grained materials.

SedImaging and its HWT-based image analysis method is one of the two main research areas detailed in this body of work. Sections 6.1.1 and 6.1.3 summarize the conclusions, significance, and broader impacts of the dissertation research involving SedImaging. Section 6.2 provides recommendations for future work using SedImaging and the HWT-based analysis method.

***

Image-based soil analysis methods can also enhance the capabilities of existing soil characterization systems (rather than simply replacing them). An example of this is the Vision Cone Penetrometer (VisCPT), the second main research area of this dissertation. The VisCPT equips a traditional cone penetrometer (CPT) with camera(s) that capture video and images of in-situ soil as the CPT is advancing through a soil profile. In doing so, the VisCPT refines CPT results and even detects thin (several centimeters thick) soil layers that are undetected in CPT boring logs. This thin layer soil detection is particularly useful when these layers are liquefiable soils in an earthquake-prone site (Section 6.2). Up until the research in this dissertation, VisCPT soil images were mainly analyzed using several of the textural indices from the Spatial Gray Level Dependence Method (SGLDM) proposed by Haralick et al. (1973). These textural indices were used to delineate soil layers. This dissertation documents research using the third generation VisCPT. Part of this involved also analyzing VisCPT images using the HWT-based analysis method from SedImaging. Through this research, the possibility of combining the results of the HWT and

Haralick textural indices to analyze a wide range of soil types both ex-situ with SedImaging and in-situ with the VisCPT is explored. If successful, this would dramatically expand the applications of these two systems. This VisCPT work using the HWT-based method also revealed a new discovery regarding the impact of camera magnification on the HWT method's sieve-defined calibration equation. The HWT's *CA-PPD* equation was found to be a function of camera magnification. The equation will be readjusted to consider this dependency. This realization is crucial to all future image analysis work for both the VisCPT and SedImaging. Sections 6.1.2 and 6.1.3 summarize the conclusions, significance, and broader impacts of the current VisCPT research, while Section 6.2 discusses recommendations for future research with this system.

6.1 Summary

This section lists the main milestones and conclusions of this dissertation for both SedImaging (Section 6.1.1), the VisCPT (Section 6.1.2), and their image analysis methods. Section 6.1.3 underscores the importance and broader impacts of the research of this dissertation on the wider field of soil characterization in civil engineering and related disciplines.

6.1.1 Summarizing SedImaging research

- A field-portable SedImaging system known as "FieldSed" was developed in 2017. It uses smaller and more transportable equipment than the original SedImaging system (referred to throughout this dissertation as "LabSed"). FieldSed is nearly identical in operation to LabSed, with several exceptions. Unlike LabSed, which is made of aluminum hardware, FieldSed uses low-cost and lightweight acrylic hardware, allowing for simultaneous parallel testing of many soil specimens. With FieldSed, four different images of the settled soil specimen are captured. This is possible because of the FieldSed's clear, square acrylic

sedimentation column (as opposed to LabSed's larger aluminum column). By capturing more images of the soil assembly with FieldSed than with LabSed, a larger percentage of the specimen is used in the image analysis to determine a soil's PSD. Additionally, smaller soil specimens can be tested in the FieldSed as compared to LabSed. The same HWT-based image analysis used with LabSed is also used with FieldSed. Therefore, the same strong agreement between LabSed and sieving PSDs is also present with the FieldSed. SedImaging via the FieldSed has the same advantages as does LabSed over sieving, but FieldSed has its own additional advantages over LabSed.

- Like LabSed, the range of testable soils for FieldSed is limited to fine and medium sands per the Unified Soil Classification System (USCS), or soil particle sizes between 0.075mm (standard US No. 200 sieve) and 2.0mm (standard US No. 10 sieve). In response to this limitation, a prewashing procedure was developed to use before testing a soil in the FieldSed. This procedure cleanly removes soil particles that fall outside of the testable size range for FieldSed. Without the need for oven drying, the procedure determines the percentage of a soil specimen that is coarser than the US No. 10 sieve, and perhaps more significantly, the percentage of fines (finer than the US No. 200 sieve). After testing in the FieldSed and analyzing the captured soil images, the soil's SedImaging-based PSD is adjusted for any material removed during the prewashing procedure. By determining a soil specimen's percentage of fines, the prewashing procedure expands FieldSed's range of testable soils beyond clean medium and fine sands. Lastly, even though the prewashing procedure was created with the FieldSed, the process can be used with any of the SedImaging systems.

- The FieldSed was used with the prewashing procedure as part of a large-scale soil characterization project along several miles of the state of Michigan's Kalamazoo River in 2017. Over 110 sands were tested in the FieldSed for this project. The FieldSed testing was conducted in a temporary field laboratory constructed next to the river. A small number of specimens were selected for quality control testing to determine the reproducibility of the SedImaging results. Sieve analyses were also performed to establish the accuracy of SedImaging via the FieldSed. The control test results demonstrated that the FieldSed is a promising portable device that can rapidly, accurately, and repeatedly determine PSDs in (nontraditional) field labs for geotechnical and geoenvironmental applications.

- A third SedImaging system was developed in 2020. Called "Sed360", this system replaced the square acrylic tubing of the FieldSed with circular cross-sectioned tubing. The circular tube sits atop a precision rotating stage. The stage rotates at a preset speed while a camera captures images of the settled sand specimen every four degrees. The collection of images are automatically stitched together to form a seamless "unwrapped cylinder" image of the tested soil specimen. This combined image is analyzed using the original HWT-based method to generate the soil's PSD. The rotation stage and image stitching of the Sed360 have, for the first time, nearly fully automated SedImaging, all while still yielding PSDs with excellent agreement to sieving results. Also for the first time with SedImaging, coarse sands are successfully tested in the Sed360. This expands the range of testable soil particles for SedImaging to encompass the entire sand range (according to the USCS, between US Standard sieves No. 4 [4.75mm] and No. 200 [0.075mm]).

- The expanded range of testable soils in the Sed360 necessitated a reexamination of the HWT-based image analysis method used with SedImaging. There were two key outcomes from this research. (1) The calibration equation used in the HWT-based analysis method was reformatted to reflect the expanded range of testable particle sizes. (2) While keeping the fundamentals of the HWT-based analysis, the method was extensively restructured to automatically adjust the procedure to the size of the soil particles that it is analyzing at any given point. These two advancements were crucial to ensure that the strong agreement between sieving and SedImaging results were maintained for the Sed360's expansion of testable soils. This restructured HWT-based method can also be used with the LabSed and FieldSed systems.

6.1.2 Summarizing VisCPT research

- In 2019 a prototype of the third generation VisCPT was fabricated by ConeTec Investigations Ltd. The prototype contains a 13 Megapixel UVC USB camera and an internal LED board for photographing and illuminating soil particles at the system's viewing window. The author conducted extensive benchtop calibration testing with the prototype. Part of this research focused on the original Haralick textural indices that were used with the first and second generation VisCPTs. It was shown that when using the high magnification camera and updated hardware of the newest VisCPT prototype, several of the Haralick textural indices are promising methods for determining soil particle size across the medium sand to silt range (as defined by the USCS).

- Another area of the benchtop research with the VisCPT prototype involved the HWT-based analysis method. Narrow particle size ranges of a glacio-fluvial material referred to as

"2NS" (MDOT 2010) were photographed using the VisCPT prototype and analyzed by the HWT-method which, until this research, was mostly used only with SedImaging. The results yielded a strong relationship between soil particle size and the HWT-method index "*CA*". However, the magnitude of this relationship is different from that determined for the same 2NS material when it was tested in the SedImaging systems. This led to the new discovery that camera magnification (which is several times greater in the VisCPT than in any of the SedImaging systems) is also a factor to be considered in the HWT-based grain sizing method. This factor can be quantified in future research (Section 6.2).

- The final focus of the benchtop testing of the VisCPT prototype involved photographing different soils. Eight soils, including 2NS, with particles of different sizes, colorings, translucencies, and shapes were photographed at a constant illumination by the VisCPT. The images were analyzed both by the HWT-based method and the Haralick textual indices. The goal of this preliminary research is to eventually use both of these analysis methods to differentiate and accurately characterize a breadth of soil types. If successful, this can strengthen the accuracy and widen the application of both the VisCPT and SedImaging systems. Section 6.2 mentions this as an area of future research.

- In 2022, ConeTec fabricated the finalized third generation VisCPT. It contains an 18 Megapixel USB3 camera with a redesigned illumination system. Images of several sands and one clay have been captured with the VisCPT. This VisCPT is primed to be used in upcoming calibration chamber testing. This testing is part of a larger project focused on thin liquefiable soil layer detection in earthquake-prone regions (Section 6.2).

6.1.3 Research Significance and Broader Impacts

The significance and broader impacts of the research discussed throughout this dissertation and are summarized here.

- Sieving is the traditional method of classifying coarse-grained materials in geotechnical engineering and related fields. However the disadvantages and limitations of the test have been well documented. Sieving is a non-automated, and time-, energy-, and noise-intensive test. In response, image-based soil characterization techniques are rapidly gaining popularity as low cost and rapid alternatives to sieving. One such method was developed by Ohm and Hryciw (2014) and is called SedImaging. The original SedImaging system had a number of powerful advantages over sieving: no noise pollution, rapid, and no need for oven-dried soil specimens prior to testing. SedImaging uses a sieve-defined calibration to generate particle size distributions (PSDs), thus there is excellent agreement between SedImaging and sieve-based PSDs. Yet the original SedImaging system was not without its own limitations. (1) The system's heavy hardware confined the system to a traditional laboratory setting, and (2) the method requires user-intervention throughout the testing procedure. Additionally, (3) the original SedImaging system was limited to classifying only medium and fine sands (as defined by the Unified Soil Classification System). The two newer SedImaging systems developed by the author, FieldSed (2017) and Sed360 (2020), were designed to help eliminate the limitations of the original SedImaging system, while still yielding excellent agreement with sieve results.

- The FieldSed is a portable system with lightweight hardware. Therefore, for the first time, SedImaging testing now extends beyond the traditional laboratory setting. The success of the FieldSed's adaptability was confirmed by its use in a 2017 large scale riverbed characterization project. The system was set up in a converted pole barn and was used to generate the PSDs of over one hundred river sediments. The converted barn was next to the river where sediments were being collected; by way of the FieldSed, the specimens were classified on site, directly after their removal from the river (i.e. the soils were not shipped to an off-site lab where they would be oven dried prior to sieving/testing). In addition to the FieldSed, a prewashing procedure was developed. Prewashing determines the percentage of material in the soil specimens that fall outside of the allowable SedImaging particle size range. The low-cost equipment of the FieldSed also enables parallel testing of multiple soil specimens. Combining FieldSed with the prewashing procedure and the parallel testing, PSD results of the riverbed sediments were generated in a fraction of the time and cost of traditional characterization methods like sieving. SedImaging has been proven to be an accurate alternative to sieving; with the introduction of the FieldSed, SedImaging is now also a portable, lightweight, and an even lower cost sieve alternative.

- Through the introduction of a rotating stage, SedImaging via the Sed360 is a nearly fully-automated soil characterization method. Unlike sieving (and even the previous SedImaging systems) Sed360 requires little user involvement throughout a test, thus increasing the testing efficiency of SedImaging. Automated image capture and image stitching make this possible with the Sed360. The new hardware of the Sed360 is still portable like FieldSed.

Additionally, the Sed360 hardware and the testing automation have now excitedly expanded the range of testable soils with SedImaging. For the first time, SedImaging via Sed360 can accurately characterize soil particles across the entire sand range. Combining this expanded testable size range with the prewashing procedure, SedImaging can now generate a PSD for all sands, as well as determine the percentage of gravel and fines in a sand specimen.

- Prior to this dissertation's research, SedImaging was shown to be an accurate alterative to sieving. However the system was limited in its portability, automation, and most significantly, its testable particle size range. Through the work within this dissertation, the FieldSed and Sed360 systems have powerfully transformed SedImaging into a portable, nearly fully-automated, yet still accurate soil characterization method that spans over two orders of magnitude of testable particle sizes. The applicability, approachability, and reliability of SedImaging have been broadened by the development of the FieldSed and Sed360. More broadly, by utilizing SedImaging over sieving as a soil characterization method, users can enjoy a cleaner and quieter testing environment, and the soil characterization process is more efficient, cheaper, and automated. Engineering firms can translate these time and cost savings into increasing their testing frequency, resulting in safer, more informed engineering designs.

- The Vision Cone Penetrometer (VisCPT) is an in-situ device that equips a CPT with a video camera to photograph the passing soil strata during probe advancement. These images are analyzed and used to identify thin soil layers (several centimeters thick) that are

missed by traditional CPT soil boring logs. Prior to the research within this dissertation, the most recent VisCPT device was developed in 2005. Smaller cameras with much greater resolutions motivated the fabrication of the third generation VisCPT by ConeTec Investigations Ltd. in 2022. Benchtop calibration testing with this third generation VisCPT was conducted. A variety of soil types and particle sizes where photographed by this VisCPT. The images were analyzed using both the original method from the earlier VisCPTs, as well as the method previously used with SedImaging. This benchtop calibration research will help finalize the image analysis procedure for the forthcoming VisCPT calibration chamber testing and in-situ testing. The VisCPT research also unexpectedly revealed a new, formerly unexplored detail of the SedImaging image analysis method. All future research with the SedImaging image analysis method will include this newly discovered detail.

- The third generation VisCPT combined with the image analysis benchtop testing rejuvenates the system as a potent full-scale in-situ soil characterization device of the future. The VisCPT will be used in earthquake prone regions to detect thin liquefiable layers missed by other in-situ soil characterization methods. By identifying these thin layers, soil improvement efforts for liquefaction mitigation or earthquake-resilient infrastructure can be more readily adopted, resulting in safer and healthier built environments.

6.2 Future Recommendations

There are several areas of suggested future research involving SedImaging, the VisCPT, and the image analysis methods used with these systems. Some of these recommendations are

based upon current or preliminary research detailed in this dissertation, while others are less explored, but are nevertheless intriguing.

- With SedImaging, a sand's percent of fines is estimated when the prewashing procedure is used prior to releasing the sand into the SedImaging water column. To estimate this, the fines are removed from the rest of the specimen. Future research can explore eliminating the need for the prewashing procedure. A specimen's fines would not be removed beforehand, and are instead also released into the SedImaging system and analyzed alongside the rest of the particles. The percentage of fines would also be characterized by image analysis. A second higher magnification camera (such as the one used in the third generation VisCPT) can be added to the SedImaging hardware to photograph the fines. Unlike the existing SedImaging camera, this second camera's field of view would be limited to only a few millimeters near the top of the soil assembly. Using this camera, the volume of fines in the soil assembly could be determined. A soil's fines percentage could also be calculated without the use of image analysis. Instead, the SedImaging hardware could be equipped with additional testing devices, such as pressure transducers or capacitive sensors, which can be calibrated to estimate the amount of fines in a soil specimen within the SedImaging water column.

- If it becomes possible to determine a soil's percentage of fines within the SedImaging system, then the functionality of the SedImaging presorter tube ought to be reexamined. It may be possible to even fully eliminate the presorter tube and redesign the SedImaging sedimentation column to provide a way to break up soil clods prior to photographing a soil

assembly. Without the need for the presorter, SedImaging testing time would be reduced even further, and the system would take another step towards becoming a fully automated soil characterization procedure.

- Soils with different particle colors, angularities, reflectivity, and opacities can be tested more extensively by SedImaging. Similar to the preliminary conclusions after testing eight soils with the VisCPT (Section 5.4.3), creating a family of SedImaging calibration curves for different soil types will further broaden the application of this system. Figure 6.1 shows the "unwrapped" images of three different soils tested in the Sed360. Figure 6.1(a) is a poorly-graded mono-colored sand from Brady, Texas; Fig. 6.1(b) is Ottawa sand, and Fig. 6.1(c) is from Nesika Beach, Oregon. The soils in Figs. 6.1(b) and 6.1(c) were also part of the Section 5.4.3 work with the VisCPT. Unlike those in Fig. 5.13, in Fig. 6.1 these soils are not separated into narrow particle size ranges. These three soils are visually quite different from 2NS (and similar soils) that has been extensively (and successfully) tested with SedImaging.

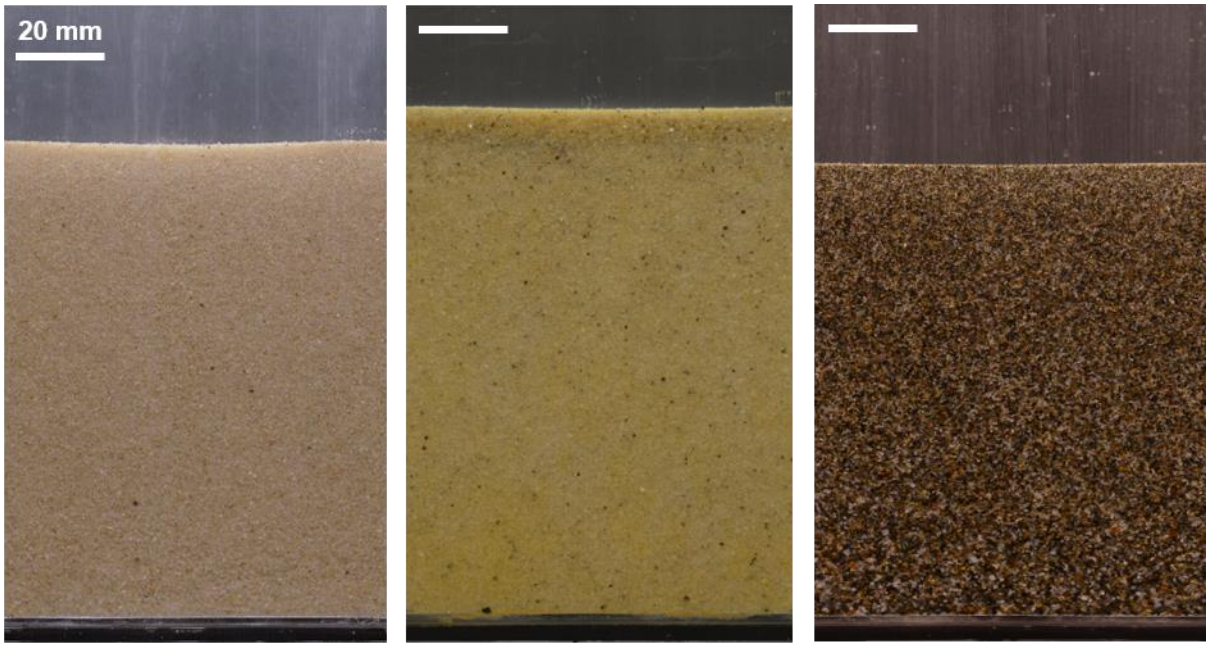

Figure 6-1. Different sands tested in the Sed360. (a) Brady, Texas, (b) Ottawa, and (c) Nesika Beach.

Calibrating SedImaging's HWT-based analysis method used 2NS soil images. Therefore using the existing HWT-based calibration equation (Eq. 4.5) to characterize a soil that is as visually unlike 2NS as those in Fig. 6.1 would be erroneous. To illustrate this, the three sands in Fig. 6.1 were analyzed by the HWT-based method using Eq. 4.5. The PSD results are plotted as yellow data points alongside sieve data (ASTM C136/C136M-19) for the three sands. The results for the Brady sand are in Fig. 6.2, Ottawa is presented in Fig. 6.3, and Nesika Beach in Fig. 6.4. As anticipated, the SedImaging PSD does not align with the sieve data for any of the sands. Using Eq. 4.5 for these sands yields incorrect PSDs. Out of the three, the PSD for the Nesika Beach sand, which is the closest in particle coloring to 2NS, is nearest to the sieve results.

The HWT-based analysis method was performed again for these three soils. This time, the numerical constants in Eq. 4.5 were adjusted until the soil's SedImaging PSD more closely matched the sieve data. These better-fitting PSDs are plotted as cyan triangle data sets in Figs. 6.2 through 6.4. This fitting method is purely for illustration purposes, and these new constants for the calibration equations should not be used for research purposes. However in this example, the Brady and Ottawa sands use the same adjusted equation constants, while Nesika Beach's calibration equation is the most similar to Eq. 4.5. As seen in Fig. 6.1, Brady and Ottawa sands both contain highly uniform, round, translucent particles, which explains why these two sands would have similar, if not identical, SedImaging calibration equations. Though the results in Figs. 6.2 through 6.4 are unverified examples, they highlight the necessity of creating a family of HWT calibration curves to accurately analyze different soil types by SedImaging. 2NS was specifically selected as the soil to calibrate the existing HWT-based method because of this material's common coloring and grading that is seen in many other soils. Yet as Figs. 5.13 and 6.1 show, there exists soils of other colors, angularities, and opacities.

Creating a procedure (perhaps involving machine learning) that selects a specific calibration curve for a soil specimen to yield the most accurate PSD would be transformative for SedImaging.

Lastly, gap-graded and other uniquely-graded soils can also be tested more deeply with the Sed360 beyond the investigation in Section 4.2.3 and presented in Figs. 4.12(b) and 4.14.

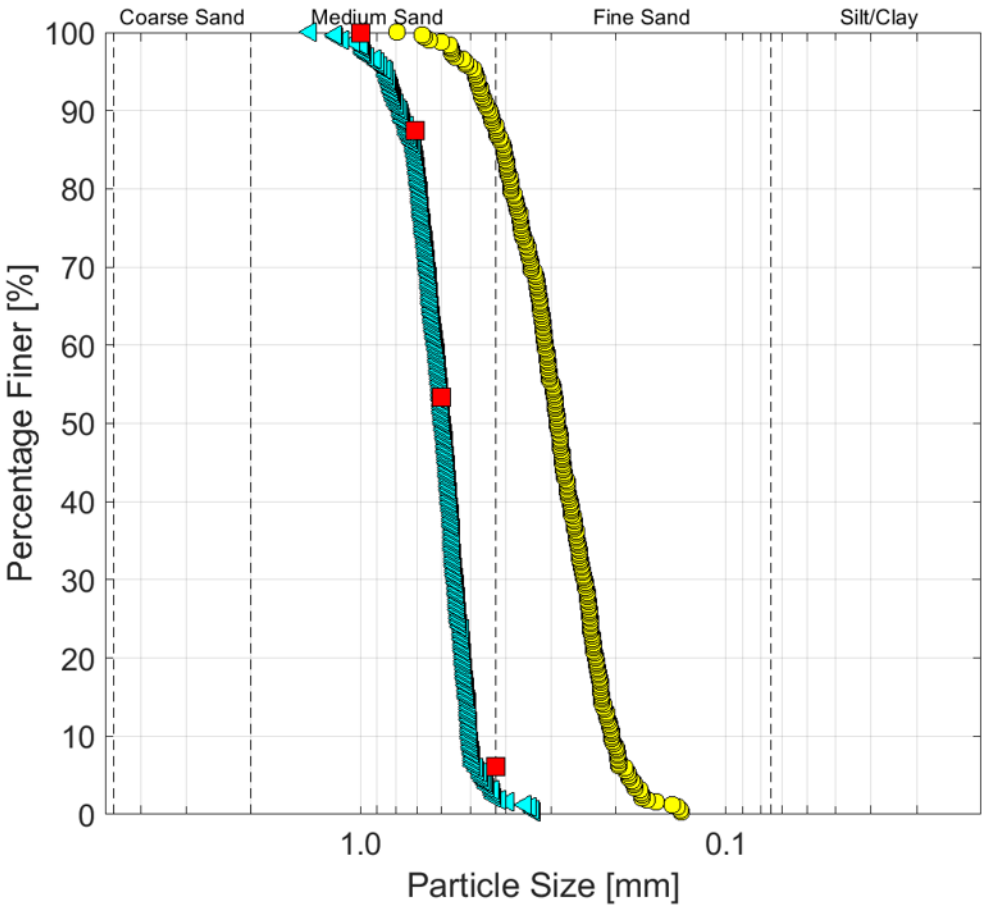

Sieve

SedImaging using current HWT calibration equation (Eq. 4.5):

$$PPD = \begin{cases} \left(\frac{CA}{2.4}\right)^{5.1} & if\ CA \leq 4.0 \\ 2.5^{(CA-1.15)} & if\ CA > 4.0 \end{cases}$$

SedImaging using better-fitted HWT calibration equation:

$$PPD = \begin{cases} \left(\frac{CA}{2.0}\right)^{5.1} & if\ CA \leq 4.0 \\ 2.45^{(CA-0.45)} & if\ CA > 4.0 \end{cases}$$

Figure 6-2. Example SedImaging PSD results for the Brady, Texas, sand in Fig. 6.1.

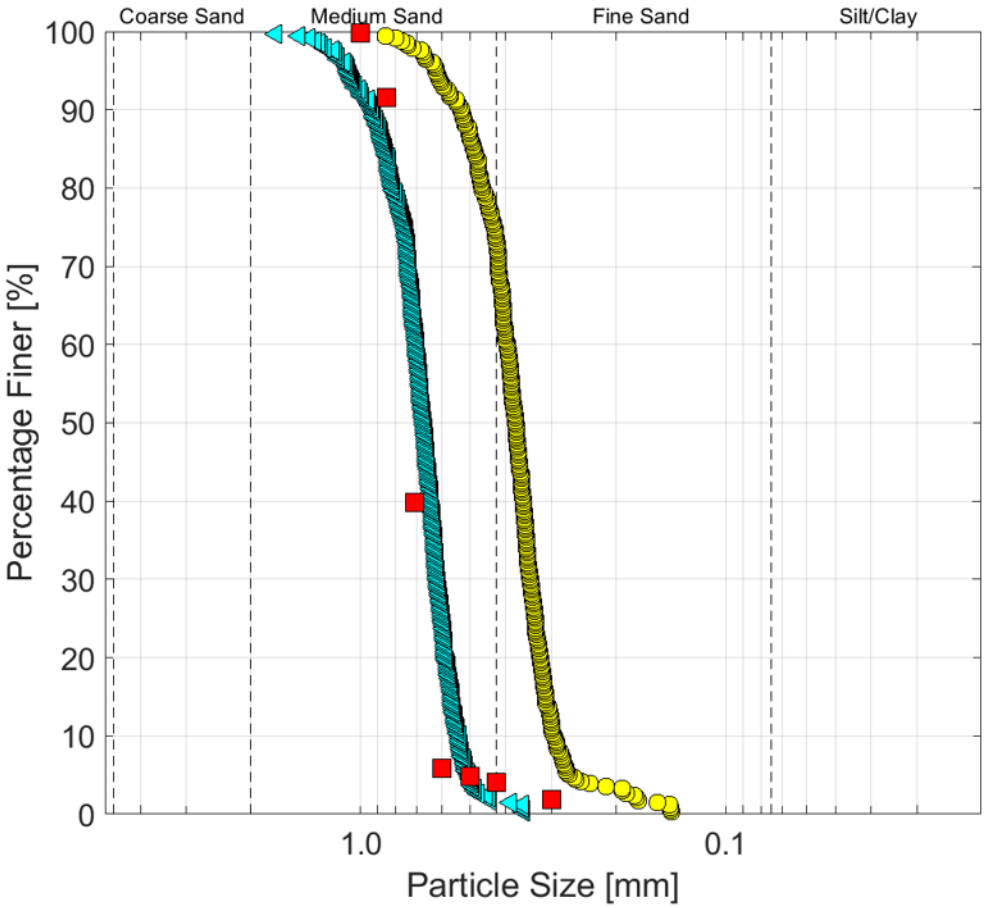

Sieve

SedImaging using current HWT calibration equation (Eq. 4.5):

$$PPD = \begin{cases} \left(\frac{CA}{2.4}\right)^{5.1} & if\ CA \leq 4.0 \\ 2.5^{(CA-1.15)} & if\ CA > 4.0 \end{cases}$$

SedImaging using better-fitted HWT calibration equation:

$$PPD = \begin{cases} \left(\frac{CA}{2.0}\right)^{5.1} & if\ CA \leq 4.0 \\ 2.45^{(CA-0.45)} & if\ CA > 4.0 \end{cases}$$

Figure 6-3. Example SedImaging PSD results for the Ottawa sand in Fig. 6.1.

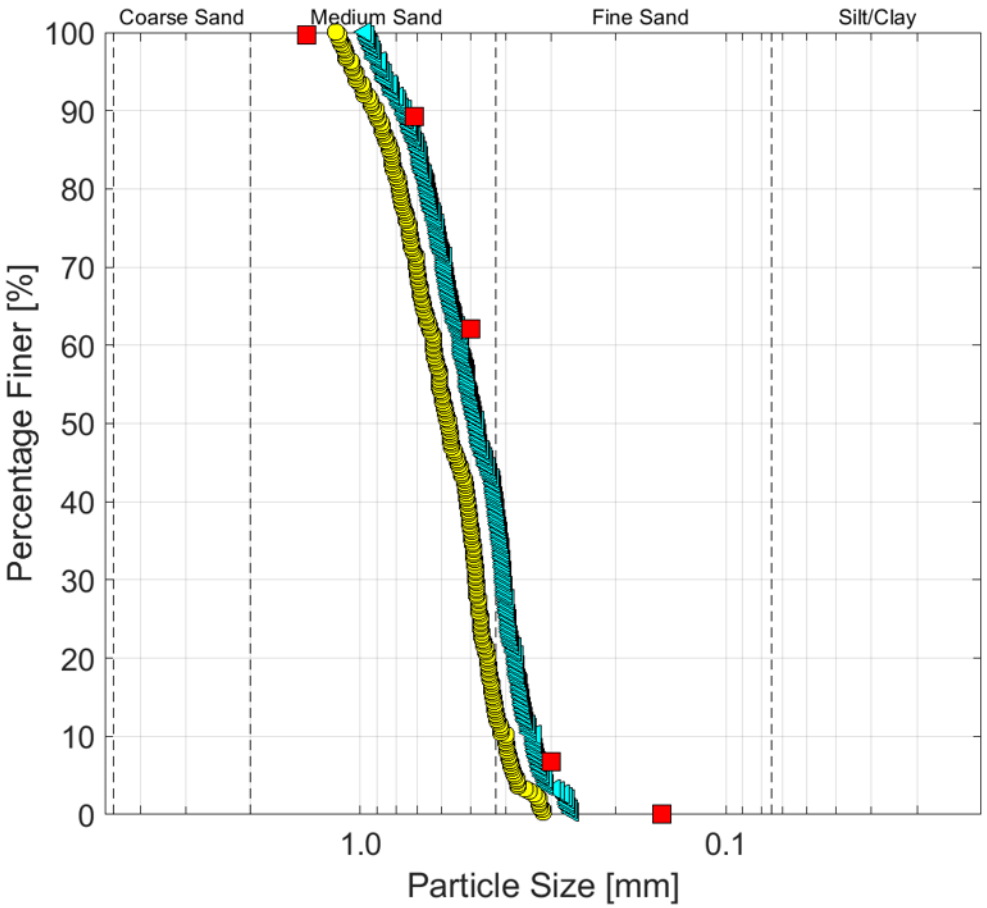

Sieve

SedImaging using current HWT calibration equation (Eq. 4.5):

$$PPD = \begin{cases} \left(\frac{CA}{2.4}\right)^{5.1} & if\ CA \leq 4.0 \\ 2.5^{(CA-1.15)} & if\ CA > 4.0 \end{cases}$$

SedImaging using better-fitted HWT calibration equation:

$$PPD = \begin{cases} \left(\frac{CA}{2.4}\right)^{5.1} & if\ CA \leq 4.0 \\ 2.5^{(CA-1.35)} & if\ CA > 4.0 \end{cases}$$

Figure 6-4. Example SedImaging PSD results for the Nesika Beach sand in Fig. 6.1.

- The third generation VisCPT is scheduled to be used in a multi-university project focused on thin-soil delineation in earthquake-prone regions, namely Christchurch, New Zealand. The project will compare traditional CPT soil boring logs to those generated from VisCPT data as well as the actual soil profile obtained by geo-slicing. It is expected that the VisCPT will detect thin soil layers that are not detected in CPT data. These results will be analyzed alongside observational surficial liquefaction manifestations from the 2010-2011 Canterbury, New Zealand earthquake sequence. Before field testing occurs, calibration chamber testing with the VisCPT will be conducted at the Virginia Tech research facilities. This calibration chamber testing will use a constructed soil profile of alternating thin (several centimeters thick) layers of clay and sand (these soils are shown in Figs. 5.7[e] and 5.7[f]). During this stage, the image analysis technique(s) (the Haralick textural indices, the HWT-based method, or a combination of the two) that will be used for the eventual field testing imaging will be determined.

- The benchtop testing of the third generation VisCPT prototype yielded exciting starting points for future research. The testing unexpectedly revealed that camera magnification affects the calibration equation used in the HWT-based method for determining particle size. This area ought to be researched further, and a readjustment of the existing HWT calibration equation to reflect this dependence may be recommended. The benchtop work also began the foundational work of using the two image analysis methods of SedImaging and the VisCPT together to delineate and characterize different soils. The related work that was presented in Section 5.4 requires deeper analysis, and a larger-scale testing schedule of different soils needs to be designed before any actionable conclusions can be made.

Appendix A: Investigating the effect of uneven particle illumination on HWT-based PSDs

As with many of the other image-based soil characterization methods presented in Chapter 2, uneven lighting across a SedImaging soil assembly erroneously affects the HWT-based analysis of the image. This leads to incorrect PSD results. Therefore, steps were taken to reduce uneven lighting across soil assembly images captured with a SedImaging system. A study was conducted into how the uneven lighting in a soil assembly image *specifically* impacts a HWT-based PSD. The study is summarized in this Appendix and the results helped inform some of the key aspects of the autoadaptive HWT-based method presented in Section 4.2.2.

Figure A.1 shows two different 5120 pixel by 1024 pixel grayscale images of sand with a particle size range between 0.3mm and 0.212mm (material retained between the US Standard No. 50 and No. 70 sieves). The images are two of the photographed sides of the same sand assembly photographed in the FieldSed. The photographs appear nearly identical. However, Image 1 (Fig. A.1[a]) is slightly more evenly-illuminated than Image 2 (Fig. A.1[b]). The bottom of Image 2 is slightly darker and its top is slightly lighter than the rest of the soil column. To confirm this, the grayscale values of Images 1and 2 were compared.

The average grayscale values were calculated for every row and column of both Image 1 and 2. The results for Image 1 are seen in Fig. A.2, and Fig. A.3 for Image 2. Since these images are from the same soil assembly, the two grayscale distributions are expected to be similar, though some minor variations between them (uneven lighting aside) is expected. This is confirmed by the

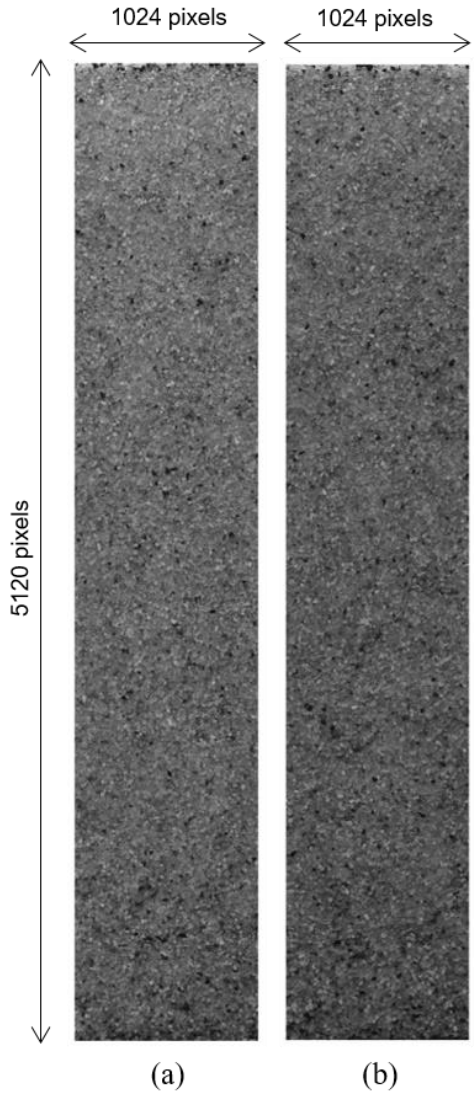

Figure A-1. Two soil images with known with a particle size range between 0.3mm and 0.212mm (material retained between the US Standard No. 50 and No. 70 sieves). (a) Image 1, (b) Image 2.

results in Figs. A.2 and A.3. Specifically, both the row and column grayscale standard deviation values (σ_{rows} and $\sigma_{columns}$ respectively) are very similar between the two images. However, as seen in Fig. A.3, Image 2 has higher average grayscale values (i.e. lighter pixel intensities) at the very top of its image, and lower values (i.e. darker pixel intensities) at the very bottom of the image. These areas are circled in yellow in Fig. A.3(a). The same is not seen as significantly within Image 1 (though Image 1 does still contain slightly darker average grayscale values at the bottom of the

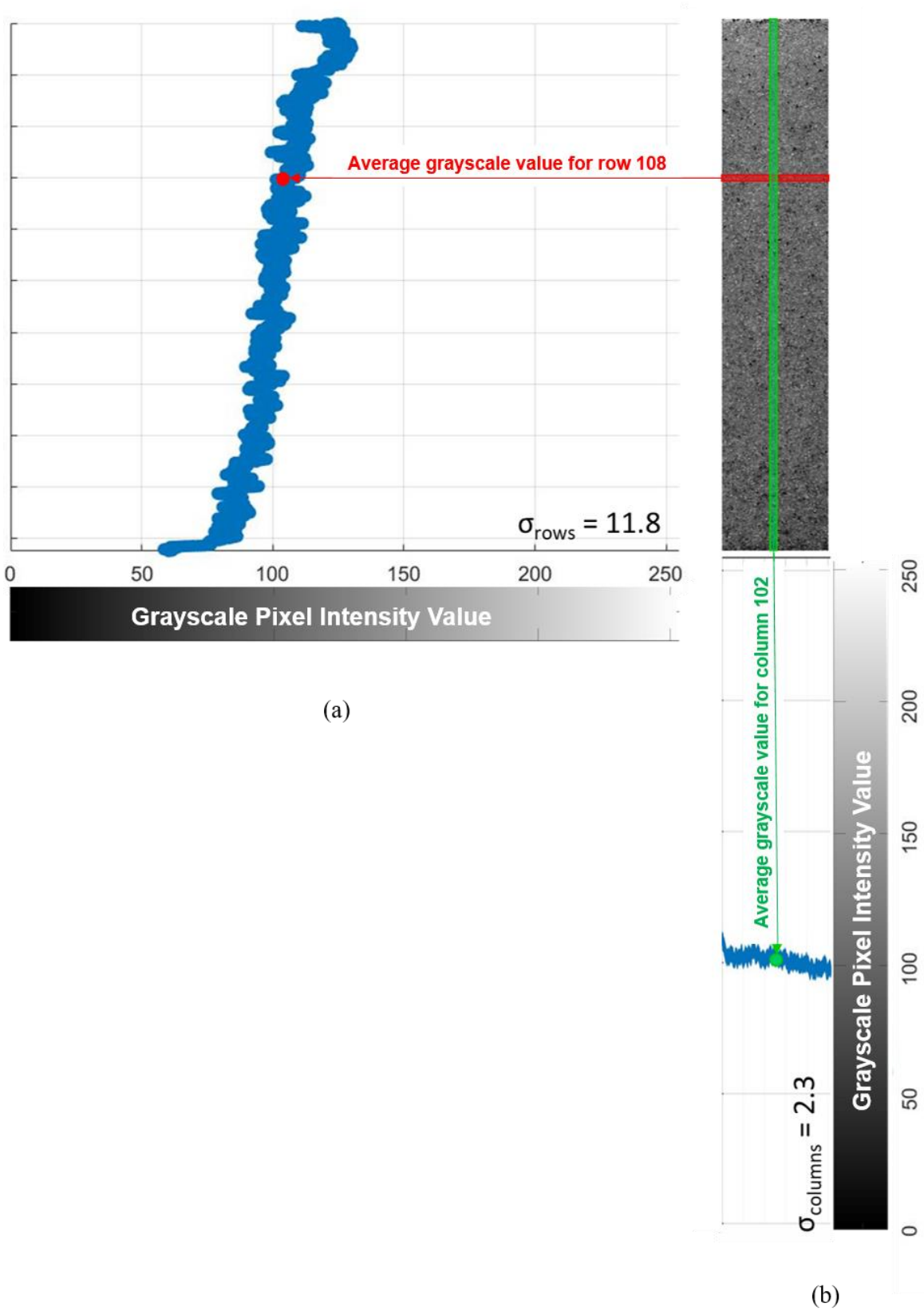

Figure A-2. Average grayscale pixel intensity values for Image 1 in Fig. A.1(a). (a) Row values, (b) Column values.

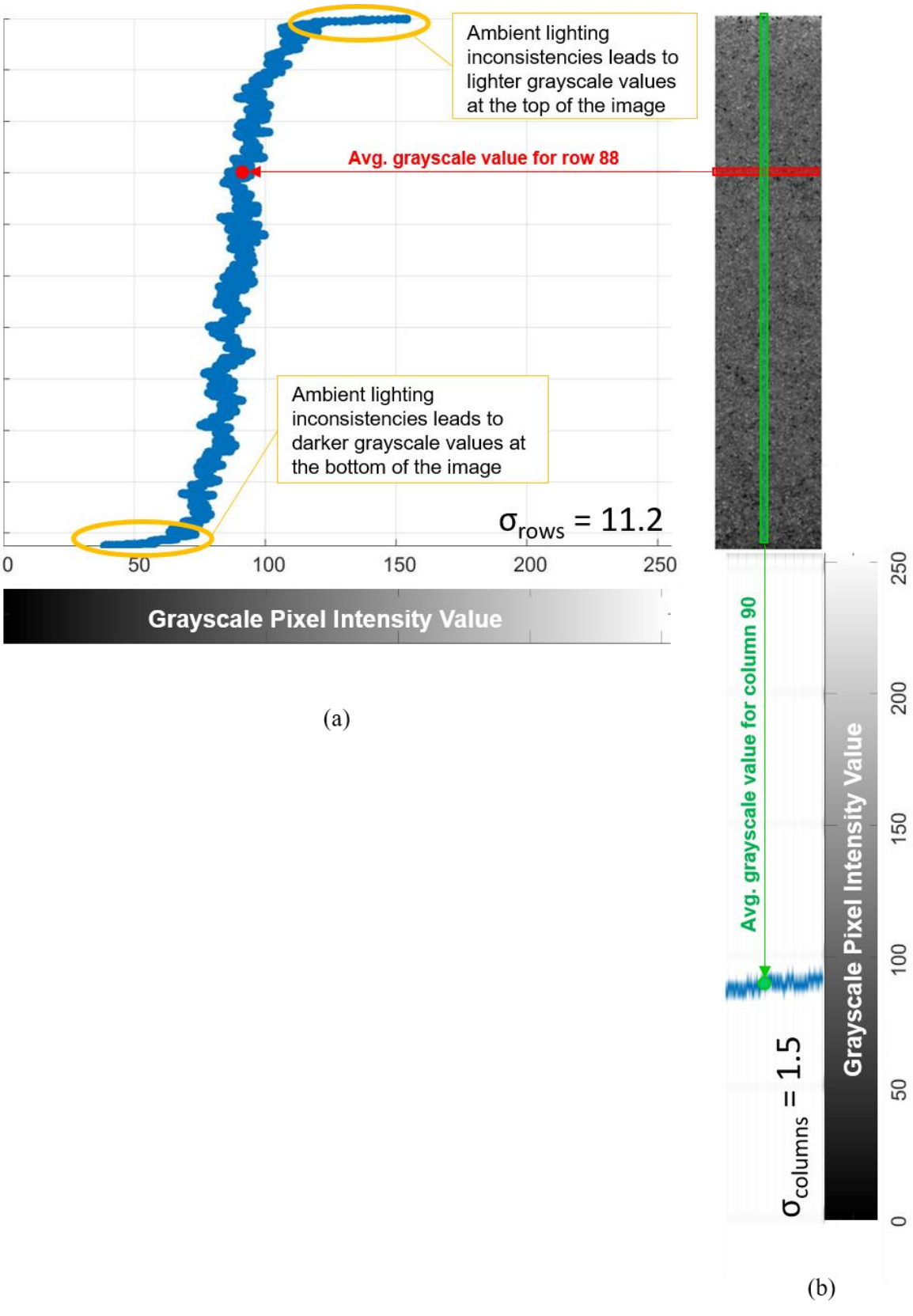

Figure A-3. Average grayscale pixel intensity values for Image 2 in Fig. A.1(b). (a) Row values, (b) Column values.

image). This supports the earlier claim that there is more uneven particle illumination within Image 2 than within Image 1. Due to the larger sample size (5120 rows), these few lighter and darker rows of Image 2 do not cause the σ_{rows} of Image 2 to vary far from that of Image 1. However, these few rows do have a noticeable effect on the image's HWT-based PSD.

To illustrate this, Images 1 and 2 were analyzed by the HWT-based method. The method was performed twice on each image, using a different analysis area size each time. Areas of 1024 x 1024 pix^2 and 512 x 512 pix^2 were used. The PSDs using both analysis area sizes were plotted. Figure A.4 includes this data for Image 1 (Fig. A.4[a]) and Image 2 (Fig. A.4[b]). The figure identifies the locations of each analysis areas within the soil images. The areas are numbered, and the particle size corresponding to each square is color coded and included in the overall PSD data. The upper and lower bound of the known particle sizes range for these soil images are plotted as dotted red and blue vertical lines.

Figure A.4 shows the sensitivity of the original HWT-based analysis method to uneven illumination within a soil image. Figures A.2 and A.3 showed that Image 2 contains more shadows and uneven lighting than Image 1. Therefore, based on the details of the HWT-based method (Section 4.1), more irregularities within Image 2's HWT-based PSD is expected here than for Image 1. This is confirmed in Fig. A.4. More of Image 2's PSDs using both 1024 x 1024 pix^2 and 512 x 512 pix^2 analysis areas fall outside of the known particle size range than do the PSDs of Image 1. Table A.1 compares the HWT-based PSD data for each of the two images.

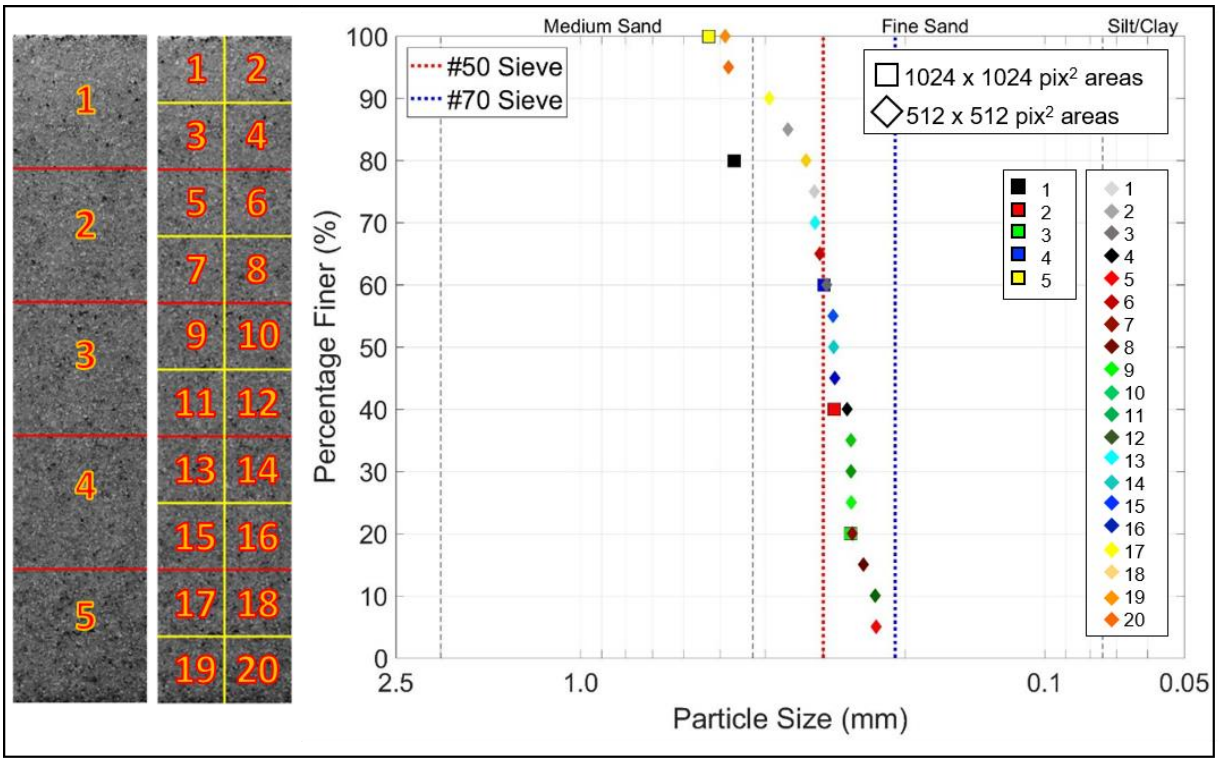

(a)

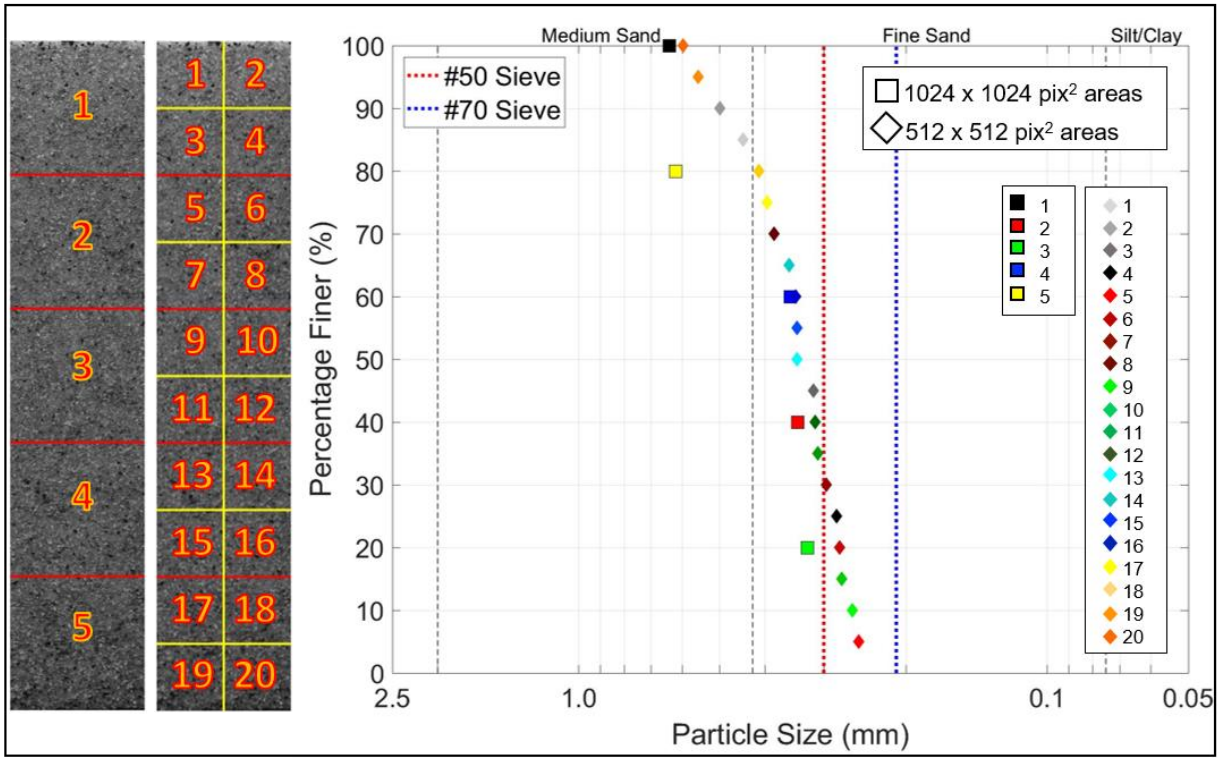

(b)

Figure A-4. PSD data using two different analysis area sizes in the original HWT-based method. (a) Image 1, (b) Image 2.

Table A-1 Comparing PSD Data for Images 1 and 2.

Analysis area size (shape of corresponding data points in Fig. A.4)	Number of data points falling within the known particle size range of the sample (% accuracy)	
	Image 1 (Fig. A.4[a])	Image 2 (Fig. A.4[b])
1024 x 1024 pix^2 (square)	3 of 5 (60%)	0 of 5 (0%)
512 x 512 pix^2 (diamond)	12 of 20 (60%)	6 of 20 (30%)

To further emphasize that uneven lighting impacts HWT results, the PSD data that falls the farthest outside of the known size range are from the top- and bottom-most analysis areas for both images. These are Squares 1 and 5 for the 1024 x 1024 pix^2 areas (respectively the black and yellow square data points). For the 512 x 512 pix^2 areas, these are Squares 1 through 4 and 17 through 20 (respectively the gray-black and yellow-orange diamond data points). Therefore, the brighter illumination at the top of the two soil images, as well as the darker regions at the bottom, are affecting the HWT particle sizing in those regions of the soil assembly. The question that still remains is *how* this affects the HWT results.

To answer this, a deeper look into Image 1's HWT energy distributions was needed. Image 1 contains a very minimal amount of uneven lighting across the soil assembly. Despite this, Fig. A.4(a) shows that this image's HWT-based PSD curves still do not fall entirely within the known particle size range. Analyzing the image's energy distributions can help reveal how even slight uneven lighting can affect the HWT results. With this knowledge, the autoadaptive HWT-based method can be designed to identify and adapt for an environmental factor like uneven lighting in a soil assembly. In doing so, HWT-based PSD results will more accurately size soil particles.

Figure A.5(a) repeats Fig. A.4(a) (for convenience). The figure more importantly includes the HWT energy distributions for all of the 512 x 512 pix^2 (Fig. A.5[b]) and 1024 x 1024 pix^2 (Fig. A.5[c]) analysis areas. For the PSD data points that fall outside of the known particle size range

(noted earlier as those for the top- and bottom-most analysis squares), their corresponding energy distributions increase at the highest decomposition levels (*DL*s). The most prominent examples of this are the 1024 x 1024 pix^2 Squares 1 and 5. In these energy distributions, the value for the 10^{th} *DL* exceeds that of the 9^{th} level. This jump causes the *CA* value to increase, and therefore, the soil particle size for these squares also jump. Thus, these two areas report far larger particle sizes than the three other 1024 x 1024 pix^2 areas.

Two other causes of this energy distribution jump were discussed in Section 4.2.2. There, it was shown that the final *DL* increases when an analysis area is improperly sized for the soil particle sizes within it, or by the proximity of similarly colored particles within the analysis area. Figure A.5 shows how uneven lighting within an analysis area can also produce the same "unacceptable" energy distributions. Of the five 1024 x 1024 pix^2 analysis areas, Squares 1 and 5 are the only "unacceptable" energy distributions. These two areas also contain the most lighting inconsistencies. Square 1 is at the very top of the photographed soil column. The overhead laboratory lighting used for image capture brightly illuminates the particles at the top of this area. Alternatively, Square 5 is at the very bottom of the soil column, and therefore has the most shadows cast on its particles. These lighting inconsistencies are virtually imperceptible by eye; as seen in Fig. A.2(a), Image 1 has an overall uniform average grayscale distribution along its vertical axis. However, when this distribution is analyzed separately using the five 1024 x 1024 pix^2 HWT analysis areas, the lighting inconsistencies become consequential.

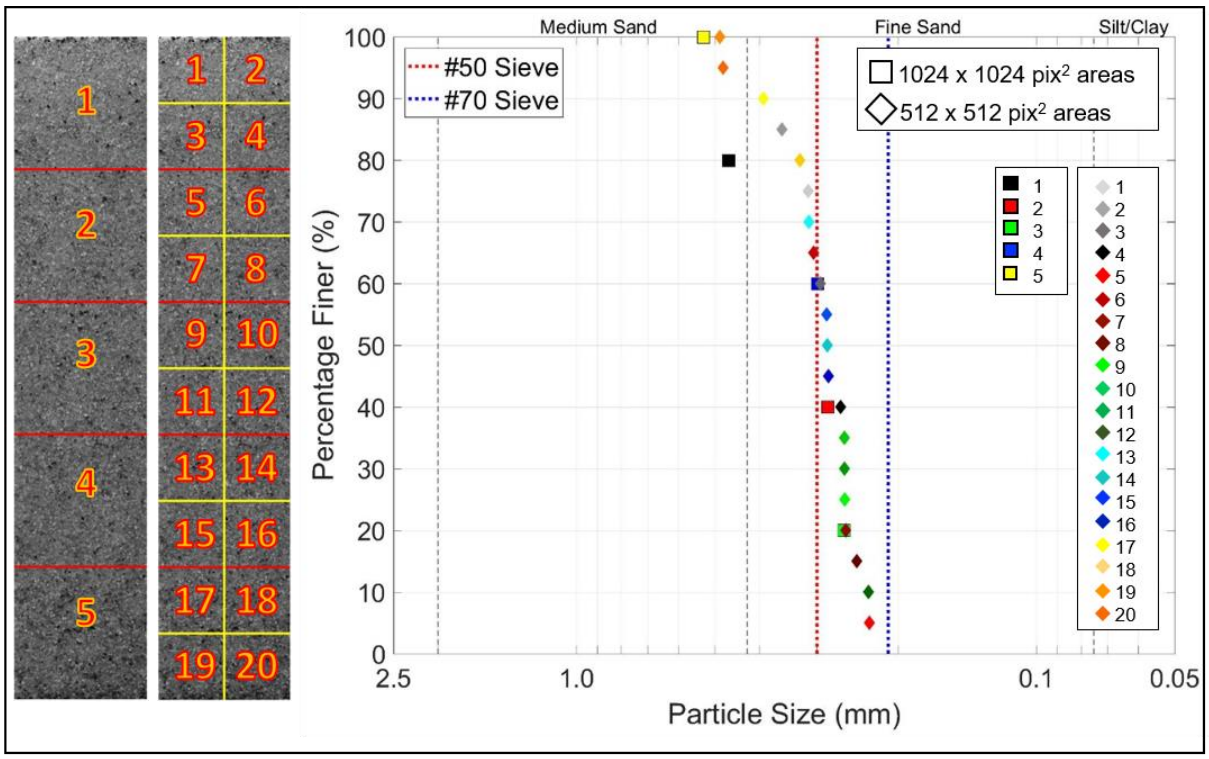

(a)

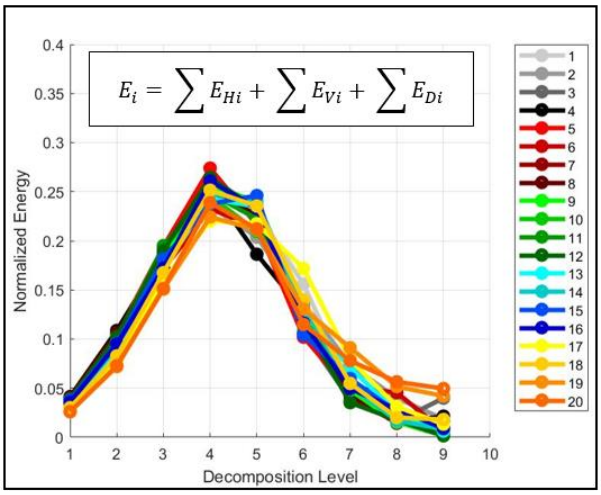

(b)

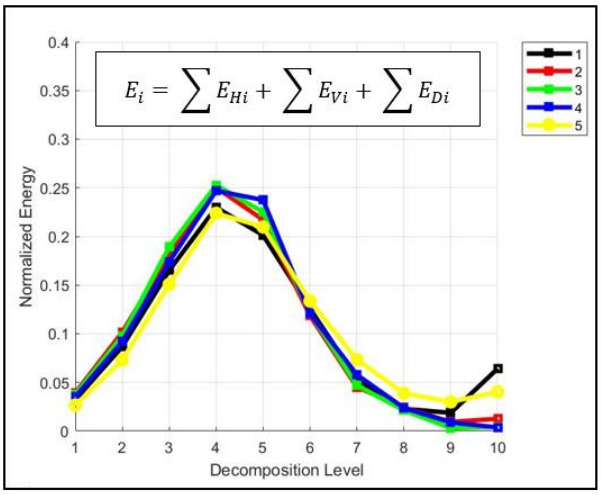

(c)

Figure A-5. Image 1 analyzed using two different analysis areas in the original HWT-based method. (a) 1024 x 1024 pix² and 512 x 512 pix² analysis areas and their PSD data points, (b) 512 x 512 pix² energy using Eq. 4.1's energy definition, (c) 1024 x 1024 pix² energy distributions using Eq. 4.1's energy definition.

Figure A.6 plots the average pixel intensity value for every row (Fig. A.6[a]) and column (Fig. A.6[b]) of Image 1's five 1024 x 1024 pix^2 analysis squares. The standard deviation of all the average values for an area's rows (σ_{rows}) and columns ($\sigma_{columns}$) are reported. The average row values for Squares 2, 3, and 4 change very little throughout the windows; their σ_{rows} are very low. The same is not true for Squares 1 and 5. These two analysis areas have noticeably larger average row grayscale distributions than the other squares. More specifically, Square 1 and 5's σ_{rows} values are over 200% larger than the other three areas' values. The top half of Square 1 has slightly larger average grayscale row values (which corresponds to lighter-colored particles). Square 5 has an approximately 40-grayscale row value drop (corresponding to darker-colored particles) in its lowest 100 pixel rows. Alternatively, in Fig. A.6(b) all five analysis squares have nearly identical average column value distributions; they also have similarly small $\sigma_{columns}$ values. An identical investigation could be performed with the 512 x 512 pix^2 analysis areas and similar conclusions could be made: vertical lighting inconsistencies are seen in the top- and bottom-most analysis areas, while little horizontal variations are seen throughout the entire soil column.

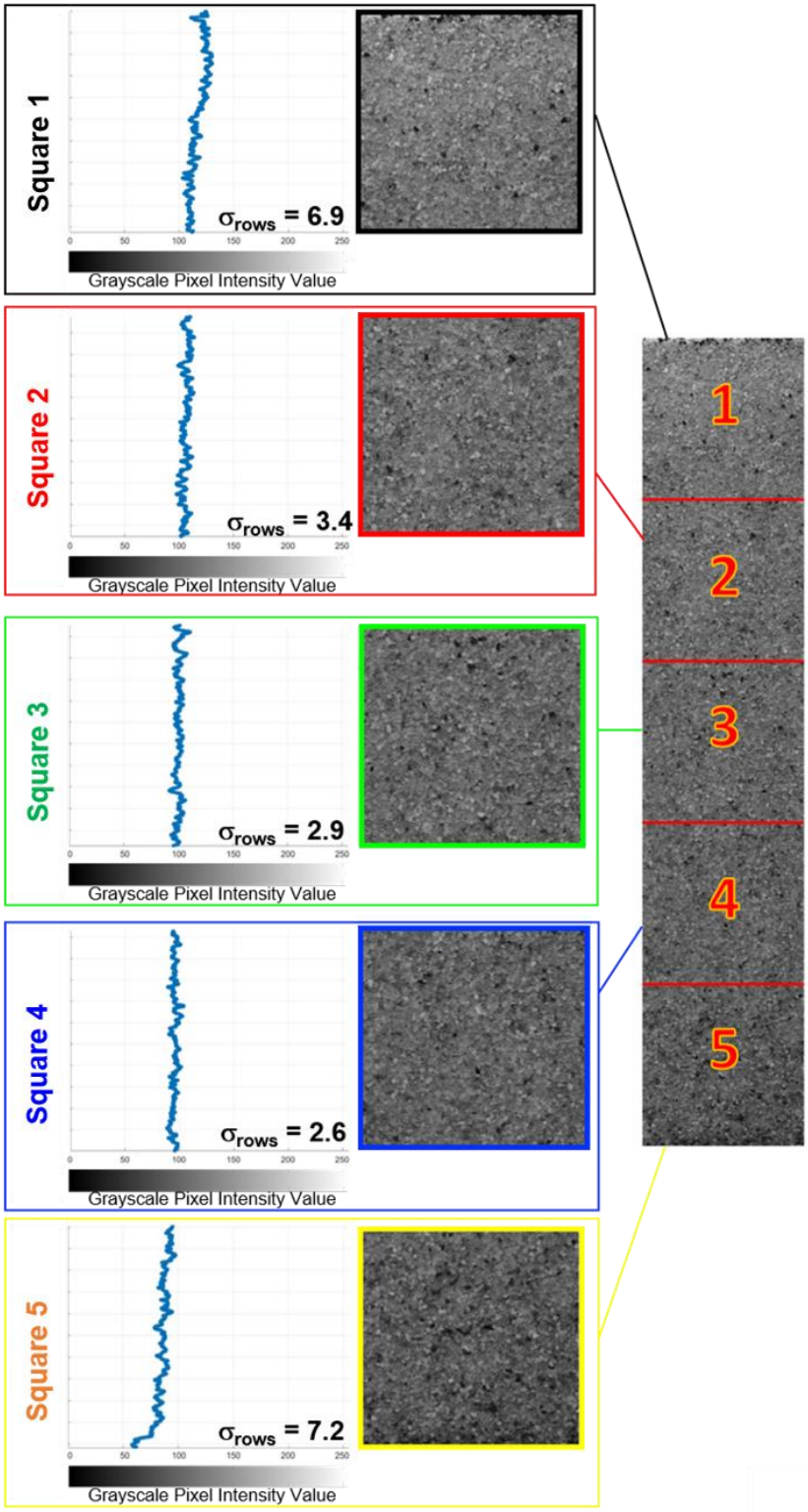

Figure A-6. Average grayscale pixel intensity values for each of Image 1's 1024 x 1024 pix^2 analysis areas. (a) Row values, (b) Column values.

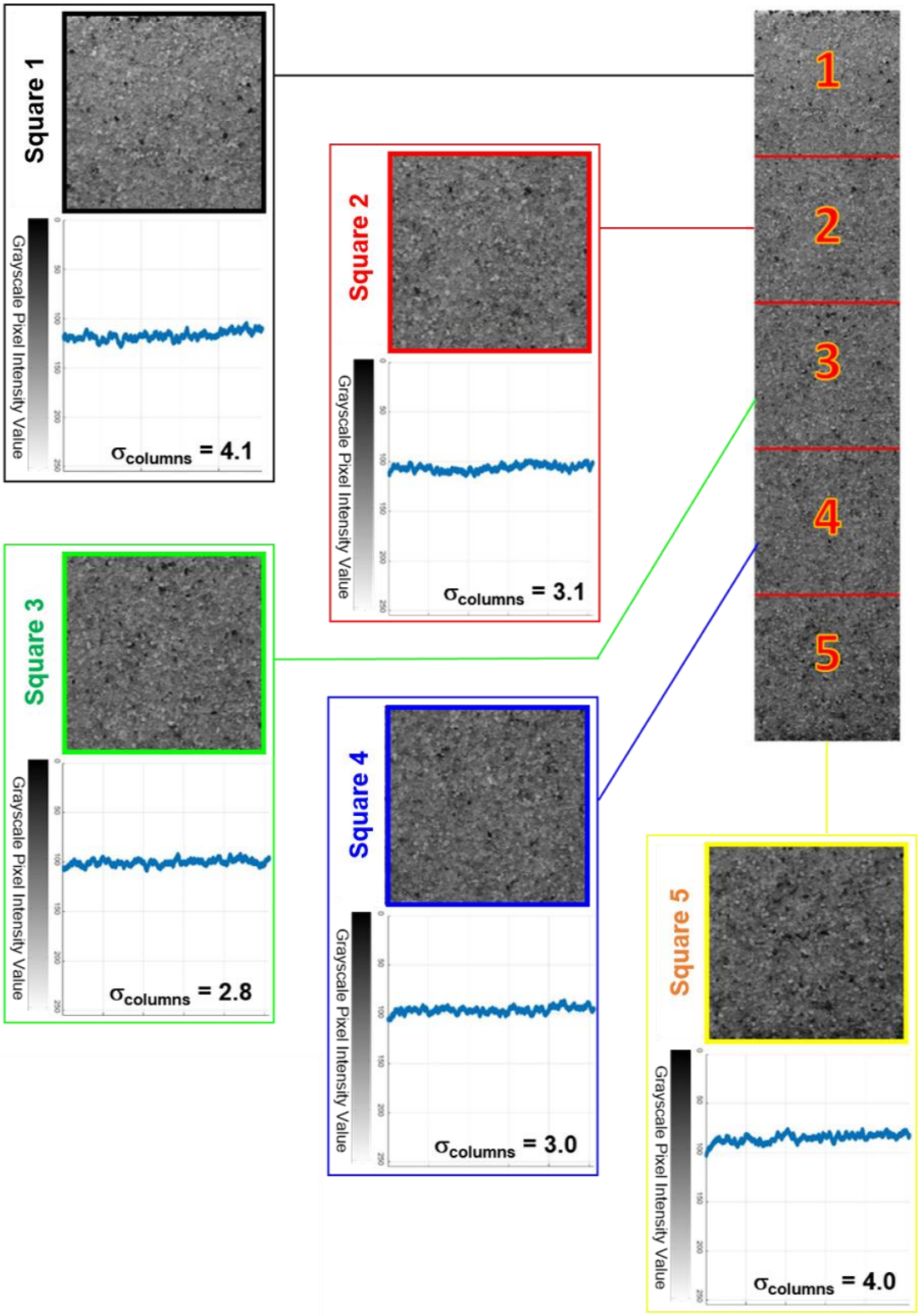

(b)

Figure A-6 Con't. Average grayscale pixel intensity values for each of Image 1's 1024 x 1024 pix^2 analysis areas. (a) Row values, (b) Column values.

While the vertical lighting inconsistencies observed in Fig. A.6(a) appear minimal, they are a source of Image 1's PSD data points erroneously falling outside of the known particle size range. To support this claim, the HWT-based analysis was performed two additional times on Image 1. Instead of using Eq. 4.1's total energy equation (as seen in Figs. A.5[b] and A.5[c]) the following equations were used:

$$E_i = \sum E_{Vi} \tag{A.1}$$

$$E_i = \sum E_{Hi} \tag{A.2}$$

As noted in Section 4.1, E_{Vi} is the energy that compares the grayscale pixel intensity values between columns and E_{Hi} compares values between rows. Therefore, for Image 1 (which contains vertical lighting inconsistencies and little to no horizontal inconsistencies), more accurate PSD data is expected when Eq. A.1 is used in the HWT method as compared to Eq. A.2. Equation A.2 will be more impacted by the uneven lighting in Fig. A.6(a).

Figure A.7 includes the PSD data (Fig. A.7[a]) and energy distributions (Figs. A.7[b] and A.7[c]) using Eq. A.1 in the HWT-based analysis of Image 1. Figure A.8 is identical to Fig. A.7, but instead Eq. A.2 is used in the HWT-based method.

The results in these two figures are informative. Figure A.8 contains PSD data that falls even farther outside of the known size range than either Figs. A.5 or A.7. The energy distributions in Fig. A.8 have even larger increases in their final *DL*s than those in Fig. A.5. The cause of this refers back to earlier claims: uneven lighting across the soil assembly. Figures A.5 and A.8 were created using HWT energy equations that contain the E_H term, which compares rows of pixel intensity values. Figure A.6(a) shows how the lighting changed vertically (i.e. between rows of pixels) throughout Image 1. Therefore, Figs. A.5 and A.8's energy distributions and thus the PSD data is directly (erroneously) impacted by the non-uniform lighting in the vertical direction.

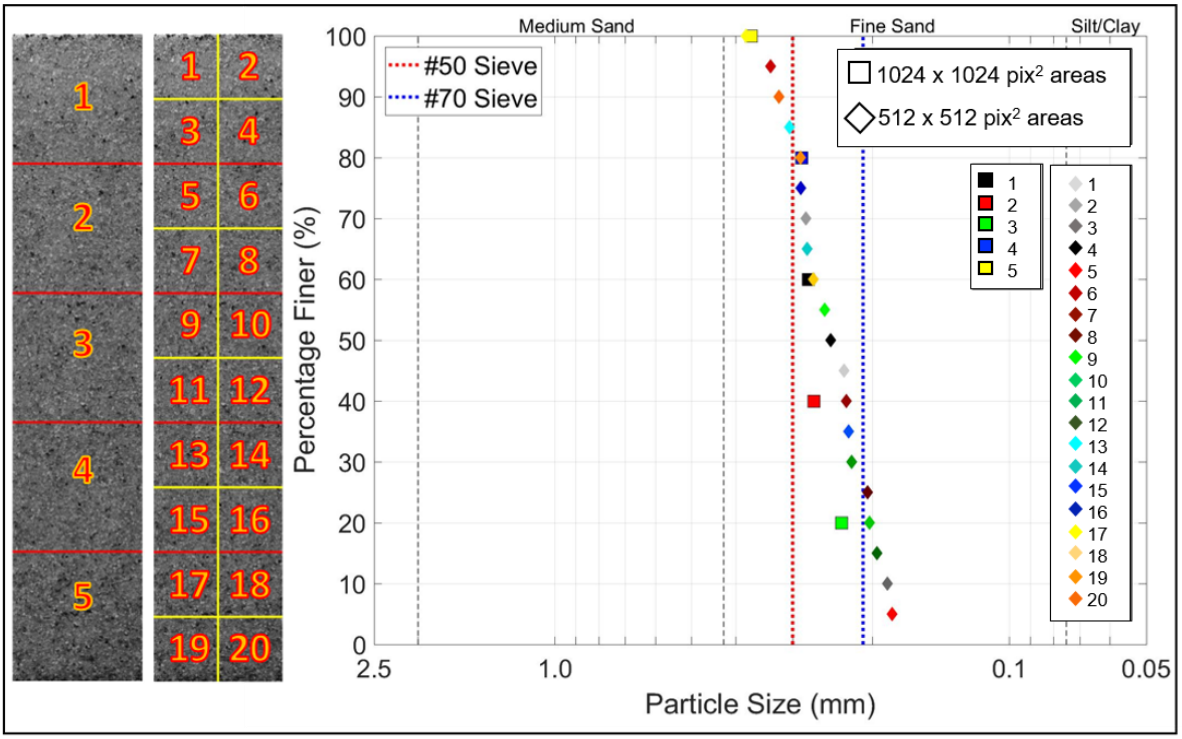

(a)

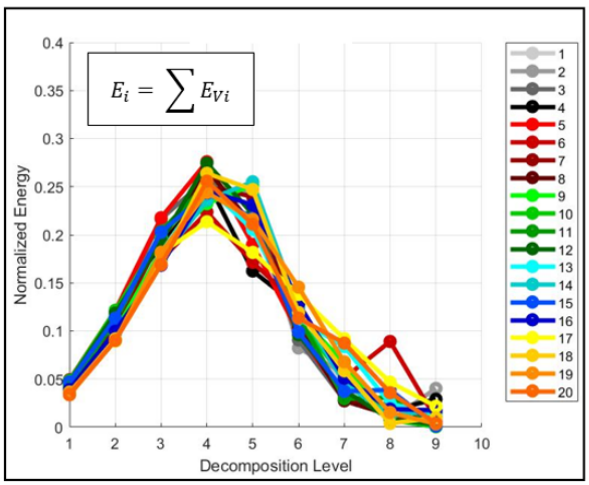

(b)

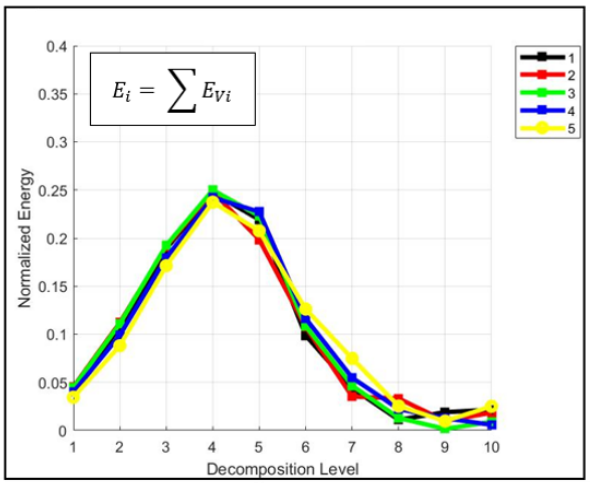

(c)

Figure A-7. Image 1 analyzed using two different analysis areas in the original HWT-based method. (a) 1024 x 1024 pix² and 512 x 512 pix² analysis areas and their PSD data points, (b) 512 x 512 pix² energy using Eq. A.1's energy definition, (c) 1024 x 1024 pix² energy distribution using Eq. A.1's energy definition.

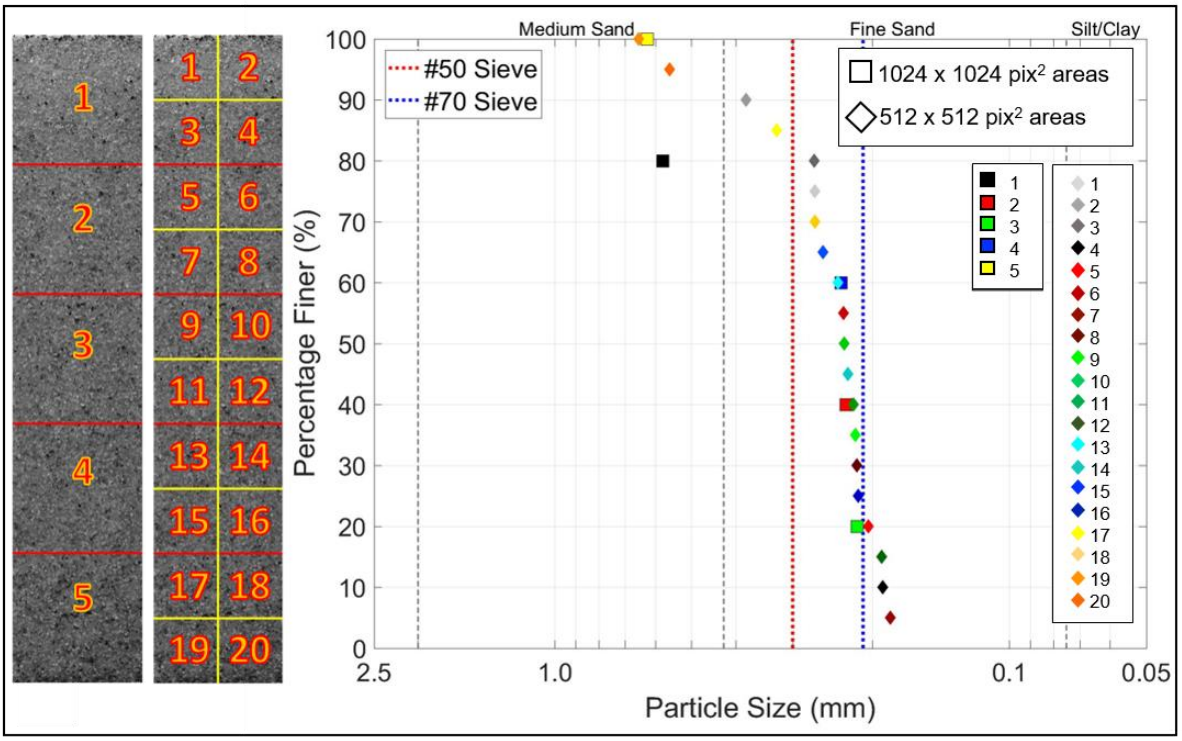

(a)

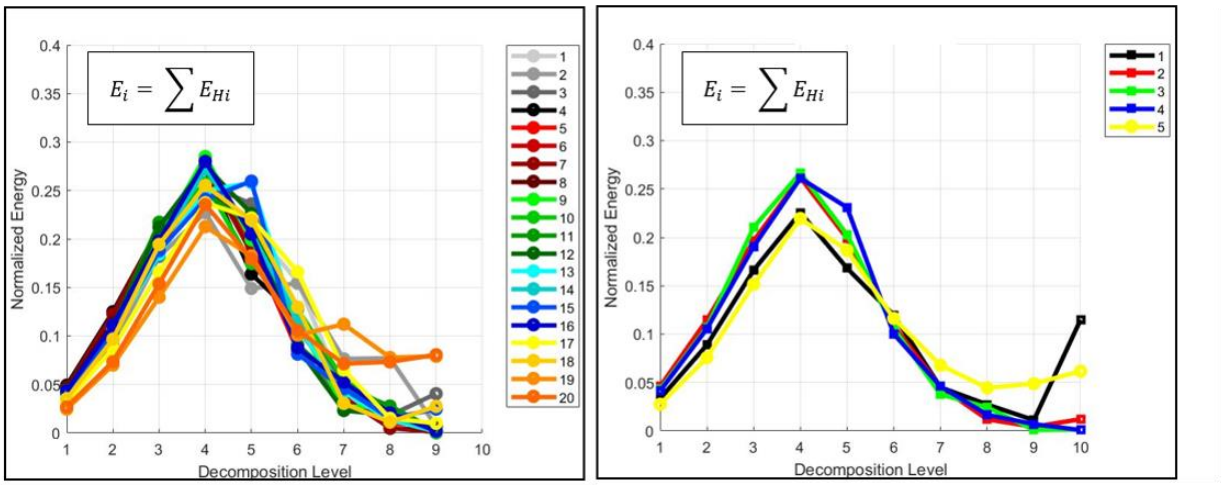

(b) (c)

Figure A-8. Image 1 analyzed using two different analysis areas in the original HWT-based method. (a) 1024 x 1024 pix² and 512 x 512 pix² analysis areas and their PSD data points, (b) 512 x 512 pix² energy using Eq. A.2's energy definition, (c) 1024 x 1024 pix² energy distributions using Eq. A.2's energy definition.

The PSD data in Fig. A.5 is *less* adversely affected by the uneven lighting (i.e. this PSD falls more closely within the known size range) than Fig. A.8 simply due to the fact that Fig. A.5's

total energy equation also consists of other terms, E_V and E_D. These energy terms are not as impacted by Image 1's lighting inconsistencies as is E_H. Figure A.7, which uses an HWT energy equation that only considers E_V, shows PSD data that almost entirely falls within the known particle size range. Figure A.7's energy equation only compares columns of pixel grayscale values. Figure A.6(b) shows that there is little to no horizontal lighting variations across Image 1; thus, Fig. A.7's energy distributions are not as impacted by lighting inconsistencies. These energy distributions increase very little (if at all) in the final *DL*, and their HWT-based particle sizing most accurately represents the soil of Image 1.

This analysis with Eqs. A.1 and A.2 could be performed again for Image 2, yielding the same conclusions. Image 2 was shown to contain more uneven lighting than Image 1. Therefore, there would be an even larger differences between the PSD data using Eqs. A.1 and A.2 than there is between the PSDs in Figs. A.7 and A.8. These results for Image 2 would only further the conclusions reached using Image 1. Image 1 was specifically chosen to show that even for an image that has only a small amount of lighting inconsistencies, HWT-based PSD data is decidedly impacted by uneven illumination.

The conclusions from this research helped form the foundation of the autoadaptive HWT-based method. The data in this Appendix showed how increasing energy values at the upper *DL*s impact an energy distribution's *CA* value. Therefore the autoadaptive HWT-based method identifies when this occurs for an analysis area, and either sets these increasing upper *DL* values to zero, or selects a different analysis area size. Consequently, the autoadaptive HWT-based method more accurately sizes soil particles.

Appendix B: Overview of Haralick et al. (1973)'s Spatial Gray Level Dependence Method (SGLDM) textural indices

To determine the Haralick SGLDM textural indices for a grayscale image **I**(x,y) with pixel intensity values between 0 (pure black) and 255 (pure white), its co-occurrence matrix is created. The co-occurrence matrix, **P**(i,j;d), is a symmetrical 256 x 256 matrix that is a visualization of identical pixel intensity values and their spatial distribution to one another across **I**(x,y). Hryciw et al. (1998) state,

> "The co-occurrence matrix **P**(i,j;d) is…the normalized probability density function of having two image pixels of gray level values of **i** and **j**, separated by a spatial distance **d**. In other words, the matrix **I** is searched for all pixels having grayscale values **i** and **j** separate by distance **d** along the eight 45° fan rays originating from the first pixel."

Haralick et al. (1973) defined 14 textural indices that characterize an image's co-occurrence matrix. Five of these textural indices were used to analyze VisCPT images presented in this dissertation. These indices are Contrast, Correlation, Energy, Local Homogeneity, and Variance. They are defined as

$$Contrast, COR = \sum\sum \frac{[(i-j)^2 \mathbf{P}(i,j,d)]}{255^2} \quad \text{(B.1)}$$

$$Correlation, COR = \sum\sum \frac{[(i-\mu_x)(\mathbf{j}-\mu_y)\mathbf{P}(i,j,d)]}{(\sigma_x)(\sigma_y)} \quad \text{(B.2)}$$

$$Energy, E = \sum\sum \mathbf{P}(i,j,d)^2 \quad \text{(B.3)}$$

$$Local\ Homogeneity, LH = \sum\sum \frac{\mathbf{P}(i,j,d)}{1+(i-j)^2} \quad \text{(B.4)}$$

$$Variance, VAR = \sum\sum (i-\mu_x)(\mathbf{j}-\mu_{\boldsymbol{y}})\mathbf{P}(i,j,d) \quad \text{(B.5)}$$

Where "μ_x and σ_x are the mean and standard deviations of the row sums of matrix **P,** and μ_y and σ_y are analogous statistics of the column sums" (Ghalib 2001).

Appendix C: CPT vs. VisCPT data for a Treasure Island soil profile

Ghalib (2001) details a case study where the VisCPT was used at the former National Geotechnical Experimentation Site (NGES) on Treasure Island in San Francisco, California. The study compared the accuracy of the VisCPT soil profile delineation to laboratory and observational results. The VisCPT was also compared to CPT soil profile logs. Figure C.1(a) plots an example CPT log and Fig. C.1(b) plots the VisCPT results for the same profile. The CPT data contains the tip resistance, side friction, and pore pressure logs. The VisCPT data plots the profiles of two of the Haralick textural indices: Energy and Local Homogeneity. The Energy and Local Homogeneity profiles identified many clay, silt, and sand seams and lenses that are not detected in the CPT data.

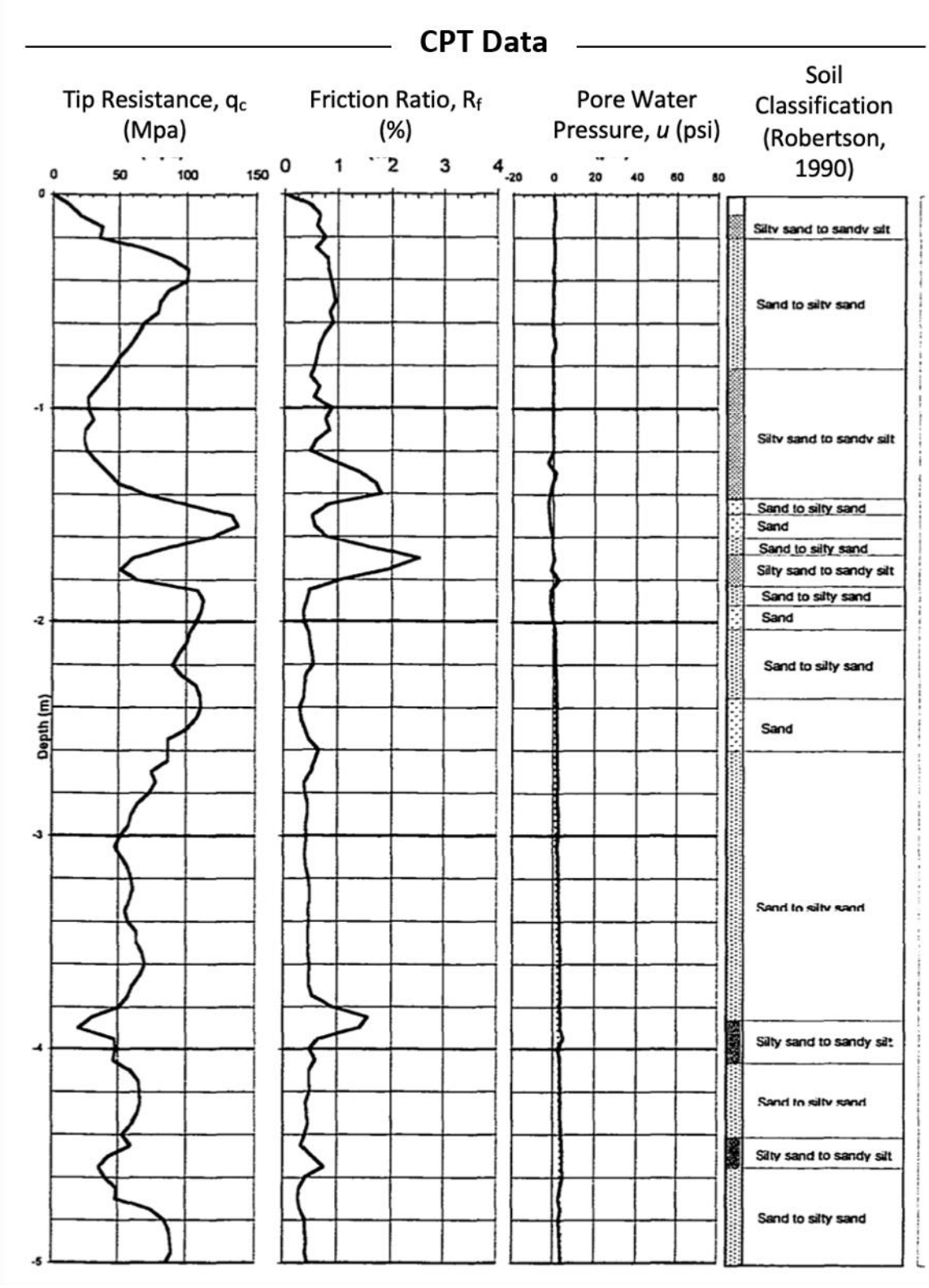

(a)

Figure C-1. Soil profile logs for a Treasure Island case study. (a) CPT data, (b) VisCPT data. (Ghalib et al. 2000).

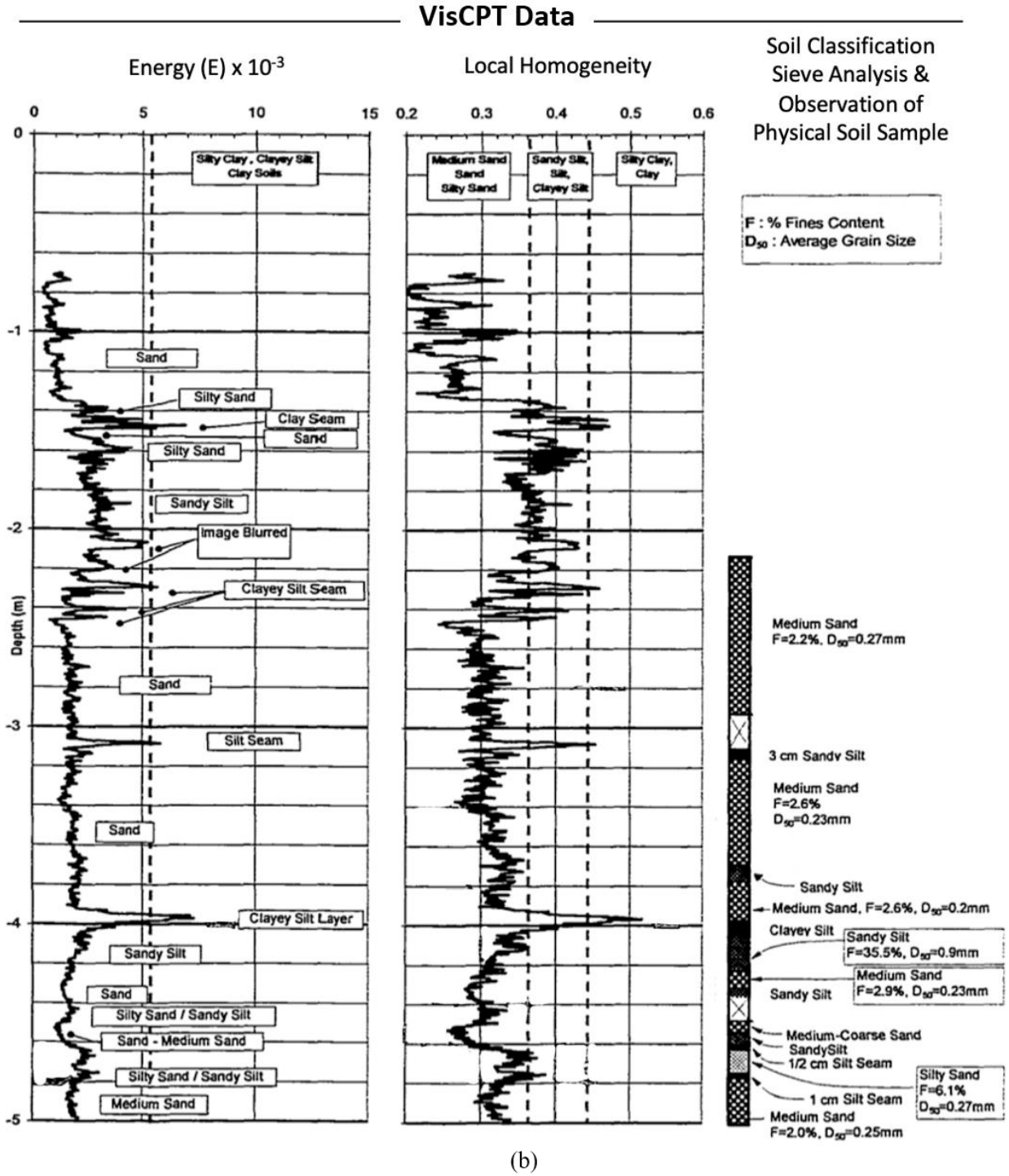

(b)

Figure C-1 con't. Soil profile logs for a Treasure Island case study. (a) CPT data, (b) VisCPT data. (Ghalib et al. 2000).

Appendix D: Section 5.4.3 separated *CA-PPD* data and corresponding trend lines for the eight soils tested with the VisCPT

Figures D.1 through D.8 plot the VisCPT *CA-PPD* data sets from Fig. 5.14 alongside their corresponding trend lines from Fig. 5.15 for each of the eight soils. The soils are separated into individual figures within this Appendix for readability. 2NS data is plotted in Fig. D.1, Costa Rica is in Fig. D.2, Nesika Beach in Fig. D.3, Upper Peninsula in Fig. D.4, Treasure Island in Fig. D.5, Scotts Valley in Fig. D.6, Ottawa in Fig. D.7, and Nevada in Fig. D.8. The colors of the data in Figs. D.1 through D.8 correspond to those used throughout Section 5.4.3. The trend lines for Upper Peninsula and Ottawa sands were omitted in Section 5.4.3 since these soils only contained two sieved size ranges of data. However, these trend lines are included in Figs. D.4 (Upper Peninsula) and D.7 (Ottawa) for completeness. The trend lines' R^2 values are purposely omitted in these two figures to emphasize these limited data sets.

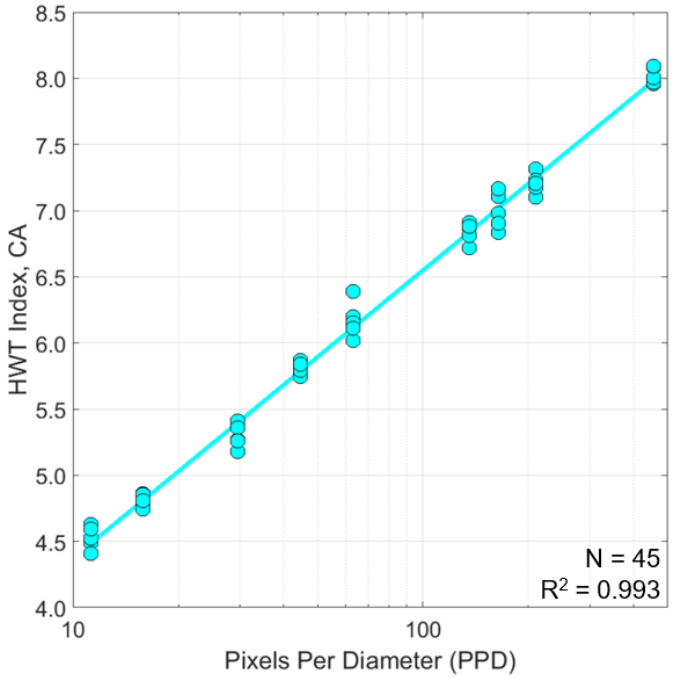

Figure D-1. 2NS CA-PPD *data in Section 5.4.3 VisCPT testing.*

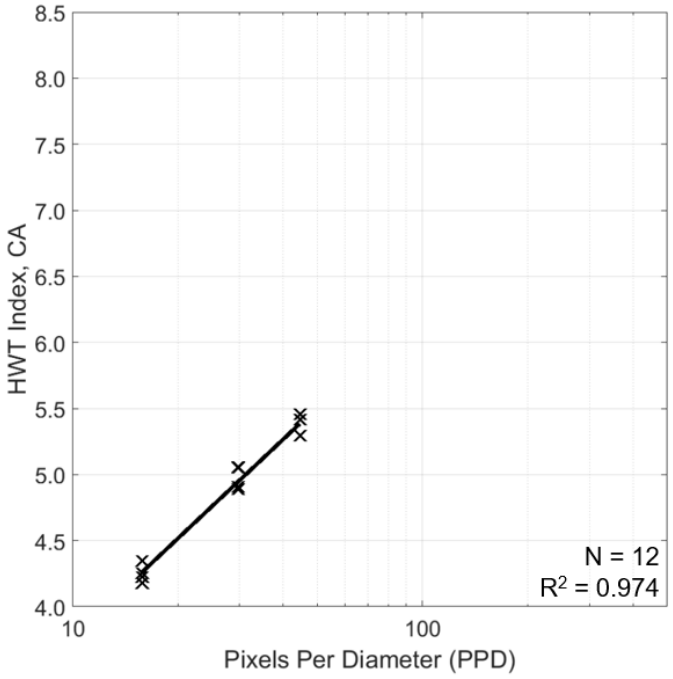

Figure D-2. Costa Rica CA-PPD *data in Section 5.4.3 VisCPT testing.*

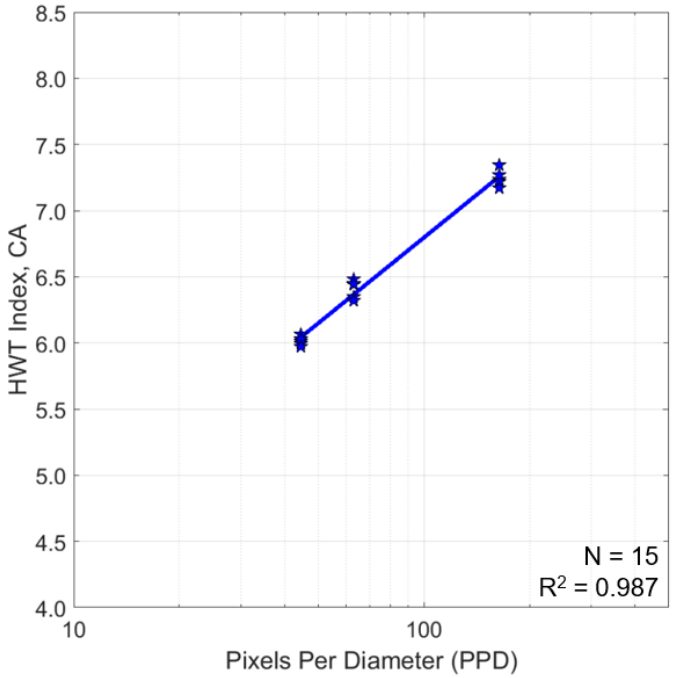

Figure D-3. Nesika Beach CA-PPD *data in Section 5.4.3 VisCPT testing.*

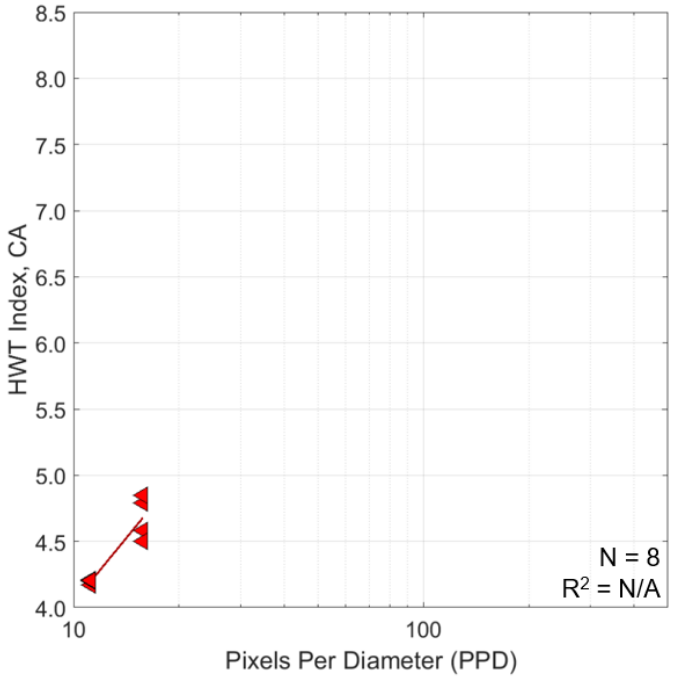

Figure D-4. Upper Peninsula CA-PPD *data in Section 5.4.3 VisCPT testing.*

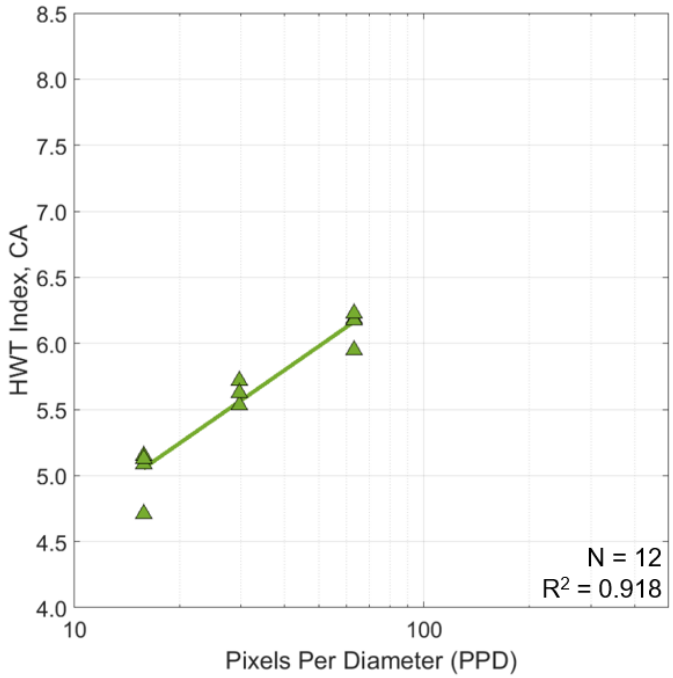

Figure D-5. Treasure Island CA-PPD *data in Section 5.4.3 VisCPT testing.*

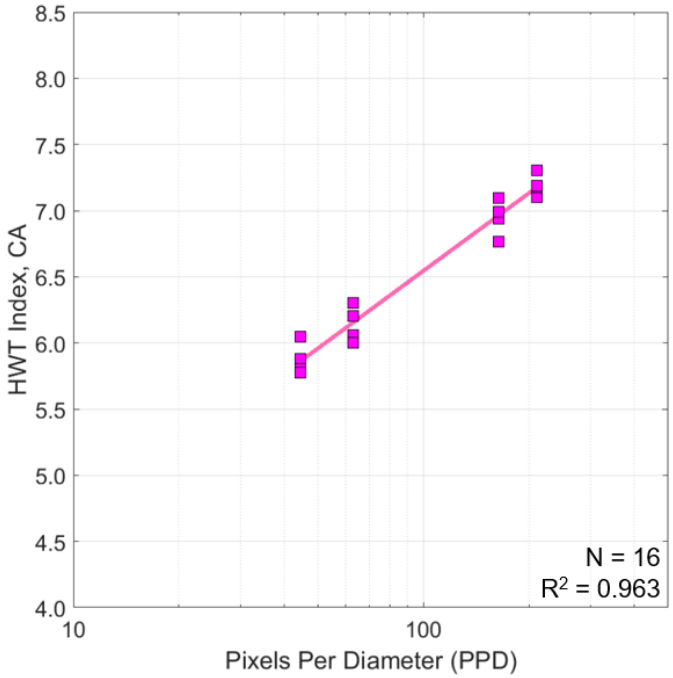

Figure D-6. Scotts Valley CA-PPD *data in Section 5.4.3 VisCPT testing.*

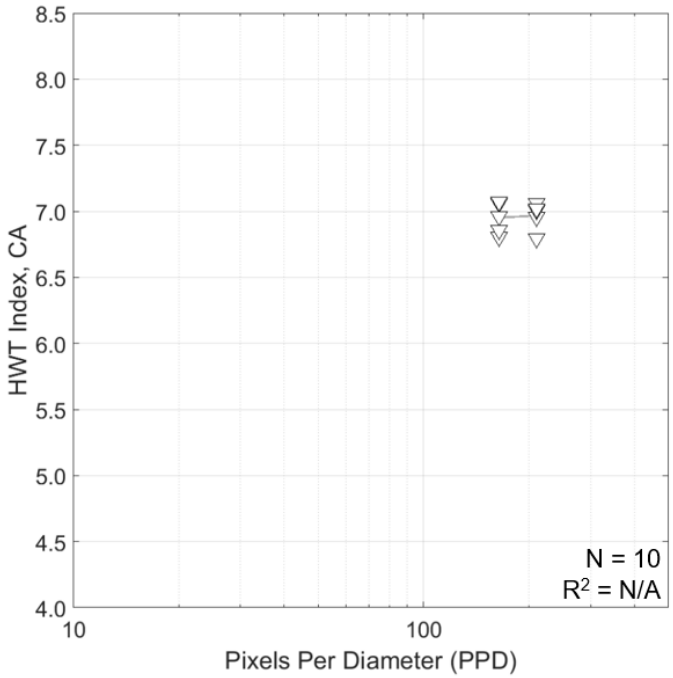

Figure D-7. Ottawa CA-PPD *data in Section 5.4.3 VisCPT testing.*

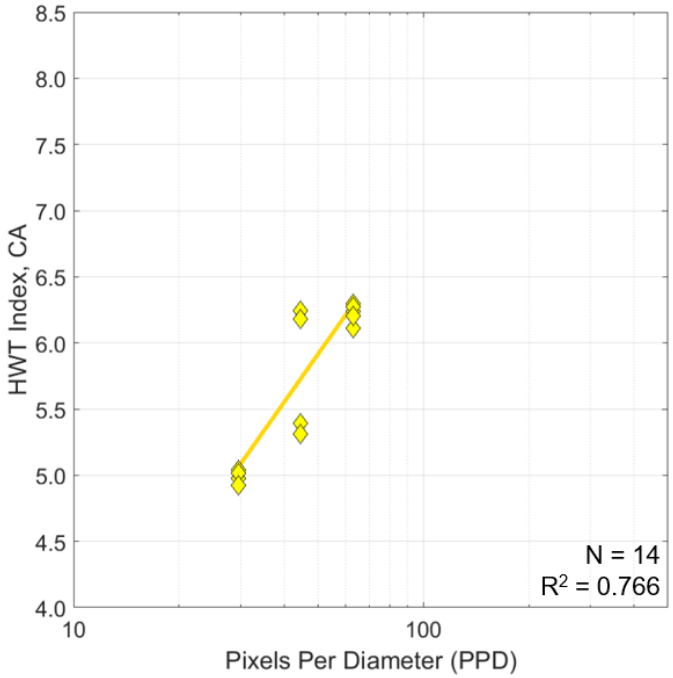

Figure D-8. Nevada CA-PPD *data in Section 5.4.3 VisCPT testing.*

Appendix E: Comparing *CA-PPD* results for different 2NS data sets gathered with the VisCPT

Figure E.1 is a *CA-PPD* plot of the two independent 2NS data sets photographed at different VisCPT illumination voltages. As noted in Section 5.4.3, these data sets have nearly identical trend lines. The data using the 4.25V illumination was originally included in Fig. 5.11; the 4.0V illumination data is separately plotted in Fig. D.1. Section 5.4.3 discusses the differences between these two data set.

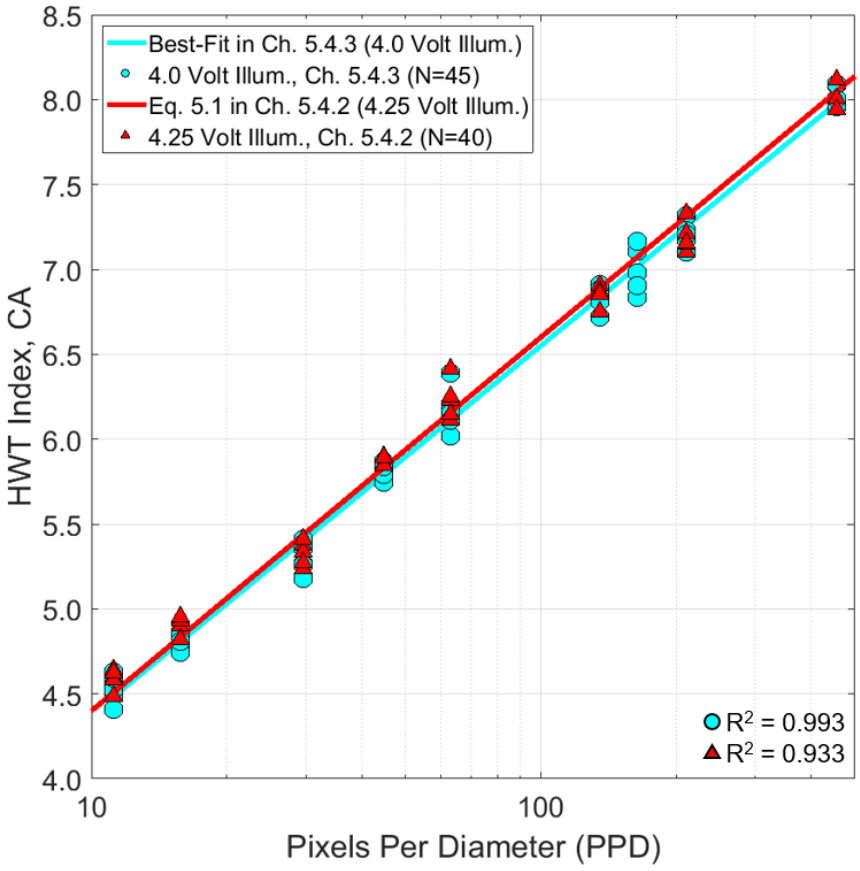

Figure E-1. CA-PPD *data for 2NS data photographed by the VisCPT at different illumination voltages.*

Bibliography

Abbaszadeh Shahri, A., A. Malehmir, and C. Juhlin. 2015. "Soil Classification Analysis Based on Piezocone Penetration Test Data – A Case Study From a Quick-Clay Landslide Site in Southwestern Sweden." *Engrg. Geology.* 189: 32-47. https://doi.org/10.1016/j.enggeo.2015.01.022

Abhik, M., C. Debashish, B. Kousik, and H. Arpan. 2016. "Development of a Mass Model in Estimating Weight-Wise Particle Size Distribution Using Digital Image Processing." *Int'l J. of Mining Science and Technology*, 27: 435-443. https://doi.org/10.1016/j.ijmst.2017.03.015

Altuhafi, F., C. O'Sullivan, and I. Cavarretta. 2013. "Analysis of an Image-Based Method to Quantify the Size and Shape of Sand Particles." *J. Geotech. Geoenviron. Engrg.*, 139(8): 1290-1307. https://doi.org/10.1061/(ASCE)GT.1943-5606.0000855

ASTM International. 2017. *Standard Practice for Classification of Soils for Engineering Purposes (Unified Soil Classification System)*. ASTM D2487-17ε1, West Conshohocken, PA: ASTM International, approved December 15, 2017. https://doi.org/10.1520/D2487-17E01

ASTM International. 2019. *Standard Test Method for Sieve Analysis of Fine and Coarse Aggregates*. ASTM C136/C136M-19, West Conshohocken, PA: ASTM International, approved December 1, 2019. https://doi.org/10.1520/C0136_C0136M-19

Black, M., P. Carbonneau, M. Church, and J. Warburton. 2014. "Mapping Sub-Pixel Fluvial Grain Sizes with Hyperspatial Imagery." *Sedimentology.* 61: 691-711. https://doi.org/10.1111/sed.12072

Buscombe, D., D. M. Rubin, and J. A. Warrick. 2010. "A Universal Approximation of Grain Size From Images of Noncohesive Sediment." *J. of Geophysical Research: Earth Surface*. 115, no. F2. https://doi.org/10.1029/2009JF001477

Cabrera-Navarrete, E., G. Ronquillo-Jarillo, and A. Markov. 2020. "Wavelet Analysis for Spectral Inversion of Seismic Reflection Data." *J. of Applied Geophysics*. 177: 104034. https://doi.org/ 10.1016/j.jappgeo.2020.104034

Chatterjee, P. 2015. *Wavelet Analysis in Civil Engineering*, 1st Ed. Boca Raton, FL: CRC Press.

Chávez, G. M., D. Sarocchi, E. Arce Santana, and L. Borselli. 2015. "Optical Granulometric Analysis of Sedimentary Deposits by Color Segmentation-Based Software: OPTGRANS-CS." *Computers & Geosciences*. 85: 248-257. https://doi.org/10.1016/j.cageo.2015.09.007

Ching, J., J-S. Wang, C. H. Juang, and C-S. Ku. 2015. “Cone Penetration Test (CPT)-Based Stratigraphic Profiling Using the Wavelet Transform Modulus Maxima Method.” *Canadian Geotech. J.* 52, no. 12: 1993-2007. https://doi.org/10.1139/cgj-2015-0027

Coban, H. S., Q. Sun, B. Cetin, and J. Zheng. 2020. “Particle Size Characteristics of Unconventionally Large Aggregate Particles by Stereophotography.” In *Geo-Congress 2020 GSP*. 317: 183-191. Reston, VA: ASCE. https://doi.org/10.1061/9780784482803.020

Damadipour, M., M. Nazarpour, and M. T. Alami. 2019. “Evaluation of Particle Size Distribution Using and Efficient Approach Based on Image Processing Techniques.” *Iranian J. of Sci. and Tech., Transactions of Civil Eng.* 43 (S1): 429-441. DOI: https://doi.org/10.1007/s40996-018-0175-3

Detert, M., and V. Weitbrecht. 2012. “Automatic Object Detection to Analyze the Geometry of Gravel Grains: A Free Stand-Alone Tool.” *River Flow 2012*, R. M. Munos, ed., Taylor & Francis, London, 595-600.

Detert, M., and V. Weitbrecht. 2013. “User Guide to Gravelometric Image Analysis by BASEGRAIN.” *Advances in Science and Research,* S. Fukuoka, H. Nakagawa, T. Sumi, and H. Zhang, eds., Taylor & Francis, London, 1789-1795.

Ding, L., L. Ma, H. Luo, M. Yu, and X. Wu. 2011. “Wavelet Analysis for Tunneling-Induced Ground Settlement Based on a Stochastic Model.” *Tunneling and Underground Space Tech.* 26 no. 5: 619-628. https://doi.org/10.1016/j.tust.2011.03.005

Frey, B. J., and D. Dueck. 2007. “Clustering By Passing Messages Between Data Points.” *Science,* 315(5814): 972–976. https://doi.org/10.1126/science.1136800

Ghalib, A.M. “Laboratory and In-Situ Soil Characterization by Computer Vision.” Diss. U of Michigan, 2001.

Ghalib, A.M., R. D. Hryciw, and S. C. Shin. 1998. “Image Texture Analysis and Neural Network for the Characterization of Uniform Soils.” *Proc. ASCE Congress on Computing in Civil Engineering*, 671-682.

Ghalib, A.M., R. D. Hryciw, and E. Susila. 2000. “Soil Stratigraphy Delineation by VisCPT.” *Proc. ASCE Geo-Institute Innovations and Applications in Geotechnical Site Characterization*, 65-79. https://doi.org/10.1061/40505(285)5

Gislao, M. 2009. “Performing a Grains Analysis in 5 Easy Steps.” (http://www.olympus america.com/seg_industrial/files/Grains123_092509.pdf)

Graham, D. J., I. Reid, and S. P. Rice. 2005a. "Automated Sizing of Coarse-Grained Sediments: Image-Processing Procedures." *Math. Geol.* 37, 1-28. https://doi.org/10.1007/s11004-005-8745-x

Graham, D. J., S. P. Rice, and I. Reid. 2005b. "A Transferrable Method for the Automated Grain Sizing of River Gravels." *Water Resources Research* 41 W07020. https://doi.org/10.1029/2004WR003868

Gouveia, L., F. Rodrigues, and L. Costa. 2010. "Multiscale Curvature Analysis of Asphaltic Aggregate Particles." *J. Comput. Civ. Eng.* 24(6): 506-513. https://doi.org/10.1061/(ASCE)CP.1943-5487.0000057

Guida, G., F. Casini, and G. M. B. Viggiani. 2017. "Contour Fractal Analysis of Grains." *EPJ Web of Conferences: Powders & Grains*. 140: 05008. https://doi.org/10.1051/epjconf/201714005008

Haar, A. 1910. "Zur Theorie der Orthogonalen Functionensysteme." *Mathematische Annalen,* 69, no. 3: 331-371.

Haralick, R. M., K. Shanmugam, and I. Dinstein. 1973. "Textural Features for Image Classification." *IEEE Transactions on System, Man, and Cybernetics,* 3(6): 610-621. https://doi.org/10.1109/TSMC.1973.4309314

Hryciw, R. D., A. M. Ghalib, and S. Raschke. 1998. "In-situ Soil Characterization using Vision Cone Penetrometer (VisCPT)." In Geotechnical Site Characterization. Balkema, Rotterdam, Netherlands.

Hryciw, R. D., E. Susila, and S. Shin. 2005. "CPT Readings, VisCPT Observations, and Advanced FEM Modeling of Penetration through Soil Interfaces." In Site Characterization and Modeling GSP. 138: 1-12. Reston, VA: ASCE. https://doi.org/10.1061/40785(164)10.

Hryciw, R. D., and Y. Jung. 2008. "Accounting for void ratio variation in determination of grain size distribution by soil column image processing." Proc., GeoCongress 2008, ASCE, Reston, VA, 966–973. https://doi.org/10.1061/40972(311)121

Hryciw, R. D., Y. Jung, E. Susila, and A. Ibrahim. 2009. "Thin soil layer detection by VisCPT and FEM simulations." *Proc., 17th Int'l Conf. on Soil Mechanics and Geotechnical Engineering (ICSMGE),* IOS, Amsterdam, Netherlands, 1052-1055. https://doi.org/10.3233/978-1-60750-031-5-1052

Hryciw, R. D. and H.-S. Ohm. 2012. “Feasibility of Digital Imaging to Characterize Earth Materials.” Research Report Number RC1557, Michigan Department of Transportation, 345 pp.

Hryciw, R. D. and H.-S. Ohm. 2013. “Soil Migration and Piping Susceptibility by the VisCPT.” In Geo-Congress 2013: Stability and Performance of Slopes and Embankments III. 192-195. Reston, VA: ASCE. https://doi.org/10.1061/9780784412787.020

Hryciw, R. D., H.-S. Ohm, and J. Zhou. 2015. “Theoretical basis for optical granulometry by wavelet transformation.” *J. Comput. Civ. Eng*. 29, no. 3: 04014050. https://doi.org/10.1061/(ASCE)CP.1943-5487.0000345

Jung, Y., R. D. Hryciw, and D. Elsworth. 2008. “Vision Cone Penetrometer Calibration for Soil Grain Size.” *Proc. Of the 3rd Int. Conf. on Site Characterization*, Taipei, Taiwan: 1303-1308.

Koh, T. K., N. J. Miles, S. P. Morgan, and B. R. Hayes-Gill. 2009. “Improving Particle Size Measurement Using Multi-Flash Imaging.” *Minerals Engineering* 22: 537-543. https://doi.org/10.1016/j.mineng.2008.12.005

Kozakiewicz, J. 2018. “Image Analysis Algorithm for Detection and Measurement of Martian Sand Grains.” *Earth Science Informatics* 11: 257-272. https://doi.org/10.1007/s12145-018-0333-y

Kulhawy, F. H. and P. W. Mayne. 1990. *Manual on Estimating Soil Properties for Foundation Design.* Report EL-6800, Electric Power Research Institute, Palo Alto, p. 306.

Kumara, J. J., K. Hayano, and K. Ogiwara. 2012. “Image Analysis Techniques on Evaluation of Particle Size Distribution of Gravel.” *Int. J. of GEOMATE* 3 (1): 290-297. https://doi.org/10.21660/2012.5.1261

Kuo, C-Y., and J. D. Frost. 1996. “Uniformity Evaluation of Cohesionless Specimens Using Digital Image Analysis.” *J. of Geotech. Eng.* 122 (5): 390-396. https://doi.org/10.1061/(ASCE)0733-9410(1996)122:5(390)

Masad, E., and J. W. Button. 2000. “Unified Imaging Approach for Measuring Aggregate Angularity and Texture.” *Comp.-Aided Civil and Infrast. Eng.* 15 (4): 273-280. https://doi.org/10.1111/0885-9507.00191

Michigan Department of Transportation (MDOT). 2010. “Materials Source Guide.” *902,* Lansing, MI.

Mollaioli, F., and A. Bosi. 2011. “Wavelet Analysis for the Characterization of Forward-

Directivity Pulse-Like Ground Motions on Energy Basis." *Meccanica*. 47, no. 1: 203-219. https://doi.org/10.1007/s11012-011-9433-1

Nie, R., H. Wang, K. Yang, and X. Liu. 2015. "Estimation of the Grain-Size Distribution Using Semisupervised Affinity Propagation." *J. Hydrol. Eng.* 20(12): 04015040. https://doi.org/10.1061/(ASCE)HE.1943-5584.0001229

Nievergelt, Y. 1999. *Wavelets Made Easy*. Boston, MA: Birkhäuser.

Ohkami, T., J. Nagao, and S. Koyama. 2006. "Identification of Elastic Materials Using Wavelet Transform." *Computers and Structures*. 84, no. 29: 1866-1873. https://doi.org/10.1016/j.compstruc.2006.08.030

Ohm, H.-S., and R. D. Hryciw. 2013. "Enhanced soil characterization through advances in imaging technology." *Proc., 18th Int. Conf. on Soil Mechanics and Geotechnical Engineering (ICSMGE),* IOS Press, Fairfax, VA, Vol. 5, 3491–3494.

Ohm, H-S, and R. D. Hryciw. 2013. "Translucent Segregation Table Test for Sand and Gravel Particle Size Distribution." *Geotechnical Testing Journal* 36(4): 1–14. https://doi.org/10.1520/GTJ20120221

Ohm, H.-S., and R. D. Hryciw. 2014. "Size Distribution of Coarse-Grained Soil by SedImaging." *J. Geotech. Geoenviron. Eng.* 140, no. 4: 04013053. https://doi.org/10.1061/(ASCE)GT.1943-5606.0001075

Pan, T., and E. Tutumluer. 2005. "Imaging Based Evaluation of Coarse Aggregate Size and Shape Properties Affecting Pavement Performance." *Advances In Pavement Engineering.* https://doi.org/10.1061/40776(155)3

Pang, Y., N. Wang, K. Wang, Z. Liu, L. Nie, and X. Xu. 2020. "Multiscale Constrained Inversion Method for Direct Current Resistivity Tomography Based on Haar Wavelet Transform." *Inst. Of Electrical and Electronics Engrs. (IEEE) Access*. 8: 170195-170202. https://doi.org/10.1109/ACCESS.2020.3024286

Prokoph, A., and R. T. Patterson. 2004. "From Depth Scale to Time Scale: Transforming Sediment Image Color Data into a High-Resolution Time Series." In: Francus, P. (ed) *Developments in Paleoenvironmental Research 7: Image Analysis, Sediments and Paleoenvironments.* Kulwer Academic Publishers, Dordrecht, 143-164.

Raschke, S.A. and R. D. Hryciw. 1997. "Vision Cone Penetrometer (VisCPT) for Direct Subsurface Soil Observation." *J. Geotech. Geoenviron. Engrg*., 123(11): 1074-1076.

Rivera, M., O. Dalmau. 2012. "Variational Viewpoint of the Quadratic Markov Measure Field

Models: Theory and Algorithms." *IEEE Transactions on Image Processing*, 21(3): 1246-1257. https://doi.org/10.1109/TIP.2011.2168409

Robertson, P.K., R. G. Campanella, D. Gillespie, and J. Grieg. 1986. "Use of Piezometer Cone Data." *Use of In-Situ Tests in Geothn. Engrg.,* GSP 6, ASCE, Reston, VA: 1263-1280.

Rosiwal, A., 1898. "Über geometrische Gesteins-analysen. Ein facher Weg zur ziffermässigen Feststellung des Quantitätsverhältnisses der Mineral bestandteile gemengter Gesteine." *Verh. Königlich-Kaiserliches Geol. Reichsamt* (Wien), 143.

Schneider, J.A., M. F. Randolph, P. W. Mayne, and N. R. Ramsey. 2008. "Analysis of Factors Influencing Soil Classification Using Normalized Piezocone Tip Resistance and Pore Pressure Parameters." *J. Geotech. Geoenviron. Engrg*. 134(11): 1569-1586. https://doi.org/10.1061/(ASCE)1090-0241(2008)134:11(1569)

Shanthi, C., R. Kingsley Porpatham, and N. Pappa. 2014. "Image Analysis for Particle Size Distribution." *Int'l J. of Engineering and Technology,* 6(3): 1340-1345.

Shin, S. "High Resolution Subsurface Soil Characterization by Image Analysis and Vision CPT." Diss. U of Michigan, 2005.

Shin, S., and R. D. Hryciw. 2004. "Wavelet Analysis of Soil Mass Images for Particle Size Determination." *ASCE Journal of Computing in Civil Engineering.* 18, no. 1: 19-27. https://doi.org/10.1061/(ASCE)0887-3801(2004)18:1(19)

Stahly, S., H. Friedrich, and M. Detert. 2017. "Size Ratio of Fluvial Grains' Intermediate Axes Assessed by Image Processing and Square-Hole Sieving." *J. of Hydraulic Engineering*, 143(6): 06017005. https://doi.org/10.1061/(ASCE)HY.1943-7900.0001286

Strom, K.B., R. D. Kuhns, and H. J. Lucas. 2010. "Comparison of Automated Image-Based Grain Sizing Method to Standard Pebble-Count Methods." *J. of Hydraulic Engineering*, 136(8): 461-473.

Sudarsan, B., W. Ji, V. Adamchuk, and A. Biswas. 2018. "Characterizing Soil Particle Sizes Using Wavelet Analysis of Microscope Images." *Computers and Elect. in Agriculture*. 148: 217-225. https://doi.org/10.1016/j.compag.2018.03.019

Tutumluer, E., C. Rao, and J. Stefanski. 2000. "Video Image Analysis of Aggregates." *Final* Project Report, FHWA-IL-UI-278, Civil Eng. Studies UILU-ENG-2000-2015, Univ. of Illinois Urbana-Champagne, Urbana, IL.

Vassiliou, M., and N. Makris. 2011. "Estimating Time Scales and Length Scales in Pulselike

Earthquake Acceleration Records with Wavelet Analysis." Bulletin of the Seismological Society of America. 101 no. 2: 596-618. https://doi.org/10.1785/0120090387

Ventola, A., and R. D. Hryciw. 2019. "On-Site Particle Size Distribution by FieldSed." In Geo-Congress: Engineering Geology, Site Characterization, and Geophysics, edited by C. Meehan, S. Kumar, M. Pando, and J. Coe, 143-151. Reston, VA: ASCE. https://doi.org/10.1061/9780784482131.015

Ventola, A., R. Dolling, and R. D. Hryciw. 2020a. "Image Analysis and Hardware Developments for the Vision Cone Penetrometer (VisCPT)." In Geo-Congress 2020 GSP. 317: 640-648. Reston, VA: ASCE. https://doi.org/10.1061/9780784482803.068

Ventola, A., G. Horstmeier, R.D. Hryciw, C. Kempf, and J. Eykholt. 2020b. "Particle Size Distribution of Kalamazoo River Sediments by FieldSed." J. Geotech. Geoenviron. Eng. 146, no. 12: 05020012. https://doi.org/10.1061/(ASCE)GT.1943-5606.0002421

Ventola, A., and R. D. Hryciw. 2022a. "The Sed360 Test for Rapid Sand Particle Size Distribution Determination." accepted, pending publication, Geotech. Testing Journal, ASTM Int'l, West Conshohocken, PA.

Ventola, A., and R. D. Hryciw. 2022b. "An Autoadaptive Haar Wavelet Transform Method for Particle Size Analysis of Sands," submitted, Acta Geotechnica.

Wettimuny, R., and D. Penumadu. 2004. "Application of Fourier Analysis to Digital Imaging for Particle Shape Analysis." J. of Computing in Civil Engineering, 18(1): 2-9. https://doi.org/10.1061/(ASCE)0887-3801(2004)18:1(2)

White, D. J. 2003. "PSD Measurement Using the Single Particle Optimal Sizing (SPOS) Method." Géotechnique 53, no. 3: 317-326. https://doi.org/10.1680/geot.2003.53.3.317

Zhang, Z., J. Yang, L. Ding, and Y. Zhao, Y. 2012. "An Improved Estimation of Coal Particle Mass Using Image Analysis." Powder Technology, 229: 178-184. https://doi.org/10.1016/j.powtec.2012.06.027

Zheng, J., R. D. Hryciw. 2014. "Optical Flow Analysis of Internal Erosion and Piping in Soil Images Captured by the VisCPT." In Tunneling and Underground Construction GSP. 242: 55-64. Reston, VA: ASCE. https://doi.org/10.1061/9780784413449.006

Zheng, J., R. D. Hryciw, and H.-S. Ohm. 2014. "Three-Dimensional Translucent Segregation Table (3D-TST) Test for Soil Particle Size and Shape Distribution." Proc. of the International Symposium on Geomechanics from Micro to Macro, Cambridge, UK, CRC Press, 1037-1042.

Zheng, J. and R. D. Hryciw. 2016. “Segmentation of Contacting Soil Particles in Images by Modified Watershed Analysis.”, Computers and Geotechnics, 73: 142-15. https://doi.org/10.1016/j.compgeo.2015.11.025